

**Development of core elements for the LISA optical bench -
Electro-optical measurement systems and test devices**

Von der Fakultät für Mathematik und Physik
der Gottfried Wilhelm Leibniz Universität Hannover
zur Erlangung des Grades

Doktor der Naturwissenschaften
- Dr. rer. nat. -

genehmigte Dissertation
von

Dipl.-Phys. Christian Diekmann
geboren am 28.10.1980 in Cloppenburg

2013

Referent: Prof. Dr. Karsten Danzmann
Korreferent: Prof. Dr. Ernst Rasel
Tag der Promotion: 08.02.2013

Kurzzusammenfassung

Die „Laser Interferometer Space Antenna“(LISA) ist ein geplanter Gravitationswellendetektor im Weltraum, dessen Ziel es sein wird, Gravitationswellen im Frequenzbereich zwischen 0.1 mHz und 1 Hz zu detektieren. Diese Detektion wird durch Messung der Abstandsänderungen zweier frei fallender Testmassen bewerkstelligt. In diesem Zusammenhang sind zwei Meilensteine auf dem Weg zu LISA zu nennen: Die „LISA Pathfinder“ Mission wird den freien Fall von zwei Testmassen experimentell überprüfen und das Projekt „LISA Optical Bench“(LOB). In diesem soll ein Prototyp einer optischen Bank entwickelt, gebaut und getestet werden, welcher die Abstandsänderungen der Testmassen bei LISA messen kann. Diese Doktorarbeit wurde im Rahmen dieser Prototypenentwicklung geschrieben.

Eine grundsätzliche Frage in diesem Zusammenhang ist, ob heterodyne Interferometrie in der Lage ist, die durch die Testmasse verursachten Änderungen der optischen Weglänge und der Strahllage, mit der geforderten Genauigkeit zu messen. Die Charakterisierung der entsprechenden Rauschquellen der heterodynen Interferometrie wurde mithilfe zweier quasi-monolithischer Mach-Zehnder Interferometer (MZI) durchgeführt. Eine Längenmessung mit einem optischen Weglängenrauschen von $1.5 \text{ pm}/\sqrt{\text{Hz}}$ für alle Frequenzen oberhalb von 20 mHz und mit einem ansteigenden $1/f$ -Verlauf bei niedrigeren Frequenzen wird demonstriert. Die Auslesung der Strahllage wird mit einem Rauschen von $3 \text{ nrad}/\sqrt{\text{Hz}}$ für Frequenzen oberhalb von 5 mHz und einem ansteigenden $1/f$ -Verlauf bei niedrigeren Frequenzen nachgewiesen. Das gemessene Rauschen der optischen Weglänge und der Strahllageauslesung ist unterhalb der Anforderungen.

Die LOB wird mithilfe von Simulatoren charakterisiert, welche die Schnittstellen zur Testmasse und zum Teleskop schließen. Ein weiterer Satz von MZI wird zum Überprüfen der optischen Weglängenstabilität von Aktuatoren benutzt. Diese sind für die Funktionsfähigkeit der Simulatoren notwendig. Es wird experimentell nachgewiesen, dass die optische Weglängenstabilität dieser Aktuatoren durch den Einsatz von thermischen Kompensationsstufen verbessert und kompatibel mit den Anforderungen für die optischen Weglängenstabilität im Testmasseninterferometer der LOB gemacht werden kann. Dabei wird das optische Weglängenrauschen eines elegant kompensierten Aktuators auf $0.6 \text{ pm}/\sqrt{\text{Hz}}$ für Frequenzen oberhalb von 20 mHz und mit einem ansteigenden $1/f^2$ -Verlauf bei niedrigeren Frequenzen bestimmt.

Quadrantenphotodetektoren sind notwendig um die LOB zu testen. Schlüsselaspekte, um einen Detektor, der kompatibel mit den Anforderungen wie Leistungsaufnahme, Bandbreite und Stromeingangsrauschen ist, zu entwickeln, werden diskutiert. Ein Quad-

rantenphotodetektor mit einer Leistungsaufnahme von 380 mW, einer -3 dB-Bandbreite von 20 MHz und einem Stromeingangsrauschen von weniger als $4 \text{ pA}/\sqrt{\text{Hz}}$ unterhalb von 25 MHz wird vorgestellt.

Das „Backlink“-Fasereperiment am Albert-Einstein-Institut hat aufgezeigt, dass die Messgenauigkeit der heterodynen Interferometrie auf der LOB stark durch Streulicht beeinträchtigt wird. Die Ergebnisse dieses Experiments werden überprüft. Neue Umsetzungen des „Backlink“-Pfads, welche die Beeinträchtigung des Messsignals durch Streulicht komplett vermeiden, werden diskutiert und entsprechende Experimente zum Überprüfen der Konzepte werden vorgeschlagen.

Schlagerworte: Gravitationswelle, Weltrauminterferometrie, elektro-optische Komponenten

The Laser Interferometer Space Antenna (LISA) is a planned space-based gravitational-wave detector which aims to detect gravitational waves in the frequency range between 0.1 mHz and 1 Hz. The detection of gravitational waves is performed by reading-out distance fluctuations between free-floating Proof Masses (PMs). Two milestones have to be mentioned in this context: the LISA Pathfinder mission which aims to verify the free fall of two PMs and the LISA Optical Bench (LOB) project in which a prototype of an optical bench to detect distance fluctuations between PMs in LISA shall be built and tested. This thesis is written in the framework of the development of this prototype.

An elementary question in this context is if heterodyne interferometry can measure an optical pathlength change and beam pointing introduced by a moving PM to the required precision. The characterisation of the respective noise sources of heterodyne interferometry is performed using the example of two quasi-monolithic Mach-Zehnder Interferometers (MZI)s. A length measurement with an optical pathlength noise of $1.5 \text{ pm}/\sqrt{\text{Hz}}$ for all frequencies above 20 mHz increasing with $1/f$ towards lower frequencies is demonstrated. A beam pointing read-out noise of $3 \text{ nrad}/\sqrt{\text{Hz}}$ for frequencies above 5 mHz increasing with $1/\sqrt{f}$ towards lower frequencies is experimentally confirmed, too. The measured optical pathlength noise as well as the beam pointing read-out noise is below the requirement.

The LOB will be characterised by using simulators, which close the interfaces to the PM and the telescope. Another set of MZI is used to test the optical pathlength stability of actuators, that are required for the functionality of the simulators. It is verified that the optical pathlength stability of these actuators can be improved via thermal compensation to be compatible with the requirement for the optical pathlength stability of the PM interferometer of the LOB. Thereby an optical pathlength noise of an elegant compensated actuator of $0.6 \text{ pm}/\sqrt{\text{Hz}}$ for frequencies above 20 mHz increasing with $1/f^2$ towards lower frequencies is established.

Quadrant photodetectors are needed to test the LOB. Key aspects to develop a detector being compatible with the requirements of power consumption, bandwidth, and input current noise are discussed. A quadrant photodetector with a power consumption of approximately 380 mW, a -3 dB bandwidth of all four channels of 20 MHz, and an input current noise of less than $4 \text{ pA}/\sqrt{\text{Hz}}$ up to 25 MHz is presented.

The backlink fibre experiment at the Albert-Einstein-Institut revealed that the precision of heterodyne interferometry on the LOB will be degraded by straylight. The results of this experiment are reviewed. New implementations of the backlink path, which

fully avoid the degradation of the measurement signal by straylight, are discussed and corresponding technology demonstrator experiments are proposed.

Keywords: gravitational wave, space interferometry, electro-optical devices

Contents

Kurzzusammenfassung	iii
Abstract	v
Table of Contents	vii
List of Figures	xi
List of Tables	xv
List of Abbreviations	xvii
1 Introduction	1
2 Picometer experiment	5
2.1 Introduction	5
2.2 Previous work	6
2.3 Experimental setup	8
2.3.1 Phase measurement systems	8
2.3.1.1 LISA Pathfinder phase-measurement system	8
2.3.1.2 Down-conversion LISA Pathfinder	9
2.3.1.3 LISA phase-measurement system	10
2.3.2 Modulation bench	12
2.3.3 Optical bench	14
2.4 Results	14
2.4.1 Phasemeter sensitivity	15
2.4.2 Active stabilisations	18
2.4.3 Data post-processing	19
2.4.3.1 Optical pathlength combinations	20
2.4.3.2 Straylight	20
2.4.3.3 Laser frequency noise	21
2.4.3.4 Beam pointing noise	22
2.4.3.5 Laser intensity noise	28
2.4.3.6 Temperature noise	29
2.5 Noise projections	31

2.6	Conclusions	31
3	Actuator experiment	33
3.1	Introduction	33
3.2	Previous work	35
3.3	Comparison and selection of actuators	37
3.4	Experimental setup	37
3.4.1	Phase measurement system	37
3.4.2	Optical bench	38
3.5	Results	40
3.5.1	Laser intensity noise	41
3.5.1.1	Experimental setup	41
3.5.1.2	Results	42
3.5.2	Laser frequency noise	44
3.5.2.1	Experimental setup	44
3.5.2.2	Results	45
3.5.3	Temperature noise	46
3.5.3.1	Optical pathlength matching	47
3.5.3.2	Temperature measurement system	50
3.5.3.3	Temperature noise suppression	51
3.5.4	Actuator length stability	54
3.5.4.1	Uncompensated actuator	54
3.5.4.2	A simple compensated actuator	57
3.5.4.3	An elegant compensated actuator	58
3.6	Conclusions	63
4	LISA Photodetector	65
4.1	Introduction	65
4.1.1	Imaging optics	66
4.1.2	Photodiode	66
4.1.3	Transimpedance amplifier	67
4.1.4	Phasemeter	69
4.1.5	Requirements and goals	71
4.1.5.1	Photodiode	71
4.1.5.2	Transimpedance amplifier	72
4.2	p-i-n photodiode	72
4.2.1	Layer structure and properties	73
4.2.1.1	Efficiency	73
4.2.1.2	Bandwidth	74
4.2.1.3	Impedance	76
4.2.2	Selection of p-i-n photodiodes	76
4.2.2.1	Silicon	76
4.2.2.2	InGaAs	77
4.2.2.3	Avalanche photodiode	78
4.2.3	Measurement results	79
4.2.3.1	Impedance	79
4.2.3.2	Efficiency	81
4.3	Transimpedance amplifier	84
4.3.1	Model	84
4.3.2	Design	86

4.3.3	Results of the second prototype	91
4.3.3.1	Power consumption	91
4.3.3.2	Transfer function	91
4.3.3.3	Input current noise	92
4.4	Conclusions	93
5	Optical bench backlink	95
5.1	Introduction	95
5.2	Previous work	98
5.3	Straylight degraded backlink path	101
5.3.1	Straylight influence	101
5.3.2	Suppression of straylight	105
5.3.2.1	Balanced detection	105
5.3.2.2	Attenuation	106
5.3.2.3	Direct measurement	111
5.4	Straylight free backlink path	113
5.4.1	Frequency separation	113
5.4.2	Polarisation	115
5.4.3	Free beam backlink	117
5.5	Technology demonstrator experiments	121
5.5.1	Comparison and selection	122
5.5.2	Attenuation demonstrator	124
5.5.3	Backlink free-beam demonstrator	124
5.5.4	Frequency separation demonstrator	125
5.5.5	LISA like backlink path demonstrator	127
5.6	Conclusions	128
6	Conclusions	129
	Appendix	131
1	Matlab code for data post-processing	131
2	Mathematica code for straylight calculations	133
3	Backlink fibre experiment	136
4	Stability analysis	138
4.1	DC coupled transimpedance amplifier	138
4.2	AC/DC decoupled transimpedance amplifier	139
5	DC coupled photodetector	141
6	Schematics	142
7	Data sheets	149
	Bibliography	155
	Acknowledgements	165
	Curriculum vitae	167
	Publications	169

List of Figures

1.1	LISA technology package.	2
1.2	Schematic of the LISA constellation [1, p. 49]. The active transponder scheme is highlighted in the detail picture.	3
1.3	Schematic of a LISA arm.	3
1.4	OptoCad layout of the LISA OB.	4
2.1	Read-out methods of the PM alignment.	6
2.2	Optical pathlength and beam pointing noise of the LTP OB.	7
2.3	Schematic of the LTP PMS.	9
2.4	Schematic of the down-conversion topology.	9
2.5	Beat notes and noise within the down-conversion topology.	10
2.6	Equivalent optical pathlength noise measured with the down-conversion topology.	11
2.7	Schematic of the LISA PMS.	11
2.8	First measurements with a LISA-style phasemeter.	12
2.9	Schematic of the LTP MB and OB.	13
2.10	Photographs of the picometer experiment.	14
2.11	Photograph of the LTP-style phasemeter PM3.	15
2.12	DC amplitude sensitivity of PM3 measured with artificial signals.	16
2.13	Heterodyne amplitude noise of PM3 measured with artificial signals.	17
2.14	Phase noise of PM3 measured with artificial signals.	18
2.15	Pathlength noise measured with PM3 using a frequency generator and optical signals.	19
2.16	Optical pathlength measurements.	20
2.17	Optical pathlength noise of length measurement, π , and Null measurement.	21
2.18	Impact of photodiode combinations on the optical pathlength noise.	22
2.19	Optical pathlength noise of the length measurement in data post-processing.	23
2.20	Measurement of the laser frequency coupling coefficient.	24
2.21	Schematic of differential wavefront sensing.	24
2.22	Raw data and read-out noise of the beam pointing.	25
2.23	Equivalent beam pointing and read-out noise via DWS.	26
2.24	Schematic for correcting noise sources in data analysis.	27
2.25	Equivalent beam pointing and read-out noise via beam centroid measurement.	28

2.26	Measurements of the laser intensity noise at different frequencies.	29
2.27	Schematic of a Wheatstone bridge which is a part of the FPGA thermometer.	29
2.28	Schematic of the setup inside the vacuum chamber.	30
2.29	Temperature measurement system and temperature induced optical path-length noise.	31
2.30	Equivalent optical pathlength noise of measured and calculated noise sources.	32
3.1	OptoCad layout of the telescope simulator.	34
3.2	Optical pathlength stability of actuators.	36
3.3	Schematic of the optical bench.	39
3.4	Optical pathlength noise of the interferometers.	40
3.5	Transfer function of the AM input of the iodine-stabilised laser.	42
3.6	Open-loop gain of the DC laser intensity stabilisation.	43
3.7	Relative intensity noise of the unstabilised and intensity stabilised iodine-stabilised laser.	43
3.8	Schematic of the frequency stability measurement setup.	45
3.9	Influence of laser frequency shift onto optical pathlength.	46
3.10	Temperature noise measurements on aluminium and ULE.	49
3.11	Beam propagation in a 50/50 beam splitter.	49
3.12	Read-out noise of a FPGA thermometer equipped with PT10k and NTC sensors.	51
3.13	Schematic of the thermal shield.	53
3.14	Improvement of the thermal shield.	53
3.15	Uncompensated actuator assembly.	54
3.16	Tip/tilt coupling into optical pathlength noise.	56
3.17	Compensated actuator assembly.	58
3.18	Effective CTE of the "simple" actuator assembly.	59
3.19	Elegant compensated actuator assembly.	60
3.20	Effective CTE of the elegant compensated actuator assembly.	61
3.21	Photograph of the heating cell.	62
3.22	Time series of optical pathlengths compared to actuator temperature.	62
3.23	Change of the effective CTE with machining accuracies.	63
4.1	Schematic of a possible setup of the LOB interferometer output.	65
4.2	Shielding effectiveness of an aluminium housing.	67
4.3	Shielding efficiency of a GORE PTFE cable.	68
4.4	Electrical properties of a GORE PTFE cable.	69
4.5	Physical structure and circuit of a p-i-n photodiode.	73
4.6	Absorption coefficient of different semiconductor materials.	74
4.7	Relation between efficiency and bandwidth of a photodiode.	75
4.8	Equivalent circuit of a p-i-n photodiode.	79
4.9	Impedance of the GAP1000Q and QP22-Q photodiode.	81
4.10	Responsivity of the QP22-Q as a function of bias voltage.	82
4.11	Amplitude response of photodiodes.	83
4.12	Responsivity of the QP22-Q photodiode as a function of bias voltage and temperature.	83
4.13	Transimpedance amplifier noise equivalent circuit.	84
4.14	Input current noise of the GAP1000Q photodiode.	86
4.15	Schematic of an AC/DC decoupled transimpedance amplifier.	87

4.16	First prototype of a quadrant photodetector.	88
4.17	Transfer functions of the first prototype.	89
4.18	Second prototype of a quadrant photodetector.	89
4.19	Transfer function of the LOB photodetector.	92
4.20	Noise of the LOB photodetector.	94
5.1	Depiction of the orbits for the LISA satellites.	96
5.2	Different implementations of the in-field pointing concept for LISA.	97
5.3	Picture of the MOSA.	98
5.4	Schematic of the backlink fibre setup.	99
5.5	Optical pathlength and non-reciprocity of a fibre.	100
5.6	Composition of backreflection of a fibre.	101
5.7	Influence of straylight on a measurement signal within a heterodyne interferometer	102
5.8	Schematic of the influence of straylight onto a phase measurement.	103
5.9	Schematic of two optical benches connected via a backlink fibre.	107
5.10	Optical pathlength noise induced by straylight.	110
5.11	Schematic of two optical benches connected via a backlink fibre using direct straylight measurement.	112
5.12	Schematic of two optical benches connected via a backlink fibre using frequency separation.	114
5.13	Schematic of two optical benches connected via a backlink fibre using different polarisations.	116
5.14	Schematic of two optical benches connected via a free beam backlink.	118
5.15	Simplified schematic of the free beam backlink path.	118
5.16	Optical pathlength change induced by an actuator tilt in the backlink path.	120
5.17	Technology demonstrator experiment for TX laser comparison via a fibre backlink and attenuation of straylight.	125
5.18	Technology demonstrator experiment for TX laser comparison via a free beam backlink.	126
5.19	Technology demonstrator experiment for TX laser comparison via a fibre backlink and frequency separation.	127
1	Schematic of a backlink fibre experiment with movable OBs.	137
2	Equivalent circuit of a DC coupled TIA.	138
3	Equivalent circuit of an AC/DC decoupled TIA.	139
4	Transfer function and input current noise of a prototype QPD and a simple TIA.	141
5	Schematic of a low frequency laser intensity stabilisation.	143
6	Schematic of the FPGA-thermometer.	144
7	Schematic of a photodiode tester.	145
8	Schematic of the first prototype of the LOB quadrant photodetector.	146
9	Schematic of the second prototype of the LOB quadrant photodetector.	147
10	Schematic of a DC-coupled quadrant photodetector.	148
11	Data sheet of the GAP1000Q photodiode from GPD, Page 1 of 2.	150
12	Data sheet of the GAP1000Q photodiode from GPD, Page 2 of 2.	151
13	Data sheet of the GORE PTFE Cable, Page 1 of 3.	152
14	Data sheet of the GORE PTFE Cable, Page 2 of 3.	153
15	Data sheet of the GORE PTFE Cable, Page 3 of 3.	154

List of Tables

2.1	Parameters for PM3 settings within picometer experiment.	16
3.1	Comparison of piezo-driven tip/tilt stages.	37
3.2	Comparison of piezo-driven linear translation stages.	38
3.3	Parameters for PM3 settings within actuator experiment.	38
3.4	Armlength mismatches on the actuator OB	45
3.5	Calculation of the effective CTE of the actuator assembly.	55
3.6	Calculation of the effective CTE of the simple actuator assembly.	58
3.7	Calculation of the effective CTE of the Astrium actuator assembly.	60
4.1	Silicon QPDs with the required efficiency at 1064 nm.	77
4.2	InGaAs photodiodes with the required capacitance.	77
4.3	Fitted parameters of an equivalent circuit of a QP22-Q photodiode.	80
4.4	Fitted parameters of an equivalent circuit of a GAP1000Q photodiode.	80
4.5	Properties of the LMH6624 OpAmp.	86
4.6	Power consumption of the second prototype of the quadrant photodetector to test the LOB.	92
5.1	Straylight levels and straylight suppression in the backlink fibre experiment.	106
5.2	Properties of optics on a possible LISA Optical bench and in the Backlink fibre experiment.	108
5.3	Ratios of straylight and signal amplitudes on a possible LISA Optical bench and in the Backlink fibre experiment.	109
5.4	Read-out limit of the optical pathlength due to electronic noise for a LOB with straylight attenuation.	111
5.5	Characteristics of the signals within the Optical Bench (OB) interferometers, when the frequency separation topology is used for the comparison of the TX lasers.	114
5.6	DWS coupling factors for both actuators of the free beam backlink path for different waist positions.	119
5.7	Trade-off table for the impact of different straylight suppression techniques on the current LISA baseline design.	122
5.8	Beat signals within the additional interferometers of the frequency separation topology.	126

Acronyms

AC	Alternating Current.
ADC	Analog to Digital Converter.
AEI	Albert Einstein Institute.
AM	Amplitude Modulation.
AMP	AMPLifier.
ANU	Australian National University.
AOM	Acousto-Optic Modulator.
APD	Avalanche PhotoDiode.
AR	Anti-Reflection.
COTS	Commercial Of The Shelf.
CTE	Coefficient of Thermal Expansion.
DAC	Digital to Analog Converter.
DAQ	Data Acquisition.
DC	Direct Current.
DCO	Down-Conversion Oscillator.
DFACS	Drag-Free Attitude and Control System.
DI	Digital Interferometry.
DRS	Disturbance Reduction System.
DSC	Discovery Semiconductor.
DUT	Device Under Test.
DWS	Differential Wavefront Sensing.
eLISA	Enhanced LISA.
EOM	Electro-Optic Modulator.
EPP	Enhanced Parallel Port.
FIOS	Fibre Injector Optical Subassembly.
FOV	Field of View.
FPGA	Field Programmable Gate Array.
GBWP	Gain-BandWidth Product.
GRS	Gravity Reference Sensor.

GW	Gravitational Wave.
HR	High Reflectivity.
InGaAs	Indium-Gallium-Arsenide.
InGaAsP	Indium-Gallium-Arsenide-Phosphide.
LISA	Laser Interferometer Space Antenna.
LISO	Linear Simulation and Optimization.
LMB	LISA Measurement Band.
LO	Local Oscillator.
LOB	LISA Optical Bench.
LPF	LISA Pathfinder.
LSD	Linear Spectral Density.
LTP	LISA Technology Package.
MB	Modulation Bench.
MI	Michelson Interferometer.
MLI	Multi-Layer Insulation.
MOSA	Movable Optical SubAssembly.
MS	Measurement Signal.
MZI	Mach-Zehnder Interferometer.
Nd:YAG	Neodymium-Doped Yttrium Aluminum Garnet.
OB	Optical Bench.
OBS	Optical Bench Subsystem.
OGSE	On-Ground Support Equipment.
OLG	Open-Loop Gain.
OpAmp	Operational Amplifier.
OPD	Optical Pathlength Difference.
PA	Phase Accumulator.
PAAM	Point-Ahead Angle Mechanism.
PBS	Polarising Beam Splitter.
PC	Personal Computer.
PCB	Printed Circuit Board.
PIC	Proportional Integral Controller.
PLL	Phase-Locked Loop.
PM	Proof Mass.
PMS	Phase-Measurement System.
QPD	Quadrant PhotoDiode.
REF	REference.
RF	Radio Frequency.
RIN	Relative Intensity Noise.
RX	Received.

S/C	SpaceCraft.
SBDFT	Single Bin Discrete Fourier Transform.
SEPD	Single Element PhotoDiode.
SLS	StrayLight Signal.
SNR	Signal-to-Noise Ratio.
SPI	Suspension Platform Interferometer.
SUK	Schäfter + Kirchhoff.
TDI	Time Delay Interferometry.
TIA	TransImpedance Amplifier.
TS	Telescope Subsystem.
TX	Transmitted.
UGF	Unity-Gain Frequency.
UGL	University of GLasgow.

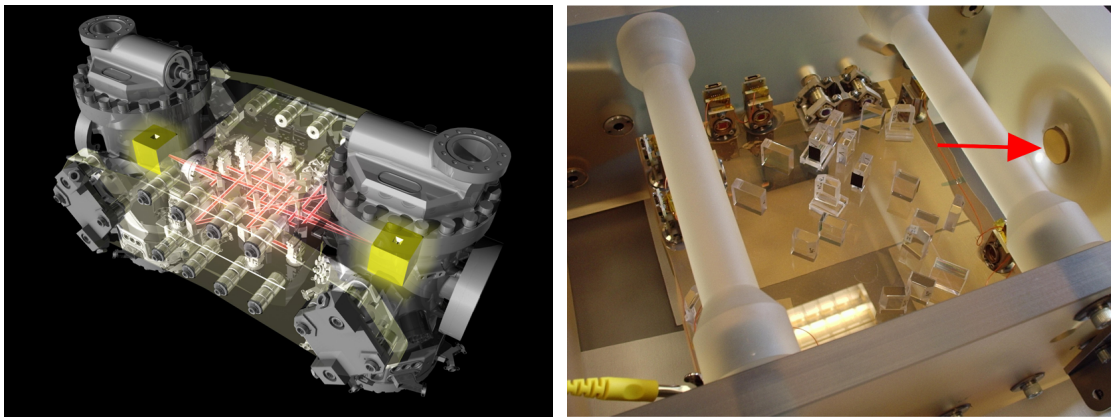
CHAPTER 1

Introduction

Earth-bound gravitational-wave detectors are in service since many decades. The first direct detection of a Gravitational Wave (GW) is awaited within the next years. Large interferometric detectors are VIRGO, LIGO, and GEO 600 [2, 3, 4, 5]. The general layout of them is based on a modified Michelson Interferometer (MI) [6, pp. 12]. The core elements of such a MI are the central beam splitter and the end mirrors of the arms. In current GW detectors these optics are integrated into sophisticated suspension systems to reduce external influences, i.e. mechanical vibrations [7].

The LISA Pathfinder (LPF) mission is a technology demonstrator for core elements of planned space-based GW detectors [8]. It will be launched mid 2014 [9]. The core element of the LPF mission is the LISA Technology Package (LTP) which includes two Proof Masses (PMs). These are cubes, made of a gold-platinum alloy and are depicted in Figure 1.1(a). The device to measure the distance fluctuations between the PMs are heterodyne Mach-Zehnder Interferometers (MZIs). One of the main tasks of the LTP is to prove the principle of the Disturbance Reduction System (DRS) whose counter parts are suspension systems in Earth-bound GW detectors. In space a PM is free-floating when it is absolutely undisturbed and follows the geodesic of space-time. A free-floating PM is realised in a first step by placing it into a vacuum chamber to remove the influence of the residual gas onto the PM. In a second step, a sophisticated control system, called Drag-Free Attitude and Control System (DFACS) in LTP, will take care that the satellite, which comprises the measurement system to measure the distance fluctuations between two free-floating PMs, will follow the free-floating PM [10]. A cornerstone in the LPF mission was a laboratory realisation of the LTP. In this version the PMs were replaced by gold coated mirrors, highlighted in Figure 1.1(b).

Laser Interferometer Space Antenna (LISA) is a planned space-based gravitational-wave detectors [1, 13]. A schematic of the triangular LISA constellation is shown in Figure 1.2. Each satellite comprises two free-floating PMs, whereby the distance fluctuations are measured between two opposite PMs. The distance between those opposite PMs will be increased from about 300 mm in case of LPF to 5 million kilometers to get a reasonable strain sensitivity for GW detection [6, pp. 51]. The long propagation distance between the main SpaceCraft (S/C) and the remote S/C would result in a power of a few hundred picowatt of laser light impinging on the PM in the remote S/C. Assuming



(a) Artwork of the LTP [11]. The free-floating PMs and the beams of the heterodyne MZIs are highlighted. (b) Photograph of the quasi-monolithic heterodyne MZI interferometers of the LTP[12, p. 116].

Figure 1.1: The LISA technology package.

that this amount of light is reflected at the PM of the remote S/C and directly sent back towards the main S/C the light power at the main S/C will be at the order of 10^{-20} W. Therefore LISA is planned to be operated in an active transponder scheme, which is depicted in the detail picture in Figure 1.2. This means that a high power laser on the remote S/C will be phase locked to the incoming weak light. The light of the high power laser will be sent out to the other S/C.

The current baseline for LISA foresees that each satellite consists of two Movable Optical SubAssembly (MOSA). Each MOSA is pointing along one arm of the triangular LISA formation towards the MOSA of the opposite satellite, see Figure 1.3. One MOSA consists of a Gravity Reference Sensor (GRS) head, an Optical Bench Subsystem (OBS), and a Telescope Subsystem (TS). A GW changes the distance between two free-floating PMs on the opposed MOSAs. The measurement of this is split into three separate ones: the distance fluctuations between the OBs and the distance fluctuations between each PM and the according OB, see Figure 1.3. The core element of the MOSA is the OBS which performs the measurements to obtain the GW signal. This OBS is explained in the following.

Figure 1.4 depicts an OptoCad layout of a planned OBS, which is called LISA Optical Bench (LOB). The development of the LOB is a major step towards LISA [15, 1]. A LOB comprises four interferometers: science, reference, PM, and Point-Ahead Angle Mechanism (PAAM). The science interferometer is used to phase lock the Transmitted (TX) laser to the Received (RX) laser and to read-out the distance fluctuations between the opposing OBs. The reference interferometer compares the TX laser to the Local Oscillator (LO) laser. The source of the LO laser beam is the TX laser of the second OB on the same satellite, which is guided via the backlink path (a fibre) to the first OB. A portion of the local TX light is also directed to the reference interferometer on the second OB and serves as LO there. With both reference interferometers the TX lasers can be compared. The PM interferometer is used to read-out the distance fluctuations between the OB and its PM. The RX beam and the TX beam have an angular offset at the telescope interface, which is introduced by the fact that beam propagation between the satellites takes about 16.6 s while the satellites are moving. Therefore the PAAM introduces a lead angle to the TX

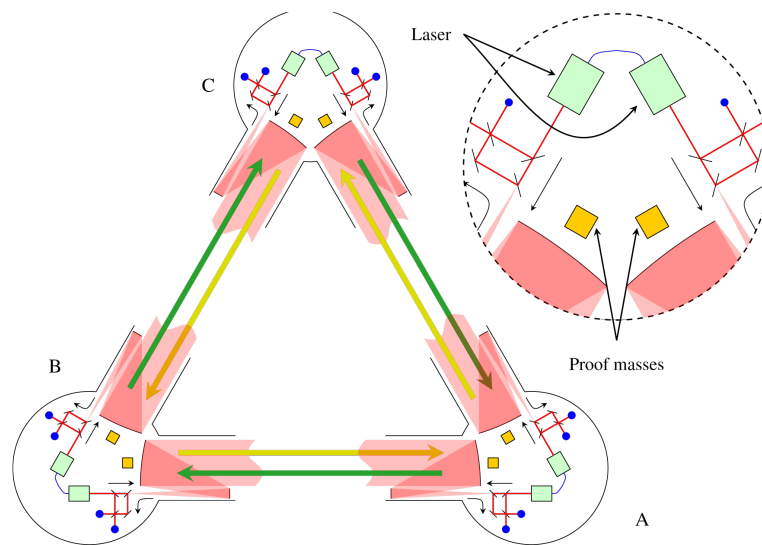


Figure 1.2: Schematic of the LISA constellation [1, p. 49]. The active transponder scheme is highlighted in the detail picture.

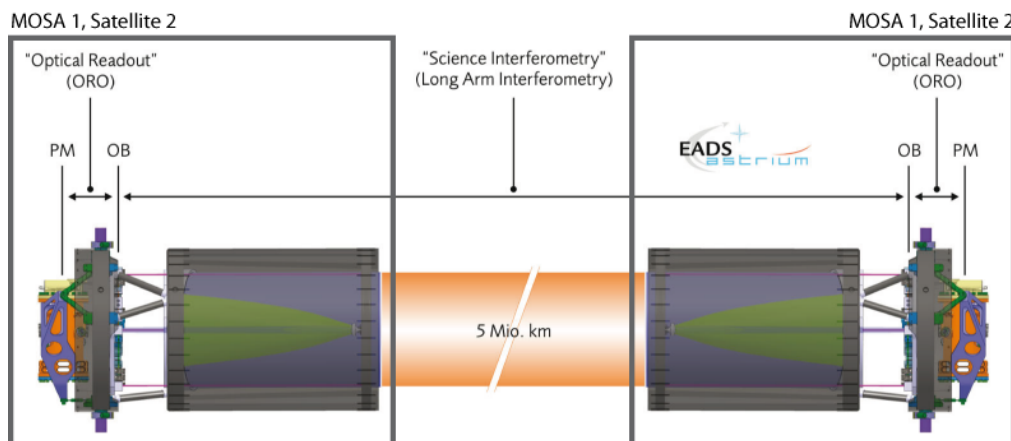


Figure 1.3: One LISA arm is composed of two MOSAs and the distance measurement between the PMs is performed via three individual distance measurements [14].

beam. The PAAM interferometer reads out the behaviour of the PAAM.

Outline of this thesis

This thesis was written in the context of the development of the LOB. The treated topics outline the steps that were taken from the beginning of the project until now.

At the beginning of the LOB project, the concepts and requirements of the LOB were reviewed. In Chapter 2 the read-out methods of the PM position with respect to the LOB are presented and their impacts on the sensitivity of the LOB interferometer are theoretically estimated. Due to the fact that the required sensitivity was not demonstrated until that time, one read-out method is used to verify experimentally the sensitivity requirements for the read-out of the PM position with respect to the LOB. This read-out method is analysed in detail.

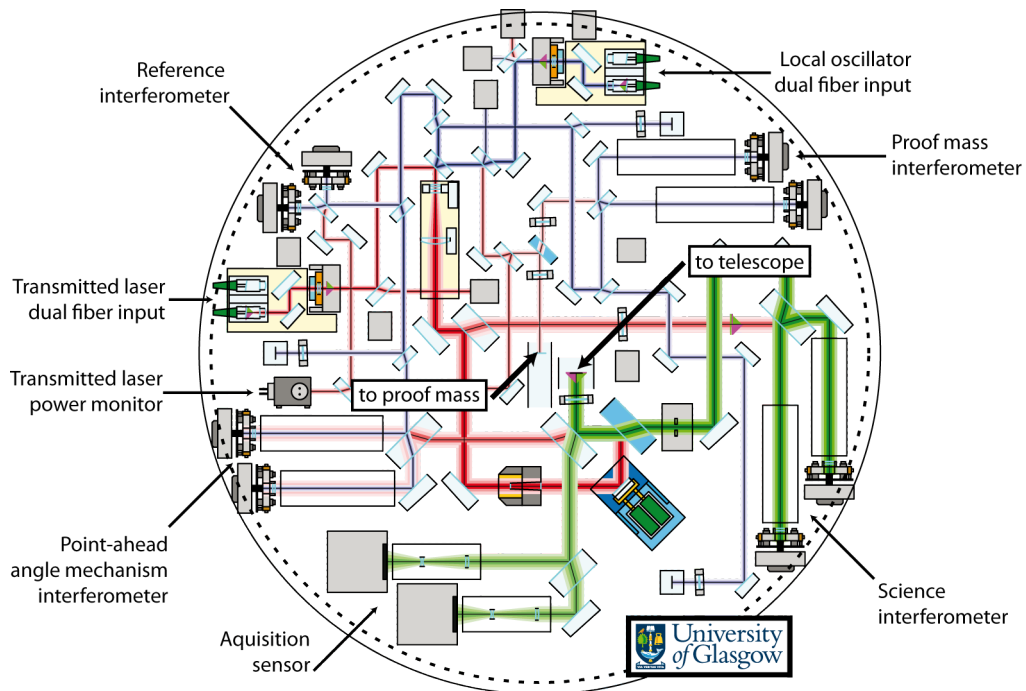


Figure 1.4: OptoCad layout of the OB for LISA. The fibre inputs of the lasers, the different interferometers / photodetectors, and the most important interfaces are highlighted.

In the design phase of the LOB project test devices, which were required to close the interfaces of the LOB to the PM and to the telescope, were developed. A critical component of these test devices were actuators. In Chapter 3 the question, whether Commercial Of The Shelf (COTS) actuators can be made compatible to the stringent optical pathlength stability requirements of the LOB, is answered. An experiment to measure the optical pathlength stabilities of actuators is characterised in detail. A method to reduce the optical pathlength stability of the COTS actuators is presented and experimentally verified.

The quadrant photodetectors for the read-out of the heterodyne interferometers of the LOB were developed in the design phase of the LOB project, too. In Chapter 4 photodiode semiconductor materials are investigated and the impact of their properties on the read-out limit of the science interferometer of the LOB is analysed. Methods to develop a quadrant photodetector from a single element photodetector to test the LOB are explained. A quadrant photodetector is presented, which is tested successfully against the LOB requirements.

During the assembly and integration phase of the LOB project a revision of the LOB project was performed. A central issue of the current implementation of the backlink path of the LOB is the degradation of the optical pathlength noise of the LOB interferometers due to straylight. In Chapter 5 precursor investigations of a backlink path using a fibre are reviewed. New implementations of the backlink path are proposed to completely avoid straylight degradation of the optical pathlength noise of the LOB interferometers.

Low-frequency length measurements at the picometer level

This chapter presents an experiment to characterise and summarise the remaining noise sources of the LPF measurement scheme with respect to the LISA requirements for the optical pathlength and beam pointing noise levels of the PM interferometer. At the beginning of this chapter the importance of the PM surface displacement and pointing read-out to pm and nrad accuracy is motivated and the investigations already performed are summarised. Afterwards the experimental setup is explained, focusing on different available technologies for the measurement scheme. This is followed by a presentation of the results for the phasemeter performance, the improvements of the measurements by active stabilisations and by using data post-processing algorithms. In the end the results are summarised and conclusions for the other measurement schemes that have not been tested yet are drawn.

2.1 Introduction

The measurement of the distance fluctuations between the opposite PMs in one arm of the LISA constellation is split into three measurements: one measurement of the distance fluctuations between the OBs and two measurements of the distance fluctuations between the OBs and the according PMs, see Chapter 1. In this chapter the main focus is on the read-out of the PM displacement and pointing with respect to the OB. Figure 2.1 depicts two methods to read-out the PM position with respect to the OB. The method on the left hand side is used within the LPF mission. The separation of the incoming and outgoing measurement beam on the PM surface is realised via a small angle of incidence. The disadvantage of this method is that the measurement beam is laterally shifted with respect to the reference beam on the Quadrant PhotoDiode (QPD), when the PM is not in its nominal position. This will change the coupling factor between PM surface pointing noise and measured beam pointing noise, also called Differential Wavefront Sensing (DWS) [16]. The method presented on the right hand side uses polarising optics to separate the incoming and the outgoing measurement beam on the PM surface and it is the baseline for the read-out of the PM position within the current LISA design. The p-polarised measurement beam is transmitted by a Polarising Beam Splitter (PBS). Afterwards its polarisation is changed to circular polarised by a quarter-wave plate. After the circular polarised beam has been reflected by the PM surface its

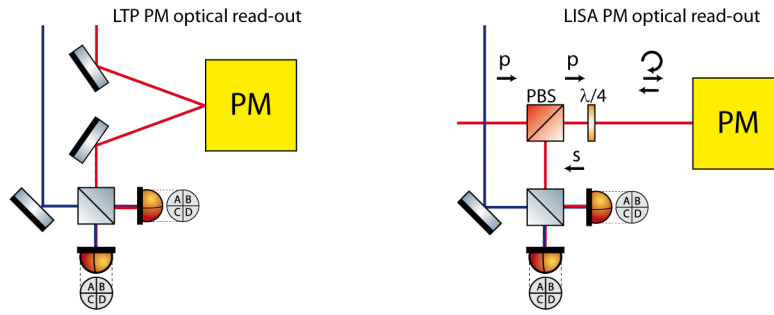


Figure 2.1: Read-out methods of the PM alignment with respect to the OB reference frame. In the LTP the PM alignment is read-out with a beam, which is by design not perpendicular to the PM surface. In LISA the measurement beam is perpendicular to the PM surface and the beam separation is done via polarisation optics.

polarisation is changed to s-polarisation by the already mentioned quarter-wave plate. The PBS reflects the s-polarised beam. Then the measurement beam is guided to the PM interferometer. The compatibility of the polarising optics with the requirements for LISA was investigated in detail and confirmed in [17, pp. 59]. This work focuses on phase measurement techniques to measure to such a precision. Therefore the LISA requirements for the read-out of the PM position with respect to the OB are introduced.

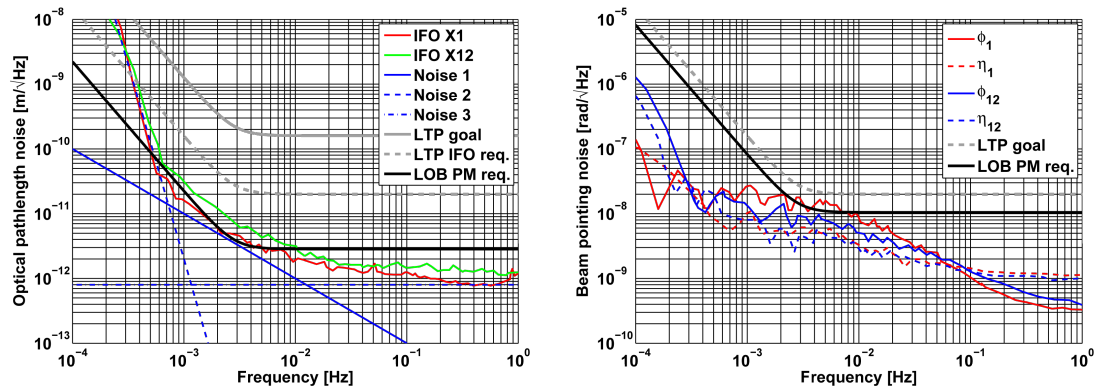
Within the LISA noise budget the read-out of the PM alignment has the most stringent requirement with $1.42 \text{ pm}/\sqrt{\text{Hz}} \cdot u_1(f)$ for the displacement noise and $5.24 \text{ nrad}/\sqrt{\text{Hz}} \cdot u_1(f)$ for pointing noise of the PM surface. $u_1(f)$ is hereby the typical frequency dependence for LISA requirements which is constant between 1 Hz and 2.8 mHz and increases with $1/f^2$ towards lower frequencies [14, pp. 100].

$$u_1(f) = \sqrt{1 + \left(\frac{2.8 \times 10^{-3} \text{ Hz}}{f [\text{Hz}]} \right)^4} \quad (2.1)$$

According to the right part of Figure 2.1 the displacement and the jitter of the PM surface is measured under nominal incident with respect to the OB reference frame. Therefore the induced optical pathlength change and the induced beam pointing change that will be measured with the PM interferometer are twice the displacement and pointing changes of the PM surface. Thus the requirements used for this experiment are $2.84 \text{ pm}/\sqrt{\text{Hz}} \cdot u_1(f)$ for the optical pathlength measurement and $10.48 \text{ nrad}/\sqrt{\text{Hz}} \cdot u_1(f)$ for the beam pointing measurement.

2.2 Previous work

The experiment was set up and performed at the beginning of 2010. Until this time optical pathlength and beam pointing measurements of a moving optical PM surface dummy were only performed for the LTP within the LPF mission [18]. A photograph of the LTP OB and the positions of the PM surface dummies can be seen in Figure 1.1(b) on page 2. Figure 2.2 summarises the results of the two main LTP measurement interferometers, whereby the PM surfaces were simulated by static ZerodurTM mounted mirrors. The first interferometer (X1) measures the relative position of PM 1 with respect to the LTP OB and the second (X12) measures the relative position of the two PM to each other. In Figure 2.2(a) the optical pathlength noise of both interferometers corrected with the optical



(a) Optical pathlength noise of the two measurement interferometers (X1) and (X12). The optical pathlength noise from the reference interferometer has already been subtracted. Additionally the LTP and LISA requirements are plotted as well as the assumed noise sources Noise 1-3.

(b) Beam pointing noise of the two measurement interferometers X1 and X12. Additionally the LTP and LISA requirements are plotted.

Figure 2.2: Results of the optical pathlength and beam pointing noise of the LTP OB, whereby the PM are simulated by ZerodurTM-mounted stable mirrors [18].

pathlength noise measured in the reference interferometer are plotted against the LTP and LISA requirements. Both interferometers show a noise of less than $2.84 \text{ pm}/\sqrt{\text{Hz}}$ for frequencies higher than 10 mHz. For lower frequencies the noise is first increasing with a $1/f$ towards 0.7 mHz, below this frequency the noise increases with a steep $1/f^6$ characteristic. The shape of the interferometer noise can be approximated by three noise sources, which will be identified later.

The DWS measurements that were performed with the LTP interferometer are presented in Figure 2.2(b). Again the according LTP and LISA requirements are plotted. The measurements themselves show a sufficiently low noise level of the beam pointing noise with respect to the LISA beam pointing noise read-out requirement. Nevertheless the read-out noise for the beam pointing has to be characterised to identify in which frequency ranges the DWS measurements are limited by sensor noise.

Other important experiments at the Albert Einstein Institute (AEI) that used heterodyne MZIs and the LTP modulation scheme are the backlink fibre experiment and the polarisation optic experiment [19, pp.5] [17, pp. 59]. The backlink fibre experiment was not compatible with the goal of determining optical noise sources because it was suffering from straylight. More details of this experiment can be found in Chapter 5. The setup of the polarisation optic experiment was not finished at the beginning of 2010 and its complexity was not ideal to search for read-out noise.

A consequence of this was that the results, presented in Figure 2.2 were the best analysed results with respect to the read-out of the PM displacement at that time. Therefore this experiment was started to analyse the remaining noise sources of the optical read-out of the PM displacement with respect to the OB reference frame. A general requirement for this experiment has been the similarity to the equipment that will be used during testing of the LOB.

2.3 Experimental setup

The experimental setup was composed of three parts: the Phase-Measurement System (PMS), the Modulation Bench (MB) and the ZerodurTM-based heterodyne MZI. This section starts with an introduction to the available PMS at the AEI and selects the most appropriate one for the verification of the requirements. This is followed by a description of the MB for generating the heterodyne signal, which is determined by the selected PMS. In the end the ZerodurTM-based heterodyne MZI is explained.

2.3.1 Phase measurement systems

The PMS is a device which measures the phase difference between two sinusoidal signals or the difference of a single sinusoidal signal with respect to a master clock. A short introduction into techniques to measure this phase difference can be found in [20, pp. 38]. This subsection focuses on the description of the available PMS at the AEI at the beginning of 2010 and compares their advantages and disadvantages. Thereby two aspects are taken into account: first, the verification of the requirements with the picometer experiment and second the testing of the LOB. This subsection ends with the selection of the appropriate PMS for the verification of the requirements in Section 2.1 and gives an outlook for the testing of the LOB.

2.3.1.1 LISA Pathfinder phase-measurement system

The working principle of the LTP PMS is described in great detail in [21, pp. 33]. Figure 2.3 briefly summarises these information. The heterodyne signals of the interferometers have a stable frequency in the kHz range. They are detected by QPDs based on silicon and Indium-Gallium-Arsenide (InGaAs). The bias voltage for the photodiodes is generated by the PMS. The photocurrent of each photodiode element is converted via a TransImpedance Amplifier (TIA) inside the PMS into a proportional voltage. In a next step the signals are low-pass filtered. The corner frequency of the filter is chosen according the Nyquist criterion to suppress anti-aliasing within the Analog to Digital Converter (ADC). The digital data is then analysed by a Field Programmable Gate Array (FPGA), which performs a Single Bin Discrete Fourier Transform (SBDFT) to derive the phase difference between the heterodyne interferometer signal and an internally generated reference signal of the same frequency. Each channel of the LTP PMS has its own TIA, ADC and FPGA. One additional FPGA collects the data from all channels and transfers the data via an Enhanced Parallel Port (EPP) interface to a Personal Computer (PC).

With slight modifications the LTP PMS and the LTP modulation scheme can be used for testing of the LOB. These adoptions are necessary to fulfill the requirements for the science interferometer on the LOB and are driven mainly by the electronic noise sources described in Chapter 4.1.4. The silicon photodiodes have to be replaced by InGaAs. Due to the higher efficiency of the InGaAs photodiodes (0.7 A/W to 0.15 A/W) the current amplitude of the signal and the ratio of signal to shot noise is increased. Additionally the shot noise current induced by the LO in the science interferometer is increased which reduces the influence of electronic noise onto the read-out limit. A TIA with a bandwidth of at least approximately 20 kHz has to be connected directly to the InGaAs photodiode. The input current noise of the TIA needs to be below the requirement of $4 \text{ pA}/\sqrt{\text{Hz}}$ at the heterodyne frequency. The Relative Intensity Noise (RIN) of the laser beams at the

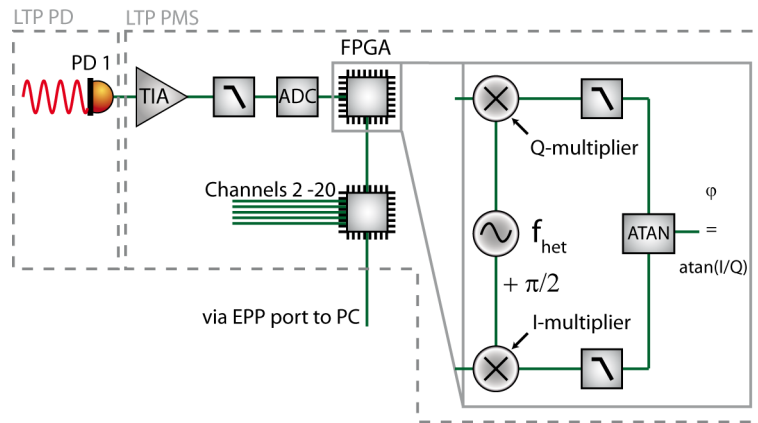


Figure 2.3: Schematic of the LTP PMS, which measures heterodyne optical signals with constant kHz frequencies and computes their phase and additional data.

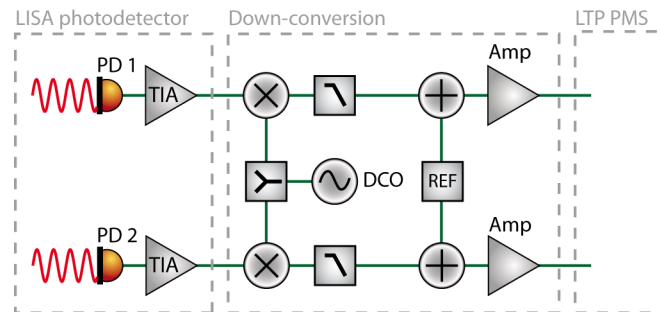


Figure 2.4: Schematic of the down-conversion topology, which converts the LISA MHz beat notes to kHz signals compatible with the LTP PMS.

heterodyne frequency need to be stabilised to a level which allow shot-noise limited read-out in the science interferometer. The electronic noise is uncritical for the other interferometers.

2.3.1.2 Down-conversion LISA Pathfinder

The LTP PMS can also be used in combination with the LISA modulation scheme and LISA photodiodes if the heterodyne signals of the interferometers with a frequency of up to 25 MHz are down-converted to a few kHz in an intermediate step. Figure 2.4 depicts this method. The MHz beat notes are detected via dedicated LISA photodetectors. Their output signal is then multiplied within a mixer with the signal of a Down-Conversion Oscillator (DCO), which has a frequency offset of a few kHz with respect to the MHz beat notes. The output of the mixer is low pass filtered to obtain only the kHz beat notes between the two signals. To make this signal compatible with the LTP PMS a small offset from a voltage REFERENCE (REF) is added. In the same step the signals are multiplied with an AMPLIFIER (AMP). Afterwards the phases of the kHz beat notes are measured with the LTP PMS. The down-conversion relies strongly on the phase-stability of the power splitters, which distribute the down-conversion oscillator to the individual channels.

The advantage of this measurement scheme is that the well-known LTP PMS can be used in combination with LISA-compatible photodetectors and modulation scheme. Figure 2.5 illustrates this measurement process in the frequency domain. The measured

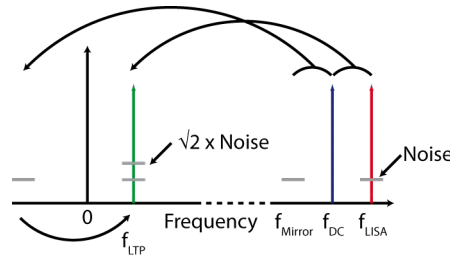


Figure 2.5: Beat notes and noise within the down-conversion scheme, which enables the LTP PMS to be used with LISA heterodyne frequencies.

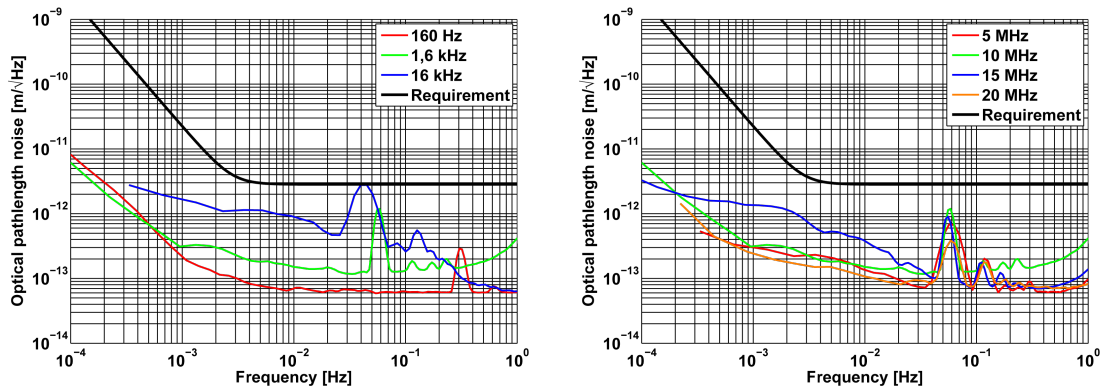
beat note at frequency f_{LISA} is converted with the signal at f_{DC} to a beat note at f_{LTP} . Unfortunately, also the noise at frequency f_{Mirror} is converted to frequency $-f_{LTP}$. During the phase estimation for the signal at frequency f_{LTP} the noise at frequency $-f_{LTP}$ is added uncorrelated. This increases the read-out limit for the science interferometer due to electronic noise, shot noise and relative power noise by a factor $\sqrt{2}$ [20, pp. 129].

For the testing of the LOB this increased noise can be accepted because the noise source is known and can be implemented in the noise budget of the science interferometer. The stability in the science interferometer has then to be tested against a requirement which is relaxed by a factor of $\sqrt{2}$. It has to be taken into account that other noise sources that are powered by temperature or frequency noise are not influenced. An additional stabilisation of the laser power is not needed because the amplitude stability of a Neodymium-Doped Yttrium Aluminum Garnet (Nd:YAG) laser is shot-noise limited for frequencies higher than 10 MHz for a few mW detected power.

The performance of the down-conversion technique was investigated with signals from a frequency generator in a bachelor thesis at the AEI [22]. It could be verified that this measurement scheme is able to detect the phase difference between the MHz beat signals to a level which is sufficient for testing of the LOB. The main results which were obtained with artificial signals from a frequency generator can be seen in Figure 2.6. To obtain these results the mixers were passively temperature stabilised. Figure 2.6(a) shows the phase noise, expressed as equivalent optical pathlength noise of a 10 MHz beat note signal which was down-converted to different frequencies. The curves show the lower the down-conversion frequency the better the performance. Figure 2.6(b) shows the equivalent optical pathlength noise of beat note signals at different frequencies which were down-converted to 1.6 kHz. The optical pathlength noise of the beat signal at 15 MHz is for frequencies below 40 mHz above the other curves but still under the requirement. Therefore this difference was not investigated further.

2.3.1.3 LISA phase-measurement system

A schematic of the LISA PMS can be seen in Figure 2.7. The beat notes within the LISA measurement scheme are in the range of 1 to 30 MHz and are slowly drifting. The change is driven by a Doppler shift which is induced by the relative motion of the satellites [23]. Therefore a LISA PMS has to track the beat notes. This is done by implementing a control loop (digital Phase-Locked Loop (PLL)) in the PMS. The low-pass filtered I-part of the quadrature mixing scheme (upper part of FPGA inner structure in Figure 2.7) is used as the sensor for a Proportional Integral Controller (PIC) which is the input signal for a Phase Accumulator (PA). The PA is used to derive from the look-up table, represented by



(a) Artificial LISA beat note at a frequency of 10 MHz (b) Artificial LISA beat note at different frequencies down-converted to 1.6 kHz [22].

Figure 2.6: Phase noise, expressed as equivalent optical pathlength noise of the difference of two channels of the down-conversion topology of LISA beat signals to LPF frequencies.

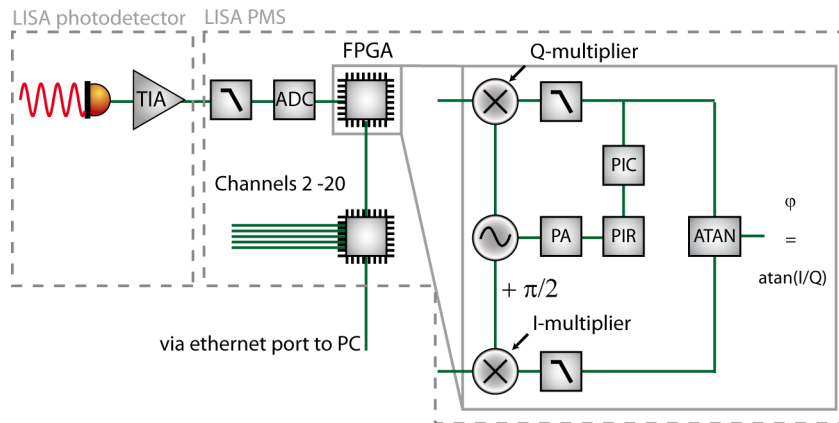
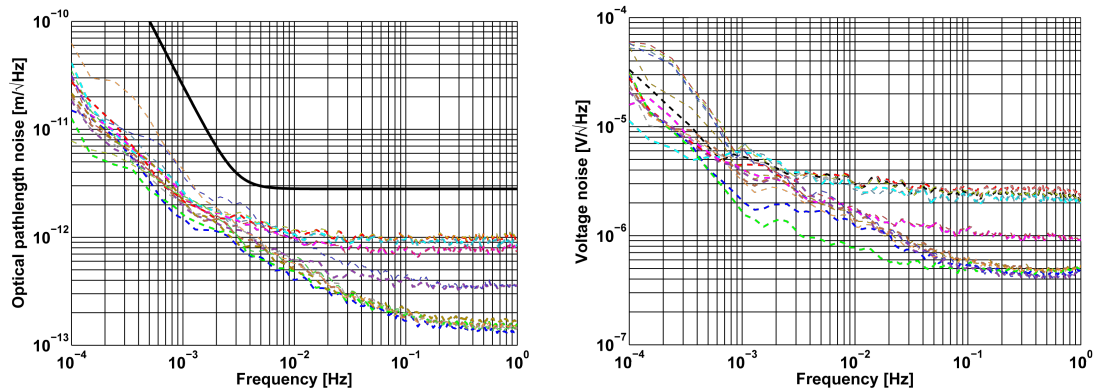


Figure 2.7: Schematic of the LISA PMS. Two of the main differences to the LTP PMS are that the TIA is located close to the photodiode and the phase estimation algorithm inside the FPGA is able to track beat notes with varying frequency.

the frequency generator symbols in Figure 2.7, the sine and cosine signals with the right frequency. Detailed information about the LISA PMS can be found in [24, pp. 25].

A LISA-style phasemeter for the testing of the OB was developed by Oliver Gerberding at the AEI in 2012. The used hardware was a Virtex-6 FPGA ML605 evaluation kit from Xilinx and an analog-to-digital converter board FMC-116 with 16 channels from 4dsp [25] [26]. The code for the FPGA programme was based on the code presented in [24, pp. 25]. First tests of this phasemeter have been performed in the laboratory at the end of October 2012. The measurement signals for the 16 channels were generated by splitting the signal from a frequency generator via a resistive splitter, which is impedance matched to 50Ω . The pilot tone, which was used to correct the ADC jitter noise, was generated of a frequency generator signal. This was filtered by a PHP-50 high pass filter from Mini-Circuits and split afterwards 16 times by PSC-2-1 power splitters from Mini-Circuits [27] [28]. Afterwards the measurement signal and the pilot tone were added by PSC-2-1 from Mini-Circuits and fed into the phasemeter.

Figure 2.8 shows the results of a measurement with the LISA-style phasemeter. The



(a) Optical pathlength noise of the difference of Channel 1 to 2...16. (b) Voltage noise of the difference of Channel 1 to 2...16.

Figure 2.8: Results of the first measurements with a LISA-style phasemeter at a measurement signal frequency of 13 MHz and a pilot tone frequency of 35.5 MHz. Different cable lengths were used for the measurement signals. Input signals were produced by a function generator.

measurement signal frequency was 13 MHz and the pilot tone frequency was 35.5 MHz. Different cable lengths (0.5 m, 0.7 m and 2 m) were used between the resistive splitter of the measurement signal and the PSC-2-1 adder. The phase noise of the measurement signals were corrected with phase noise of the pilot tone signals. The resulting phase noise, expressed as equivalent optical pathlength noise of the difference of two channels of the measurement signals in Figure 2.8(a) was well below the requirement for all cable lengths. A second result was that the longer the cable the higher the optical pathlength noise. This effect was also seen in the measurement of the heterodyne amplitude noise, presented in Figure 2.8(b). The investigations on the LISA-style phasemeter are on-going and first measurements at the pm level with optical signals are awaited for the beginning of 2013.

Thus no LISA PMS with a sufficient number of channels and sensitivity was available at the AEI at the beginning of 2010. Other experiments that used the LISA modulation scheme and LISA phasemeter were not performed at the beginning of 2010 at the AEI. Additionally the development of the TIA of the LISA photodetectors was not finished. The non-finished TIA of the LISA photodetectors were also the reason for not using the down-conversion technique. Therefore the LPF PMS and the modulation scheme was chosen to perform the picometer experiment to verify the requirements presented in Section 2.1. Nevertheless the baseline for testing the LOB was a LISA PMS using the according photodetectors. The similarity between the PMSs allowed to transfer the knowledge about the optical noise sources, which were found with the LTP modulation scheme, to the LISA modulation scheme. The down-conversion technique was developed as a fall-back solution to test the LOB, if the LISA PMS would not have been available at the right time.

2.3.2 Modulation bench

A detailed schematic of the MB can be seen on the left hand side of Figure 2.9. The input laser frequency f_0 was generated by a fibre-coupled iodine-stabilised Nd:YAG laser from Innolight [29]. More details on its amplitude and frequency stability can be

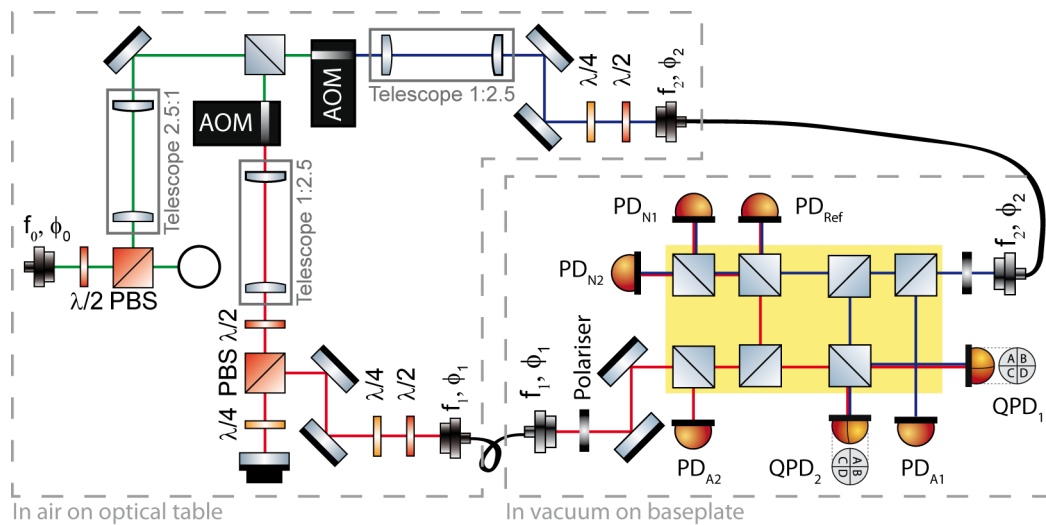
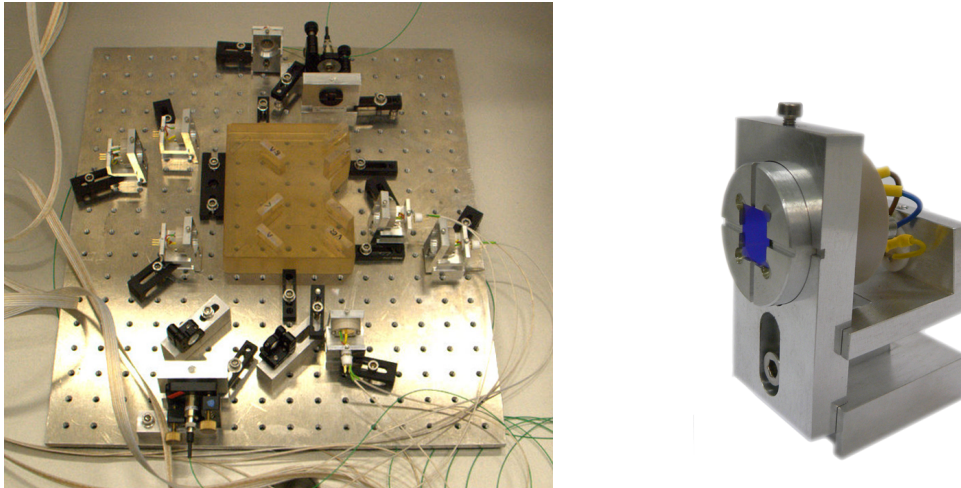


Figure 2.9: The LTP MB on the left hand side generates two frequency shifted beams via AOMs out of one beam. The OB on the right hand side contains two MZIs which allow to perform length measurements.

found in Subsection 3.5.1 and Subsection 3.5.2. The available power at the input of the interferometer could be varied by the combination of a half-wave plate and a polarising beam splitter at the entrance of the modulation bench. Other solutions to change the input power like the adjustment of the driving power for the Acousto-Optic Modulator (AOM) and the misalignment of the fibre coupling efficiency have been used at the backlink fibre experiment [19, pp. 5].

Afterwards the input beam was split by a 50/50 beam splitter and each beam was frequency-shifted via an AOM from Isomet [30]. More details on the characteristics of the used AOMs can be found in [31, pp. 307]. The AOMs shift the frequencies by an amount of $80 \text{ MHz} \pm 812 \text{ Hz}$. The electronic for the generation of the Radio Frequency (RF) signals is described in detail in [21]. One of the main disadvantages of this modulation scheme is that crosstalk between the high power RF drivers of the AOMs induces sidebands on the optical signals, which limit optical pathlength measurements between the MZIs. The influence is proportional to the amount of crosstalk. The problem can be overcome by stabilising the differential phase between the two beams at the input of the stable MZI. Therefore a piezo-mounted mirror was located in the beam path of one of the laser beams in the MB. In other experiments, the mirror was placed under an angle of incidence of 0° plus a small tilt, to separate the incoming and outgoing beam on the mirror. This had the disadvantage, that at incident angles which deviated significantly from 0° , the beam would have been shifted, when the mirror moved. This in the end spoiled the fibre coupling efficiency. In this setup the separation between incoming and outgoing beam was realised by a quarter-wave plate and a polarising beam splitter, which made the alignment of the beams much easier. The measurement beams were guided via fibres to the experiment, which was located in a vacuum chamber. The polarisation of the light was matched to the fibre axis via quarter- and half-wave plates using a polarimeter from Schäfter und Kirchhoff. [32] This reduced the effect of the fibres to act as wave plates. In combination with the polarisers at the output of the fibres, the intensity noise of the beam was reduced. [19, pp. 55]



(a) Photograph of the OB on the aluminium baseplate (b) Detailed photograph of the photodiode mount in the vacuum chamber.

Figure 2.10: Photographs of the picometer experiment.

2.3.3 Optical bench

The main measurements have been performed on a stable OB made of ZerodurTM, which contained two MZI, see right hand side of Figure 2.9. The building process is described in detail in [12, Ch. 2.2.1].

Directly after the fibre output couplers of the OB polarising beam splitter were placed to clean up the polarisation of the light. At the input of the interferometer 50/50 beam splitters were used to monitor the laser intensity noise, which could then be used to stabilise the laser intensity via the AOMs. The polarisation was also cleaned up at the output of the interferometers with Polarcor[®] filters [19, p. 42]. These were mounted in front of the photodiodes, see Figure 2.10(b).

One of the two MZI was used as the reference interferometer, which served two purposes. First, measurement and subtraction of the external noise sources from the second MZI. Second, the phase of the reference interferometer was later used to stabilise the pathlength difference between the two beam paths from the first beam splitter on the MB to the beam combiner of the reference interferometer via actuation on the piezo-mounted mirror on the MB. One of the two output ports of the beam combiner of reference interferometer was split again to make a Null measurement. This measurement was used to obtain information about the lower limit for the optical pathlength read-out noise, which included the electrical chain between the photodiodes and the phasemeter.

The other MZI was used on the one hand for the length measurement and on the other hand to measure the angular jitter of the beam via DWS and obtain the read-out limit for the DWS. For this purpose both output ports of this MZI were equipped with QPDs. More details on DWS can be found in [33] [34] [35] and in Subsection 2.4.3.4.

2.4 Results

This section presents the results accomplished with the picometer experiment. It starts with a characterisation of the LTP-style phasemeter using electrical signals and a comparison to a measurement with optical signals. Afterwards length measurements on



Figure 2.11: LTP-style phasemeter PM3 with 20 input channels. Additionally the transimpedance signals from channel 13 to 20 can be monitored directly with an oscilloscope. The sum of four channels in a row, starting at channel 1, can be monitored, too. Outputs for the bias voltage are also available. The cables of the inputs are shielded.

an ultra-stable OB made of ZerodurTM are presented, whereby step by step well-known stabilisation techniques for a LTP modulation scheme were turned on. To decrease the noise of the length measurements below the requirements the measured data had to be analysed and a correction method had to be applied.

2.4.1 Phasemeter sensitivity

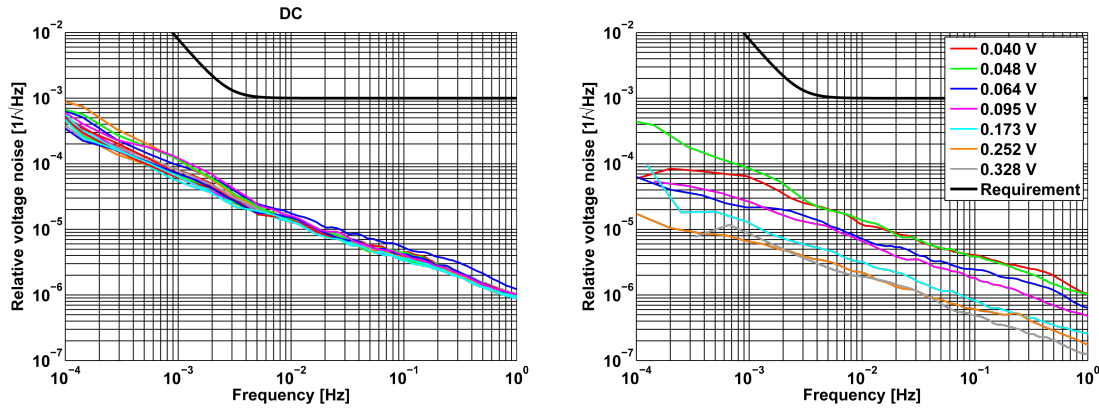
Figure 2.11 shows a picture of the LTP-style phasemeter, which was used for this experiment. Its working principle was described in Subsection 2.3.1.1. In contrast to its precursor version that was used at the backlink fibre experiment each channel was shielded individually to suppress cross-coupling of the channels. Shielded RG174 cables were used outside of the vacuum chamber. In vacuum GORE PTFE cables were used, see Subsection 4.1.3. Special care was taken to suppress ground loops at the input channels by connections in a star-shaped manner.

The details on the operating parameters of the phasemeter are listed in Table 2.1. They are a reasonable basis for the analysis of the phasemeter read-out noise. The most important parameters are the heterodyne frequency of about 1624 Hz and the output data rate of approximately 32 Hz.

The operational reliability and the performance of the phasemeter was tested by applying the same signal from a frequency generator to all phasemeter input channels. Since the phasemeter input channels are configured as transimpedance amplifiers, an adapter had to be built. It consisted of an input for the signal from a function generator. The signal was then split via 20 resistors in parallel and fed into the input of the phasemeter channels. The same resistors as in the phasemeter TIA were used (5 k Ω) to have a gain of 1. For the low heterodyne frequencies of the LTP modulation scheme impedance matching via power splitters was not needed.

Table 2.1: Detailed Parameters for PM3 settings within picometer experiment.

Parameter	Unit	Value	Remark
Heterodyne frequency f_{het}	Hz	1623.38	$f_{\text{het}} = f_{\text{samp}}/N_{\text{SBFT}} \cdot m$
Sampling frequency f_{samp}	kHz	800	
Length of sampled dataset N_{SBFT}	Samples	24640	
Frequency component m corr. to f_{het}		50	
Phase measurem. output frequency f_{ϕ}	Hz	32.47	$f_{\phi} = f_{\text{samp}}/N_{\text{SBFT}}$
Maximum input current	mA	0.66	



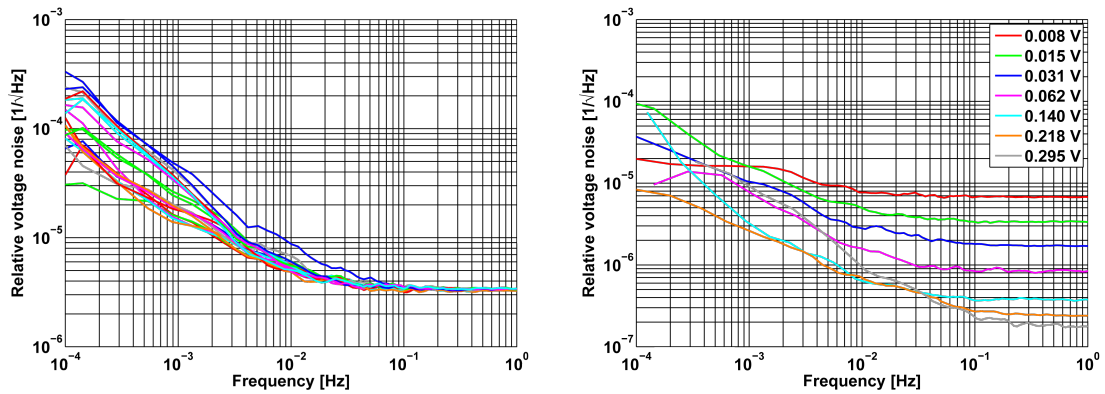
(a) DC amplitude noise of channel 1 minus 2...20 at 0.048 V DC amplitude. (b) DC amplitude noise of channel 1 minus 2 at different DC amplitudes.

Figure 2.12: DC amplitude sensitivity of the phasemeter using a heterodyne frequency of 1624 Hz supplied via a simple resistive splitter and a frequency generator.

Figure 2.12(a) shows the relative voltage noise of the Direct Current (DC) signal of channel 1 and channels 2...20 at a DC voltage of 0.048 V. At 1 Hz Fourier frequency all traces show the same relative voltage noise of around $1 \cdot 10^{-6} / \sqrt{\text{Hz}}$ increasing with $1/\sqrt{f}$ to lower frequencies. This read-out noise was well below the requirement which is at a level of $1 \cdot 10^{-3} \text{ V}/\sqrt{\text{Hz}} \cdot u_1(f)$. At 1 mHz Fourier frequency, the traces vary by a factor of two. The noise source for this difference in the DC amplitude noise has not been identified yet. It is possible that the thermal coefficients of the transimpedance resistors varied up to an order of magnitude due to the manufacturing process. As long as it is not identified, the upper noise curve (blue) will be used as a limit for the DC noise performance of the phasemeter.

Figure 2.12(b) shows the relative voltage noise of channel 1 in comparison to channel 20 at different amplitudes of the DC signal. It can be seen, that the relative voltage noise is decreasing with an increasing DC signal amplitude. This behaviour is expected because the Signal-to-Noise Ratio (SNR) is the better the higher the DC signal level.

Figure 2.13(a) shows the relative voltage noise of the difference of the heterodyne signal amplitudes between channel 1 and channel 2...20 at 0.015 V heterodyne signal. At 1 Hz Fourier frequency, all traces show the same noise of $3 \cdot 10^{-6} / \sqrt{\text{Hz}}$ increasing with $1/f$ at frequencies lower than 50 mHz. At 1 mHz the traces vary by a factor of 5. The noise source for this difference in the heterodyne amplitude noise at low frequencies has not been identified yet but it is thought to be the thermal coefficient of the resistors, too. As long as it is not identified clearly, the upper blue noise curve will be used as a limit



(a) Heterodyne amplitude noise of channel 1 minus 2...20 at 0.015 V heterodyne amplitude. (b) Heterodyne amplitude noise of channel 1 minus 2 at different heterodyne amplitudes.

Figure 2.13: Heterodyne amplitude noise of the phasemeter using a heterodyne frequency of 1624 Hz supplied via a simple resistive splitter and a frequency generator.

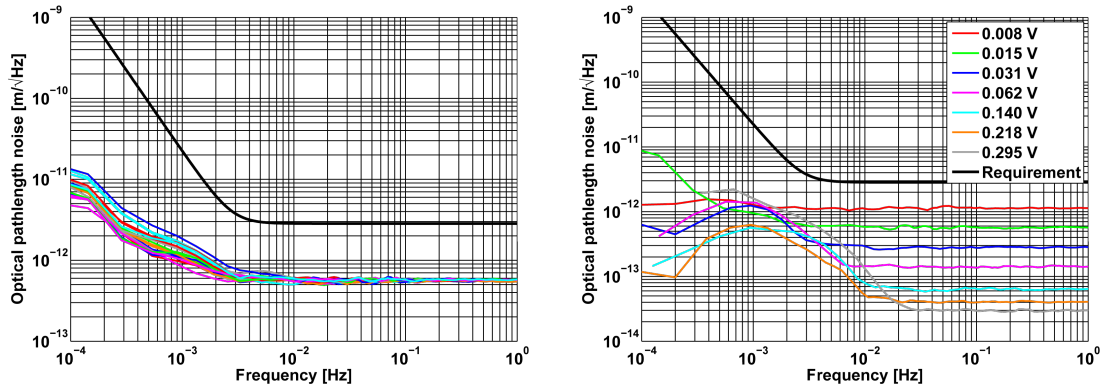
for the heterodyne amplitude noise performance of the phasemeter.

Figure 2.13(b) shows the relative voltage noise of channel 1 in comparison to channel 20 at different amplitudes of the heterodyne signal. The level of the white noise shape is decreasing with increasing heterodyne amplitude but the $1/f$ noise shape stays at the same level. Therefore the $1/f$ noise can be seen as inherent to the phasemeter and the white noise level is the lower limit for the heterodyne amplitude.

Figure 2.14(a) shows the phase noise, expressed as equivalent optical pathlength noise between channel 1 and channel 2...20 at 0.015 V heterodyne signal amplitude. The traces reached a minimum optical pathlength noise of $6 \cdot 10^{-13} \text{ m}/\sqrt{\text{Hz}}$ increasing with $1/\sqrt{f}$ at frequencies lower than 4 mHz. They were all below the requirement of $2.84 \text{ pm}/\sqrt{\text{Hz}}$ for the optical pathlength noise multiplied with the shape factor $u_1(f)$.

Figure 2.14(b) shows the phase noise, expressed as equivalent optical pathlength noise between channel 1 and channel 2 at different heterodyne signal amplitudes ranging from 0.008 V to 0.295 V. At 8 mV signal amplitude a maximum noise floor of $1.2 \text{ pm}/\sqrt{\text{Hz}}$ was achieved. With increasing signal amplitude the optical pathlength noise floor decreased down to below $30 \text{ fm}/\sqrt{\text{Hz}}$ at 0.295 V signal amplitude. The noise source of the shoulder below 20 mHz can also be induced by the temperature.

In Subsection 2.3.3 it was mentioned that one of the beam combiner outputs of the reference interferometer was split again. These two beam splitter outputs (detected at PD_{N1} and PD_{N2} in Figure 2.9) have been used to measure the absolute lower limit for the optical pathlength read-out with the phasemeter using optical signals. This included the noise of photodiodes, preamplifiers and the phasemeter. It will be called Null measurement in the following, because the beams have a phase offset of zero at the photodiodes. Figure 2.15 compares the phasemeter performance with signals from a frequency generator and with optical signals from photodiodes. During the measurement with optical signals the Optical Pathlength Difference (OPD) and a low frequency intensity stabilisation of the laser beams was turned on, see Section 2.4.2. Both curves are at a level of around $0.35 \text{ pm}/\sqrt{\text{Hz}}$ at frequencies higher than 2 mHz. This means that in this frequency range the phase read-out of optical signals with a LTP phasemeter can be estimated with artificial signals before it is integrated into an experiment. At lower



(a) Equivalent optical pathlength noise of channel 1 minus 2...20 at 0.015 V heterodyne amplitude. (b) Equivalent optical pathlength noise of channel 1 minus 2 at different heterodyne amplitudes.

Figure 2.14: Phase noise, expressed as equivalent optical pathlength noise of the phasemeter using a heterodyne frequency of 1624 Hz supplied via a simple resistive splitter and a frequency generator.

frequencies the read-out of the optical signals has an additional $1/f$ noise shape, which is not present in the read-out noise with the frequency generator. The noise source for this is assumed to originate from temperature fluctuations of the photodiode, whereby these can be introduced by DC laser intensity noise or the temperature stability within the vacuum chamber. The outcome is that the read-out noise of the optical pathlength with optical signals is well below the requirement for all frequencies.

2.4.2 Active stabilisations

This subsection describes briefly the step by step implementation of standard techniques to improve the optical pathlength measurements within heterodyne MZIs using the LTP modulation scheme. Details are neglected here because these techniques have already been used several times [36] [21] [37].

The first optical pathlength measurement was performed in a non-evacuated but closed vacuum chamber. The LTP modulation scheme was used without any additional stabilisation. Figure 2.16(a) shows that even under these conditions, the optical pathlength noise is better than $40 \text{ pm}/\sqrt{\text{Hz}}$ at high frequencies increasing with $1/f$ at frequencies lower than 30 mHz. The high frequency noise with the typical shoulder shape is induced by sidebands on the electrical signals for the AOMs [37].

The influence of the sidebands was minimised by stabilising the differential pathlength between both measurement beams via a feedback circuit using the output of an analog phase comparator as error signal. Its 1.624 kHz input signals came from the photodiode PD_{REF} and from the AOM driver electronics. The actuator of the feedback loop was the piezo-mounted mirror on the MB. In Figure 2.16(b) the optical pathlength noise of the photodiode PD_{REF} without and with stabilisation of the differential pathlength is shown. The stabilisation suppressed the optical pathlength noise to a level of $6 \text{ nm}/\sqrt{\text{Hz}}$. Compared to Figure 2.16(a) the optical pathlength noise of the length measurement in air with OPD stabilisation was reduced to $0.2 \text{ pm}/\sqrt{\text{Hz}}$ at frequencies above 500 mHz increasing with $1/f$ at lower frequencies.

The next step was to evacuate the vacuum chamber, which pushed the corner frequency

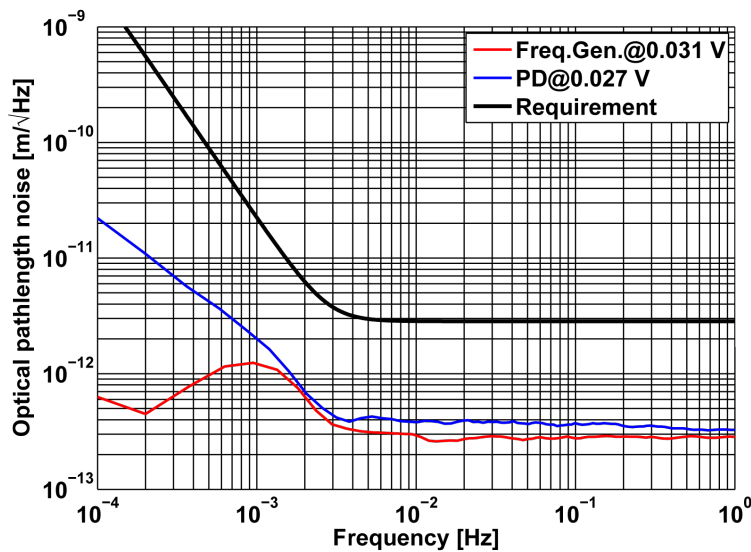


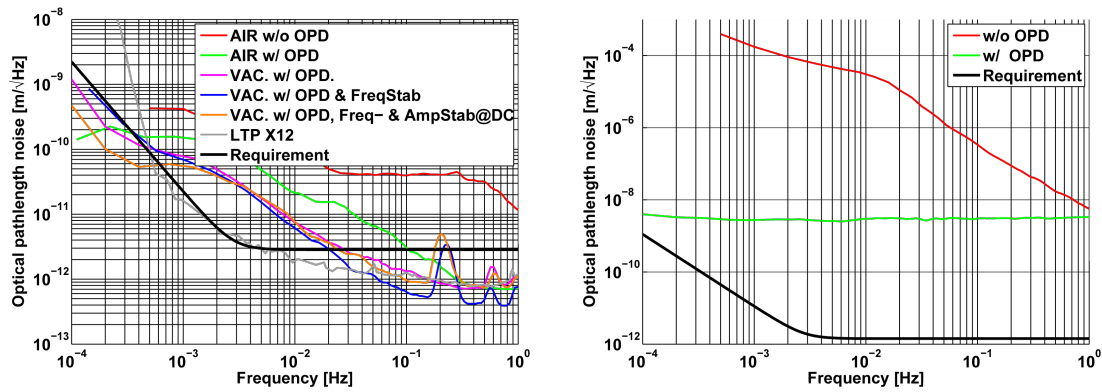
Figure 2.15: Optical pathlength noise measured with PM3 using a frequency generator and optical signals (Null measurement comparing PD_{N1} and PD_{N2}).

of the optical pathlength noise of the length measurement in Figure 2.16(a) down to 300 mHz. The stabilisation of the laser frequency with the build-in iodine stabilisation did not improve the length measurement. Also the DC laser intensity stabilisation, which has improved the performance at the backlink fibre experiment, did not improve the length measurement in the picometer experiment. So there is another noise source, that has to be identified. The bump at 200 to 250 mHz in the two curves “Vac. w/ OPD & FreqStab” and “Vac. w/ OPD & Freq- and AmpStab@DC” was induced by a running scroll pump inside the laboratory.

The final results for the optical pathlength noise with all active stabilisations running can be seen in Figure 2.17. The Null measurement in Figure 2.17 was at least one order of magnitude better than the optical pathlength noise requirement in the whole frequency range. The π -measurement at the single element photodiodes was also below the requirement for all frequencies. Only the π -measurement at the quadrant photodiodes was for high frequencies above the requirement. This behaviour is not understood, yet. The length measurement was below the requirement for frequencies higher than 30 mHz and for frequencies below 0.6 mHz. The improvement of the length measurement by data post-processing will be presented in the next subsection.

2.4.3 Data post-processing

This subsection deals with the improvement of the measured optical pathlength noise by using additional measured data to correct the optical pathlength measurement. At the beginning the composition of the optical pathlength measurement from the different photodiodes is investigated. Afterwards straylight correction is applied to suppress spurious unwanted beat notes at the heterodyne frequency. Then the DWS signals are used to correct for beam jitter induced optical pathlength noise. Next, the DC intensity noise is used to further reduce the noise and in the end low frequency optical pathlength noise is reduced by temperature correction.



(a) Improvement of the optical pathlength measurement of the length measurement via active stabilisations. (b) Optical pathlength noise of the reference photodiode without and with OPD stabilisation in air.

Figure 2.16: Length measurements within the experiment.

2.4.3.1 Optical pathlength combinations

A length measurement is the difference between the measured optical pathlengths of two MZIs. Each of the MZIs is equipped with at least two photodiodes. Therefore the length measurement can be obtained via different combinations of the photodiodes. Figure 2.18(a) shows six different combinations. At frequencies higher than 20 mHz a difference between the length measurement combinations at a level of $1 \text{ pm}/\sqrt{\text{Hz}}$ can be seen. For lower frequencies the difference vanishes in the high noise. Therefore Figure 2.18(b) compares the length measurement of (QPD1-SEPD1) to other combinations. The difference to the combinations where QPD1 is also used is below the picometer level. The difference to the combinations which used QPD2 are at the level of the π measurement performed with the QPDs. This underlines the general procedure to optimize the π measurements before reasonable length measurements can be performed.

2.4.3.2 Straylight

Straylight is a well-known noise source from the backlink fibre experiment and detailed descriptions and investigations on this topic can be found in [19] or in Chapter 5. The influence of straylight can be seen in a π -measurement. If straylight exists the optical pathlength noise (in $\text{rad}/\sqrt{\text{Hz}}$) of a π -measurements is at a level comparable to the ratio of straylight to the measurement signal. For example, if the straylight is emitted from a fibre port with a remaining reflectivity of a per cent or less, the π -measurement is at a level of $\text{mrad}\sqrt{\text{Hz}}$ phase noise.

The identification of straylight is rather simple, when all output ports of the beam combiners are equipped with photodiodes and their signals are measured with a phasemeter. Then the straylight correction can be applied by subtracting the signals from both output ports of one beam combiner. Figure 2.19 shows, that the length measurement is slightly improved by the straylight correction at frequencies higher than 30 mHz.

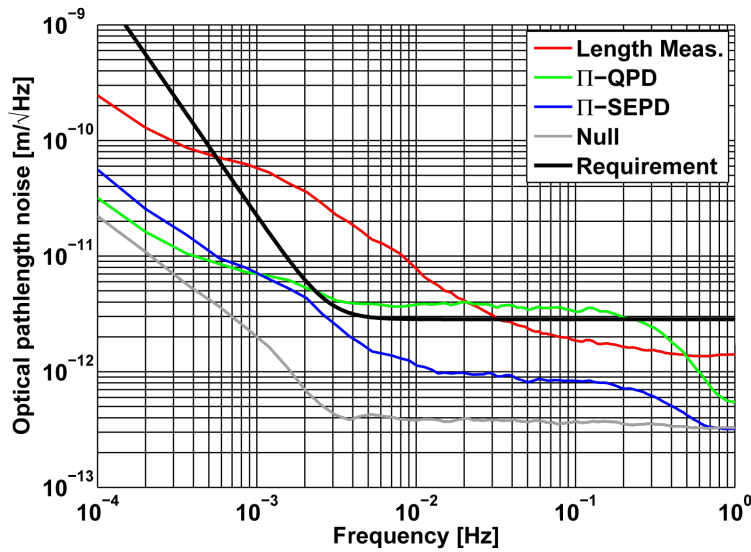


Figure 2.17: Optical pathlength noise of the length measurement, π , and Null measurement with all active stabilisations running.

2.4.3.3 Laser frequency noise

In this subsection the influence of the laser frequency noise on the length measurement noise will be estimated. This is done by modulating the laser frequency and recording the length measurement at the same time. From this measurement the coupling coefficient can be estimated, which can then be used to project the noise of an unstabilised and a frequency stabilised laser into the graph with the length measurement noise.

In an equal armlength MZI laser frequency noise perfectly cancels [6, pp. 154]. When the arms of the MZI differ in length, the laser frequency noise does not cancel any more. The influence is described by the the following equation

$$\delta\varphi = \frac{2\pi\delta\nu}{c}\Delta L \text{ [rad]} \quad (2.2)$$

$$\Rightarrow \delta l = \frac{\lambda\delta\nu}{c}\Delta L \text{ [m]} \quad (2.3)$$

$\delta\varphi$ is the measured peak-to-peak amplitude in rad of the length measurement, δl is the measured peak-to-peak amplitude in m of the length measurement, $\delta\nu$ the peak-to-peak amplitude of the frequency modulation, c is the speed of light, λ the laser wavelength and ΔL the armlength difference between the interferometers [38, p. 17].

The frequency coupling coefficient $\delta l/\delta\nu$ was measured by modulating the temperature of the laser crystal of the used Nd:YAG laser from Innolight with a sinusoidal signal from a frequency generator. The frequency of the modulation was set to 0.1 Hz and the amplitude was $0.5 V_{pp}$ computed for a 50Ω load. The output impedance of the frequency generator is 50Ω and the input impedance of the laser crystal temperature $1 M\Omega$. Therefore the effective modulation voltage is $1 V_{pp}$. According to the datasheet of the laser, this is equivalent to a frequency change of 3 GHz [29]. The peak-to-peak amplitude of the length measurement modulation can be seen in the time series presented in Figure 2.20(a). It is 9.9 nm.

Figure 2.20(b) shows the time series of the π -measurements and the Null measurements during the frequency modulation of the laser. The influence of the frequency modulation

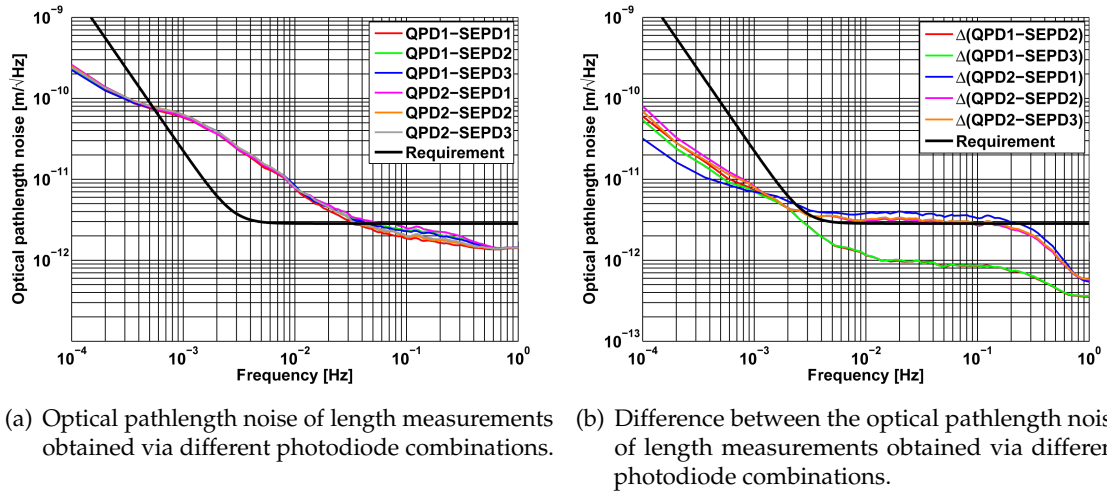


Figure 2.18: Investigations on the impact of photodiode combinations on the optical pathlength noise. $\Delta(x)$ denotes the pathlength difference between QPD1-SEPD1 and x

on the π measurement performed with the QPDs is orders of magnitudes higher than on the π -measurements performed with the SEPD or the Null measurement.

Using the peak-to-peak amplitude of the length measurement modulation obtained from Figure 2.20(a) the frequency coupling coefficient is

$$\frac{\delta l}{\delta \nu} = \frac{9.9 \cdot 10^{-9} \text{ m}}{3 \cdot 10^9 \text{ Hz}} \quad (2.4)$$

This corresponds to a length difference between both interferometers of 0.924 mm. This value is in the range of the optical pathlength differences which have been measured at the backlink fibre experiment and at the polarisation optics experiment [19, pp. 53] [17, pp. 117]. This optical pathlength difference is induced by alignment errors during the building process and cannot be further reduced. The influence of the frequency stability of the iodine-stabilised laser onto the length measurement was projected with the coupling coefficient into the optical pathlength measurement in Figure 2.30. It is orders of magnitude below the requirement.

2.4.3.4 Beam pointing noise

A well-known effect in heterodyne MZIs is the coupling of the laser beams jitter into longitudinal optical pathlength noise. This effect is introduced by the limited size of the photodiodes, which detect the interferometer signal. If one of the beams is wobbling the average of both beams on one photodiode is slightly changing because the phase fronts are cut at the boundaries of the active area [39, pp. 153]. Therefore two techniques to measure the mismatch in the overlap between two beams have been developed. First the measurement of the relative tilt between two phase fronts on a QPD and secondly the measurement of the beam intensity centroid on a QPD. The first one is the most important one for this purpose. Thus it will be introduced and explained first. A method to use the knowledge of the relative tilt between two phase fronts for the correction of the optical pathlength noise was implemented and presented. In the end the second method to measure the beam jitter is explained and its usage within heterodyne MZIs is motivated.

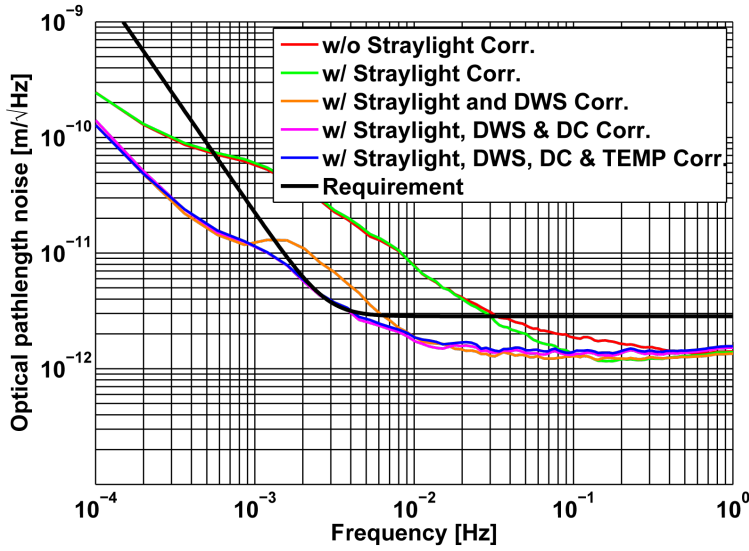


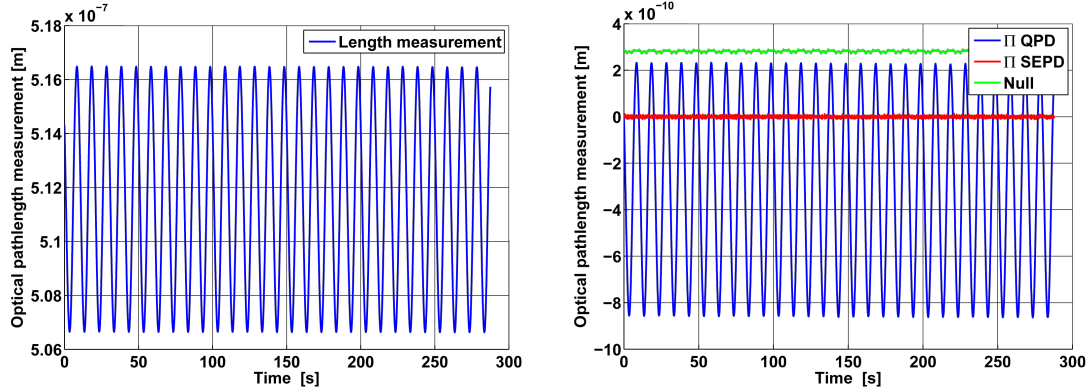
Figure 2.19: Improvements of the optical pathlength noise of the length measurement in data post-processing.

The measurement of a spatially varying phase difference between two beams by the usage of multi-element photodiodes has been mathematically described in [33] and is called differential wavefront sensing. This technique can be used to derive information about the mismatch in the overlap between the phase fronts at the output of an interferometer. The first experimental demonstration was done by stabilising the orientation of two mirrors in a 10-m long suspended Fabry-Perot cavity in the 10 m prototype laser interferometer gravitational-wave detector in Glasgow [34]. This technique was adopted for heterodyne MZI within the LFP mission to read-out the pointing jitter of the PM. Detailed information about the implementation within the LFP measurement scheme and comparisons between theoretical and experimentally obtained pointing jitter of a moving PM can be found in [39, pp. 11].

Picture 2.21 depicts the principle of DWS for the detection of PM jitter. The PM is rotated by an angle $\Delta\phi$, which changes the angle of the measurement beam (blue) by an amount of $2\Delta\phi$. The measurement beam is then superimposed at a beam combiner with a stable reference beam. The beat signal at the heterodyne frequency $|f_1 - f_2|$ is then detected with one QPD per output port. The image magnification of QPD 1 shows that the upper part of the QPD will see a phase shift $-\Delta\Phi$ and the lower part $+\Delta\Phi$ resulting in a difference of the two segments of $2 \cdot \Delta\Phi$. Therefore a tilt of the PM by $\Delta\phi$ leads to measurable signal of $2 \cdot \Delta\Phi$.

The DWS signals can be calculated in several ways, which depend on the labeling of the quadrants of the QPD and the constitution of the measured phases. In this investigation the labeling of the quadrants is used according to Picture 2.21. This means that the upper left quadrant in the beam direction is called A, the upper right B, the lower right C and the lower left D. The LTP-style phasemeter calculates for each quadrant/channel DC value, real and the imaginary part of the measurement vector in the complex plane. The read-out programme of the phasemeter calculates from the real and imaginary part of the measurement vector the amplitude A and the phase ϕ of the heterodyne signal. With these two values the measurement vector \vec{r} in the complex plane can be described with

$$\vec{r}_{A,B,C,D} = A_{A,B,C,D} \cdot e^{i\phi_{A,B,C,D}} \quad (2.5)$$



- (a) Time series of the length measurement during a modulation of the laser frequency at 0.1 Hz.
- (b) Time series of the π measurement obtained from the QPD and the SEPD and the Null measurement. The laser frequency modulation has not only an influence on the length measurement but also on the π measurement obtained from the QPDs. The influence on the Π measurement obtained from the SEPD and the Null measurement is negligible.

Figure 2.20: Measurement of the laser frequency coupling coefficient of the picometer experiment.

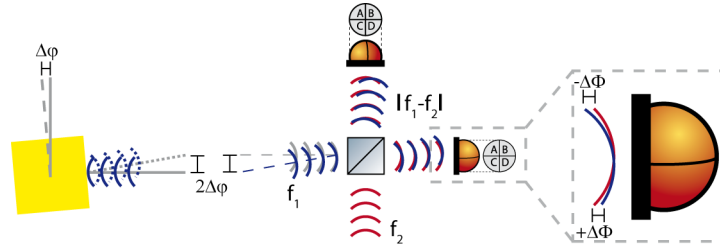


Figure 2.21: Depiction of differential wavefront sensing.

whereby the index A,B,C,D refers to the segments of the QPD. The measured DWS angle for an angular beam change in the horizontal plane is called DWS_ϕ and in the vertical plane it is called DWS_η . They are calculated with

$$DWS_\phi = \arg\left(\frac{\vec{r}_A + \vec{r}_C}{\vec{r}_B + \vec{r}_D}\right) \quad (2.6)$$

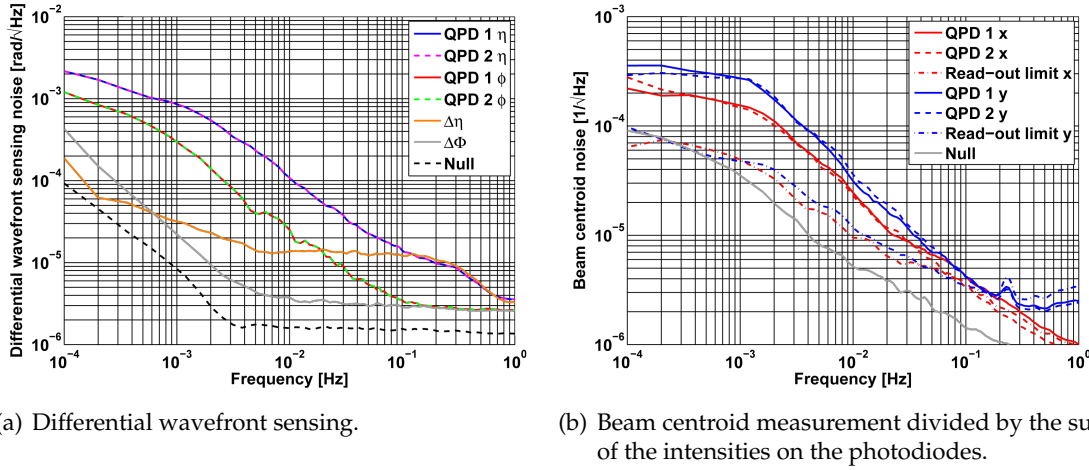
$$DWS_\eta = \arg\left(\frac{\vec{r}_A + \vec{r}_B}{\vec{r}_C + \vec{r}_D}\right) \quad (2.7)$$

Arg is a function which gives out the angle of a complex number in the complex plane with the real axis.

The read-out noise for the DWS signals is obtained by measuring with identical QPDs at both output ports of a beam combiner. It has to be taken into account that for a beam change in the horizontal plane (DWS_ϕ) the DWS signals have an offset of π due to the reflection (energy conservation) at the beam combiner. Therefore the equations for the DWS read-out noise are

$$\Delta DWS_\phi = \frac{1}{\sqrt{2}} (DWS_{\phi,1} + DWS_{\phi,2}) \quad (2.8)$$

$$\Delta DWS_\eta = \frac{1}{\sqrt{2}} (DWS_{\eta,1} - DWS_{\eta,2}) \quad (2.9)$$



(a) Differential wavefront sensing.

(b) Beam centroid measurement divided by the sum of the intensities on the photodiodes.

Figure 2.22: Raw data of the beam pointing and the according read-out noise obtained via two methods.

The index number is the number of the QPD. The factor $\sqrt{2}$ is used to obtain the noise for a single QPD under the assumption that the DWS read-out noise is non common-mode for both QPDs.

Figure 2.22(a) presents the raw data of the DWS signals and the DWS read-out noise within the picometer experiment. The lower limit for the phase read-out is set by the phase noise for the read-out of one phasemeter channel with optical signals, which is called Null and is obtained from the two single-element photodiodes called PD_{N1} and PD_{N2} in Figure 2.9. For frequencies above 3 mHz it is below $2 \mu\text{rad}/\sqrt{\text{Hz}}$ increasing with $1/f$ towards lower frequencies. The read-out of the horizontal DWS signal $\Delta\Phi$ is approximately a factor two above the Null measurement within the complete LISA Measurement Band (LMB). The read-out of the vertical DWS signal $\Delta\eta$ is at a level of $15 \mu\text{rad}/\sqrt{\text{Hz}}$ or better for frequencies above 6 mHz and is increasing with a $1/\sqrt{f}$ towards lower frequencies. The horizontal and vertical absolute DWS signals $QPD_{\eta 1,2}$ and $QPD_{\phi 1,2}$ are limited by the read-out noise of the DWS signals for frequencies above 200 mHz. For lower frequencies the SNR becomes approximately 10.

One of the goals of this experiment was to verify that beam pointing noise can be read-out below the requirement of $10.48 \text{ nrad}/\sqrt{\text{Hz}} \cdot u_1(f)$. The picometer experiment did not implement a movable mirror to obtain the PM pointing jitter. This was not needed because only stable beams with comparable parameters like laser intensity and beam waist size are needed.

The equations that have been presented in [33], indicate that there is a large optical amplification factor between beam tilt and measured DWS phase. The coupling factor K_{DWS} between DWS angle ($2 \cdot \Delta\Phi$) and angular jitter ($\Delta\phi$) of the PM was derived for the LPF mission in [16, 40]. It is

$$K_{\text{DWS}} = \frac{2 \cdot \Delta\Phi}{\Delta\phi} \quad (2.10)$$

$$= 4\sqrt{2\pi} \frac{\omega_m}{\lambda} \left[1 - \frac{L_{\text{PM}}}{R_m} \right] \quad (2.11)$$

whereby λ is the laser wavelength and L_{PM} the lever arm between the PM and the photodiode. ω_m is the beam waist and R_m the wavefront curvature at the photodiode

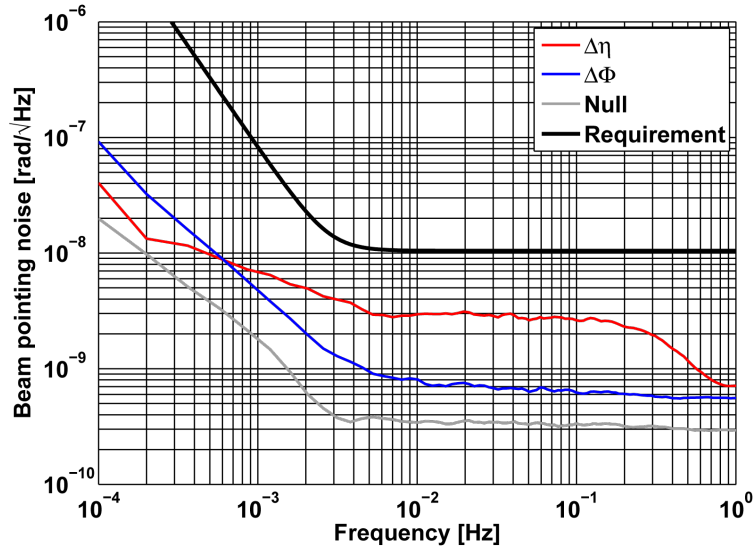


Figure 2.23: Equivalent beam pointing and read-out noise obtained via DWS obtained from the coupling coefficient of the LOB.

position defined by

$$\omega_m(z) = \omega_0 \sqrt{1 + \frac{z^2 \lambda^2}{\pi^2 \omega_0^4}} \quad (2.12)$$

$$R_m(z) = z \left[1 + \frac{\pi^2 \omega_0^4}{z^2 \lambda^2} \right] \quad (2.13)$$

ω_0 is the beam waist. The parameters for the calculation of the DWS coupling factor for the LOB have been set during its design phase. The beam waist radius is 1 mm and its position is approximately on the PM surface. The distance between the PM surface and the QPD of the interferometer is 500 mm [41, pp. 141]. With these numbers the coupling factor can be computed to

$$K_{DWS} = 9288 \left[\frac{\text{rad}_\Phi}{\text{rad}_\phi} \right] \quad (2.14)$$

With the before mentioned comparable beam parameters the coupling coefficient K_{DWS} of the PM within the LOB can be used to obtain a lower limit for the read-out of the beam pointing noise. A projection of the measured absolute beam jitter makes no sense in this context, because it was introduced by the fibre couplers of the picometer experiment which have a different DWS coupling coefficient than the LOB PM.

Figure 2.23 presents the projected DWS read-out noise for the beam pointing noise on the LOB. The read-out noise of the ϕ angle was at a level of $0.6 \text{ nrad}/\sqrt{\text{Hz}}$ increasing with $1/f$ at frequencies below 20 mHz. The read-out noise of the η angle showed a shoulder shape. For frequencies below 200 mHz it was at a level of $3 \text{ nrad}/\sqrt{\text{Hz}}$ increasing with $1/\sqrt{f}$ for frequencies below 6 mHz. The read-out noise for both degrees of freedom was well below the requirement.

For the correction of the length measurement a fitting algorithm was used which is described in Figure 2.24. It was similar to the one presented in [35, pp. 146]. It started with an estimation of coefficients for a filter. The frequency range for the filter was

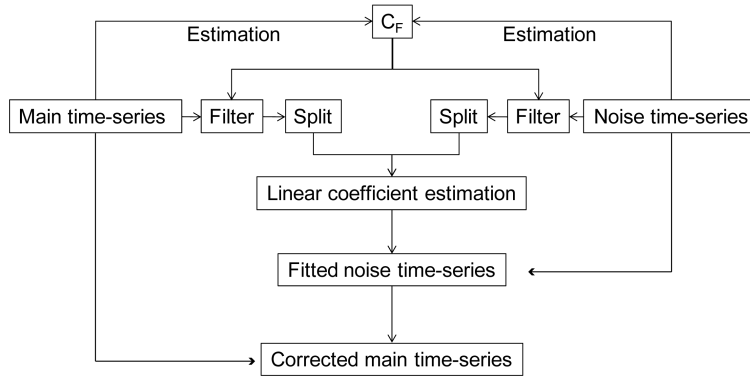


Figure 2.24: Schematic for correcting noise sources in data analysis.

set by the noise source, which was used for the data-correction and its read-out noise. A second constraint for the frequency range of the filter was given by the frequency range in which the noise source limits the optical pathlength measurement. For this the noise shapes or the time series of the noise and the length measurement had to be compared. From these two constraints the corner frequencies of the appropriate filter that was used for filtering the optical pathlength and the noise source measurement was chosen. Afterwards the time series of the filtered noise source was fitted to the filtered optical pathlength measurement via an linear fit. The estimated coefficients were then used with the unfiltered noise source to get an correction for the unfiltered length measurement. In the end the difference between the original time series of the optical pathlength measurement and the fitted one yield to the corrected time series. The correction of the measured optical pathlength noise with the measured DWS signals improved the optical pathlength noise in Figure 2.19 on page 23 from the green curve to the orange curve. The orange curve was close to the requirement.

Another way to measure the beam pointing noise with a QPD is to measure the centroid of the intensity of both beams, assuming that one beam is centred and stable and the second one is moving. The coupling factor between a tilt of the PM and the measurable angle is

$$K_{DC} = \frac{P_M}{P_M + P_R} \sqrt{\frac{2}{\pi} \frac{4L_{PM}}{\omega_M}} \quad (2.15)$$

according to [41, p. 147] the reference beam has a power of 1.12 mW on each QPD and the measurement beam 45.2 μ W. The other values are identical to the one used for K_{DWS} and therefore the coupling coefficient for the DC centroid read-out is

$$K_{DC} = 61 \left[\frac{1}{\text{rad}_\phi} \right] \quad (2.16)$$

This value is much lower than the value for the DWS read-out. This is due to the fact that the power of the beam, which was used to monitor the PM was much lower than the power of the reference beam. The measurement beam had to have a lower power to reduce the effect of radiation pressure noise on the PM. The DC centroid signal is useful because it has a wider dynamic range with respect to the PM movement. It can be used during the initial PM alignment procedures before heterodyne signals are available.

Figure 2.22(b) shows the raw-data of the beam-centroid measurement within the picometer experiment. The read-out noise for the x and the y -directions was at 100 mHz

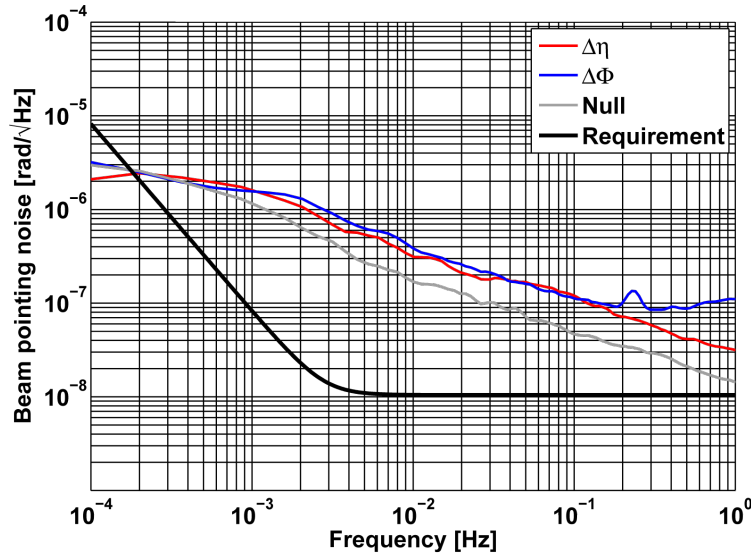


Figure 2.25: Equivalent beam pointing and read-out noise obtained via beam centroid measurement using the coupling coefficient of the LOB.

at a level of $35 \mu/\sqrt{\text{Hz}}$ increasing with $1/\sqrt{f}$ towards lower frequencies. For the whole frequency range the beam-centroid read-out noise was limited by the read-out noise of the phasemeter represented by the Null measurement. Above 100 mHz the beam centroid noise was limited for all axis by the read-out noise. For lower frequencies the beam-centroid noise was higher than the read-out noise.

Figure 2.25 shows the same measurement but projected with the coupling coefficient K_{DC} to the beam pointing noise. As for the DWS measurements the absolute pointing jitter $\text{QPD}_{\eta,1,2}$ and $\text{QPD}_{\phi,1,2}$ was only valid for the picometer experiment because of the different coupling coefficients and therefore it was not plotted in this graph. The main information of this graph is that the read-out noise for both angles are above the requirement in the complete LMB.

2.4.3.5 Laser intensity noise

The coupling factor between the laser intensity noise and the optical pathlength noise of the length measurement has not been estimated by the standard method. This would have been done by modulating the laser intensity via the driving power of the AOMs and measuring the response of the length measurement as in [19, pp. 45]. The intensity modulation via the AOM did not yield a reasonable signal in the uncorrected length measurement. The coupling factor was instead obtained from the correction scheme presented in Subsection 2.4.3.4. For this the time series of the length measurement and the DC laser intensities on the photodiodes were used. The measurement of the DC laser intensity noise can be seen in Figure 2.26(a). The DC noise was not limited by sensor noise at frequencies higher than 0.7 mHz. Therefore this frequency range was used for the filter in the correction scheme. Figure 2.19 shows, that the length measurement was improved by the correction scheme between 1 and 7 mHz.

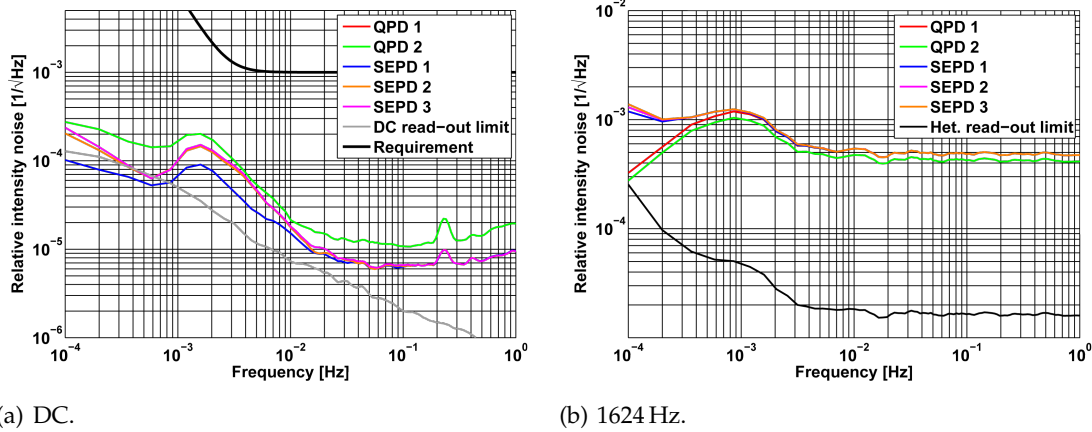


Figure 2.26: Measurements of the laser intensity noise at different frequencies. The laser intensity noise are compared to the read-out obtained by $(PD_{N1} - PD_{N2})$.

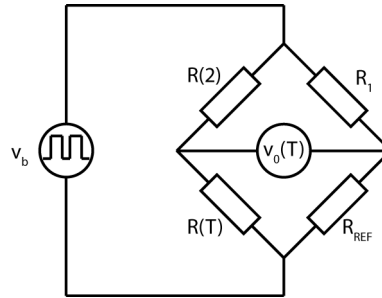


Figure 2.27: Schematic of a Wheatstone bridge which is a part of the FPGA thermometer.

2.4.3.6 Temperature noise

The temperature measurement system was developed by Gerhard Heinzl at the AEI and is based on the LTP measurement system presented in detail in [42, pp. 23]. The sensor for the temperature measurement in this experiment was a PT10k resistor based on platinum and a resistance R_0 of 10 k Ω at 0 $^\circ$ C. The time constant of the PT10k sensors was in the order of 10 s. Therefore only slow measurements of the temperature were possible. In the temperature range between 0 $^\circ$ C and 850 $^\circ$ C its resistance $R(T)$ could be approximated by the following equation

$$R(T) = R_0 (1 + a \cdot T + b \cdot T^2) \quad (2.17)$$

The constants a and b are defined by the industry standard DIN EN 60751 [43].

The sensor was integrated into a Wheatstone bridge and the resistance of the sensor was measured via the difference of the drop voltage between the two arms of the bridge, see Figure 2.27 [44, pp. 54]. The output voltage was given by

$$v_0(T) = V_b \left[\frac{R_{\text{ref}}}{R_{\text{ref}} + R_1} - \frac{R(T)}{R(T) + R_2} \right] \quad (2.18)$$

The bridge was nulled at room temperature to remove the offset temperature and to increase the amplification of the error signal from the bridge. This increases effectively the SNR. The output voltage of the bridge was read-out with an Alternating Current

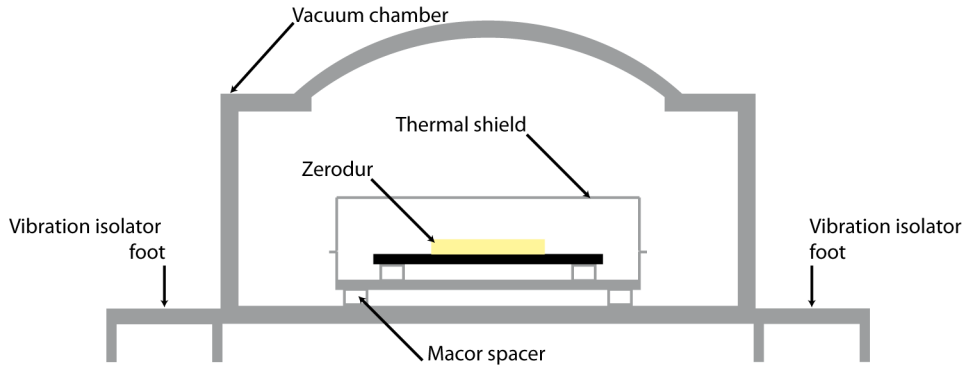


Figure 2.28: Schematic of the setup inside the vacuum chamber. A thermal shield and Macor spacer reduce the thermal coupling between the experiment and the chamber.

(AC) voltage to reduce the DC drift of the output voltage. A schematic of the input stage of the FPGA thermometer can be seen in Figure 6 in Appendix 6.

Eight PT10k sensors were spread in the vacuum chamber for the measurement of the temperature noise. The vacuum chamber is sketched in Figure 2.28. Three sensors were placed at the bottom of the vacuum chamber and three on the ZerodurTM baseplate inside the thermal shield. This was done to measure the read-out noise with the FPGA thermometer.

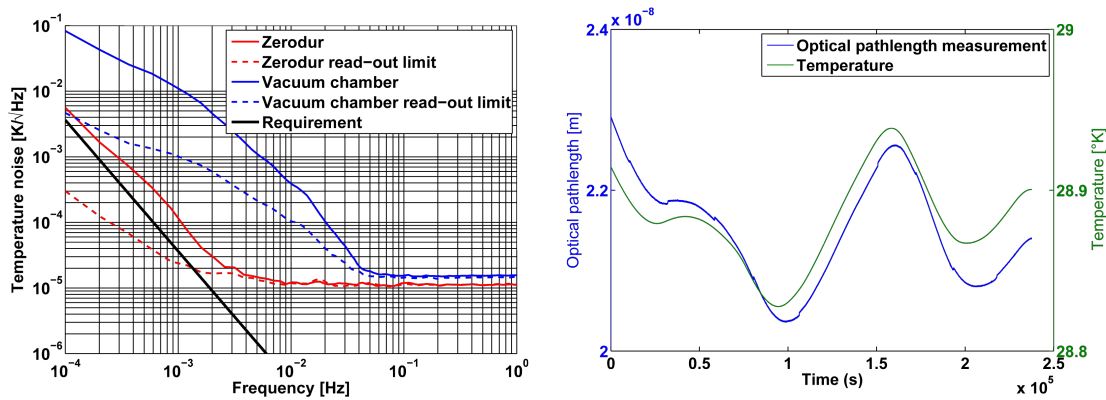
In Figure 2.29(a) the measurement of temperature noise on the optical bench and at the bottom of the vacuum chamber can be seen. The temperature noise of the vacuum chamber was white and at a level of $15\mu\text{K}/\sqrt{\text{Hz}}$ for frequencies above 50 mHz increasing with $1/f^2$ towards lower frequencies. The temperature noise on the ZerodurTM baseplate was at a level of $10\mu\text{K}/\sqrt{\text{Hz}}$ for frequencies above 4 mHz increasing with $1/f^2$ towards lower frequencies. The read-out noise for the PT10k sensors on the ZerodurTM baseplate was at a level of $10\mu\text{K}/\sqrt{\text{Hz}}$ for frequencies above 4 mHz increasing with $1/f$ towards lower frequencies. The sensor noise of the PT10k sensors installed at the bottom of the vacuum chamber is much higher. This is driven by the non-linearity of the sensors. The main information of this graph is that a reasonable SNR of the temperature measurement on the OB was only given for frequencies below 1 mHz

Figure 2.29(b) shows a comparison between a time series of an optical pathlength measurement on the ZerodurTM baseplate and the according temperature on the baseplate. The relation between both is clearly visible. The temperature coupling coefficient was estimated by measuring the temperature and the optical pathlengths at the reversal points at approximately $1 \cdot 10^5$ and $1.5 \cdot 10^5$ s. The result is a coupling coefficient of

$$c_{\text{TEMP}} = \frac{\Delta L}{\Delta T} \quad (2.19)$$

$$= 19.7 \left[\frac{\text{nm}}{\text{K}} \right] \quad (2.20)$$

The time offset between the turning points of the optical pathlength measurement and the temperature measurement were also calculated. These were 4600, 2300, 5500 and 10200 s. The time offset was in the order of several thousands seconds and was not stable over time. This behaviour was not expected because it was assumed that for time scales longer than 1000 s everything that is located inside the thermal shield in the vacuum chamber is in equilibrium.



(a) Absolute temperature and read-out noise measured with PT10k sensors and the FPGA thermometer. (b) Time series of a temperature and a length measurement on a ZerodurTM baseplate.

Figure 2.29: Characterisation of the temperature measurement system and the temperature induced optical pathlength noise of the length measurement.

At frequencies lower than 1 mHz the measurements on the ZerodurTM were not limited by sensor noise and therefore this frequency was used as the corner frequency in the fitting algorithm. Figure 2.19 shows that the length measurement is improved by this correction at frequencies lower than 0.1 mHz.

2.5 Noise projections

One of the main tasks of the picometer experiment was to identify the remaining noise sources of the LPF measurement scheme with respect to the LISA requirements for the optical pathlength stability. Thus the measured and estimated coupling coefficients between the noise sources and the optical pathlength noise from the data post-processing subsection were used to project the noise sources to the optical pathlength noise of the length measurement. The results are presented in Figure 2.30. At frequencies higher than 10 mHz the DWS corrected length measurement is limited by the read-out noise of the DWS angle η . In the frequency range between 1 and 10 mHz the DC laser intensity noise corrected length measurement is limited by the read-out noise of the DC laser intensity. At frequencies lower than 1 mHz the optical pathlength read-out noise (Null measurement) is the limiting noise source. This information can be used in future LISA interferometers to improve the optical pathlength noise of length measurements.

2.6 Conclusions

In conclusion, a phasemeter noise level of $0.3 \text{ pm}/\sqrt{\text{Hz}}$ increasing as $1/\sqrt{f}$ for frequencies below 4 mHz was measured using electrical input signals.

The noise level of the phase measurement chain consisting of photodiodes, preamplifier and LTP phasemeter was measured as $0.4 \text{ pm}/\sqrt{\text{Hz}}$ increasing as $1/f$ for frequencies below 4 mHz.

In the interferometer setup an optical pathlength noise of the length measurement below the requirement for frequencies below 0.6 mHz and above 20 mHz was measured

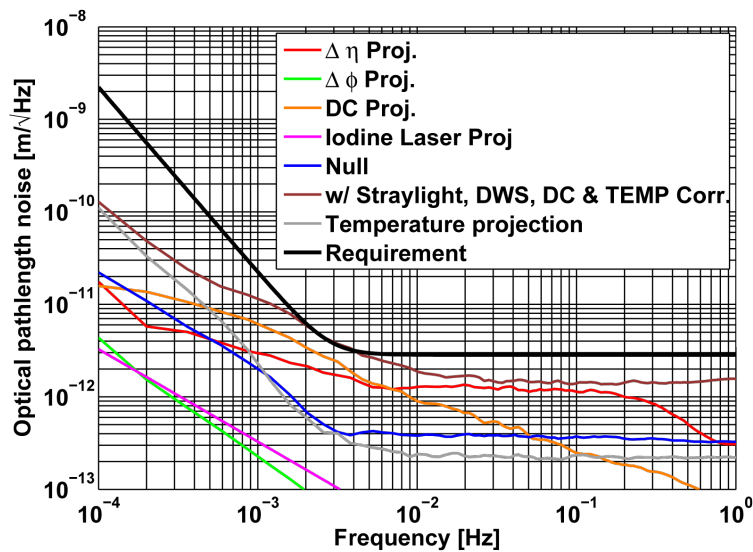


Figure 2.30: Equivalent optical pathlength noise of the measured and calculated noise sources obtained with the according coupling coefficients in comparison to the length measurement.

using optical pathlength, frequency and DC laser intensity stabilisations. With noise subtractions in data post-processing, the length measurement could be further improved to be below the requirement for optical pathlength noise for the complete frequency range using straylight, DWS, DC laser intensity and temperature correction.

For a pathlength difference of 0.7 mm on the picometer bench, a temperature noise level of $20 \mu\text{K}/\sqrt{\text{Hz}}$ increasing as roughly $1/f^2$ to lower frequencies was sufficient to reach the optical pathlength noise requirements. A temperature measurement system with a noise level of $10 \mu\text{K}/\sqrt{\text{Hz}}$ was used.

Length measurement noise was limited by DWS read-out noise for frequencies above 10 mHz and DC amplitude noise between 1 and 10 mHz. A beam pointing read-out noise of $3 \text{ nrad}/\sqrt{\text{Hz}}$, being a factor of 3 below the requirement was measured. The adjustable fibre coupler made of metal have to be replaced by monolithic fibre coupler which are only adjustable during the bonding stage. With this exchange the beam jitter correction is expected to be not required any more.

The results were obtained with heterodyne signals at 1.624 kHz and mW power level and need to be transferred to MHz heterodyne signals and 100 pW light power.

Thus the setup developed within this work represents an ideal test bed for the LISA PMS including photo detectors. Alternatively, the down-mixing scheme can be used to test LISA photo detectors with an LTP-style phasemeter, at the expense of increased shot noise in weak-light conditions.

Testing the actuators for LISA optical bench

This chapter presents the experimental investigations on actuators which are required for testing the LOB. The requirements for these actuators are motivated at the beginning of this chapter, followed by a summary of already performed investigations on different types of actuators at other experiments at the AEI. This information is used to find actuators that fit into the requirements of the LOB. One of them is selected for further testing. Afterwards the measurement setup is introduced. First measurements of the sensitivity of the measurement setup and the stability of the actuators are summarised briefly [45, 46]. The static behaviour of the actuators are analysed in greater detail than in [45], which the author has supervised. Methods to improve their properties are developed and experimentally verified.

In the process of debugging a measurement system for the actuator stability, several other investigations were conducted. The intensity and frequency stabilities of the frequency stabilised laser that has been introduced in Chapter 2 was analysed. An intensity stabilisation at low frequencies was developed for this laser system. The FPGA-based temperature measurement system and the thermal shield within the vacuum chamber were improved. The analysis and improvements of these parts are beneficial for other interferometers and for testing of the LOB, too. Thus they are also described in this chapter.

3.1 Introduction

Chapter 1 introduced the “split interferometry” as the baseline design for the read-out of the distance fluctuations between two PMs on separate satellites within the LISA constellation. Within this architecture each OB has at least two optical interfaces: the interface to the telescope and the interface to the PM. The complete OB has to be tested before integration into a satellite. Therefore special devices closing these optical interfaces are needed for the testing of the OBs. These devices are from now on called simulators. They will be part of the On-Ground Support Equipment (OGSE). The simulators have to be able to mimic the situation onboard the satellites in space. This means that beam parameters like optical power, waist diameter, waist position, pointing stability, and the pointing range should be comparable to the expected parameters in space.

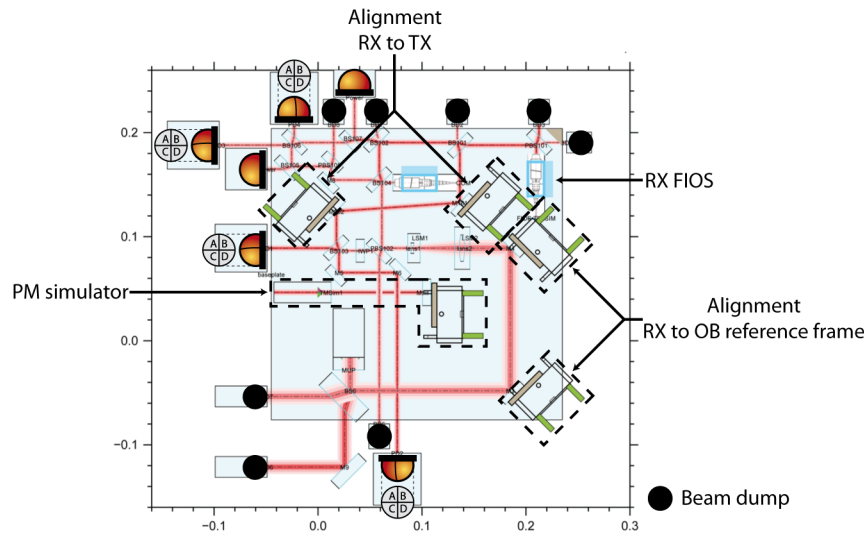


Figure 3.1: OptoCad layout of the telescope simulator for the LOB, which also includes the PM simulator [47].

According to Chapter 1 the telescope is located “above” the LOB and the PM is situated “below” the LOB with both beam axes orthogonal to the OB surface. The beams are directed via 45° out-of-plane mirrors into the according directions. During the design phase of the LOB it was agreed that the extra complexity induced by two individual simulators can be decreased by using only a single baseplate for both. Thus an 45° out-of-plane mirror is placed in the beam path of the PM measurement beam before the original an out-of-plane mirror. The additional mirror reflects the measurement beam upwards towards the PM simulator. Figure 3.1 presents the OptoCad layout of the telescope simulator for the LOB, which includes the PM simulator. This baseplate will be placed on the LOB on feet made of ULE. A key component of both simulators are actuators. Mirrors are mounted to them to control the pointing of the measurement beams. For the PM simulator these actuators should enable low-noise optical pathlength measurements of a static mirror surface (PM surface) with a well-defined angular mismatch of the PM surface with respect to the LOB reference frame as well as dynamic measurements to verify the interferometer behaviour to a moving PM. For the telescope simulator adjustable mirrors are needed to align the incoming RX beam and the outgoing TX beam to a well-defined direction with respect to the LOB reference frame. The stability of the actuators is almost as important as for the PM simulator.

Detailed requirements for the PM and telescope simulators were derived from an internal project document [14]. The requirements for the telescope simulator actuators could be relaxed in contrast to the one for the PM simulator. This is due to the fact that the optical pathlength read-out limit in the science interferometer is around $9 \text{ pm}/\sqrt{\text{Hz}}$ dominated by shot noise, see Subsection 4.1.5.1, in contrast to the optical pathlength requirement for the read-out noise of the PM interferometer without simulator, which is around $2.84 \text{ pm}/\sqrt{\text{Hz}}$. The extra noise added by the actuators is less critical within the science interferometer noise budget. Therefore the requirements for the stability of the actuators in the PM interferometer are taken as reference.

In Chapter 2 the requirements for the read-out of the optical pathlength noise and the beam pointing noise of the PM were verified. The PM onboard a LISA satellite will be a

free-floating device to measure GWs. A PM simulator for the LOB will not measure GW but has to verify the read-out requirements of the PM interferometer. An unavoidable effect will be that the read-out will be degraded by the actuators in the PM simulator. The requirements for the read-out of the PM interferometer including simulator are derived on the basis of the requirements for the read-out of the PM interferometer without simulator, which were presented in Section 2.1. A reasonable procedure is that the overall requirement for the read-out noise of the PM interferometer with actuators, \tilde{R}_{PA} , is worse by more than 10 % compared to the read-out noise for the PM interferometer without actuator \tilde{R}_{PM} . The requirement for the optical pathlength stability of the actuators, \tilde{R}_{AC} , can be derived assuming that the read-out noise of the PM interferometer is independent from noise induced by the actuators

$$\tilde{R}_{PA} = 1.10 \cdot \tilde{R}_{PM} \quad (3.1)$$

$$= 3.12 \cdot 10^{-12} \frac{\text{m}}{\sqrt{\text{Hz}}} \quad (3.2)$$

$$\tilde{R}_{PA} = \sqrt{\tilde{R}_{PM}^2 + \tilde{R}_{AC}^2} \quad (3.3)$$

$$\Leftrightarrow \tilde{R}_{AC} = \sqrt{1.10^2 \cdot \tilde{R}_{PM}^2 - \tilde{R}_{PM}^2} \quad (3.4)$$

$$= 1.30 \cdot 10^{-12} \frac{\text{m}}{\sqrt{\text{Hz}}} \quad (3.5)$$

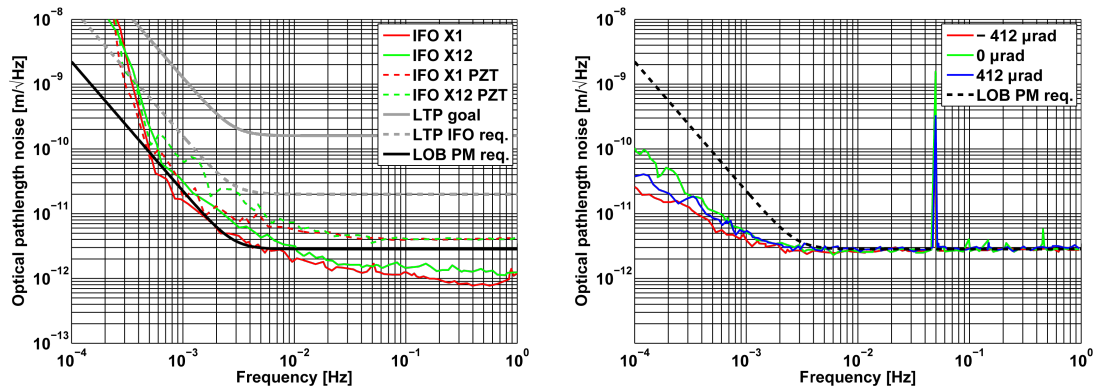
The results of the beam jitter measurements within the picometer experiment, presented in Figure 2.23 on page 26 have shown that the absolute pointing noise introduced by the fibre coupler and the adjustable mirror mounts was above the read-out noise of the beam pointing and that the read-out noise of the beam pointing was well below the requirements. Assuming that the actuators induce approximately the same beam pointing noise as the fibre couplers and adjustable mirror mounts the requirement for the beam pointing read-out noise including actuators could not be relaxed

The alignment range and the step width of the actuators (tip, tilt and along the beam) were derived from the behaviour of a real PM. The actuators had to be able to move the PM mirror linearly along the direction of the beam, whereby a limit was set by the housing of a real PM. The gap between a PM and its housing is in the order of a few mm. The step width of the linear actuator had to be well below half the laser wavelength λ ($\lambda = 1064 \text{ nm}$) to scan the interferometer length below one fringe. The step width for tip or tilt of the actuators was required to align the DWS signals within the PM interferometer via the PM mirror to an optimum position for the measurement. This angle was $\pm 10 \mu\text{rad}$ [14, R<130-040>]. The actuation range for tip and tilt had to be above the value for the maximal misaligned PM, which was $\pm 500 \mu\text{rad}$ for the angle of the beam returned from the PM [14, R<130-040>].

A requirement for the dimensions of the actuators was not given, but the actuators will be implemented within the simulators. Their dimensions can significantly change the design. Furthermore the actuators had to be vacuum compatible to a level of 10^{-5} mbar or better to prevent outgassing of materials and their settlement on the optics. Therefore the smallest vacuum compatible actuator, which fulfilled the presented requirements was chosen as baseline actuator for the simulators.

3.2 Previous work

In Section 2.2 the read-out limits of the LTP PM interferometers were discussed. The results were obtained with ZerodurTM mounted mirrors, which were rigidly connected



(a) Optical pathlength noise of the two length measurements with the interferometers X1 and X12 of the LTP optical bench with and without piezo-mounted mirrors [18]. Additionally the LTP and LISA requirements are plotted. (b) Optical pathlength noise of the PAAM for different angular misalignments of the actuator [49].

Figure 3.2: Optical pathlength stability of actuators tested at the AEI.

to the LTP OB. In Figure 3.2(a) both measurement interferometers X1 and X12 show an optical pathlength noise including piezo-stack actuators of around $6 \text{ pm}/\sqrt{\text{Hz}}$ from 1 Hz down to 20 mHz increasing with $1/f^2$ towards lower frequencies. A comparison with the measurements using only ZerodurTM mounted mirrors indicated that in the measurements with actuators the optical pathlength noise for frequencies above 0.6 mHz was introduced by the actuators themselves [18]. The supply voltage for the actuators was identified to be the noise source. This type of actuator needed to be driven by voltage references to stay at a fixed position. The optical pathlength noise of piezo-stack actuators could be reduced by a reduction of their active length. This would have reduced the actuation range. Thus a higher supply voltage was needed to be compatible with the requirement for the actuation range. Voltage references with a stable voltage at low frequencies were only available for low voltages [48].

Another piezo-stack actuator will be used for the PAAM on the LOB. It was tested at the AEI [49]. Figure 3.2(b) shows the optical pathlength noise for different misalignments of the PAAM. The stability of the PAAM was sufficient to be able to measure an optical pathlength noise which was below the required $2.84 \text{ pm}/\sqrt{\text{Hz}}$ in the complete frequency range. Its disadvantage was that it could change the angle of the mounted mirror only in one angular degree of freedom. Therefore it was not compatible with a telescope simulator or PM simulator. Both interface simulators need two degrees of freedom. Additionally its pointing range and its dimensions were not compatible with the simulators. Therefore piezo-stack actuators have not been taken into account for the LOB interface simulators.

The piezo slip-stick actuators AG-LS25 and AG-MN100 from Newport have been used in the past for the test-setup of the Suspension Platform Interferometer (SPI) at the AEI [50, 51, 52]. The tests focused on the dynamic characteristics of the actuators due to the fact that the attached mirror simulated a moving end mirror of a MZI. The main outcome for the usage of both actuators within the LOB were that the measured step width of the actuators was varying although the step width was fixed in the electronics. The effect became smaller the bigger the step width in the electronics was chosen. The tip/tilt

Table 3.1: Comparison of piezo-driven tip/tilt stages.

Manufacturer	Thorlabs	Newport	Attocube
Part number	KS1-ZST	AG-M100LV6	ANGp101
Range [°]	±4	±2	±5.4
Resolution [μrad]	5	1	0.9
Dimensions [mm]	54 x 55 x 135	54 x 54 x 24	24 x 24 x 22
Vacuum compatibility [mbar]	No	10 ⁻⁵	10 ⁻⁸

actuator had non-negligible cross-coupling between the axes. Both properties were not critical for the testing of the LOB.

3.3 Comparison and selection of actuators

The information on the already tested actuators presented in the last section was taken into account for the selection process of the actuators. Thus the search was focused on actuators that can remain at a certain position without any supply voltage. A summary of the search of tip/tilt actuators is shown in Table 3.1. Three actuators fulfilled the requirements. The Thorlabs actuator was not selected because of its dimensions conflicting with a highly integrated and small setup. The characteristics of the Attocube actuator were not much better than the one of the Newport actuator. According to the quotes its price was a factor of 20 higher. Finally, the AG-M100LV6 was chosen because it was vacuum compatible to the required level [51].

Table 3.2 presents the linear actuators that fulfilled the requirements of the PM simulator. From the presented five actuators AG-LS25V6 from Newport was chosen as the baseline linear actuator [50]. The first reason was its vacuum compatibility to the required level. The second one was that its dimensions were relatively small in comparison to the other ones and the third reason was that the tip/tilt actuator was provided by the same company.

3.4 Experimental setup

In this section the experimental setup for testing the actuators is introduced. The setup of the LTP-style modulation bench is identical to the one presented in Figure 2.9 on page 13. Therefore a description is omitted here. The modifications on the phasemeter with respect to the one that was used for the picometer experiment (see Chapter 2) are explained. The essential part for the measurements was the OB, which will be introduced in detail.

3.4.1 Phase measurement system

The actuator experiment used the same LTP modulation scheme and PM3 phasemeter as the picometer experiment that was presented in Section 2.3. The heterodyne frequency in the actuator experiment was changed to 17858.5 Hz. This was done due to experiences gained at the backlink fibre experiment. A higher heterodyne frequency yielded a better stability against mechanical vibrations acting on the setup. The phasemeter parameters are summarised in Table 3.3. N_{SBFT} had to be changed within the phasemeter algorithm

Table 3.2: Comparison of piezo-driven linear translation stages.

Manufacturer	Linors	Linors	Newport
	Photonics	Photonics	
Part number	MS 15	MS 30	AG-LS25V6
Linear range [mm]	3.5	8	12
Step width [nm]	20	15	50
Max. travel speed [mm/s]	1.5	1.5	> 0.5
Dimensions [mm]	15 x 15 x 7.0	30 x 30 x 12.5	26 x 35 x 13
Vacuum compatibility [mbar]	Optional	Optional	10^{-5}
Manufacturer	Physik	Physik	
	Instrumente	Instrumente	
Part number	M-662	M-663	
Linear range [mm]	20	19	
Step width [nm]	50	300	
Max. travel speed [mm/s]	500	400	
Dimensions [mm]	28 x 28 x 8	35 x 35 x 15	
Vacuum compatibility [mbar]	10^{-7}	10^{-6}	

Table 3.3: Detailed parameters for PM3 settings within actuator experiment.

Parameter	Unit	Value	Remark
Heterodyne frequency f_{het}	Hz	17858.5	$f_{\text{het}} = f_{\text{samp}}/N_{\text{SBFT}} \cdot m$
Sampling frequency f_{samp}	kHz	800	
Length of sampled dataset N_{SBFT}	Samples	24640	
Frequency component m corr. to f_{het}		550	
Phase measurem. output frequency f_{ϕ}	Hz	32.47	$f_{\phi} = f_{\text{samp}}/N_{\text{SBFT}}$
Maximum input current	mA	0.66	

to 24640 to maintain the sample rate of 32.47 Hz. The frequency component m was set to 550 to get a heterodyne frequency of 17858.5 Hz.

3.4.2 Optical bench

The layout of the interferometers on the OB which were used for the analysis of the stability of the actuators is shown in Figure 3.3. The layout of the interferometers was originally developed to measure the optical pathlength stability of one reflective and one transmissive component [46, pp. 37]. In contrast to the OB used in Chapter 2 the fibre injectors, polarising and non-polarising optics were glued with a standard glue to a baseplate made of ULE [53] [46, p. 29]. The polarisation of the incoming light beams were cleaned up with polarising beam splitters directly after the input fibre couplers. 50/50 beam splitters were used to monitor the light intensities of the measurement beams. A reference interferometer (Ref) was used to measure the optical pathlength noise from the MB to the input of the OB and to stabilise the OPD between the measurement beams [37]. The reflective optic under test was optic number 1 in Figure 3.3 [46, pp. 37]. Its optical pathlength stability was measured with reflection interferometer (R). The transmissive component under test could be placed between optic number 2 and 3 in Figure 3.3.

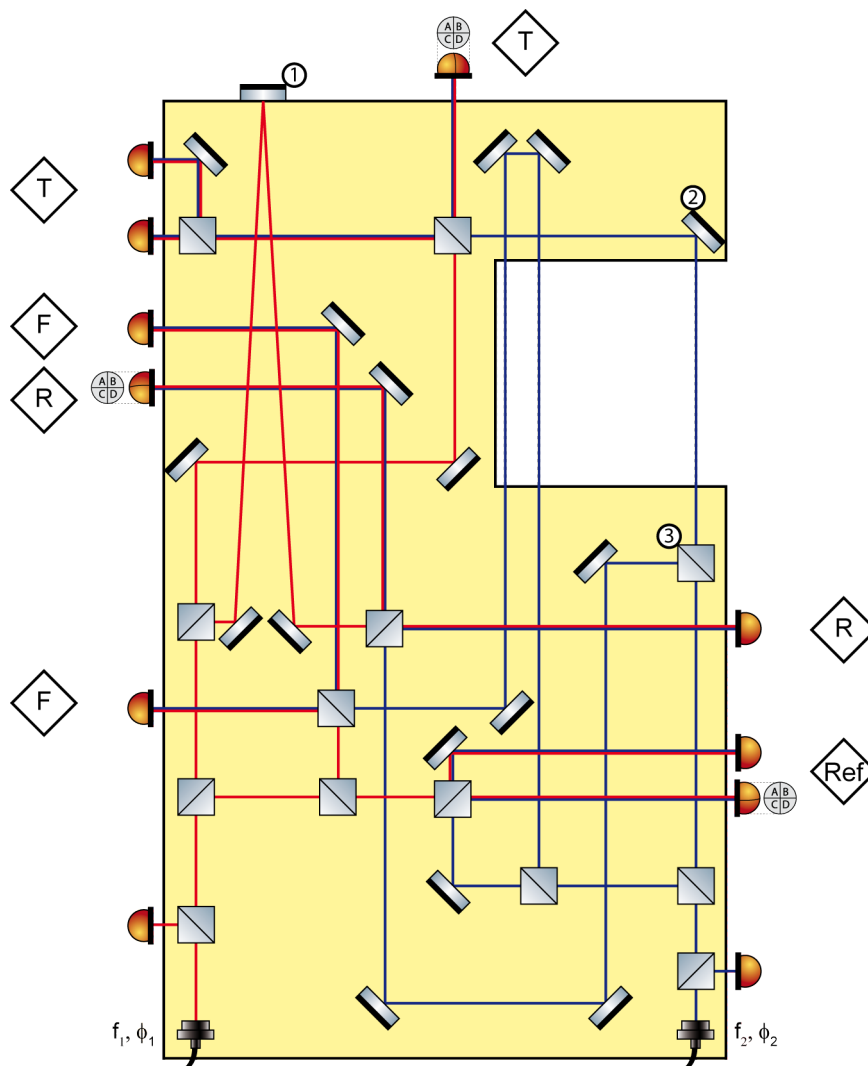


Figure 3.3: The sketched OB contains four interferometers. A reference, a reflection, a transmission, and a frequency interferometer. The stability of the actuators including their mirror are measured by replacing mirror 1.

Its optical pathlength stability was measured with the transmission interferometer (T). An additional frequency interferometer (F) with unequal armlengths compared to the reference interferometer could be used to monitor or stabilise the frequency noise of the laser source [38, pp. 54].

The final performance of the interferometers stated in [46, pp. 37] is depicted in Figure 3.4. The performance was one order of magnitude above the optical pathlength noise requirements for the LISA OB. In view of the knowledge that was gained since 2005 the limiting noise of that experiment are now thought to be

- in the high frequency range the usage of a software phasemeter, which used an analog data acquisition card for the read-out of the photodiodes [19, pp. 35].
- in the mid-frequency range the lack of a laser intensity stabilisation at DC and at the heterodyne frequency, see Subsection 2.4.3.5.
- in the low frequency range the absence of a thermal shield inside the vacuum

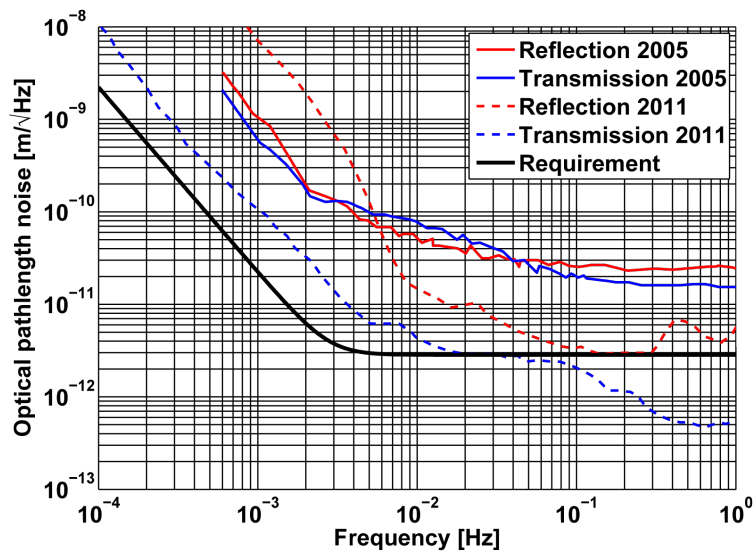


Figure 3.4: Optical pathlength noise of the interferometers on the ULE OB presented in [46, 45].

chamber, see Subsection 2.4.3.6.

Therefore this OB was chosen to test the actuators for the LOB in spite of not having shown sufficient performance during its last operation. Interferometer (R) and optic number 1 were used to measure the optical pathlength stability of the actuators. How the actuators were integrated into the experimental setup is described in Subsection 3.5.4.2. Interferometer T could be used to check the optical pathlength stability obtained with the interferometer R because a transmissive optics is not placed between optics number 2 and 3.

The rebuild of the OB and the integration of the actuators into the OB were part of a bachelor thesis at the AEI in 2011, which the author had supervised [45]. Key elements of the rebuild were: first, the silicon photodiodes, which were directly glued to the OB were exchanged by photodiodes including mounts and polarisers from the picometer experiment. Thereby each interferometer was equipped with one QPD and one SEPD. With these photodiode mounts the photodiodes could be aligned to the beams properly. Second, the OB and a thermal shield were integrated into a vacuum chamber. The thermal shield was developed and tested as part of another bachelor thesis at the AEI in 2011 [54]. Third, a OPD stabilisation compatible with the 17858.5 Hz heterodyne frequency was set up.

3.5 Results

This section starts with the characterisation of the low frequency intensity noise of the iodine-stabilised laser and its stabilisation. In the following a closer look at the low frequency frequency noise of the iodine-stabilised laser is taken. Afterwards three ways of reducing temperature induced optical length noise are investigated. First, the matching of the optical pathlengths seen by both measurement beams in an MZI. Second, the improvement of the temperature measurement system to subtract temperature induced optical pathlength noise in data post-processing. Third, the reduction of temperature noise at the experiment. In the end measurements of the optical pathlength stabilities of

different actuator assemblies are presented.

3.5.1 Laser intensity noise

The intensity fluctuations of the measurement beams of a heterodyne MZI can influence the optical pathlength noise of the length measurements. Thereby two frequency ranges of the intensity noise can be distinguished: the measurement band, which is 0.1 mHz to 1 Hz for LISA and the beat note band, which is 1 MHz to 20 MHz for LISA. The intensity noise within the first frequency band does influence the optical pathlength noise of the length measurement via the change of energy deposition within the photodiode. This changes the efficiency of the photodiode and its capacitance. The intensity noise within the second frequency band introduces an electronic noise, which degrades a shot noise limited length measurement by a certain amount. See Subsection 4.1.4. This subsection deals with the implementation of an intensity stabilisation in the measurement band.

3.5.1.1 Experimental setup

The laser source for this experiment was a Nd:YAG laser from Innolight, which was stabilised to an iodine transition [55]. More information on this laser system can be found in [56] which deals with a precursor version of the commercially available one. The frequency stabilised light was coupled into a polarisation-maintaining single-mode fibre for 1064 nm from Schäfter + Kirchoff (SUK) [57]. The polarisation of the light was aligned to the fibre axis at the input via quarter- and half-wave plates with the help of a polarisation analyser from SUK. In this way the change of polarisation at the fiber output could be reduced. More information on this alignment procedure can be found in [19, pp. 55].

The laser intensity was monitored with two silicon photodiodes PC50-6 from First Sensor at the two output ports of the same beam splitter [58]. The schematic of the amplitude stabilisation circuit can be seen in Appendix 6 in Figure 5. The circuit is based on an amplitude stabilisation, which has been used at the LTP experiments [38, p. 140]. It was modified to be compatible with the requirements of the LOB and was slightly improved. The bias voltage for the photodiodes was generated by a MAX6126 voltage reference with an additional transistor to increase the output current. In the input stage of the electronic each photo current was converted separately into a voltage, which could be measured. The calculated bandwidth of the TIA with the PC50-6 was approximately 0.5 MHz. The error signal was derived by subtracting the TIA output from a voltage reference and in the same stage the error signal was amplified. This error signal was monitored with an analog Data Acquisition (DAQ) card. The monitoring of the error signal instead of the photodiode signal had the advantage that the error signal fluctuated around zero. Thus the analog input range U of the DAQ could be decreased and with it the minimal detectable voltage change Q was reduced [20, pp. 184]. Q is given by

$$Q = \frac{U}{2^B} \quad (3.6)$$

and B is the resolution in bits of the DAQ. The lower limit for the monitoring of laser intensity is calculated by the shot noise of the laser power on the photodiode [59, pp. 147]. The noise shape is white and its value is

$$RIN_{SN} = \sqrt{\frac{2 \times e}{\rho P_{PD}}} \left[\frac{1}{\sqrt{\text{Hz}}} \right] \quad (3.7)$$

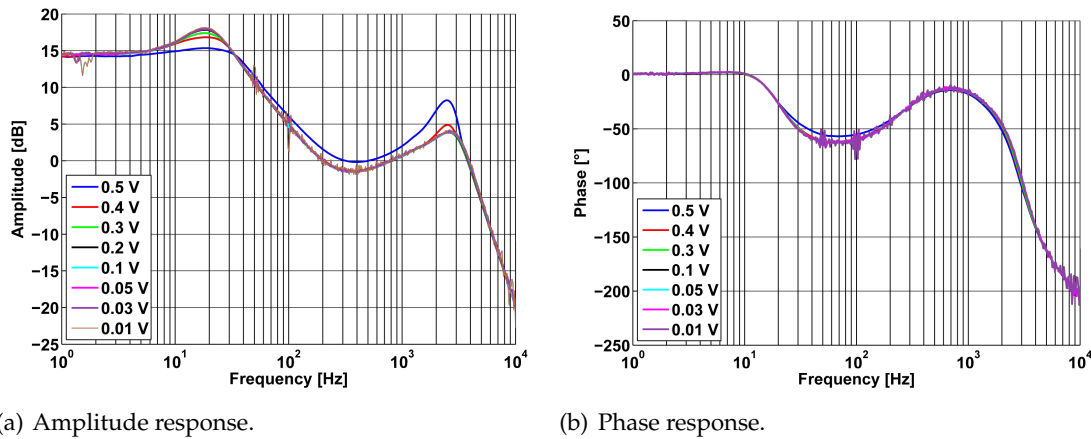


Figure 3.5: Transfer function of the AM input of the iodine-stabilised laser to the power monitor output of the DC laser intensity stabilisation.

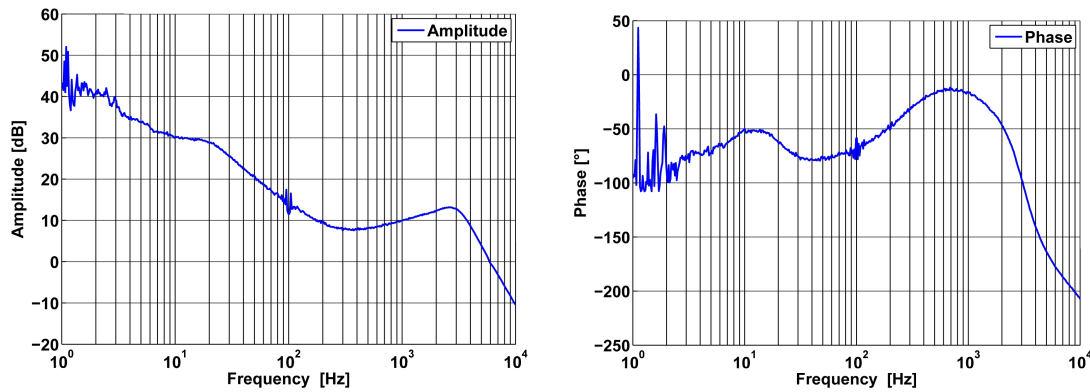
whereby ρ is the responsivity of the PC50-6 photodiode of around 0.15 A/W and the power P_{PD} on the photodiode is approximately 1 mW. Thus the lower limit is $4.6 \cdot 10^{-8} / \sqrt{\text{Hz}}$. This is well below the requirement of $1 \cdot 10^{-3} \cdot u_1(f) / \sqrt{\text{Hz}}$.

3.5.1.2 Results

The characterisation of the low frequency intensity stabilisation started with a measurement of the transfer function from the Amplitude Modulation (AM) input of the iodine-stabilised laser to the power monitor output of the DC laser intensity stabilisation. The information encoded in the transfer function was used to optimise the controller for the laser intensity stabilisation. Afterwards the Open-Loop Gain (OLG) of the control loop was measured. This is followed by the comparison of the low frequency laser intensity stability without and with stabilisation.

Figure 3.5 presents the measured transfer function from the AM input of the iodine-stabilised laser to the power monitor output of the DC laser intensity stabilisation, whereby the stabilisation was switched off. The transfer function was measured at different excitation voltages ranging from 0.01 V to 0.5 V. The measured amplitudes of the transfer functions, shown in Figure 3.5(a), were identical for frequencies below 6 Hz. Above 6 Hz and for excitation voltages higher than 0.2 V the amplitude transfer functions were differing from each other. Assuming that the transfer function of the TIA of the amplitude stabilisation was linear, the AM input of the iodine-stabilised laser was non-linear for frequencies above 6 Hz. The phase response of the transfer functions, shown in Figure 3.5(b) were identical for excitation voltages below 0.5 V. This information was used to set the corner frequency of the controller within the amplitude stabilisation. It was set to 16 Hz by choosing the RC time-constant of the proportional-integral controller as shown in Appendix 6 in Figure 5.

The OLG was determined according to the procedure described in [60, pp. 121]. Figure 3.5 presents the measured OLG of the DC laser intensity stabilisation in combination with the iodine-stabilised laser, whereby the stabilisation was switched on. The amplitude and phase slopes of the iodine-stabilised laser which were presented in Figure 3.5 are clearly visible. The Unity-Gain Frequency (UGF) was around 6 kHz according to



(a) Amplitude response.

(b) Phase response.

Figure 3.6: Open-loop gain of the DC laser intensity stabilisation for testing of the LOB. Unity gain frequency was measured as approximately 6 kHz with 5° phase margin.

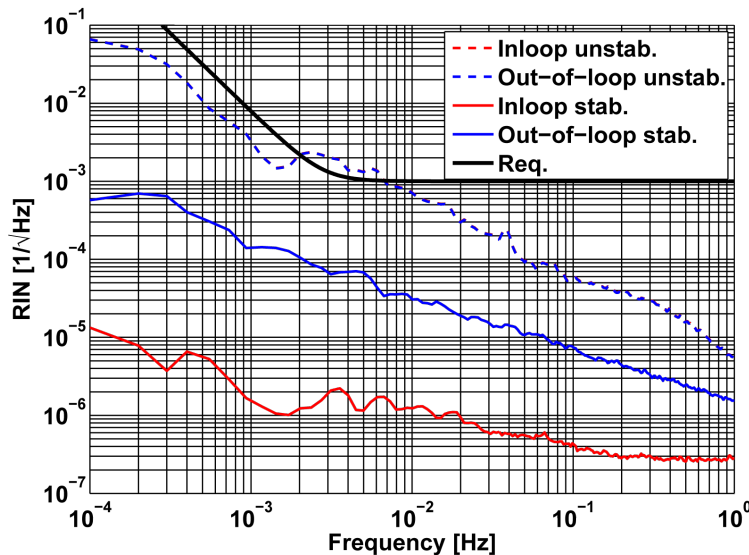


Figure 3.7: Comparison of the relative intensity noise of the unstabilised and intensity stabilised iodine-stabilised laser 1.

Figure 3.6(a). The phase margin was 5° according to Figure 3.6(b).

The low frequency intensity stability of the iodine-stabilised laser was measured without and with DC laser intensity stabilisation. The results can be seen in Figure 3.7. Without stabilisation the relative intensity noise was at a level of $5 \cdot 10^{-6} / \sqrt{\text{Hz}}$ at 1 Hz increasing with $1/f$ towards lower frequencies. When the intensity stabilisation was turned on the relative intensity noise measured with the out-of-loop photodiode was at a level of $1.6 \cdot 10^{-6} / \sqrt{\text{Hz}}$ at 1 Hz increasing with $1/\sqrt{f}$ towards lower frequencies. Thus the measured relative intensity noise was well below the requirement in the complete frequency range. The relative intensity noise measured with the in-loop photodiode was at a level of $3 \cdot 10^{-7} / \sqrt{\text{Hz}}$ at 1 Hz increasing with $1/f^{1/3}$ towards lower frequencies. Thus the relative intensity noise measured with the out-of-loop photodiode would be further improved if it is required.

3.5.2 Laser frequency noise

The measurement of the frequency noise of a laser with a state of the art frequency stabilisations is a challenging task. The laser frequency has to be compared to another standard, which has at least the same or better frequency stability. The standard method at the AEI is to use a second identical laser system including frequency stabilisation [60, 61]. This technique requires twice the resources. Another method to monitor the frequency stability of a laser utilises an unequal armlength MZI according to Subsection 2.4.3.3. The effect of a frequency shift $\delta\nu$ in an unequal armlength MZI on the optical pathlength change δl is [38]

$$\delta l = \frac{\lambda \cdot \delta\nu}{c} \Delta L \text{ [m]} \quad (3.8)$$

Monitoring and stabilisation of the laser frequency with this method was investigated for the LTP and for the polarisation optics experiment at the AEI [38, pp. 57] [17, pp. 117]. The best result of a frequency stabilisation with an unequal armlength interferometer was achieved at the polarisation experiment. The armlengths were mismatched to about 271 mm and the frequency noise of the laser could be stabilised to a level of 10 kHz/ $\sqrt{\text{Hz}}$ for frequencies above 10 mHz increasing with $1/\sqrt{\text{Hz}}$ towards lower frequencies [17, pp. 117]. The OB for testing of the actuators had an interferometer with an armlength mismatch of about 700 mm. Thus the question came up, whether the sensitivity for the measurement of frequency noise via an unequal armlength MZI can be further increased with an elongation of the armlength mismatch or whether other noise sources arise. This questions will be answered in the next subsection by comparing the two introduced methods of the laser frequency measurement.

3.5.2.1 Experimental setup

Figure 3.8 depicts the experimental setup to measure the frequency stability of the iodine-stabilised laser from Innolight by beating it against a second identical system [29, 62]. The laser beams from the two fibre-coupled iodine-stabilised lasers were guided to a small setup on an optical table. The half-wave plate and PBS combinations at the inputs of the setup were used to adjust the power levels. Both beams were interfered at a beam combiner. The interfered beam was focused with a lens on a photodetector with a bandwidth of about 500 MHz. Iodine-stabilised laser 1 was stabilised on the iodine transition “a1”, which was commonly used. Iodine-stabilised laser 2 was stabilised on the iodine transition “a2” according to the datasheet [29]. This yield a beat note frequency of about 129 MHz. The frequency of the beat note was measured with a SR620 frequency counter from Stanford Research System and was recorded via a PC [63].

The frequency noise of the beat note is defined by the frequency noise contributions of the individual systems. If the noise of both laser systems is equal uncorrelated, the frequency noise of one laser system is the frequency noise of the beat note divided by $\sqrt{2}$.

The second method to measure the frequency noise of the iodine-stabilised laser 1 utilises the unequal armlength interferometer of the actuator OB. The experimental setup is described in Section 3.4. The frequency noise of the laser was measured by subtracting the measured optical pathlengths in the reference interferometer from the frequency interferometer in Figure 3.3. The frequency noise was than calculated via the knowledge of the armlength mismatch ΔL using Equation 3.8.

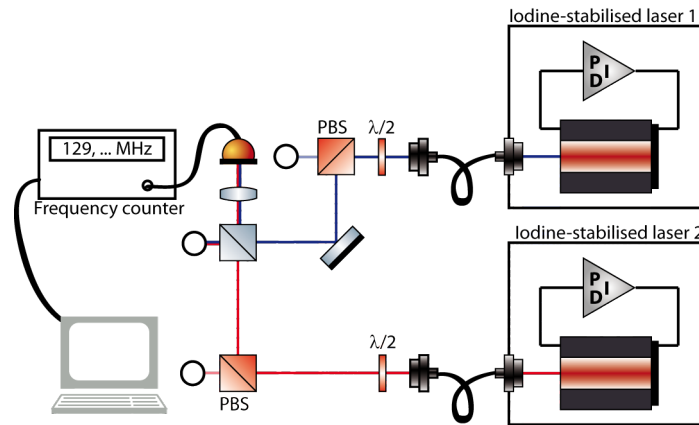


Figure 3.8: Schematic of the experimental setup to measure the frequency stability of the iodine-stabilised laser by beating it against a second identical system.

Table 3.4: Armlength mismatches of the three interferometers R, T, and F with respect to the reference interferometer shown in Figure 3.3 for a laser frequency modulation with 600 MHz peak-to-peak amplitude.

	Amplitude L	ΔL
Interferometer	[nm]	[mm]
Frequency	1450	681.0
Reflection	27	12.7
Transmission	12	5.6

3.5.2.2 Results

In a first step the mismatch of the armlengths of the interferometers R, T, and F with respect to the reference interferometer of the OB were measured. The reflective mirror number 1 in the reflection interferometer, shown in Figure 3.3, was already replaced by an actuator combination. The mirror attached to the actuator was at its nominal position. Thus the obtained armlength mismatch is also valid for other actuator combinations. The value for the armlength mismatch in the frequency interferometer is approximately 700 mm as stated in [46, pp. 39]. The armlength mismatch was measured according to the procedure described in Subsection 2.4.3.3. The frequency of the iodine-stabilised laser 1 (frequency stabilisation switched off) was modulated with a frequency generator acting on the laser crystal temperature. The frequency was 25 mHz and the peak-to-peak amplitude 600 MHz. The modulation of the length measurements obtained with the interferometers R, T, and F is shown in Figure 3.9(a). The modulation depth of the length measurement obtained with the frequency interferometer was more than a factor of 50 higher than the other two length measurements. Table 3.4 summarises the peak-to-peak amplitudes of the length measurement modulation and presents the calculated armlength mismatches according to Equation 3.8. The armlength mismatch of the frequency interferometer was calculated to 681 mm. This value will be used to compare the frequency noise measurements obtained with the frequency interferometer and the frequency counter.

Figure 3.9(b) presents the results of the frequency noise measurements of the iodine-stabilised laser 1 obtained with the SR 620 frequency counter and the frequency inter-

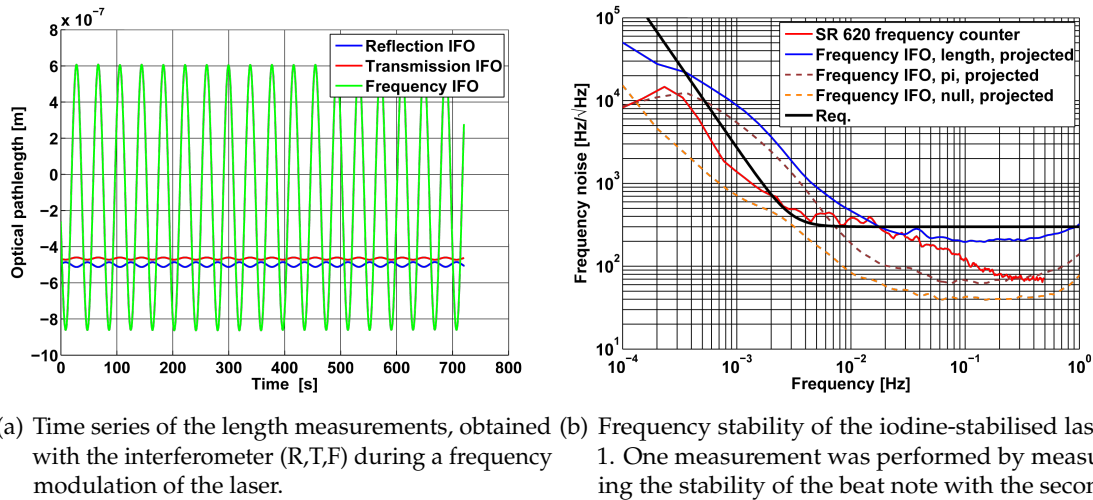


Figure 3.9: Influence of a laser frequency shift onto the optical pathlength.

ferometer. The frequency noise measured with the frequency counter was at a level of $70 \text{ Hz}/\sqrt{\text{Hz}}$ at 500 mHz increasing with $1/\sqrt{f}$ towards lower frequencies. At 4 mHz the slope is changing to $1/f$. The frequency noise measured via the projection of the length measurement in the frequency interferometer was at a level of $200 \text{ Hz}/\sqrt{\text{Hz}}$ at 100 mHz increasing with a $1/f$ towards lower frequencies. The projected frequency noise was above the directly measured frequency noise in the whole frequency range. Nevertheless the projected frequency noise was close to the requirement for the frequency stability of the laser. The π measurement of the frequency interferometer and the null measurement of the transmission interferometer were projected with the coupling coefficient of the frequency interferometer into Figure 3.9(b). The length measurement in the frequency interferometer was at low frequencies on the same noise level as the π measurement. A results of Subsection 2.4.3.1 was that a π -measurement in an interferometer gives a lower limit for the length measurement obtained with that interferometer. The lower limit for the π measurement was indicated by the null measurement. If the π measurement can be improved in the future down to the level of the null measurement the length measurement in the frequency interferometer will be improved, too. With these improvements the frequency interferometer can indicate if the iodine-stabilised laser has a reduced frequency stability or falls out of lock. Thus the method of using an unequal armlength interferometer to monitor the frequency stability of an iodine-stabilised laser is a cost-effective method in comparison to buying an additional iodine-stabilised laser.

3.5.3 Temperature noise

LISA technology demonstrator experiments are performed normally inside a thermal shield, which is located in a vacuum chamber. The temperature noise in such an environment is below $1 \cdot 10^{-4} \text{ K}/\sqrt{\text{Hz}}$ at frequencies higher than 1 mHz increasing with $1/f$ towards lower frequencies. Nevertheless the measured optical pathlength noise of such experiments are degraded by temperature noise for frequencies lower than 1 mHz. Thus a closer look at the matching of the optical pathlengths of both measurement beams in an

MZI is taken. Afterwards the temperature measurement system has been improved to be able to subtract temperature-induced optical pathlength noise in data post-processing. In the end the temperature noise of the experiment has been improved.

3.5.3.1 Optical pathlength matching

Matching of the optical pathlengths of both measurement beams of a heterodyne MZI is critical for all LISA-related experiments at low frequencies. In this context low frequencies mean sub mHz range. Therefore this section introduces different coupling mechanism by which temperature modifies the differential optical pathlengths of both measurement beams. The emphasis is put on the measurement setup for testing of the actuators. Starting point is the influence of the refractive index of air, followed by the expansion of the OB material and finally the influence of material of optics.

Air

The change of the refractive index of air via temperature, pressure and composition was analysed in detail in the past [64]. The variations of the refractive index of air influence the optical pathlengths of the measurement beams in a MZI. Thereby the differential optical pathlength change between both measurement beams is in the order of $30 \text{ pm}/\sqrt{\text{Hz}}$ for frequencies above 30 mHz increasing with $1/f$ towards lower frequencies, see Figure 2.16(a) on page 20. This is introduced by the fact that the refractive index of air is varying in a relative small space in comparison to a MZI. To overcome this problem all LISA experiments, which require differential optical pathlength stability in the pm range at low frequencies are operated under vacuum conditions. For this purpose a pressure level of less than 1 mbar has been found to be sufficient, whereas an upper level was not determined.

Ultra-low expansion baseplate

The estimation of the optical pathlength change between both measurement beams due to the expansion of the ULE baseplate is based on the knowledge of the baseplate's Coefficient of Thermal Expansion (CTE) and the temperature noise of the baseplate. Therefore both characteristics are analysed separately and combined afterwards.

The actuator experiment was setup on an ULE baseplate, of which the grade was not defined in the according reference [46, p. 29]. Thus it is assumed that it is a ULE standard grade baseplate with a CTE of $(0.0 \pm 3 \cdot 10^{-8})/\text{K}$ in the temperature range between 5°C to 35°C [53]. The following reasoning is based on the data obtained from the ZerodurTM datasheets [65, 66], because the information was not available for ULE. This procedure is valid because the production process and the physical properties are similar. The CTE of ZerodurTM class 0 is $(0.0 \pm 2 \cdot 10^{-8})/\text{K}$ in the temperature range between 0°C to 50°C [65]. The non-zero CTE originates from the non-uniform expansion of a piece of ZerodurTM over its surface, which is driven by a non-uniform cooling process during the production of the ZerodurTM blank [66, pp. 11]. The introduced inhomogeneity is smaller than $1 \cdot 10^{-8}/\text{K}$ for a ZerodurTM blanket up to 300 kg [66, pp. 11]. Thus a worst case assumption for the CTE properties of an OB made of ZerodurTM is that the overall CTE is $2 \cdot 10^{-8}/\text{K}$ and the variations across the OB (ΔCTE) are $1 \cdot 10^{-8}/\text{K}$. These numbers imply that the optical pathlength change ΔL_L along two equally long measuring lengths

L on different parts of the same blank of ZerodurTM (or ULE) due to a temperature change δT is

$$\Delta L_L = L \cdot \Delta \text{CTE} \cdot \delta T \quad (3.9)$$

The differential optical pathlength change is increased additionally by the mismatch if the optical pathlengths of both measurement beams are not matched. The optical pathlength change ΔL_L between both measurement beams is the product of the baseplate CTE, the temperature change δT and the optical pathlength difference ΔL . Including the optical pathlength change of equally long arm lengths the total induced optical pathlength noise ΔL_{total} is

$$\Delta L_{\text{total}} = (L \cdot \Delta \text{CTE} + \Delta L \cdot \text{CTE}) \cdot \delta T \quad (3.10)$$

This equation has to be taken into account during the design phase of a MZI. The optical pathlengths within the interferometer design need to be as short as possible. If long arms are needed the CTE of the material has to be reduced. The standard is currently ZerodurTM class 0 with $(0.0 \pm 2 \cdot 10^{-8}) / \text{K}$. A better grade called class 0 EXTREME is available with $(0.0 \pm 7 \cdot 10^{-9}) / \text{K}$ between 0°C to 50°C [65].

The temperature stability of the baseplate needs to be known in order to calculate the optical pathlength noise. Figure 3.10 summarises the results of a measurement to estimate the temperature distribution across two surfaces. A first measurement was performed on the surface ($40 \times 80 \text{ mm}^2$) of an aluminium block, see Figure 3.10(a). The PT10k temperature sensors were equally distributed across this surface and attached with thermally conductive adhesive tape. The mean of all eight PT10k sensors was calculated and individually subtracted afterwards from all channels to calculate the temperature distribution across the surface. The derived temperature noise of all channels was at a level of $1.5 \cdot 10^{-5} \text{ K} / \sqrt{\text{Hz}}$ for frequencies above 30 mHz increasing with $1/\sqrt{f}$ towards lower frequencies. A second measurement was performed on the surface ($300 \times 500 \text{ mm}^2$) of the used ULE baseplate, see Figure 3.10(b). Again the eight PT10k temperature sensors were equally distributed across the ULE baseplate and attached with thermally conductive adhesive tape. The temperature noise measured with each PT10k sensor was derived in the same way as for the first measurement. The temperature noise of all sensors was at level of $1.5 \cdot 10^{-5} \text{ K} / \sqrt{\text{Hz}}$ for frequencies above 30 mHz increasing with $1/\sqrt{f}$ towards lower frequencies. The measured temperature noise distributions across the ULE baseplate and across the metallic block were identical. The measurement of the temperature distribution across the metallic block is one method to estimate the read-out noise of the temperature measurement system. Thus the measurement of the temperature distribution across the ULE baseplate was read-out noise limited. Therefore it is a good assumption that the maximum temperature noise difference on a ULE (or ZerodurTM) baseplate is at level of $1.5 \cdot 10^{-5} \text{ K} / \sqrt{\text{Hz}}$ or lower for frequencies above 30 mHz increasing with $1/\sqrt{f}$ towards lower frequencies in a typical LISA lab environment at the AEI. The comparison to the measurement performed on the metallic surface points out that the temperature on this OB only needs to be measured at one point. For an OB with active components like photodetectors this statement has to be verified.

The influence of temperature noise onto the optical pathlength noise in the reflection interferometer of the actuator experiment is estimated now using Equation 3.10. The absolute length L 0.72 m from the OptoCad layout in [46, p. 41]. The differential length ΔL was measured in Subsection 3.5.2 and is 12.7 mm. ΔCTE is $1 \cdot 10^{-8} / \text{K}$ and the CTE is $3 \cdot 10^{-8} / \text{K}$. The temperature noise of the ULE baseplate is at 1 mHz $100 \mu\text{K} / \sqrt{\text{Hz}}$ according

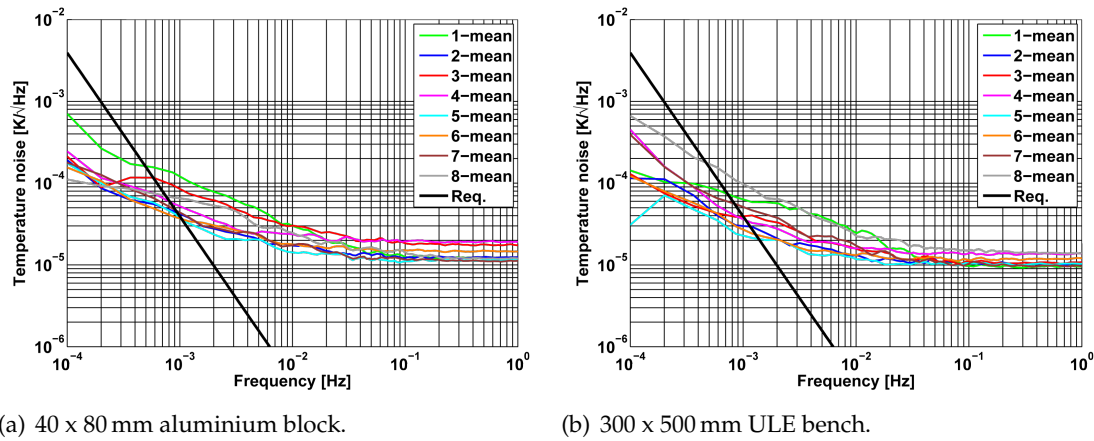


Figure 3.10: The Pt10k sensors of the FPGA thermometer were equally distributed on two types of surfaces to measure the temperature stability across both surfaces.

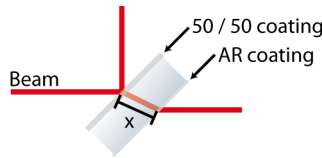


Figure 3.11: Beam propagation in a 50/50 beam splitter.

to Figure 3.10(b). The induced optical pathlength length noise ΔL_{total} is calculated as $0.76 \text{ pm}/\sqrt{\text{Hz}}$. This value can be seen as uncritical with respect to the requirement for the actuators, because it was calculated on a worst case assumption.

Properties of components

The mirror that was attached to the actuator assembly, was not at the position of optic number 1 in Figure 3.3. The offset was approximately 10 mm in the beam direction. Therefore the contrast of the interferometer R was reduced by the beam offset. This beam offset was compensated by placing an Anti-Reflection (AR)-coated component in the beam path between the mirror on the actuator assembly and the beam combiner of interferometer R. The optical pathlengths of both measurement beams propagating within components have a high influence on the differential optical pathlength [38, pp. 99]. Figure 3.11 shows a typical beam splitter with a dielectric coating on the front face and an anti-reflective coating on the rear. The coating are neglected for this consideration. The following equation describes the optical pathlength change ΔL_{OP} seen by one measurement beam while propagating through a component due to the refractive index

$$\Delta L_{\text{OP}} = \delta T \cdot x \cdot [\text{CTE}_{\text{OP}} \cdot (n_{\text{OP}} - 1)] \quad (3.11)$$

δT is the change of the temperature, x the geometrical length, CTE_{OP} is the CTE of the optical component and n_{OP} the refractive index of the optical component. The standard material for optics used for LISA is fused silica. The CTE of fused silica is $5.5 \cdot 10^{-7} / \text{K}$ which is more than an order of magnitude higher than the CTE of ZerodurTM and ULE [67]. The refractive index n_{OP} is about 1.45 [68]. A temperature change δT of 100 μK at 1 mHz in combination with a geometrical length x of 5 mm in fused silica introduces an

optical pathlength change of $\Delta L_{OP} = 0.275$ pm. This is well below the 1 pm requirement of LISA.

Unfortunately the optical pathlength is also varied by the change of the refractive index with temperature $\Delta n_{OP}/\Delta T$. Therefore the equation for ΔL_{OP} has to be extended.

$$\Delta L_{OP} = \delta T \cdot x \cdot [\text{CTE}_{OP} \cdot (n_{OP} - 1) + \Delta n_{OP}/\Delta T] \quad (3.12)$$

The change of the refractive index with temperature $\Delta n_{OP}/\Delta T$ is $11.8 \cdot 10^{-6}$ /K for the operating wavelength of 1064 nm [68]. This is a factor of 20 larger than the CTE of fused silica. Under the before mentioned conditions the length change ΔL_{OP} is around 5.6 pm. An implication of this is that the optical pathlengths within the optics have to be matched well for both measurement beams. A rule of thumb is that the number of optics in both measurement beam paths have to be identical. Therefore an AR-coated optic was also placed at the other input of the beam combiner in interferometer R.

3.5.3.2 Temperature measurement system

At low frequencies a correction in data post-processing of a measured optical pathlength change with a measured temperature change is a well-known technique at LISA experiments [19, pp. 73]. The knowledge of read-out noise of the thermometer is essential for the correction because it defines the frequency range of the correction.

The FPGA thermometer used at the AEI was introduced in Subsection 2.4.3.6. The standard temperature sensor was a PT10k resistor which offered linearity over a large temperature range in comparison to NTC resistors. The absolute temperature of the LOB will be within a range of approximately ± 2 °C around room temperature. This absolute temperature range is required due to the properties of ZerodurTM and ULE. Its CTE will increase significantly for higher or lower temperatures [66]. The temperature stability on the LOB will be comparable to the one shown in Figure 3.10(b). Therefore the non-linearity of the NTC resistors is negligible. The temperature coefficient of the resistance of NTC resistors is approximately ten times higher than the one of PT10k sensors [69]. This property can be used to increase the SNR of the temperature measurement and to decrease the read-out noise.

The exchange of the PT10k sensor by NTC sensors was done according to the following procedure. The absolute temperature of the laboratory was measured. The output voltage $v_0(T)$ of the Wheatstone bridge with the NTC sensor was nulled for this temperature by choosing an appropriate fixed resistor for the second half of the measurement arm, see Figure 2.27 on page 29. For the fixed resistor a standard SMD resistor with a tolerance of 1% and a stability of ± 55 ppm/K was used. Additionally the amplification of a differential amplifier at the input of the FPGA thermometer was reduced to maintain the temperature measurement range with the NTC sensor. Figure 3.12 presents a temperature noise measurement inside the actuator vacuum chamber. Three of the eight PT10k sensors have been replaced by NTC sensors. The first NTC sensor was attached to the actuator assembly, the second was attached to the ULE baseplate on the ULE baseplate and the third was attached to the aluminium baseplate. One PT10k sensor was placed on the aluminium baseplate in the near of a NTC sensor and one PT10k sensor was placed on the ULE baseplate in the near of a NTC sensor. The difference between the ULE and aluminium sensors is the read-out noise of the sensors. According to Subsection 3.5.3.1 this is a valid method because for low frequency the temperature noise inside the thermal shield was equally distributed. The curves in Figure 3.12 show that the read-out noise of

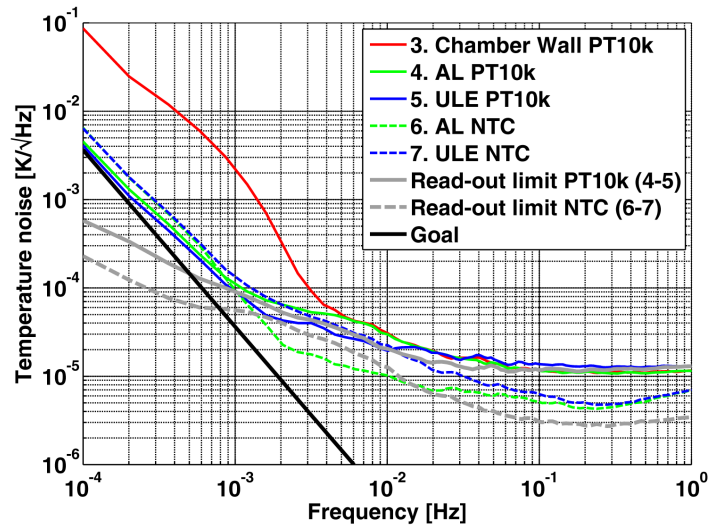


Figure 3.12: Comparison of the read-out noise of the FPGA thermometer equipped with PT10k and NTC sensors.

the NTC sensors at high frequency was approximately an order of magnitude lower than for the PT10k sensors and decreasing at lower frequencies to a factor of 3.

3.5.3.3 Temperature noise suppression

The temperature noise measured at the experiment inside a “simple” thermal shield, shown in Figure 3.12, is not below the goal for testing of the LOB. Thus alternative approaches to stabilise the temperature noise have been investigated.

The transmittance of a 25 mm thick ZerodurTM Class 0 baseplate within the visible wavelength range is approximately 90% [70]. This value changes for wavelengths longer than 5 μm , where it becomes almost 0% [70]. It is further assumed that the heat radiation inside a vacuum chamber has a distribution of black body radiation. The wavelength of maximum radiation at a room temperature of 22 $^{\circ}\text{C}$ can be calculated via Wien’s displacement law [71, pp. 78]

$$\lambda_{\max} = \frac{2897.8\mu\text{m}}{T [\text{K}]} \quad (3.13)$$

$$\approx 9.8\mu\text{m} \quad (3.14)$$

This value indicates that a ZerodurTM baseplate is absorbing almost the complete thermal radiation emitted by a vacuum chamber. The same is true for the used ULE baseplate [72]. This effect could be suppressed by coating the baseplate with a broadband reflective coating for thermal radiation after the optics have been bonded. Coating before the bonding step is incompatible with the bonding procedure itself [73, pp. 158]. Nevertheless, the coating after the bonding steps was not feasible for the laboratory usage because of constraints given by budget and schedule.

Alternative approaches for stabilising the temperature at the experiment have also been discussed; namely the increase of the thermal mass of the vacuum chamber and an active stabilisation of the temperature of the vacuum chamber. This work was done in cooperation with Maiké Lieser at the AEI. The increase of the thermal mass of the vacuum

chamber is explained now. The mass of the vacuum chamber is around 656 kg. It has a specific heat capacity of 500 J/(kg·K) (stainless steel X5CrNi18-10). Thus the thermal mass is about 328 kJ/K. The thermal mass can be increased by adding water basins on each foot of the vacuum chamber. The specific heat capacity of water is 4180 J/(kg·K). Assuming on each foot a water basin with a diameter of 300 mm and a height of 360 mm is placed the thermal mass of the additional water is 425 kJ/K. This would have doubled the thermal mass of the vacuum chamber and thereby reduced the corner frequency of the low pass of the thermal mass by a factor of two. This solution was not further investigated due to the risk of having water nearby the electronic and the experiment. The active stabilisation of the vacuum chamber temperature is challenging due to the high thermal mass and the low corner frequency of the control loop. Therefore this solution was not further investigated.

A more practical solution of the thermal noise suppression via the reduction of energy transport (heat conduction and radiation) was chosen. The suppression of thermal noise below the goal for testing the LOB via a thermal shield was demonstrated at the AEI [35, pp. 35]. The thermal shield consisted of an inner and outer layer of aluminium. The vacuum chamber and the thermal shield layers were thermally isolated using Macor spacers. The temperature noise at the experiment was at a level of $10\mu\text{K}/\sqrt{\text{Hz}}$ or lower for frequencies above 0.5 mHz increasing with a steep $1/f^5$ towards lower frequencies. Therefore the reduction of the thermal noise at the actuator experiment was focused on the improvement of the thermal shield.

Figure 3.13 shows the current status of the thermal noise reduction system within the LOB vacuum chamber, which was extended to this state step-by-step. At the beginning the baseplate for the actuator testing was placed inside a simple thermal shield without Multi-Layer Insulation (MLI) foil. Thus the thermal shield was comparable to the one of the picometer experiment. The thermal shield was placed on spacers made out of Macor. The aluminium had a high thermal mass and therefore it behaves like a capacitor with respect to heat conduction. The Macor spacer behaves like a thermal resistance with respect to heat conduction. Both together form the equivalent of a RC-filter. The aluminium was polished and had a reflectivity of more than 98 % at wavelengths longer than 1 μm [74]. Therefore most of the thermal radiation was reflected back towards the vacuum chamber and not absorbed by the thermal shield. The polished surface was a thermal resistance with respect to thermal irradiation. Therefore the thermal shield decouples the ULE from the vacuum chamber in a certain range and improves the thermal stability at the experiment. The Macor spacer reduces the heat conduction from the bottom of the vacuum chamber. This improved the thermal noise at the experiment from the red curve down to the green curve in Figure 3.14(a).

The isolation of the thermal shield was improved by attaching MLI foil to the outer part of the aluminium. The MLI foil type Coolcat 2 from RUAG consists of 10 layers double side aluminised, 6 μm thick perforated polyester film, interleaved with 10 layers of polyester knit-woven spacer [75]. Figure 3.14(a) shows the temperature noise after the installation of the MLI foil. At frequencies lower than 3 mHz the thermal noise could be improved by a factor of 3. At higher frequencies the read-out noise of the FPGA thermometer had been improved between the measurements. Another source of thermal noise at the experiment was believed to be heat conduction via the cabling. An intermediate thermal mass, which was thermally isolated from the experiment and the vacuum chamber, was implemented to suppress the heat conduction via the cabling. All cables had to pass this intermediate thermal mass before they were guided to the

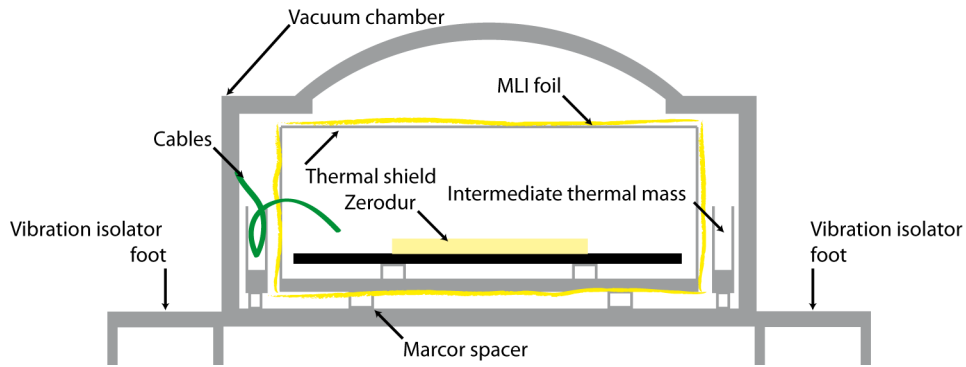
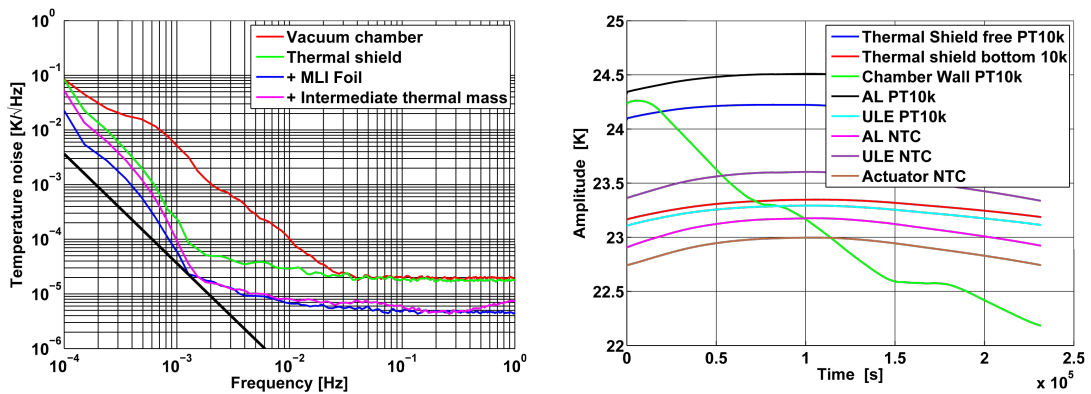


Figure 3.13: Schematic of the thermal shield used at the actuator experiment.



(a) Temperature noise on the ULE baseplate with different versions of the thermal shield. (b) Long time series of the temperature sensor amplitudes in the vacuum chamber.

Figure 3.14: Improvement of the thermal shield.

experiment. Unfortunately this did lead to a degradation of the thermal stability at the experiment. See Figure 3.14(a).

Additionally to the spectra the transfer functions from the temperature of the vacuum chamber to the temperature of the ULE baseplate were calculated. This was done for several measurements of the temperature with a “simple” thermal shield, with MLI foil and with the intermediate thermal mass. The result was that the transfer functions differed significantly for the same development stage of the thermal shield. Long term measurements of the laboratory temperature revealed that the inlet air of the laboratory was stabilised but not the laboratory temperature itself. Therefore the vacuum chamber temperature was changing by more than 2 °C in three days when the outdoor temperature was changing, see Figure 3.14(b). During this outdoor temperature change the measured temperature noise at the ULE baseplate was changing by a factor of 4 and also the transfer function were changing. Thus the lab temperature control will be changed in the near future. The effect of the MLI foil and the intermediate thermal mass on the temperature noise at the experiment have to be repeated with a stable laboratory temperature to estimate their influence.

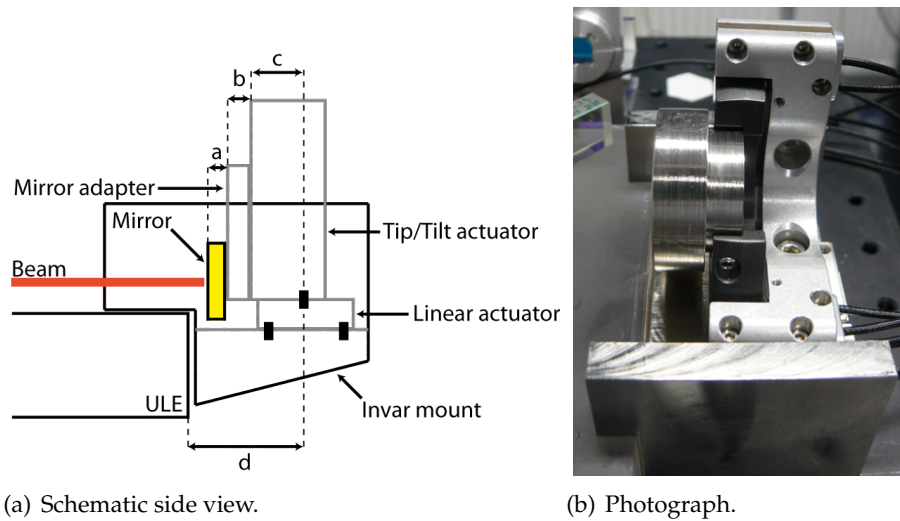


Figure 3.15: Actuator assembly including mirror and mirror adapter on the Invar mount, which is glued to the ULE baseplate.

3.5.4 Actuator length stability

This section focuses on the measurement of the optical pathlength stabilities of the actuator assemblies. At the beginning the results that have been presented in [45] and whose were measured under the authors supervision are reviewed. This is followed by a presentation of the optical pathlength stability of an actuator assembly, which is thermally compensated by a simple construction. Afterwards a more elegant thermal compensation is introduced. First measurements of the CTE of the actuator assembly with the elegant thermal compensation are presented. This setup was analysed within stable thermal conditions but also in measurements where the temperature was modulated by purpose.

3.5.4.1 Uncompensated actuator

The optical pathlength noise of the transmission and the reflection interferometers including an uncompensated actuator assembly measured in the context of [45] can be seen in Figure 3.4 on page 40. The optical pathlength noise levels of the interferometers were significantly improved for frequencies above 6 mHz. The optical pathlength noise in the reflection interferometer was degraded for frequencies below 6 mHz in comparison to 2005. The optical pathlength noise measured with the transmission interferometer was improved at low frequencies by more than an order of magnitude. The difference between the optical pathlength noise levels in the reflection and the transmission interferometers indicated that the low frequency optical pathlength noise in the reflection interferometer was induced by the actuator assembly.

Figure 3.15(a) shows a schematic side view of the actuator assembly under test. A photograph can be seen in Figure 3.15(b). An adapter made of Invar was glued to the ULE baseplate. The CTE of Invar is $1.2 \times 10^{-6}/\text{K}$ in the temperature range between 0°C and $+100^\circ\text{C}$ [76]. The linear actuator AG-LS25V6 is connected via four M3 screws to the Invar adapter. The tip/tilt actuator AG-M100N is connected via one M4 screw to the linear actuator. The mirror is attached to the tip/tilt actuator via an adapter plate made of Invar. This adapter plate shifts the centre of the mirror from its nominal position to

Table 3.5: Calculation of the effective CTE of the actuator assembly.

Part	Material	CTE [1/K]	Label	Length [mm]	Effective CTE [nm/K]
Invar mount	Invar	$2 \cdot 10^{-6}$	d	-33	-66
Linear actuator	Stainless steel	$10 \cdot 10^{-6}$		0	0
Tip/Tilt actuator	Aluminium	$23.1 \cdot 10^{-6}$	c	14.9	344
Mirror adapter	Invar	$2 \cdot 10^{-6}$	b	11	22
Mirror	Fused silica	$0.5 \cdot 10^{-6}$	a	7.6	3.8
Sum					304.7

the pivot point of the tip/tilt actuator.

The CTE of the complete actuator assembly was only measured in the beam direction. Therefore the expansions of the individual parts of the actuator assembly were important in this degree of freedom. The expansion of the actuator assembly in this direction under a temperature change is calculated now. An expansion towards the measurement beam has a plus sign and an expansion in the other direction a minus sign. For this consideration the standard CTE in 1/K is replaced by the effective CTE in m/K. It was assumed that all parts are expanding linearly under a temperature change. Table 3.5 summarises the effective CTE calculations according to Figure 3.15(a). The linear actuator (made of aluminium) is connected via four screws to the Invar mount. The CTE of Invar is one order of magnitude smaller than that of aluminium. Thus the aluminium actuator would expand more than the Invar mount under a temperature change if they were not connected via screws. The stiffness of Invar is higher than that of aluminium. It is assumed that the force introduced by the differential expansion between both parts can be held by the friction introduced by the screws. Thus the expansion of the linear actuator is suppressed down to the expansion of the Invar mount. Therefore the length of the linear actuator for the effective CTE calculation is set to zero. Its expansion is integrated into the expansion of the Invar mount. The effective CTE of the Invar adapter is the distance between the ULE baseplate and the connection point of the tip/tilt actuator to the linear actuator (labelled d) times the CTE of Invar. The distance is -33 mm and the CTE is $2 \cdot 10^{-6}$ /K. The expansion of the tip/tilt actuator is influencing the effective CTE between the connection point to the linear actuator and the connection point of the mirror adapter. The distance c is 14.9 mm and the CTE is $23.1 \cdot 10^{-6}$ /K. The distance between the connection point of the mirror adapter and the connection point of the mirror is labelled with b and is 11 mm. The mirror adapter is also made of Invar. Finally the expansion of the mirror is calculated. It is made of Fused Silica and has a CTE of 0.55×10^{-6} /K [67]. The distance between its connection point to the mirror adapter and the reflective surface (labelled a) is 7.6 mm. The result is an effective CTE of the complete assembly of 304.7 nm/K. The induced optical pathlength change is twice the effective CTE.

In a next step the influence of the temperature coefficients of the tip/tilt degrees of freedom (rad/K) of the AG-M100N actuator are analysed. Figure 3.16 (a) depicts the influence of a tilt of the AG-M100N actuator onto the mirror displacement. When the actuator is tilted by an angle α the reflection point on the mirror surface is shifted into the direction of the beam. Thereby the centre of the mirror surface is not fixed and rotates around the pivot point of the actuator.

The movement of the mirror surface can be split into two rotations. First, shown

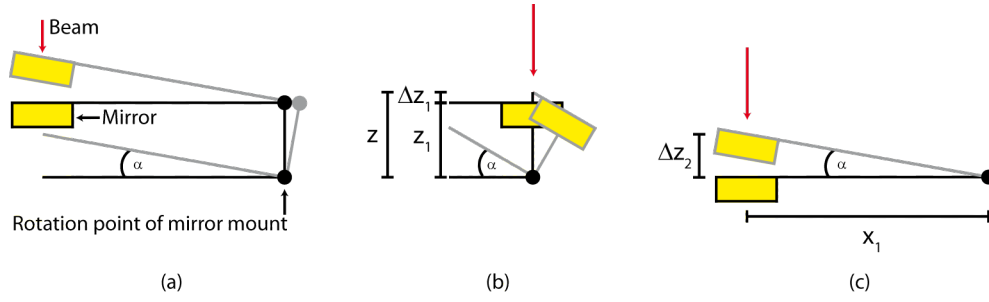


Figure 3.16: Illustration of tip/tilt coupling into optical pathlength noise. (a) depicts the complete movement. This movement can be split into two rotations. (b) depicts the influence of the displacement of the mirror surface in the beam direction. (c) depicts the influence of the lateral displacement of the mirror surface.

in Figure 3.16 (b), the influence of the displacement of the mirror surface in the beam direction by a rotation around the pivot point of the actuator by an angle α . The lateral distance to the pivot point x_1 is zero. The displacement into the beam direction is z_1 . The induced displacement Δz_1 is given by

$$z = \frac{z_1}{\cos(\alpha)} \quad (3.15)$$

$$= \frac{z_1}{\sqrt{1 - \sin^2(\alpha)}} \quad (3.16)$$

$$\Delta z_1 + z_1 = \frac{z_1}{\sqrt{1 - \sin^2(\alpha)}} \quad (3.17)$$

$$\Leftrightarrow \Delta z_1 = \frac{z_1}{\sqrt{1 - \sin^2(\alpha)}} - z_1 \quad (3.18)$$

$$\approx z_1 \left(1 - \frac{1}{2}\alpha^2 - \frac{1}{8}\alpha^4 - \dots \right)^{-1} - z_1 \quad (3.19)$$

The displacement Δz_1 is approximately zero, if $\alpha \approx 0$ rad. The second rotation is depicted in Figure 3.16 (c). The initial displacement of the mirror in the beam direction z_1 is zero and the lateral distance to the pivot point x_1 is non-zero. The mirror is rotated by an angle α around the pivot point. The induced displacement Δz_2 is given by

$$\Delta z_2 = x_1 \cdot \tan(\alpha) \quad (3.20)$$

$$\approx x_1 \cdot \left(\alpha + \frac{1}{3}\alpha^3 + \dots \right) \quad (3.21)$$

$$\approx x_1 \cdot \alpha \quad (3.22)$$

To obtain the optical pathlength this equation has to be multiplied with two. The same is true for the tip degree of freedom.

The requirement for the optical pathlength stability of the actuators is $1.3 \text{ pm}/\sqrt{\text{Hz}}$. The noise budget is further split among the lateral and the tip/tilt stability. The noise budget for the tip/tilt stability is $0.65 \text{ pm}/\sqrt{\text{Hz}}$ because the lateral and the tip/tilt stabilities are coupled and not uncorrelated. Assuming a temperature stability of $1 \cdot 10^{-4} \text{ K}/\sqrt{\text{Hz}}$ at 1 mHz the effective CTE of the actuator needs to be below 3.25 nm/K . Assuming further a thickness of the actuator assembly of 30 mm its CTE needs to be below $2.2 \cdot 10^{-7} / \text{K}$. The temperature coefficient of the tip/tilt degree of freedom of the AG-M100N actuator is $4 \text{ } \mu\text{rad/K}$. Assuming that an alignment of the reflection point with respect to the

pivot point is possible to an accuracy of 1 mm the induced optical pathlength noise is $4 \cdot 10^{-13} \text{ m}/\sqrt{\text{Hz}}$. This is below the requirement for the coupling of tip/tilt noise into the optical pathlength noise.

The calculation of the effective CTE and the coupling of tip/tilt into optical pathlength revealed that the stability of the actuator assembly is not compatible with LOB requirements. The effective CTE could not be measured in [45] due to the fact that the temperature measurement system was not installed. Assuming a temperature noise of $100 \mu\text{K}/\sqrt{\text{Hz}}$ at 1 mHz and using the effective CTE of 304.7 nm/K, calculated in Table 3.5, this leads to an optical pathlength noise of $60 \text{ pm}/\sqrt{\text{Hz}}$ at 1 mHz of the actuator assembly. The measured optical pathlength noise of the actuator assembly, shown in Figure 3.4, was at a level of $7 \text{ nm}/\sqrt{\text{Hz}}$ at 1 mHz. This was two orders of magnitude above the calculated value. The reason for this is not known, exactly.

The same concept that was used to calculate the effective CTE of the actuator assembly was used to reduce it via a redesign of the actuator assembly. This was done by adding an additional stage with the right effective CTE in the actuator assembly, which compensated the effective CTE of the rest. Additionally the material and thickness of the mirror adapter could be modified to reduce the effective CTE of the rest.

3.5.4.2 A simple compensated actuator

The principle of the CTE compensation via a compensation stage was tested using the actuator assembly shown in Figure 3.15(a). Two resistive heaters were attached via conductive tape to the Invar mount. Several temperature sensors were attached to the Invar mount and the actuator assembly. The complete structure was heated under vacuum conditions for several thousand seconds with a few Watt of electric power. Then the heaters were switched off and the structure cooled down. During heating and cooling the optical pathlength, beam pointing and temperature change was measured. Three different effective CTEs were generated by connecting the linear actuator with all four screws, with the two screws facing the ULE baseplate and with the two screws on the other side. The effective CTE was calculated from the ratio between linear drifts during heating and cooling in the optical pathlength and the temperature time series. The change in beam pointing was also taken into account but its influence on the effective CTE was negligible. A comparison to the calculated effective CTEs revealed that the simple model for the effective CTE, presented in the last subsection, is valid. Thus a simple compensation stage was designed.

Within the LOB project it was agreed that the linear actuator is not important for stability measurements. Therefore the linear actuator was replaced by the compensation stage. A schematic side view of the actuator assembly with a compensation stage to reduce the effective CTE can be seen in Figure 3.17. The CTE and the length e of the compensation stage was chosen to compensate the expansion of the Invar mount and the tip/tilt actuator including mirror.

The effective CTE of the actuator assembly with the simple compensation stage is summarised in Table 3.6. The calculated effective CTE could be reduced to -1.72 nm/K .

Figure 3.18 shows the optical pathlength noise levels and the temperature noise levels at the actuator experiment during the estimation of effective CTE in a stable temperature environment. During the measurement the OPD, the low frequency intensity and the laser frequency stabilisation were switched on. The effective CTE of the actuator assembly was measured via the ratio of the optical pathlength noise and the temperature noise at

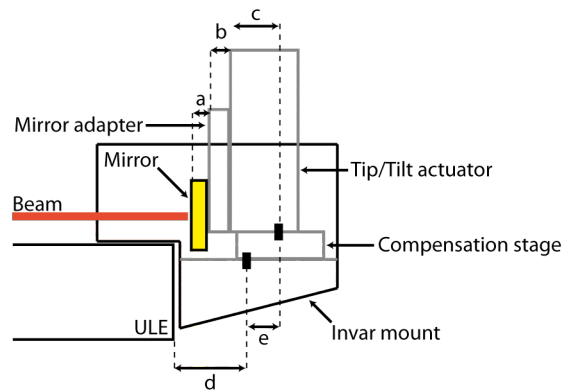


Figure 3.17: Schematic side view of the actuator assembly with a compensation stage to reduce the effective CTE.

Table 3.6: Calculation of the effective CTE of the simple actuator assembly.

Part	Material	CTE [1/K]	Label	Length [mm]	Effective CTE [nm/K]
Mount	Invar	$2 \cdot 10^{-6}$	d	-23	-46
Compensation stage	Aluminium	$23.1 \cdot 10^{-6}$	e	-14.1	-326
Tip/Tilt actuator	Aluminium	$23.1 \cdot 10^{-6}$	c	14.9	344
Mirror adapter	Invar	$2 \cdot 10^{-6}$	b	11	22
Mirror	Fused silica	$0.5 \cdot 10^{-6}$	a	7.6	3.8
Sum					-1.72

a frequency of 1 mHz. The effective CTE of the actuator assembly was approximately 50 nm/K. The level of the optical pathlength noise in the reflection interferometer as well as the measured effective CTE indicated that the stability of the actuator assembly was significantly improved by this simple compensation stage. The difference to the calculated effective CTE indicated that the model of the effective CTE of the actuator assembly had to be improved within the next development steps.

The simple mount was not compatible with the design requirements for the simulators. The actuator assemblies have to be glued via three connection points to the ZerodurTM baseplate of the simulators. Thus the stress onto the bonding connection due to a expansion of the simple compensation stage could damage the bonding connection. Therefore a more elegant compensation stage was developed, which will be tested in the next subsection.

3.5.4.3 An elegant compensated actuator

An elegant mount, which compensates the effective CTE of the actuator assembly, was designed by Astrium GmbH for the LOB project and was tested in the same actuator experiment at the AEI [77]. A schematic side view of the complete actuator assembly for the PM simulator can be seen in Figure 3.19. The key element for the reduction of the CTE was the green compensation stage at the bottom of Figure 3.19(a), onto which the rest of the actuator assembly was mounted. The compensation stage was glued via its leaf-springs to the Invar mount. Due to the fact that the front leaf-springs were parallel to the beam direction and the back leaf-spring were perpendicular to the beam

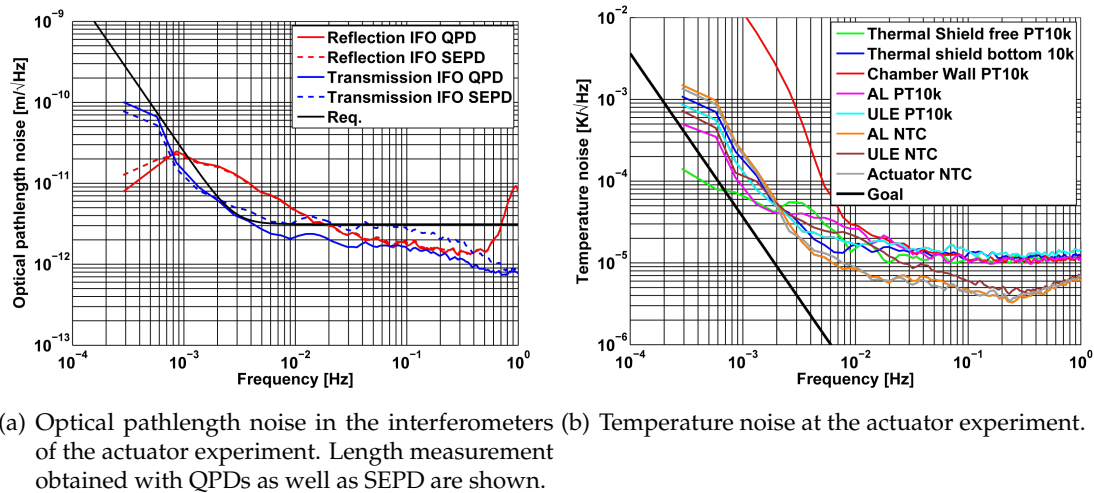


Figure 3.18: Estimation of the effective CTE of the “simple” actuator assembly in a stable temperature environment.

direction, the back leaf-springs did bend when the compensation stage expanded in the beam direction. The front leaf-springs remained at their positions. Therefore the effective CTE of the rest of the actuator assembly could be compensated via expansion of the compensation stage via the length d . The expansion of the rest of the actuator assembly was identical to the one already described in the last subsections. The length b of the mirror adapter could be used to fine tune the effective CTE of the actuator assembly including the compensation stage. Figure 3.19(b) shows a photograph of the actuator assembly for the PM simulator. The linear stage, shown in Figure 3.19 was replaced by a connection piece made of aluminium. The tip/tilt actuator was directly connected to the compensation stage via a screw. Thus the task of this connection was the alignment of the actuator height.

The calculated effective CTE of this actuator assembly could be reduced to -62 nm/K , see Table 3.7. This value was above the calculated effective CTE of the simple compensated actuator. The reason for this was that the calculated effective CTE of the elegant compensated actuator was reviewed after the measurement of its effective CTE. The measurement is presented in the next paragraphs. It was found out that the CTE of the brass mount was given for a broader temperature range. At 20°C it is $19.0 \cdot 10^{-6} / \text{K}$. Additionally the planned adhesive between the mirror and the mirror adapter and the mirror adapter and the tip/tilt actuator was not used to be able to fine tune the effective CTE via the mirror adapter. The adhesive was only used punctual at the edge of the parts. This lead to an active length of zero for the adhesive.

There are two possibilities to measure the effective CTE. First, the CTE of the temperature compensated mount can be measured via a correlation of low frequency temperature noise and the according optical pathlength noise within in a stable thermal environment. A stable thermal environment is in this context the environment in a thermal shield inside vacuum. This method has the advantage that the temperature change is identical within all parts of the temperature compensated mount due to the homogeneous radiation and the low frequency range. Its disadvantage is that the SNR is reduced at low frequencies due to other noise sources that are not referred to the CTE of the temperature

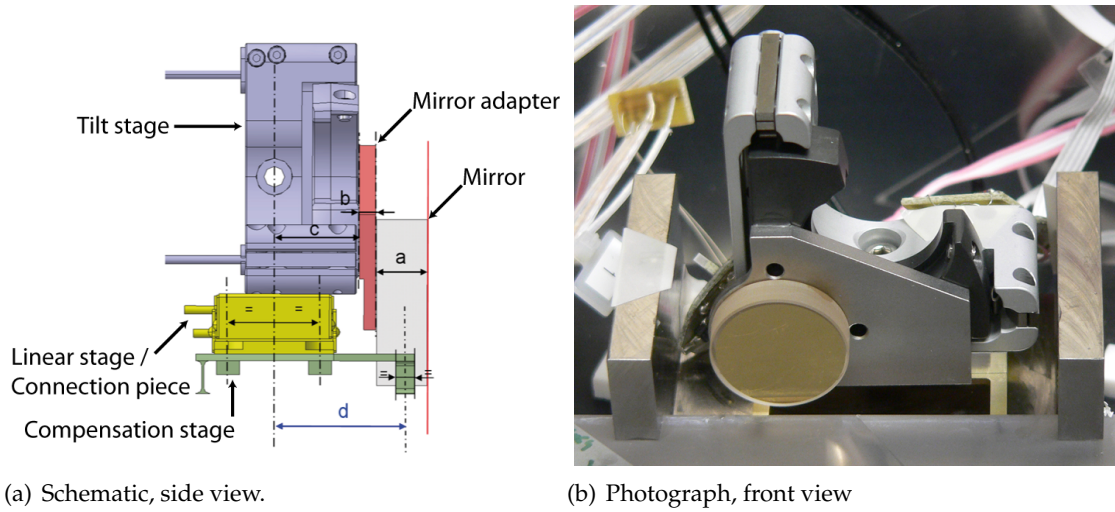


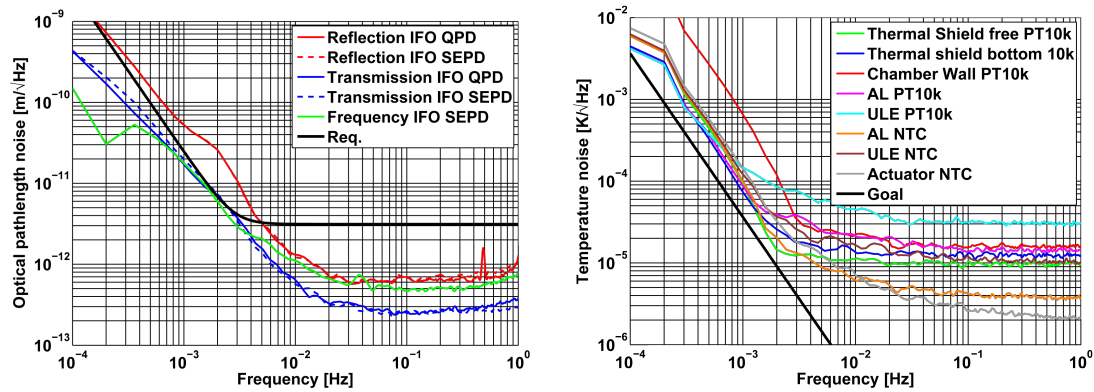
Figure 3.19: Actuator assembly including mirror and mirror adapter on the Invar mount, which is glued to the ULE baseplate [77].

Table 3.7: Calculation of the effective CTE of the Astrium actuator assembly.

Part	Material	CTE [1/K]	Label	Length [mm]	Effective CTE [nm/K]
Invar Mount	Invar	$2.0 \cdot 10^{-6}$		-2	-4
Mount	Brass	$19.0 \cdot 10^{-6}$	d	-28.5	-541.5
Connection piece	Aluminium	$23.1 \cdot 10^{-6}$		0.0	0.0
Tip/Tilt actuator	Aluminium	$23.1 \cdot 10^{-6}$	c	18.3	422.7
Adhesive	Adhesive	$70.0 \cdot 10^{-6}$		0.0	0.0
Mirror adapter	Steel	$16.0 \cdot 10^{-6}$	b	3.6	57.6
Adhesive	Adhesive	$70.0 \cdot 10^{-6}$		0.0	0.0
Mirror	Fused silica	$0.5 \cdot 10^{-6}$	a	6.3	3.15
Sum					≈ -62

compensated actuator. Second, the CTE can be measured via a well-defined temperature modulation and cross-correlation to the resulting optical pathlength modulation. The second method has the advantage of a high SNR due to the high modulation depth but it has the disadvantage that all parts might not be heated homogeneously and to the same temperature. Thus both methods are used to estimate the CTE of the temperature compensated mount and are compared.

Figure 3.20 shows the optical pathlength noise levels and the temperature noise levels at the actuator experiment used for the estimation of the effective CTE in a stable temperature environment. During the measurement the OPD, the low frequency intensity and the laser frequency stabilisation were switched on. The effective CTE of the elegant compensated actuator assembly was calculated via the ratio of the optical pathlength noise and the temperature noise at frequencies lower than 1 mHz. The effective CTE of the elegant compensated actuator assembly was approximately 177 nm/K. The temperature coefficient of the transmission interferometer was approximately 55 nm/K. This was a lower limit for the effective CTE estimation because the measurement beams of the transmission interferometer did not propagate completely on the stable ULE baseplate and did not interact with the actuator under test. The optical pathlength noise of the reflection



(a) Optical pathlength noise in the interferometers of the actuator experiment. Length measurement obtained with QPDs as well as SEPD are shown. (b) Temperature noise at the actuator experiment.

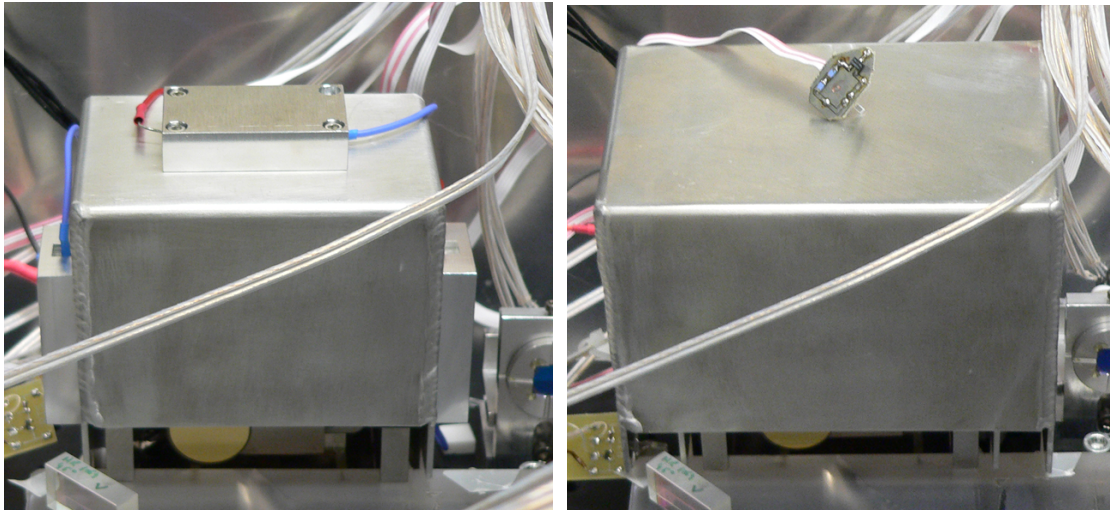
Figure 3.20: Estimation of the effective CTE of the actuator assembly in a stable temperature environment.

interferometer was dominated by temperature noise at low frequencies. Therefore the optical pathlength noise in the reflection interferometer will be completely below the requirement, if the temperature noise at the experiment, depicted in Figure 3.20(b), can be reduced below the goal.

The heating procedure, which was described in Subsection 3.5.4.2, used two resistive heaters. These were connected via thermally conductive adhesive tape to the Invar mount. Thus the heating of the assembly was not uniform. Therefore a heating cell was designed. It was made of 2 mm thick aluminium. It was placed around the complete actuator assembly and was thermally isolated from the rest of the experiment via Macor spacers, see Figure 3.21(a). Three resistive heater were connected to this heating cell via aluminium blocks. The heating of the rest of the experiment was minimised by integrating a thermal shield around the heating cell, which was thermally isolated from the rest of the experiment via Macor spacers, see Figure 3.21(b).

The effective CTE of the elegant compensated actuator assembly was measured by heating the heating cell with an electrical power of 0.5 W over half a working day. Afterwards the heaters were switched off and the actuator assembly cooled down. During heating and cooling the optical pathlength and the temperature were recorded. The optical pathlength was measured with a switched on OPD and laser frequency stabilisation. The temperatures of the tip/tilt actuator, the thermal shield around the heating cell and the ULE baseplate were measured. One measurement of the effective CTE via this method is depicted in Figure 3.22. The response of the reflection interferometer to the temperature change is clearly visible as shown in Figure 3.22(a). The response in the transmission interferometer, depicted in Figure 3.22(b) is clearly visible, too. Its amplitude is orders of magnitude lower in comparison to the response in the reflection interferometer.

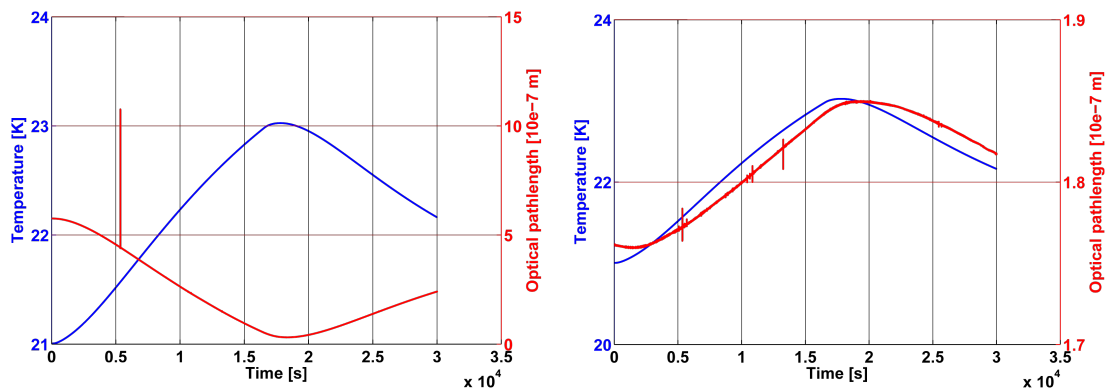
The effective CTE was estimated for a set of measurements. The average effective CTE of the elegant compensated actuator assembly was 241.5 nm/K with a precision of better than ± 20 nm/K. The effective CTE of the transmission interferometer calculated via the temperature of the elegant compensated actuator assembly was approximately 10 nm/K.



(a) Photograph of the heating cell.

(b) Photograph of the thermal shield.

Figure 3.21: Heating cell for the effective CTE measurement.



(a) Reflection interferometer.

(b) Transmission interferometer.

Figure 3.22: Time series of the optical pathlengths in the interferometers in comparison to the temperature of the actuator.

Thus the SNR ratio could be improved by modulation of the temperature of the actuator.

The effective CTE of the elegant compensated actuator assembly measured within a stable temperature environment and with a temperature modulation differed by 64.5 nm/K. This difference was introduced by the heating method itself. During the temperature modulation parts with a lower coefficient of reflection for thermal radiation were heated faster than parts with a higher one, i.e., the black part of the tip/tilt actuator and the aluminium part. Within a stable temperature environment heat conduction suppressed this effect for time scales larger than 1000 s. In this time scale (or at frequencies below 1 mHz) the optical pathlength noise introduced by the actuator assembly, was induced by temperature noise at the actuator assembly. Therefore the effective CTE of an actuator assembly has to be determined in a stable thermal environment. The temperature modulation method might be used to roughly measure the effective CTE of an actuator assembly before the effective CTE is measured in a stable environment.

Nevertheless the measured effective CTE was a factor of three above the calculated

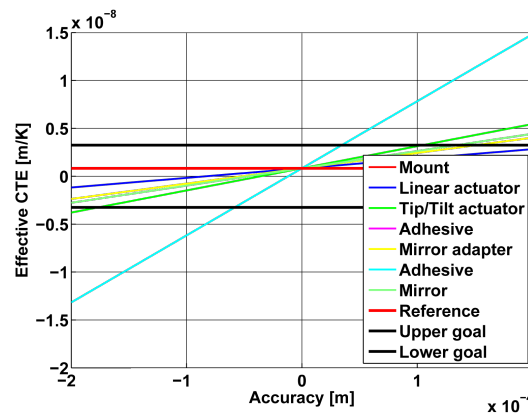


Figure 3.23: Change of the effective CTE with the machining accuracies for each part.

one. The reason for this is not known exactly, yet. Figure 3.23 gives a first insight into the stability of the effective CTE against machining accuracies. The thickness of the adhesive has the highest influence on the effective CTE. Therefore the amount of the adhesive has to be controlled with a pipette to get a well-defined thickness of the adhesive layer. All the other parts are uncritical, when machining accuracies of ± 0.1 mm are assumed. A drawback of the elegant design were the screw connections between the compensation stage and the tip/tilt actuator. It was assumed that the distances for the effective CTE have to be measured from the centre of the screws. Figure 3.23 shows that machining tolerances above ± 0.2 mm increase the effective CTE above the goal value. The assumption for the screw connection cannot be directly verified and therefore in the future these type of connection should be replaced by well-defined connections.

Another source for the remaining effective CTE was believed to be the connection piece between the compensation stage and the tip/tilt actuator. This was designed with a stop at the back to align the connection piece to the back of the compensation stage and to align the tip/tilt actuator to the connection piece. The expansion of the connection piece a temperature changes was shifted to the measurement beam due to the stop at the compensation stage. If the friction between the tip/tilt actuator and the connection piece is high enough the connection piece drags the tip/tilt actuator towards the measurement beam. Thus a new connection piece has to be designed.

3.6 Conclusions

In this chapter the telescope and the PM simulators were introduced with special focus on the optical pathlength stability of the actuators - namely a linear translation stage and a tip/tilt actuator. An experiment to test these actuators was setup, characterised, and the optical pathlength stability of the actuators was investigated.

The requirements for the optical pathlength stability and the pointing stability of the actuators were derived upon the basis of the PM simulator. A review of actuators, some of them already tested at the AEI, was used for the selection of actuators. The optical pathlength stabilities of the actuator experiment was improved by at least one order of magnitude in the complete LMB down to the requirement for the read-out of the PM simulator by implementing the knowledge gained at the picometer experiment. Beyond the objective of this experiment, a laser intensity stabilisation for an

iodine-stabilised laser was developed. A RIN of $1.6 \cdot 10^{-6} / \sqrt{\text{Hz}}$ at 1 Hz increasing with $1/\sqrt{f}$ towards lower frequencies was demonstrated. A read-out of laser frequency noise below $300 \text{ Hz} / \sqrt{\text{Hz}}$ for frequencies above 20 mHz increasing with $1/f$ towards lower frequencies was presented with an unequal arm MZI having an armlength mismatch of 681 mm. The read-out of temperature noise via a FPGA-based thermometer was decreased to a level of $2 \mu\text{K} / \sqrt{\text{Hz}}$ for frequencies above 100 mHz increasing with $1/\sqrt{f}$ towards lower frequencies using NTC sensors compared to the noise floor of $10 \mu\text{K} / \sqrt{\text{Hz}}$ for PT10k sensors. It was verified that the temperature distribution across a large ($500 \times 300 \times 25 \text{ mm}^3$) ULE baseplate in vacuum and inside a thermal shield is homogeneous to a level of better than $15 \mu\text{K} / \sqrt{\text{Hz}}$ for frequencies above 20 mHz increasing with $1/\sqrt{f}$ towards lower frequencies.

The thermal expansion of the actuator assembly was theoretically assessed. This theoretical model was experimentally verified by reducing the effective CTE of an actuator assembly by implementation of a simple compensation stage. The effective CTE of the simple compensated actuator assembly was measured in a temperature stable environment to 50 nm/K . The uncompensated actuator assembly had a calculated effective CTE of 304.7 nm/K . Thus the effective CTE could be significantly reduced. Therefore a more elegant compensation stage was designed by Astrium GmbH for the LOB project and tested at the AEI. An optical pathlength noise of $0.6 \text{ pm} / \sqrt{\text{Hz}}$ down to frequencies of 20 mHz increasing with $1/f^2$ towards lower frequencies was demonstrated in the reflection interferometer with the elegant compensated actuator assembly installed. This optical pathlength noise level was below the requirement for the read-out noise of the PM simulator for frequencies above 5 mHz. For frequencies below 5 mHz the optical pathlength noise introduced by temperature noise was close to the requirement. The effective CTE of the elegant compensated actuator assembly was measured within a stable temperature environment and by modulating the actuator assembly temperature. The respective measured effective CTEs were 177 nm/K and 241.5 nm/K . Thus the CTE reduction of actuators via a compensation stage is an effective method to make actuators compatible with LISA stability requirements. In the conducted experiment the measured effective CTE was significantly larger than the calculated one. The investigations on the actuators are ongoing. Thus in the future the effective CTE will be reduced further by improvement of the compensation stage.

The LOB will be tested with the simulators in a stable temperature environment, too. Thus the difference in the measured effective CTEs indicate that the effective CTE should be measured in a stable temperature environment in order to be comparable to the test situation. This investigation also revealed that the used method employed to measure the effective CTE is not able to measure effective CTEs below 10 nm/K . The goal for the actuator assembly is 3.25 nm/K . Therefore it is recommended to build a smaller OB, with an interferometer setup similar to the polarisation experiment [17, pp. 59]. This new setup should integrate two identical interferometers on almost the same part of the OB. One measures the position of a fixed mirror and the other measures the position of the actuator assembly. In this way the effective CTE of the actuator assembly can be measured by subtracting the optical pathlengths of both interferometers with the lower limit given by the phase read-out with the phasemeter.

Photodetector development for LISA

Photodetectors are one of the central devices in the electro-optical measurement chain in the LISA interferometers to detect the optical pathlength fluctuations generated by GWs. In the introduction of this chapter a closer look at the electro-optical chain is taken to understand the interfaces of LISA photodetectors and their requirements. This information is important to understand the necessity of a special development of photodetectors for LISA. With the definition of the electrical and mechanical interfaces the properties of the two parts of a LISA photodetector, namely the photodiode and the TIA, can be investigated in detail. The research on photodiodes was focused on the selection of a photodiode technology and material. The TIA research has extended the investigations that have been presented in [78].

4.1 Introduction

The electro-optical chain of an interferometer on the LOB is depicted in Figure 4.1. It consists of the imaging optics, the photodiode (including mount), the TIAs (including mount) and the PMS. In the next subsection the individual parts are described to understand their interactions.

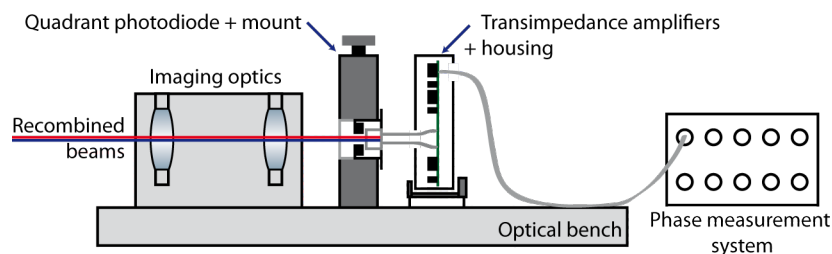


Figure 4.1: Schematic of a possible setup for the interferometer output for the LOB. Starting point is the output of a beam combiner and end point the input of the phasemeter.

4.1.1 Imaging optics

The measured optical pathlength noise levels within the LTP interferometers during measurements with mirrors, which simulated free-floating PMs, had to be corrected by angular pointing information in order to reach the requirements [18]. Coupling of beam pointing noise into optical pathlength noise is unwanted for LISA. Therefore the goal is to decouple angular pointing noise of the measurement beams from the optical pathlength noise by the use of imaging optics. The design idea of the imaging optics is based on pupil plane imaging. The interested reader is referred to [39, pp. 131], where the imaging optics are investigated with numerical simulations. Experimental investigations on imaging optics can be found in [79].

The amount of decoupling of angular pointing from optical pointing noise can be calculated for the each interferometer on the LOB using the respective requirements and characteristics. The beam pointing noise induced by PM jitter in the PM interferometer is assumed to be $150 \text{ nrad}/\sqrt{\text{Hz}}$. The requirement for the optical pathlength noise induced by PM jitter is $0.47 \text{ pm}/\sqrt{\text{Hz}}$. Assuming that a correction of the optical pathlength by beam pointing information is completely avoided, the maximum allowable coupling factor is $3.2 \text{ pm}/\mu\text{rad}$ [39, pp. 132].

Numerical simulations of a two lens imaging optics system, designed at the AEI and called AEI-D003, revealed that the tolerances for the longitudinal alignment of the lenses and QPD were uncritical. The lateral alignment of the QPD centre yield a critical value of $\pm 0.250 \mu\text{m}$ [39, pp. 148]. This alignment accuracy and stability with respect to temperature changes was not feasible under laboratory conditions. For launch conditions in a rocket the situations is getting even worse. Therefore the experimental investigations on the imaging optics are continued and numerical simulations on new lens systems will follow to relax the stringent alignment requirements. Nevertheless these values motivate why the photodiodes are mounted in adjustable mounts.

4.1.2 Photodiode

The movable mount for the fine positioning of the QPD on the LOB is based on the design of the CP1XY mount from Thorlabs [80]. The CP1XY has an actuation range of $\pm 0.25 \text{ mm}$ in x- and y-direction. The accuracy of the mount for the LOB was tested at University of GLasgow (UGL) to a level of a micron over a actuation range of $\pm 0.15 \text{ mm}$ [41, pp. 51]. The mount is also insensitive to temperature changes by a thermal compensation. This mount is not able to align the QPD to the requirement given by the imaging optics but remains the baseline for the LOB due to the fact that the imaging optics investigations are on-going.

The photodiode subassembly will be integrated in this mount. The subassembly consists of three parts: an aperture, an adapter plate, and a photodiode. The adapter plate is made of PEEK and electrically insulates the photodiode housing from the metallic mount. The black aperture is attached to the other side of the adapter plate to prevent light from the interferometer to be back reflected from bonding wires and pads of the photodiode.

The tolerances for the assembly of the photodiode subassembly are derived from the actuation range of the movable mount. The chip centre of the QPD has to be centred to the adapter plate to a few ten micrometers such as not to reduce the alignment range of the movable mount. This requires that the photodiode chip is centred to its housing within the alignment range between the photodiode and the adapter plate. The alignment range is the overlap between photodiode housing and the adapter plate minus some margin.

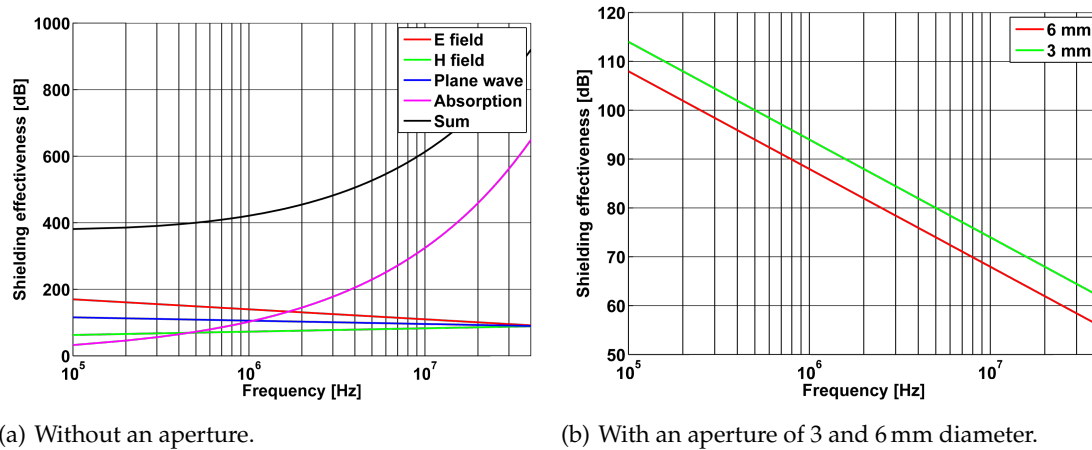


Figure 4.2: Shielding effectiveness of a 1 mm thick aluminium housing in a distance of 1 m from a electro-magnetic source.

After the photodiode subassembly has been assembled the photodiode is soldered to the TIA via flexible wires to be able to align the photodiode to the measurement beams later.

The efficiency ρ and the capacitance C_d of a photodiode are important parameters for the noise behaviour and the bandwidth of a photodetector. The influence of the efficiency ρ on the optical pathlength read-out with a phasemeter will be discussed in Subsection 4.1.4. The general behaviour of the efficiency ρ and the capacitance C_d in different photodiode technologies are investigated in Section 4.2. The influence of the capacitance C_d on the performance of a TIA is estimated in Section 4.3. The TIA is located close to the photodiode to not increase the capacitance C_d (impedance) via long wires and thereby reducing the bandwidth of the photodetector.

4.1.3 Transimpedance amplifier

The requirements for the outer dimensions of the TIA are given by the dimensions of the LOB and the optical layout of the interferometers on the LOB. The minimum size of the LOB is given by an optimal design of the interferometers without photodetectors. The maximum size is given by the dimensions of the satellites. The dimensions of the satellites are varying with different implementations of the LISA concept, which a comparison of the yellow book for LISA and Enhanced LISA (eLISA) reveals [1] [13]. Therefore a requirement for the outer dimensions of the TIA housing cannot easily be provided. During the design phase of the LOB a requirement for the outer dimensions of the TIAs including housing has been set. The lateral dimensions with respect to the measurement beams should not be bigger than $45 \times 80 \text{ mm}^2$ and the depth should not be larger than 60 mm. The beam height above the LOB was set to 20 mm.

The housing of the TIA acts as an electromagnetic shield to reduce the influence from other signal sources onto the TIA. Equations describing the shielding efficiency of a housing can be found in [81, pp. 277]. Figure 4.2(a) shows the shielding efficiency as a function of frequency of a 1 mm thick aluminium housing at a distance of 1 m from the source. The lower four curves are the contributions via an reduction of the electric field, the magnetic field and the plane wave and via absorption. The upper curve is the sum of all contributions. The shielding efficiency (sum) is for all frequencies of interest (1 MHz to 20 MHz) better than 400 dB.

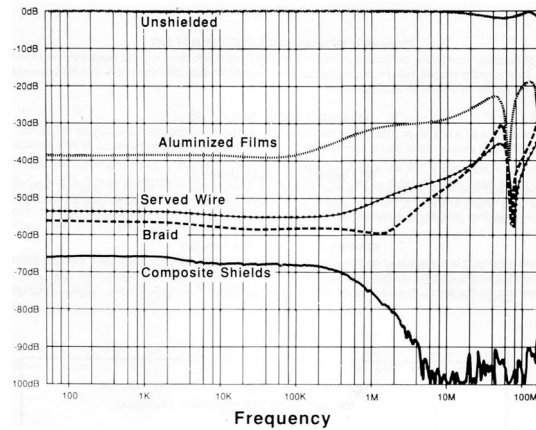


Figure 4.3: Shielding efficiency of a GORE PTFE cable. The data sheet is attached in Appendix 7.

Unfortunately a detector housing needs to have holes for the photodiode and the wiring. Thus the total shielding efficiency, shown in Figure 4.2(a) is reduced. The equation for the shielding efficiency in dB of a housing with an aperture of diameter d is given by [82, pp. 187]

$$SE = 20 \cdot \log(0.5 \cdot \lambda/d) \quad (4.1)$$

λ is the wavelength of the electro-magnetic wave. The biggest aperture in the TIA housing is the hole for the photodiode which is around 6 mm in diameter. This value is composed of the photodiode housing diameter (5.3 mm), the alignment range of the photodiode (0.5 mm) and some margin (0.2 mm). Figure 4.2(b) shows the shielding efficiency for this aperture and for a smaller 3 mm aperture that is needed for the power supply cables and the signal cables. The shielding effectiveness will be significantly reduced to at least 63 dB in the frequency range of interest. Therefore the aperture diameter has to be taken into account for the design of a TIA housing.

The wiring between the TIAs and the phasemeter, and for the power supply of the TIAs in the LOB project is planned to be the GORE Type E Teflon braided shield cable called "A03B090". This cable is not available any more from the supplier but at the AEI a sufficient quantity is in stock. Figure 4.3 shows the shielding efficiency of different types of shielded cables taken from the GORE data sheet, which is attached in Appendix 7. It shows that the braided shield has a minimum shielding efficiency of 40 dB in the frequency range of interest. This is worse than the shielding efficiency of the housing. Additional shielding can be achieved by just wrapping the cables in aluminium foil.

The length noise of signal cables can convert into phase noise of the measurement signals. Investigations on length stability of cables at low frequencies have been performed at the AEI for the distribution of the GHz sideband signals [83, pp. 29][84]. The phase stability of the GORE PTFE cable was tested by Amrit Pal-Singh at the AEI. The measurement setup is explained in [84]. The results are presented in Figure 4.4(a). For temperatures above 20 °C the phase stability was better than 5 mrad/ (K · m · GHz). The environment of the LOB will be approximately at room temperature (20 °C) or a little bit higher. The temperature stability will be comparable to the one of the vacuum chamber presented in Figure 2.29(a) on page 31. The stability of the temperature was at a level of 1 mK/√Hz at 1 mHz. This leads to a phase noise of 0.2 μrad/√Hz assuming a

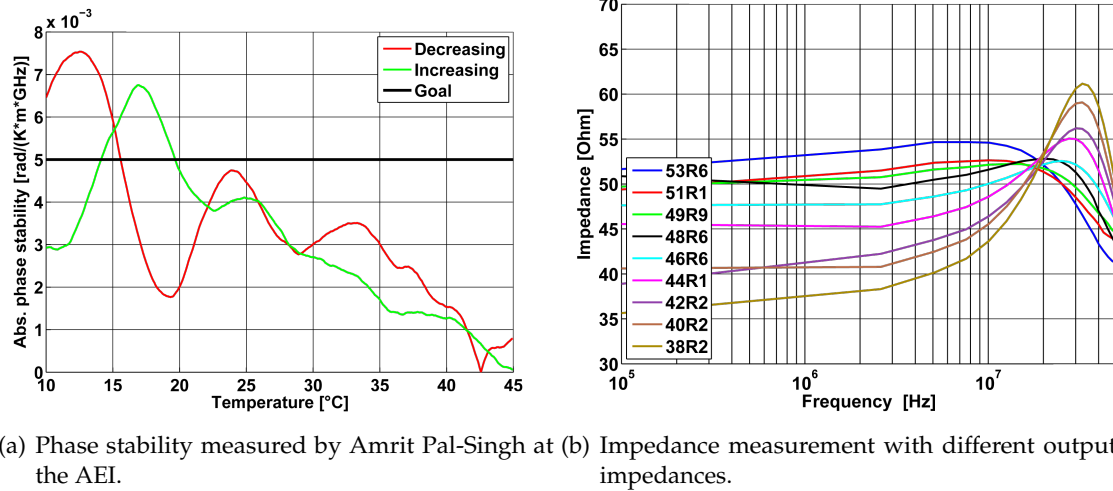


Figure 4.4: Electrical properties of the GORE PTFE vacuum-compatible cable.

signal frequency of 20 MHz and a cable length of 2 m. This is well below the $1 \text{ pm}/\sqrt{\text{Hz}}$ ($5.9 \mu\text{rad}/\sqrt{\text{Hz}}$) requirement.

For the transmission of MHz signals via cables the output and input impedances of the transmission system have to be matched to the cable impedance. Thus the impedance of the GORE PTFE cables were measured with a 4396B spectrum analyser by Agilent and the according impedance analyser kit [85]. One end of the cable was connected to the measurement device and the other end was terminated with different resistors. Then the absolute value of the impedance was measured. When the output impedance is matched to the cable impedance the measurement of the absolute value of the impedance is flat. Otherwise it has ripples. The results of the measurements are presented in Figure 4.4(b). The absolute value of the impedance was almost flat with an output impedance of 49.9 Ω . Thus the cable had an impedance very close to 50 Ω .

The influence of the TIA input current noise onto the optical pathlength read-out with the phasemeter is described in Subsection 4.1.4. A detailed description of the TIA can be found in Subsection 4.3.

4.1.4 Phasemeter

This subsection focuses on the explanation of the high impact of the photodiode and TIA properties onto optical pathlength read-out with a LISA phasemeter. A short introduction into the LISA phasemeter working principle can be found in Subsection 2.3.1.3. Detailed information about the LISA PMS can be found in [24, pp. 25].

At the photodetector interfaces three noise sources influence the optical pathlength read-out with a phasemeter. The shot noise induced by the measurement beams impinging on the photodiode and the input current noise of the TIA set a lower limit on the optical pathlength read out of a heterodyne interferometer. The RIN of the impinging beams have also a non-negligible influence. The RIN couples via two mechanism into the optical pathlength read-out. First, the RIN induces a current noise at the output of the photodiode at the heterodyne frequency similar to the shot noise. Second, the RIN at low frequencies can change the photodiode capacitance via its temperature or possibly other power dependent characteristics of the photodiode. The latter one is not treated here because it can only be accessed experimentally.

Equations for the influence of the shot noise and the input current noise in LISA have been presented in [86] and are derived in [87, pp. 51]. The treatise in [88, pp. 25] added the influence of the laser intensity noise and presented a complete signal model for the LISA metrology system from the perspective of the LISA phasemeter. Nevertheless the impact of the noise sources were calculated under the assumption that the power of the signal beam P_{sig} is orders of magnitudes smaller than the local oscillator beam P_{lo} . This approximation is valid for the science interferometer of LISA. For other interferometer configurations this is not valid. Therefore the equations for the optical pathlength read-out according to the photodetection noise processes are derived here briefly according to [89] in which the beam power approximation was not used.

The read-out limit for the optical pathlength \tilde{l} in a heterodyne interferometer is given by

$$\tilde{l} = \frac{\lambda}{2\pi} \frac{\text{Noise (LSD)}}{\text{Signal (RMS)}} \left[\frac{\text{m}}{\sqrt{\text{Hz}}} \right] \quad (4.2)$$

according to [88, pp. 121]. The AC rms signal generated by two measurement beams is given by

$$\text{Signal (RMS)} = \frac{1}{\sqrt{2}} \left(2 \frac{\tilde{N}_{\text{SE}}}{N_{\text{SE}}} \rho \sqrt{\gamma P_{\text{sig}} P_{\text{lo}}} \right) \quad (4.3)$$

The powers of the signal beam P_{sig} and of the local oscillator P_{lo} are referred to the input of the beam combiner. The outputs of a beam combiner on the LOB are equipped by default with quadrant photodetectors. The amplitudes and noise levels for using only \tilde{N}_{SE} photodiode segments can be calculated by composing the ratio of \tilde{N}_{SE} and N_{SE} , which are the total number of photodiode segments at both output ports. N_{SE} is by default 8. Thereby the beam combiner outputs have to be equipped with identical photodiodes. ρ is the photodiode responsivity, γ the heterodyne efficiency.

The Linear Spectral Density (LSD) of shot noise, electronic noise, and relative power noise at the output of the photodiode segments expressed as equivalent input current noise at the TIA input are then given by

$$\tilde{I}_{\text{shot}} = \sqrt{2q_e \rho \left(\frac{\tilde{N}_{\text{SE}}}{N_{\text{SE}}} \right) (P_{\text{sig}} + P_{\text{lo}})} \quad (4.4)$$

$$\tilde{I}_{\text{el}} = \sqrt{\tilde{N}_{\text{SE}}} \cdot n_{\text{el}} \quad (4.5)$$

$$\tilde{I}_{\text{RPN}} = \rho \left(\frac{\tilde{N}_{\text{SE}}}{N_{\text{SE}}} \right) (n_{\text{RPN,sig}} \cdot P_{\text{sig}} + n_{\text{RPN,lo}} \cdot P_{\text{lo}}) \quad (4.6)$$

The value of the amplifier input current noise n_{el} is given per channel. If comparable laser systems are used the relative power noise n_{RPN} can be assumed to be identical. This is true for LISA and therefore this simplification will be used in the following equations. q_e is the electron charge. An important thing to mention is that the input current noise and the shot noise are uncorrelated between the channels of the photodetector and the RIN induced by the laser beam is correlated between the channels of the photodetector.

Now the individual optical pathlength read-out limits \tilde{l} can be calculated

$$\tilde{l}_{\text{shot}} = \frac{\lambda}{2\pi} \sqrt{\left(\frac{\tilde{N}_{\text{SE}}}{N_{\text{SE}}}\right)^{-1} \frac{q_e (P_{\text{sig}} + P_{\text{lo}})}{\rho \gamma P_{\text{sig}} P_{\text{lo}}} \left[\frac{\text{m}}{\sqrt{\text{Hz}}}\right]} \quad (4.7)$$

$$\tilde{l}_{\text{el}} = \frac{\lambda}{2\pi} \left(\frac{\sqrt{\tilde{N}_{\text{SE}}}}{N_{\text{SE}}}\right)^{-1} \frac{n_{\text{el}}}{\rho \sqrt{2\gamma P_{\text{sig}} P_{\text{lo}}}} \left[\frac{\text{m}}{\sqrt{\text{Hz}}}\right] \quad (4.8)$$

$$\tilde{l}_{\text{rpn}} = \frac{\lambda}{2\pi} n_{\text{rpn}} \frac{(P_{\text{sig}} + P_{\text{lo}})}{\sqrt{2\gamma P_{\text{sig}} P_{\text{lo}}}} \left[\frac{\text{m}}{\sqrt{\text{Hz}}}\right] \quad (4.9)$$

These three noise sources are uncorrelated. Therefore their combined noise influence is the square-root of the sum of their quadratures

$$\tilde{l}_{\text{total}} = \sqrt{\tilde{l}_{\text{shot}}^2 + \tilde{l}_{\text{el}}^2 + \tilde{l}_{\text{RPN}}^2} \quad (4.10)$$

These equations will be used in the next sections to derive the requirements for the photodiode and the TIA.

4.1.5 Requirements and goals

The power at the input of the beam combiner in the science interferometer of the signal beam P_{sig} was set to 220 pW for the LOB [41, pp. 147]. For each combination of the input current noise of the TIA and the RIN of the laser a specific optimal LO power exists [88, pp. 30]. The power of the LO was set to 3.5 mW although this is not necessarily the optimum [41, pp. 147]. These values can be used to calculate the read-out limit for the optical pathlength noise due to shot noise, see Equation 4.7. For this consideration the responsivity ρ is set to 1 A/W. The read-out limit for the optical pathlength due to shot noise is for one output of the beam combiner 6.5 pm/ $\sqrt{\text{Hz}}$. If the responsivity ρ is smaller than 1 A/W the read-out limit for the optical pathlength read-out limit deteriorates further. This optical pathlength read-out limit is above the requirement for the optical pathlength read-out of the PM interferometer, see Section 2.1. Thus the sensitivity of the science interferometer determines the overall sensitivity of the LISA mission. The equations for the optical pathlength read-out limit (see Equation 4.8 and Equation 4.9) indicate that the impact of electronic and relative power noise is the highest in the science interferometer. This is due to the low power of the signal beam P_{sig} . Therefore the goals and requirements in this subsection are derived for the science interferometer.

4.1.5.1 Photodiode

Requirements The laser wavelength for LISA is set to 1064 ± 2 nm [14, R<010-010>]. All interferometers on the OB require quadrant photodiodes to be able to measure differential beam tilts via DWS [14, R<010-030>, R<010-040>]. Identical quadrant photodiodes and TIA designs (excluding TIA gains) should be used in all interferometers [14, R<010-040>]. This is nice to have but not strictly necessary. In fact it may be better to choose different TIA designs in different interferometers.

Goals The Equations 4.7 and 4.8 for the read-out noise of the optical pathlengths indicate that the higher the responsivity ρ the lower the optical pathlength read-out noise. The goal for the responsivity of the photodiode at a laser wavelength of 1064 nm was set to 0.7 A/W. This value is derived from the responsivity of standard InGaAs photodiodes. The optical pathlength read-out limit according to Equation 4.7 with that responsivity is 8.14 pm/ $\sqrt{\text{Hz}}$. The Equations 4.7 and 4.8 do also indicate that a lower responsivity can be compensated via an increase of the laser powers P_{sig} and P_{lo} . Thus a responsivity of 0.6 A/W or lower is compatible with LISA requirements if the laser powers P_{sig} and P_{lo} are increased.

A model for the input current noise and the bandwidth of a TIA will be presented in Subsection 4.3.1. This model indicates that the higher the capacitance the higher the input current noise at 20 MHz and the lower the bandwidth of the TIA. A capacitance of the photodiode of 20 pF or less has been found to be an acceptable value to reach an input current noise n_{el} below the goal of 4 pA/ $\sqrt{\text{Hz}}$ and a bandwidth of more than 20 MHz. These two values are explained in the next subsection.

The capacitance of the photodiode is proportional to its active area according to Equation 4.14. A reduction of the photodiode capacitance can be achieved by choosing photodiodes with smaller diameters. The lower boundary for this is given by the imaging optics, introduced in Subsection 4.1.1. The accuracies for the alignment of the lenses and the photodiode become more critical with a smaller photodiode diameter according to Section 4.1.1. With the goal of 20 pF for the photodiode capacitance one ends up with a diameter of approximately 1 mm for COTS InGaAs QPDs and 5 mm for COTS silicon QPDs.

4.1.5.2 Transimpedance amplifier

Requirements The TIAs shall have two outputs. One low frequency DC output and one high frequency AC output. The DC part of the TIA should allow a measurement of signals with frequencies of up to 20 kHz. The AC part of the TIA should allow a measurement of signals between 2 and 19 MHz [14, R<160-010>]. The output level of the AC part should be around 1 dBm at 50 Ω .

The power dissipation of each photodetector should be below 1.2 W [14, R<160-020>]. One photodetector consists of a QPD and four TIAs with AC/DC decoupling. The stability of the power dissipation should be better than $1 \cdot 10^{-4}$ W/ $\sqrt{\text{Hz}}$ [14, R<160-030>].

Goals The goal for the input current noise n_{el} for the photodetectors of the LOB was set to 4 pA/ $\sqrt{\text{Hz}}$. According to Equation 4.8 this value results in an optical pathlength read-out limit of 1.64 pm/ $\sqrt{\text{Hz}}$ due to electronic noise in the science interferometer. The optical pathlength read-out limit induced by shot noise was 8.14 pm/ $\sqrt{\text{Hz}}$. The uncorrelated sum of shot noise and electronic noise yields a value of 8.30 pm/ $\sqrt{\text{Hz}}$ for the optical pathlength read-out limit in the science interferometer.

4.2 p-i-n photodiode

Photodiodes with a p-i-n layer structure were identified in the past to be optimal for the read-out of the heterodyne signals in the LOB interferometers [78, pp. 50]. Thus a short introduction into the working principle of p-i-n photodiodes is given. This includes a theoretical assessment of the influence of the most common semiconductor materials on the p-i-n photodiode properties. The semiconductor materials under investigation

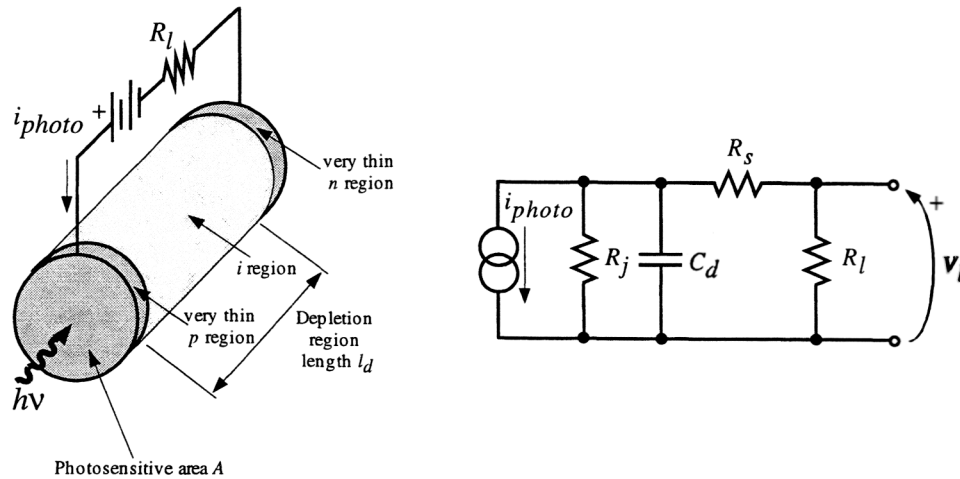


Figure 4.5: Physical structure and equivalent circuit of a p-i-n photodiode [59, p. 98].

are silicon and InGaAs and the properties are efficiency and impedance. Germanium as semiconductor material was not in discussion because the variety of germanium photodiodes was limited. The approach in this work was to compare the properties of COTS p-i-n photodiodes and select one of each semiconductor material on the basis of the requirements and goals for further testing. Afterwards the experimental setup is introduced and the performed measurements are presented. A general introduction into the photodetection process and available photodiode technologies is omitted for brevity in this section. The interested reader is referred to [78, pp. 3] and [59, pp. 49].

4.2.1 Layer structure and properties

This subsection is based on the information about p-i-n photodiodes that is provided in [59, pp. 96]. Figure 4.5 shows the physical structure of a p-i-n photodiode. In comparison to a p-n photodiode the p-i-n photodiode has a layer of intrinsic semiconductor sandwiched (undoped or marginal n-/p-doped) between the p- and n-doped layers. The light which is impinging on the p-doped part of the photodiode is completely transmitted through this layer. In the intrinsic part electron-hole pairs are generated by the photons. The electrons are traveling to the n-doped part and the holes are traveling to the p-doped part of the photodiode. There the photocurrent is generated [59, p. 98]. The length of the intrinsic layer l_d is equal to the length of the depletion region. First, the intrinsic layer increases the quantum efficiency in comparison to a p-n photodiode. Second, the junction capacitance C_d is reduced in a p-i-n photodiode in comparison to a p-n photodiode. The advantage of both points is explained in the following.

4.2.1.1 Efficiency

Figure 4.7(a) depicts the absorption coefficient α of different semiconductor materials as a function of the wavelength. The most important semiconductor materials for photodetection in interferometers are silicon and Indium-Gallium-Arsenide-Phosphide (InGaAsP), which is usually called InGaAs for brevity. At a wavelength of 1064 nm

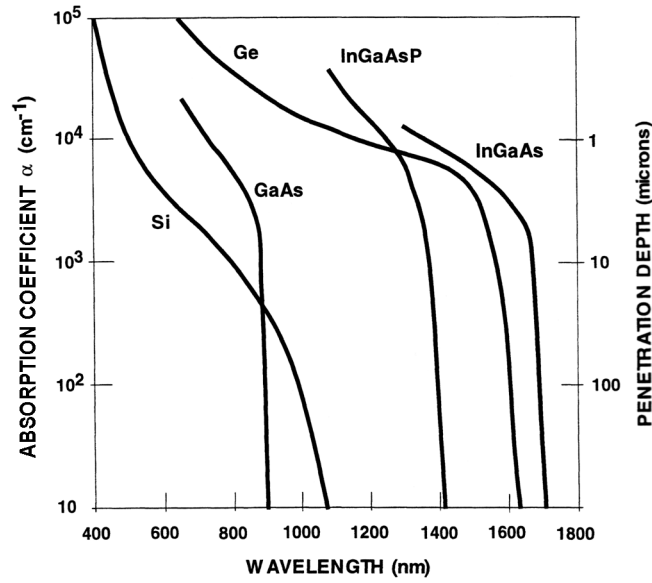


Figure 4.6: Absorption coefficient α of different semiconductor materials [59, pp. 76].

the absorption coefficient α of silicon is four orders of magnitudes smaller than that of InGaAs.

The amount of light P_{abs} , which is absorbed by a semiconductor material with absorption coefficient α is given by

$$P_{\text{abs}}(\alpha) = P_{\text{in}}(1 - R)(1 - e^{-\alpha x}) \quad (4.11)$$

whereby P_{in} is the incident power on the semiconductor material, R is the reflection coefficient of the semiconductor material, and x is the absorption length in the semiconductor material [59, p. 75]. The reflection coefficient of modern photodiodes is kept below 1% using AR-coatings [59, p. 75]. Figure 4.7(a) depicts the relative power absorption of silicon and InGaAs photodiodes as a function of the absorption length. It illustrates that the absorption layer of silicon photodiodes must be about three orders of magnitude thicker than that of InGaAs photodiodes to achieve the same relative power absorption.

4.2.1.2 Bandwidth

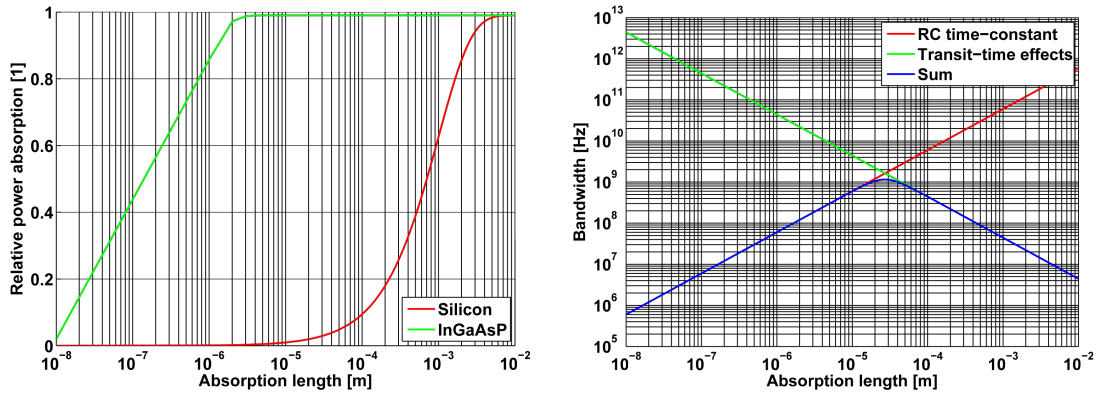
The bandwidth B of a p-i-n photodiode can be estimated with the following equation [59, pp. 98]

$$B = \frac{1}{\sqrt{\left(\frac{1}{f_{\text{RC}}}\right)^2 + \left(\frac{1}{f_t}\right)^2}} \text{ [Hz]} \quad (4.12)$$

f_{RC} is the bandwidth of the photodiode due to its RC time-constant defined as the frequency when the photocurrent has decreased by $\sqrt{2}$. This is given by [59, p. 98]

$$f_{\text{RC}} = \frac{1}{2\pi RC_d} \quad (4.13)$$

$$= \frac{l_d}{2\pi R\epsilon_0\epsilon_R A} \quad (4.14)$$



(a) Relative power absorption of silicon and InGaAs photodiodes as a function of absorption length. (b) Bandwidth of a photodiode with a series resistance due to RC time-constant and transit-time effects.

Figure 4.7: Relation between efficiency and bandwidth of a photodiode.

R is the sum of the photodiode series resistance R_s and the load resistance R_l according to Figure 4.5. The load resistance is a property of the connected circuit and is often assumed to be 50Ω in photodiode data sheets. A TIA, however, can have much smaller values of load resistance (“virtual ground”). The capacitance of the photodiode C_d can be calculated from its physical properties: the length of the depletion region l_d , the area A of the photodiode surface. ϵ_r is the relative permittivity of the material and ϵ_0 the permittivity of vacuum.

f_t is the bandwidth of the photodiode due to the carrier transit-time defined as the frequency when the photocurrent has decreased by $\sqrt{2}$. It can be expressed as [59, p. 98]

$$f_t = \frac{2.78v_s}{2\pi l_d} \quad (4.15)$$

v_s is the saturation velocity of the carrier in the material. f_{RC} and f_t are substituted into the equation for the bandwidth B of the photodiode [59, p. 99]

$$B = \frac{1}{\sqrt{\left(\frac{2\pi R\epsilon_0\epsilon_r A}{l_d}\right)^2 + \left(\frac{2\pi l_d}{2.78v_s}\right)^2}} \quad (4.16)$$

Figure 4.7(b) shows the bandwidth of a photodiode as a function of the depletion region thickness. The photodiode active area was set to 1 mm^2 . The saturation velocity for silicon is $1 \cdot 10^7 \text{ cm/s}$ and the relative permittivity is around 12. The values for InGaAs are comparable [59, p. 75]. The sum R of the load and the series resistance of the photodiode was set to 25Ω . For that value the bandwidth is maximum at a depletion region length of $25 \mu\text{m}$. The relative absorption of InGaAs is around 1 and for Silicon 0.03. InGaAs photodiodes are usually fabricated with a responsivity of 0.7 A/W and silicon photodiodes with a responsivity of 0.15 A/W at 1064 nm . According to Figure 4.7(a) and 4.7(b) InGaAs photodiodes are usually RC time-constant limited. Silicon photodiodes are transit-time limited under the assumption that the relative absorption is equal to the responsivity.

4.2.1.3 Impedance

The electric impedance of a photodiode can be modeled with an equivalent circuit. Figure 4.5 shows a standard equivalent circuit of a photodiode. A photodiode can be modeled with a current source I_{photo} which is parallel to the differential resistance R_j and the junction capacitance C_d of the photodiode. The differential resistance R_j of a reverse biased photodiode is typically greater than $10^6 \Omega$. The series resistance R_s is induced by the bulk and the contact resistances of the photodiode. It is usually of the order of a few Ohms. The load resistance R_l is used to measure the photocurrent I_{photo} via a differential voltage across R_l .

An accurate equivalent circuit of a p-i-n photodiode is needed for the design of a photodetector within LT SPICE IV at DC as well as high frequency [90, 91]. The equivalent circuit presented in Figure 4.5 can be extended to model the situation within a p-i-n photodiode more accurately. The equivalent circuit can hereby not only be used to model the bandwidth due to the RC time-constant [92]. For photodetectors with a high bandwidth the carrier transit-induced time-delay effect can be implemented as well as the stored charge effect of p-i-n photodiodes under high power operation [93, 94]. The upper beat note frequency of 20 MHz is in this context no high frequency. Thus the approach chosen for this work is to model the measured impedance of a photodiode under test with a simple equivalent circuit for simulating the photodetector in LT SPICE IV.

4.2.2 Selection of p-i-n photodiodes

In this subsection one p-i-n photodiode with silicon as semiconductor material and one with InGaAs as semiconductor material is selected for further testing. The requirements and goals for the photodiodes were introduced in Subsection 4.1.5.1. At the end of this subsection the compatibility of Avalanche PhotoDiodes (APDs) with the LISA requirements is discussed using the equations presented in Subsection 4.1.4.

4.2.2.1 Silicon

Standard silicon p-i-n photodiodes like the PC50-6 from First Sensor have a responsivity of 0.15 A/W at 1064 nm [58]. These are incompatible with the requirement for the responsivity. COTS silicon photodiodes which have a responsivity of 0.5 A/W or higher at a wavelength of 1064 nm have become recently available. The increase in responsivity is reached via two modifications of the standard p-i-n layer structure presented in Figure 4.5. First, the intrinsic layer l_d is elongated. Second, a reflective coating is applied on the back (n-doped part) of the photodiode. The characteristics of the commercially available devices are summarised in Table 4.1 [95] [96] [97]. The capacitances of all photodiode types are within the compatible range for LISA. At the same time the diameters of the active area of the photodiode models are larger than the beam diameters on the LOB. These are 2 mm for the local interferometry and around 5 mm in the science interferometer. Thus the imaging optics do not have to focus the beam and the compression ratio of one could relax the accuracies for the alignment of the imaging optics [39, pp. 131]. According to Figure 4.7(a) and 4.7(b) silicon photodiodes with a relative absorption of 0.6 are transit-time limited at a level of around 45 MHz. Therefore it has to be checked experimentally if these photodiode are compatible with the LISA requirements.

Table 4.1: Silicon QPDs with an increased efficiency at 1064 nm [95] [96] [97].

Manufacturer	Model	Diameter [mm]	Efficiency [A/W]	Capacitance [pF]	Dark noise [nA]
First Sensor	QP22-Q	5.33	0.55	6	0.4
Excelitas	YAG-444-4AH	11.30	0.5	9	< 75
OEC	SPOT-9-YAG	10.00	0.35	25	35

Table 4.2: InGaAs photodiodes with a sufficient small capacitance to test the LOB.

Manufacturer	Model	Diameter [mm]	Efficiency [A/W]	Capacitance [pF]	Dark noise [nA]
Hamamatsu	G6849-01	1	0.7	16	0.18
GPD	GAP1000Q	1	0.7	11	6
OSI	FCI-Q1000	1	0.7	25	0.5
Jenoptik	Prototype	1	0.99	7.5	1.25
DSC	Prototype	1	0.7	2.5	150

These three photodiodes share the same principle of operation. Therefore only one will be tested and the outcome should also be valid for the other two. For the investigations whether the silicon photodiodes are compatible with the LISA requirements the QP22-Q photodiode was selected. This is due to the fact that the QP22-Q photodiode was already tested for LTP [98]. Among these tests the change of the responsivity and of the dark current to irradiation was investigated. The already performed tests can be used to complement the tests that were performed in the context of this work.

4.2.2.2 InGaAs

The responsivity of standard InGaAs p-i-n photodiodes is 0.7 A/W. This is fully compatible with the sensitivity requirement, see Subsection 4.1.5. The main drawback for InGaAs as semiconductor material is the relative thin intrinsic layer in comparison to silicon. Therefore the capacitance C_d is the main selection criteria for InGaAs photodiodes. The first three photodiodes in Table 4.2 are commercially available. The diameter is limited to around 1 mm by the capacitance. The GAP1000Q photodiode is selected for testing because its capacitance is with 11 pF the lowest one of the commercially available photodiodes.

The last two photodiode types in Table 4.2 are prototypes. They are presented to underline that there is quite some room for improvement for LISA photodiodes. The photodiode from Jenoptik was developed for the squeezing group at the AEI [99]. It has a responsivity of approximately 0.99 A/W and a reduced capacitance of 7.5 pF. The higher responsivity improves the shot noise in the science interferometer in LISA and thereby reduces the optical pathlength read-out limit, see Equation 4.7. The lower capacitance increases the bandwidth of the photodetector and decreases the input current noise of the photodetector, see Subsection 4.3.1. The second photodiode was developed in a project between NASA and the company DSC. It is described in [100, 101]. The design of this InGaAs photodiode was focused on the reduction of the capacitance. The capacitance per active area was reduced by a factor of four. This was achieved by changing the layer setup of the p-i-n photodiode slightly. This results in a significantly increased dark current (150 nA). This value is uncritical because the shot noise of the dark current is well

below the shot noise of the measurement beam, and the DC value of the dark current is negligible compared to the DC current from the LO beam. The measurement of the transferfunction and the input current noise of a photodetector using a prototype of a Discovery Semiconductor (DSC) QPD with 2 mm diameter is presented in Appendix 5.

4.2.2.3 Avalanche photodiode

In Subsection 4.1.4 the three limiting noise sources for the optical pathlength read-out of a heterodyne interferometer were introduced. Namely shot noise, electronic noise of the TIA and relative power noise of the laser. With a short look on the equations it is easy to see that the first two noise sources can be suppressed by an increase of the efficiency of the photodiode. From this point of view APDs seem to yield lower optical pathlength read-out limits because they generate several electron-hole pairs from one absorbed photon [59, pp. 102]. Their responsivity can be several tens to hundreds A/W in comparison to standard InGaAs p-i-n photodiodes with around 0.7 A/W. In a next step the impact of APDs characteristics on the optical pathlength read-out limit in the science interferometer of LISA is calculated. The important characteristics of APDs are introduced according to [59, pp. 102 and pp. 142]. The read-out limit of the optical pathlength with APDs is deduced from Equation 4.7

The central element of an APD is the internal multiplication of photon generated electron-hole pairs. These are accelerated under a high electric field and generate new electron-hole pairs via collision ionisation comparable to the operation of a photomultiplier tube. The multiplication factor M is given by the ratio of the current at the output of the APD to the primary current. The primary current is the primary responsivity ρ times the received power P_{rcvd}

$$M = \frac{i_{out}}{i_{primary}} = \frac{i_{out}}{\rho P_{rcvd}} \quad (4.17)$$

For a signal the output current is given by

$$i_{signal} = \rho P_{rcvd} \cdot E\{M\} \text{ [A]} \quad (4.18)$$

whereby $E\{M\}$ is the expected value of the amplification. In contrast to this the shot noise is given by

$$i_{noise} = \sqrt{2\rho P_{rcvd} E\{M^2\}} \left[\frac{\text{A}}{\sqrt{\text{Hz}}} \right] \quad (4.19)$$

whereby $E\{M^2\}$ is the expected value of the amplification squared. For an ideal amplification process the mean of the square is identical to the square of the mean. An APD is not ideal because the characteristics do change over the active area and within the active region and therefore the mean of the square is larger than the square of the mean. This means nothing else than that the noise is amplified more than the signal.

The equation similar to 4.7 for the optical pathlength read-out limit for an APD is therefore given by

$$\tilde{l} = \frac{\lambda}{2\pi} \cdot \sqrt{\frac{q_e (P_{sig} + P_{lo})}{\gamma \rho P_{sig} P_{lo}}} \cdot \sqrt{\frac{E\{M^2\}}{E\{M\}^2}} \quad (4.20)$$

The first part of this equation is identical to the one derived for a standard p-i-n photodiode, see Equation 4.7. The additional square root of the fraction of the expected values is

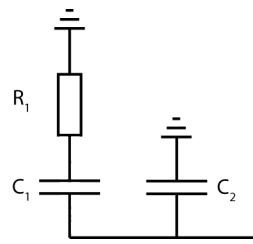


Figure 4.8: Equivalent circuit of a p-i-n photodiode to model its impedance.

larger than 1 because the mean of the square is larger than the square of the mean. The typical responsivity ρ of InGaAs p-i-n APD photodiodes is with 0.7 A/W at 1064 nm comparable to the one of standard InGaAs p-i-n APD photodiodes [102]. Therefore APDs are not suitable for LISA.

4.2.3 Measurement results

This subsection presents the results of the measurements to compare the most important properties of silicon and InGaAs photodiodes which are impedance and efficiency.

4.2.3.1 Impedance

The impedance of the Device Under Test (DUT) was measured with a 4396B spectrum analyser from Agilent and the according impedance analyser kit [85]. The bias voltage for the reverse biasing of the photodiode was generated with a so-called dual offset box, which is available at the AEI. The impedance was measured from 2 MHz to 50 MHz. The measured impedance was used to fit the values of an equivalent circuit to it. The fitting was done by using the LInear Simulation and Optimization (LISO) software package [103, pp. 197].

The first photodiode under test was the QP22-Q silicon photodiode from First Sensor [95]. The fitting procedure with LISO was performed using different equivalent circuits. The simplest equivalent circuit which yielded the best results is shown in Figure 4.8. The goal of the fitting procedure was to model the measured impedance of the photodiode for the usage in LT SPICE IV. Therefore the equivalent circuit cannot be seen as a measurement of the inner structure of the photodiode.

The results of the fitting procedure using the equivalent circuit of Figure 4.8 can be seen in Table 4.3. Thereby the impedance of the QP22-Q photodiode was measured for bias voltages ranging from 0.5 V to 10 V. The capacitance C1 was significantly dropping with a higher bias voltage. The capacitance C2 was relatively stable with respect to a bias voltage change. The resistance R1 was increasing with higher bias voltages. The errors of all values were in the range of a few percent. Therefore the equivalent circuit was a good approximation for the impedance of the QP22-Q photodiode.

The second photodiode under test was the GAP1000Q photodiode from GPD. The results of the fitting procedure using the equivalent circuit of Figure 4.8 can be seen in Table 4.4. Thereby the impedance of the GAP1000Q photodiode was measured for bias voltages ranging from 0.5 V to 5 V. The simplest equivalent circuit which yielded the best results is identical to the one used for the QP22-Q and is shown in Figure 4.8. The capacitance C1 was dropping with higher bias voltages. The capacitance C2 was relatively stable with respect to a bias voltage change. The resistance R1 was slowly

Table 4.3: Fitted parameters of an equivalent circuit of a QP22-Q photodiode from First Sensor.

Bias	C1	Error	C2	Error	R1	Error
[V]	[pF]	[fF]	[pF]	[fF]	[kΩ]	[Ω]
0.5	6.03	186.7	5.56	46.2	8.12	221.8
1	4.87	128.2	5.41	38.9	8.80	236.4
2	3.60	84.2	5.18	32.4	9.89	278.2
3	2.89	62.0	4.96	27.4	11.34	326.1
4	2.35	46.7	4.60	21.7	13.70	378.9
5	1.82	35.9	4.04	16.4	18.82	508.0
6	1.56	37.5	3.94	17.9	21.46	731.3
7	1.35	33.6	3.89	16.8	23.88	870.6
8	1.12	33.9	3.84	19.6	24.75	1233.0
9	1.03	33.7	3.83	18.3	29.41	1502.0
10	0.92	35.1	3.85	19.7	31.93	1952.0

Table 4.4: Fitted parameters of an equivalent circuit of a GAP1000Q photodiode from GPD.

Bias	C1	Error	C2	Error	R1	Error
[V]	[pF]	[fF]	[pF]	[fF]	[kΩ]	[Ω]
0.5	6.90	28.2	5.01	30.7	183.15	1.8
1.0	6.05	24.4	4.69	29.1	190.28	2.0
1.5	5.62	22.9	4.53	28.3	194.96	2.2
2.0	5.33	22.0	4.43	27.8	198.43	2.3
2.5	5.12	21.5	4.27	27.5	201.42	2.4
3.0	4.95	21.1	4.33	27.3	203.98	2.4
3.5	4.82	20.9	4.29	27.1	206.24	2.5
4.0	4.71	20.7	4.26	27.0	208.03	2.6
4.5	4.61	20.5	4.23	26.9	209.76	2.6
5.0	4.21	20.4	4.58	27.1	225.69	2.3

increasing with higher bias voltages. The errors of all values were in the range of a few percent. Therefore the equivalent circuit was a good approximation for the impedance of the GAP1000Q photodiode.

Figure 4.9 shows a comparison of the measured and the fitted impedances of the QP22-Q photodiode and the GAP1000Q photodiode. The presented impedances were measured at a bias voltage of 5 V. The measured and fitted values showed a good agreement for amplitude as well as for phase. The high noise in the phase measurement of the QP22-Q photodiode was found to be the switched off averaging for the phase measurement at the spectrum analyser. The amplitude of the complex impedance of the QP22-Q photodiode was a factor of 2 higher than the one of the GAP1000Q photodiode, see Figure 4.9(a). Although the diameter of the QP22-Q photodiode was five times bigger its capacitance was approximately a factor of two lower than the capacitance of the GAP1000Q photodiode. According to Section 4.3.1 the bandwidth of a TIA with a QP22-Q photodiode was a factor of $\sqrt{2}$ higher. This explains why for high frequency

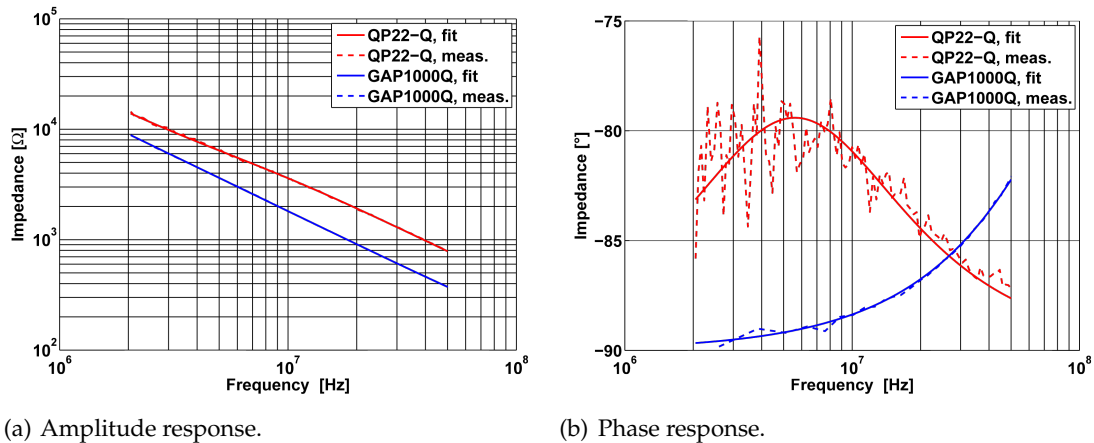


Figure 4.9: Comparison of the measured and fitted impedance of the GAP1000Q and the QP22-Q photodiode.

TIA's typically silicon photodiodes are chosen. The phase of the impedance is shown in Figure 4.9(b). The phase of the QP22-Q photodiode was dropping between 5 MHz and 50 MHz and the phase of the GAP1000Q photodiode was decreasing. The reason for this will be explained in the next subsection.

4.2.3.2 Efficiency

The efficiency of the p-i-n photodiodes at DC and at higher frequencies were measured using the circuit shown in the schematic in Figure 7 in Appendix 6. The p-i-n photodiode was put into the photodiode socket on the Printed Circuit Board (PCB). The jumper on the PCB were set to be able to measure the DC photocurrent with a multimeter. The power of the laser beam impinging on the photodiode was measured with a calibrated power meter NOVA II and the power sensor PD-300 from OPHIR [104, 105]. From these two values the responsivity in A/W was estimated. The responsivity of the QP22-Q photodiode was measured to 0.57 A/W at room temperature at a laser wavelength of 1064 nm. The responsivity of the GAP1000Q photodiode was measured to 0.71 A/W at room temperature at a laser wavelength of 1064 nm.

In a next step the jumper was set to measure with the TIA the efficiency of the p-i-n photodiode as a function of frequency. The feedback capacitor of the TIA was modified to suppress the oscillation at the UGF, see Equation 4.25. The light source was a so-called photodiode tester, which is available at the AEI. It consisted of a laser diode with a wavelength of 1060 nm and modulation electronics, which can modulate the amplitude of the laser diode from a few kHz up to 500 MHz. The spectrum analyser 4396B from Agilent was used to obtain the transfer function. Figure 4.10 shows the transfer function of the QP22-Q silicon photodiode in comparison to a C30619G InGaAs photodiode from Excelitas in the same TIA (responsivity ≈ 0.7 A/W) [106]. The InGaAs photodiode measurement served as a reference for the silicon photodiode. The details of the TIA were not of interest for this investigation. The important observation is the difference between the transfer function obtained with the QP22-Q and the C30619G. The amplitude response of the QP22-Q is plotted for different bias voltages in Figure 4.10(a). The QP22-Q photodiode needed a minimum bias voltage of 120 V to have a flat amplitude response

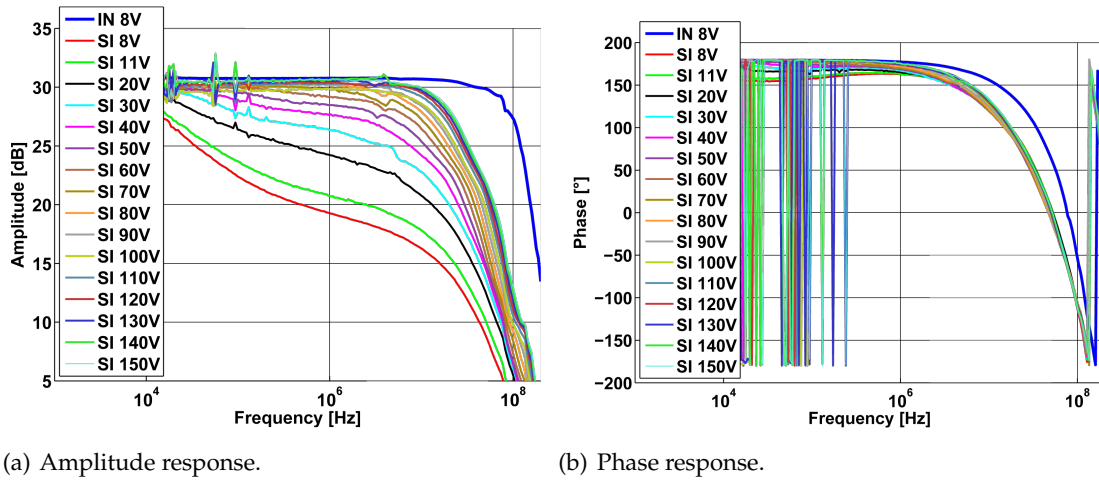


Figure 4.10: Transfer function of a TIA with the QP22-Q photodiode from First Sensor as a function of bias voltage in comparison to the same TIA with a C30619G InGaAs photodiode from Excelitas.

up to 10 MHz. Flat means in this context a drop of 1 dB in comparison to the InGaAs photodiode. The phase response of the QP22-Q photodiode was not changing any more for bias voltages higher than 50 V, see Figure 4.10(b). The estimated capacitances of the photodiode were not changing significantly for bias voltages above 10 V, see Table 4.3 on page 80. Thus the loss in amplitude in comparison to the InGaAs photodiode was not driven by the impedance of the QP22-Q photodiode.

Figure 4.11 plots the amplitude at 30 MHz of the QP22-Q photodiode as a function of bias voltage. The 30.25 dB of the InGaAs photodiode at 30 MHz is plotted as a reference. The function that was used for fitting was

$$QP22Q_{\text{fit}} = A \times \left(1 - e^{-x/X_0}\right) + c \quad (4.21)$$

whereby A is 16.5, X_0 is 50 V and c equals 10 dB. This means that 26.5 dB is the maximum amplitude response of the silicon when increasing the bias voltage further. Or 3.75 dB is the minimum loss in comparison to a InGaAs photodiode at 30 MHz.

The measurement of the responsivity as a function of frequency of the QP22-Q photodiode was performed at a room temperature of about 23°C. The responsivity of a silicon photodiode at a wavelength of 1064 nm has a temperature coefficient of 1%/K [60, pp.59]. Thermal simulations of the photodetector on the LOB inside vacuum revealed that the temperature of the photodiode is around 28.1°C [107, pp. 10]. Thus the before mentioned measurement of the responsivity as a function of frequency was performed with the QP22-Q photodiode at two temperatures and three bias voltages. The photodiode temperature was measured with a PT10k sensor glued to its back and the temperature change was induced by a small air heater. The lower temperature was set to 32°C to be comparable to the simulated temperature of the photodiode on the LOB in vacuum. The higher temperature was set to approximately 50°C to be able to clearly see an increase of the responsivity. Figure 4.12 presents the results of the measurements. The responsivity as a function of frequency had the same behavior under a bias voltage change as before. Unfortunately the responsivity at high frequencies was not increased

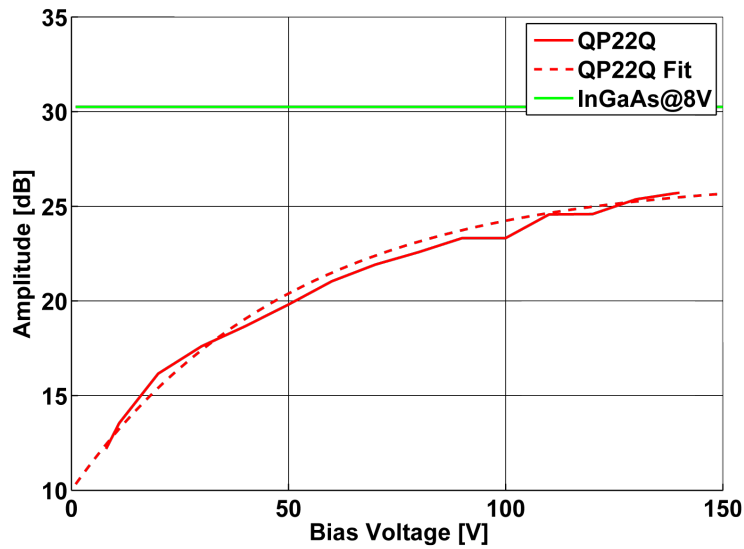
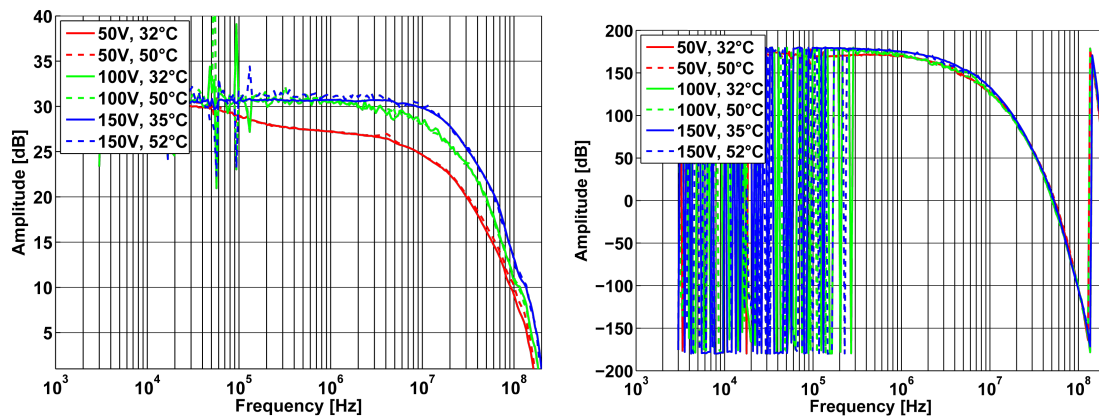


Figure 4.11: Amplitude response of photodiodes at 30 MHz as a function of bias voltages.



(a) Amplitude response.

(b) Phase response.

Figure 4.12: Transfer function of a TIA with the QP22-Q photodiode from First Sensor as a function of bias voltage and temperature.

with a higher temperature.

The results of the comparison between the properties of silicon and InGaAs photodiodes revealed that silicon photodiodes are not compatible with the requirements of the science interferometer within LISA. Their loss of responsivity in comparison to InGaAs at 30 MHz is 3,75 dB. This is equal to a responsivity of 0.45 A/W and far below the goal of 0.7 A/W. This drop in responsivity can be explained with the transit-time of the electrons in silicon photodiodes. The transit-time of the electrons is increased further in comparison to standard p-i-n photodiodes by the reflection of the non-absorbed light at the reflective coating on the n-doped part of the p-i-n photodiode [108]. The generation and use of the high bias voltage onboard the satellites can also be seen as critical. Furthermore a higher bias voltages increases the thermal power of the photodiode. Therefore the silicon photodiodes with a higher responsivity are rejected to be used in the LISA interferometers. For further testing within the TIA the GAP1000Q photodiode is selected.

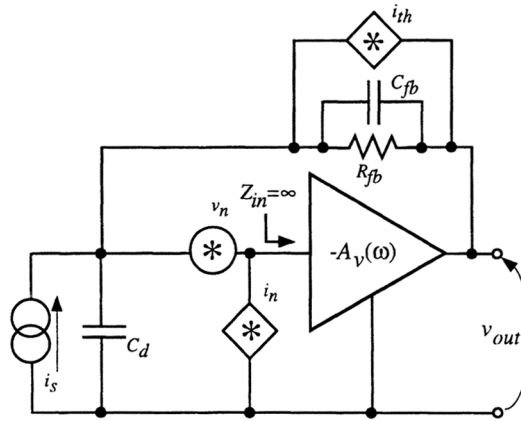


Figure 4.13: Transimpedance amplifier noise equivalent circuit [59, p. 192].

4.3 Transimpedance amplifier

This section introduces a simple model for the noise and the bandwidth of a TIA, which is sufficient to understand the most important properties of a TIA for LISA [109]. The interested reader is referred to [59, pp. 121, pp. 173], which explains the noise model and the design of a TIA in more detail. Afterwards the TIA design, which has been identified to be optimal for LISA in [78] is introduced briefly. The work that is presented here focuses on two topics: first, the optimisation of the aforementioned TIA design with respect to the requirements; second, the development of a quadrant photodetector, based on this TIA design, which can later be used to test the LOB. After the explanation of the design of the quadrant photodetector, the measurements of its power consumption, its bandwidth and its input current noise are presented.

4.3.1 Model

A simple model of a TIA including photodiode can be seen in Figure 4.13. The photodiode is represented by the current source i_s and the capacitance C_d . The amplifier with gain $-A_v(\omega)$ is the core element of the TIA. Its input current noise i_n and its input voltage noise v_n are represented by the according voltage and current noise sources. The input impedance Z_{in} of the amplifier is infinite. Thus the photocurrent i_s flows through the feedback resistor R_{fb} . This introduces a differential voltage between the input and output nodes of the amplifier. The thermal noise of the feedback resistor is represented by the current noise source i_{th} . The amplifier reduces the voltage at its input node to zero (an Operational Amplifier (OpAmp) reduces the voltage difference between its input nodes) by applying an output voltage v_{out} . This is given by the equation

$$v_{out} = R_{fb} \cdot i_s \quad (4.22)$$

which is valid for low frequencies. The feedback capacitor C_{fb} is used to suppress an oscillation of the feedback loop at the unity gain frequency of the open-loop gain. The most important equations for the design of photodetectors for LISA are the one for the bandwidth B_{PD} of a photodetector and for the input current noise n_{el} . The bandwidth of a photodetector can be calculated from a simple equation when an OpAmp is used as

amplifier [59, p. 193]

$$B_{PD} = \sqrt{\frac{GBWP}{2\pi R_{fb} C_t}} \quad (4.23)$$

whereby GBWP is the gain-bandwidth product of the amplifier. This is the -3 dB bandwidth, while for a LISA photodetector the -1 dB bandwidth is important. This -1 dB bandwidth is a little smaller than the -3 dB bandwidth. The capacitance C_t is composed of two capacitances

$$C_t = C_d + C_{in} \quad (4.24)$$

C_{in} is the input capacitance of the amplifier. The value for the feedback capacitor C_{fb} is calculated from [110]

$$C_{fb} = \sqrt{\frac{C_d + C_{in}}{2\pi GBWP R_{fb}}} \quad (4.25)$$

The input current noise of a photodetector is composed of the uncorrelated sum of three noise sources: the input current noise i_n of the amplifier, the Johnson noise i_{th} of the feedback resistor R_{fb} , and the input voltage noise v_n of the amplifier. The last-mentioned is converted via the transimpedance resistance into an input current noise. This yields an input current noise n_{el} of the photodetector of [109]

$$n_{el} = \sqrt{i_n^2 + \frac{4k_B T}{R_{fb}} + \frac{v_n^2}{R_{fb}^2} (1 + 2\pi f R_f C_t)^2} \quad (4.26)$$

k_B is the Boltzmann constant and T the temperature of the resistor.

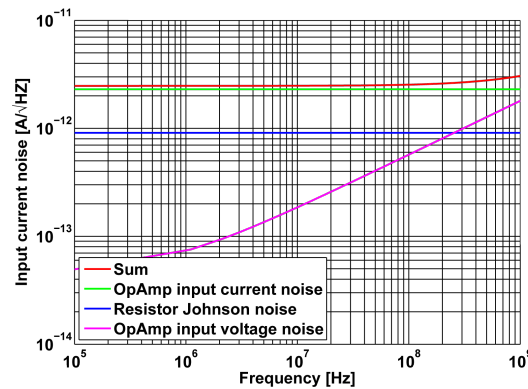
In an example the power consumption, the bandwidth B_{PD} , and the input current noise n_{el} of a DC coupled photodetector are calculated to get a notion which parameters are more important than the others. In this example the OpAmp LMH6624 from Texas Instruments is selected as amplifier [110]. Table 4.5 summarises its properties. The power supply of the LMH6624 is set to +1 V and -5 V. The power consumption based on the supply current of a DC coupled quadrant photodetector is 288 mW at minimum. The power consumption will be increased significantly by the required AC/DC decoupling of the signals. This decoupling needs additional OpAmps. The power consumption is further increased by the bias voltages of the photodiode times the photocurrent. The driving current and output voltages of the OpAmps increase the power consumption, too. Therefore the minimum power consumption of 288 mW can be seen as critical with respect to the power requirement of photodetectors of 1.2 W, see Subsection 4.1.5.2.

The QPD GAP1000Q from GPD was selected in Subsection 4.2.3 for the photodetectors on the LOB. Its capacitance C_d at 5 V bias voltage is around 10 pF. The feedback resistor R_{fb} is set to 20 k Ω . With these values the bandwidth B_{PD} and the input current noise n_{el} of the photodetector can be calculated. The -3 dB bandwidth B_{PD} is calculated as 31.34 MHz with Equation 4.23. The input current noise n_{el} as a function of frequency is presented in Figure 4.14.

The input current noise n_{el} is well below the requirement within the complete frequency range. At frequencies below 2 MHz the input current noise n_{el} is dominated by the Johnson noise of the feedback resistor i_{th} and the input current noise of the OpAmp i_n . Towards higher frequencies the capacitance of the photodiode C_d together with

Table 4.5: Properties of the LMH6624 OpAmp from Texas Instruments [110].

Parameter	Typical	Units
Gain-bandwidth product	1500	MHz
Input current noise	2.3	$\text{pA}/\sqrt{\text{Hz}}$
Input voltage noise	0.92	$\text{nA}/\sqrt{\text{Hz}}$
Input capacitance	1.9	pF
Supply current	12	mA

Figure 4.14: Calculated input current noise of the GAP1000Q photodiode with the LMH6629 OpAmp and a feedback resistor R_{fb} of 20 k Ω .

the input voltage noise of the OpAmp v_n dominate the input current noise n_{el} . The investigations in [109] indicated that the measured input current noise n_{el} for frequencies above 10 MHz can be a factor of two above the calculated values. This high noise is caused by parasitics within the OpAmp and the circuit. Thus it can be assumed that the measured values for the input current noise n_{el} for the LMH6624 OpAmp in combination with the GAP1000Q photodiode will be approximately a factor of two above the calculated values for frequencies higher than 10 MHz. The input current noise is then above the requirement of $4 \text{ pA}/\sqrt{\text{Hz}}$, see Subsection 4.1.5.2. Therefore the input voltage noise of a TIA is in this context as important as its input current noise.

4.3.2 Design

The research on TIA designs for LISA was started by Gerhard Heinzl and Benjamin Sheard at the AEI in 2006. The output of this research were two TIA designs: one design was based on OpAmps, the other design was based on transistors. Both designs have been used to offset phase-lock two lasers at power levels comparable to the science interferometer of LISA [87, pp. 64]. The TIA based on transistors had better properties with respect to power consumption, bandwidth and input current noise. In 2010 the research on TIA designs was restarted to verify these results and to implement new findings since 2006 [78]. This was performed at the institute of Theoretical Electrical Engineering of the Leibniz Universität Hannover in cooperation with the AEI. The author contributed to this research. The main result of the restarted research on TIA technologies for LISA confirms the findings from 2006. TIA based on transistors do have best properties with respect to the LISA requirements [78, pp. 88]. So far, the research

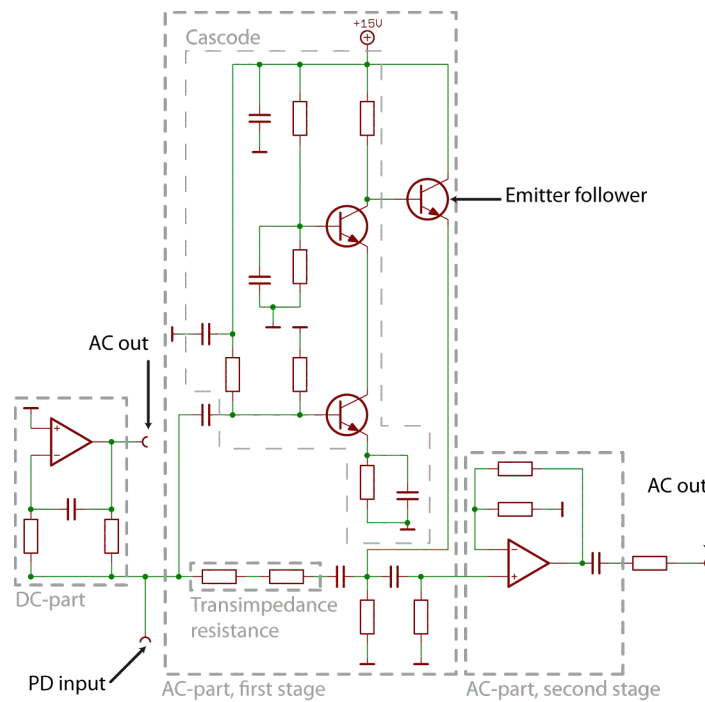
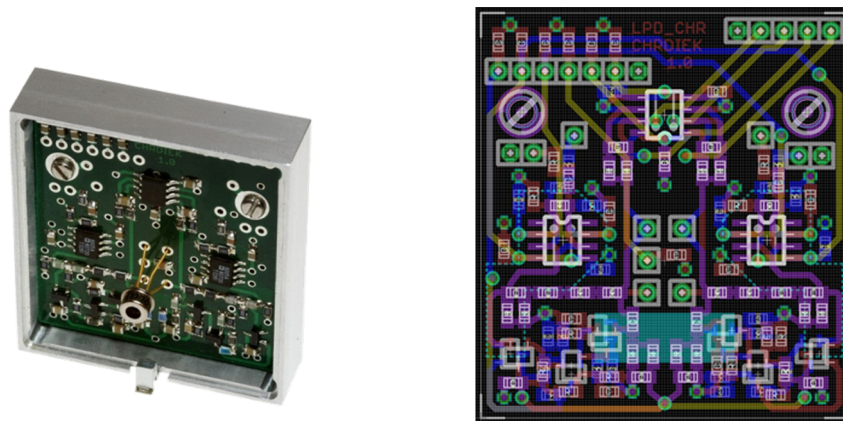


Figure 4.15: Schematic of an AC/DC decoupled TIA. The first stage of the AC part is based on transistors.

on TIA designs was concentrated on single element photodetectors. Thus the research in the context of this work was concentrated on the design of a quadrant photodetector, which can be used for read-out of the interferometer signals on the LOB. Therefore the TIA design for a single element photodetector will be introduced briefly. Afterwards the methods to design a quadrant photodetector starting from a single element photodetector are described. This includes a description of methods to optimise the TIA design with respect to the LISA requirements.

In general, the transistor design was based on ideas presented in [111, 112]. A schematic of a single element TIA can be seen in Figure 4.15. The anode of the photodiode was connected to the pin named “PD input”. The AC output of the TIA is labelled “AC out” and the DC output is labelled “DC out”. The most important element of this circuit was the first stage of the AC-part. The three transistors were connected in form of a cascode and an emitter follower. The BFR181 from Infineon was used as transistor [113]. The values of the components in this part of the circuit were critical for the stability of the AC part of the TIA. A general procedure for the design of this type of transistor circuit can be found in [114] or with special regard to LISA in [78, pp. 88] and [87, pp. 66]. At the end of the design phase the transistor stage acted like an OpAmp with a single input, i.e. like an AC-coupled inverting amplifier. In combination with the two resistors labelled “Transimpedance resistor” the transistor stage formed the AC TIA. The OpAmp at the output of the AC part was used as buffer to drive the $50\ \Omega$ output load. The other OpAmp was used for the DC TIA.

At the beginning the design of the quadrant photodetector was concentrated on minimisation of the circuit layout in terms of PCB dimensions and number of components. This was necessary to be compatible with the requirements for the dimensions of the photodetector. 4.16(a) shows a photograph of the first prototype of a quadrant photode-



(a) Photograph. The cover of the housing was removed to see the PCB. (b) Eagle PCB view.

Figure 4.16: First prototype of a quadrant photodetector for testing the LOB.

tor, built on a four layer PCB. The schematic can be found in Appendix 6 in Figure 8. The QPD is connected via five pins to the center of the PCB. The electronic components for two AC/DC decoupled channels are located on the top layer of the PCB and the components for the other two channels are located on the bottom layer of the PCB. The transistor stages of the AC parts of the TIAs can be seen at the bottom of the PCB. The OpAmp buffer stages of the AC parts can be seen above the transistor stages. The DC parts of two channels are combined in a dual OpAmp, located above the QPD connectors. The cables for the power supply and the signals will be soldered to the PCB from the back. The outer dimensions of the housing are $45 \times 49 \text{ mm}^2$.

The layout of the transistor stages of the first prototype were to some extent asymmetric as shown in Figure 4.16(b). This arrangement was required to fit all four channels of the required dimensions on a single PCB.

The AC transfer functions of the first prototype of the quadrant photodetector are shown in Figure 4.17. The measurement process is described in Subsection 4.3.3. The amplitude responses of the four channels were identical up to 11 MHz. Above 11 MHz the amplitude responses were differing by more than 3 dB. The -3 dB bandwidth of channel 3 was below 20 MHz. The phase responses of the four channels were identical up to 2 MHz. At 20 MHz the phase responses were differing up to 100° . The transfer functions were obtained after a long series of measurements in which the values of the components were changed step-by-step to identify the problem. The final outcome was that this first prototype was limited by the layout of the PCB. The transistor part of the photodetector was very sensitive to impedance changes. These changes were introduced by unequally long wires in the transistor stages between the channels. Therefore asymmetries between the four channels in this part of the circuit layout have to be avoided without any exceptions.

Therefore, a second prototype was developed. A photograph of the second prototype can be seen in Figure 4.18(a). The schematic can be found in Appendix 6 in Figure 9. It was based on two identical PCBs. Each PCB comprised two AC/DC decoupled channels. One AC channel was located on the left-hand side of the top layer of the PCB. The second AC channel was located on the right-hand side of the bottom layer of the PCB

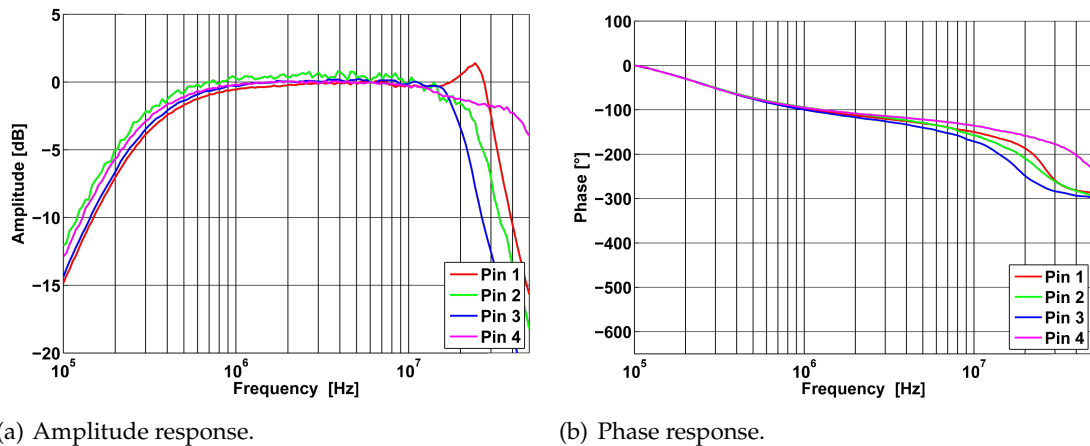


Figure 4.17: Transfer functions of the first prototype in combination with the GAP1000Q photodiode.

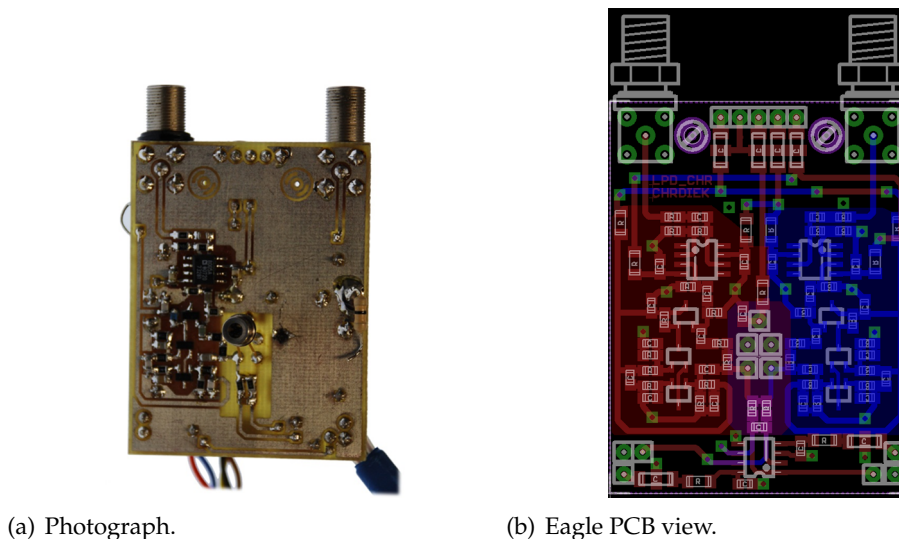


Figure 4.18: Second prototype of a quadrant photodetector for testing the LOB.

in Figure 4.18(a). The DC parts of both channels were combined in one dual OpAmp TIA, which was located below the photodiode on the bottom layer of the PCB. A further reduction was achieved by spreading the channels over two PCBs. If all four channels were located on one PCB its dimensions violated the requirement for the dimension of the photodetector. Thus the TIAs were spread over several PCB to reduce the size in the critical dimensions and increase the size in an uncritical dimension. Two copies of the second prototype PCBs were arranged successively to form a quadrant photodetector. An overview of the PCB, shown in Figure 4.18(b), depicts two fully symmetric AC stages.

A further reduction of the PCB dimensions was achieved by spatially separating the voltage regulators of the power supply from the photodetector. Thus only one power supply circuit was needed for a set of photodetectors. This decreased the overall power consumption because of the non-negligible power consumption of the voltage regulators themselves. The transistor circuitry was sensitive to changes of the supply voltages.

Thus it was checked whether the separation of the power supply from the photodetector circuit was critical or not. The temperature stability of the power supply cables (GORE PTFE, see Appendix 7) in vacuum were comparable to the temperature stability of the vacuum chamber shown in Figure 2.29(a) on page 31. The temperature coefficient of the resistance of copper is $3.93 \cdot 10^{-3} / \text{K}$. Thus temperature induced variations of the supply voltage were smaller than $3.93 \cdot 10^{-5} / \sqrt{\text{Hz}}$ at 1 mHz. This stability was compatible with the requirement of the power stability presented in Subsection 4.1.5.2. The voltage drop across the power supply cables was also calculated. The cables had a diameter of 0.3 mm, which was equivalent to a cross-section area A of 0.07 mm^2 . The specific resistance ρ of the copper material is $1.68 \cdot 10^{-8} \Omega \cdot \text{m}$ and the length l of the power supply cables was assumed to be 2 m. The resistance of the cables was calculated to

$$R = \rho \frac{l}{A} = 0.476 [\Omega] \quad (4.27)$$

Table 4.6 on page 92 presents the power consumption of the second prototype photodetector. The highest current flowed via the +15 V power supply cable. The current was 12.2 mA. This value lead to a voltage drop of 5.7 mV across the GORE PTFE cables using the calculated resistance of 0.47Ω . This voltage drop was uncritical for the circuit. Therefore the spatial separation of the in-vacuum photodetectors and the power supply circuit can be seen as uncritical.

The separation of the power supply circuit and the photodetector required proper bypass of the power supply on the photodetector PCB [115, 116]. Bypass of the power supply for the first prototype of the quadrant photodetector is described now. A capacitor with $2.2 \mu\text{F}$ was used at the connection point of the power supply on the photodetector PCB. The bypassing of the power supply at high frequencies (above 10 MHz) was improved with two capacitors of 100 nF and 10 nF in parallel directly at the load to keep the impedance to the ground small. For the second prototype the bypass was slightly changed. The $2.2 \mu\text{F}$ capacitors at the inputs of the photodetector power supplies were replaced by NFM41PC204 feed-through capacitors [117]. Feed-through capacitors have a lower impedance at high frequencies compared to standard capacitors with the same capacitance [118]. The first version of the quadrant photodetector had oscillations on the supply voltages due to crosstalk between the loads of the different channels. Thus the loads were separated by integrating ferrites between the input of the power supply and the individual channels of the photodetector. The Wuerth ferrites had their maximum impedance at a frequency of 30 MHz [119]. This suppressed the oscillations between the loads in the MHz range.

Special care was taken in the design of the ground plane. First, the fragmentation of the ground plane was kept as low as possible to keep the impedance of the ground plane low even for high frequencies [120]. Second, the ground plane had to be removed under certain circuit elements. For instance the input node of the AC transistor stage is sensitive to a capacitance against ground. Therefore the ground plane was removed below the input node of the transistor stage and the according wires. The ground layers of the two PCBs of the second prototype were only connected at one point to avoid ground loops.

During the development of the AC/DC decoupled photodetectors for LISA, it was observed that the outputs of the TIAs oscillate at a certain frequency. This behaviour could not be explained in the beginning. The simulated transfer functions of the individual TIAs as well as the DC/AC combinations did not predict any oscillation. The same holds for the input current noise simulations done with LT Spice IV. The oscillations were identified in the OLG of the AC/DC decoupled TIA. These were introduced by an interaction of the low pass of the DC part and the high pass of the AC part. The

corner frequencies have to be chosen in a way to not violate the stability criterion for the combined OLG. The calculation to obtain the OLG of an AC/DC decoupled TIA can be found in the Appendix 4.

The power consumption of the photodetector was further reduced by two changes compared to its precursors from 2006 and 2010. First, different OpAmps for the DC stage and the AC output stage were chosen. Second, the supply voltage for the OpAmps were adapted to the range of their output signals. The bandwidth of the OpAmp for the DC stage was uncritical. Therefore the dual OpAmp 2177 from Analog Devices was selected for the DC stage [121]. Its supply current is 400 μ A per amplifier and the Gain-BandWidth Product (GBWP) is 1.3 MHz. The bandwidth of the OpAmp for the AC output stage was required to be sufficient to amplify signals of frequencies up to 20 MHz at least by a factor of two. Therefore the OpAmp AD8005 from Analog Devices was chosen [122]. Its supply current is 400 μ A per amplifier and the GBWP is 270 MHz.

4.3.3 Results of the second prototype

The measurements of the power consumption, the transfer function and the input current noise of the second prototype of the photodetector are presented in this subsection. The photodetector was operated with the GAP1000Q photodetector from GPD, see Section 4.2.

4.3.3.1 Power consumption

The power consumption was measured with a multimeter. The multimeter was connected between the power supply and the photodetector to measure the current flow. This was done without laser light and with amplitude modulated (20 MHz) laser light impinging on the photodiode. The results are summarised in Table 4.6, which includes the values calculated with LT Spice IV. Without light shining on the photodiode the measured power consumption was almost identical to the one calculated with LT Spice IV. With laser light on the photodiode the power consumption was almost doubled. The current on the +15 V supply did not change, but the current on the other voltage supplies did. The +5 V increased because the photodiode was irradiated. The ± 15 V supply was connected to the OpAmp of the DC output, which had a signal of around -10 V at its output. This explains why this OpAmp only increases the -15 V current. The ± 5 V supply line was connected to the OpAmp of the AC output. It had a 20 MHz sinusoidal signal without an offset at its output. That is the reason, why it increased both supply currents. The LT Spice IV simulation had a signal source, too. This means that LT Spice IV does not calculate the power consumption of OpAmps properly.

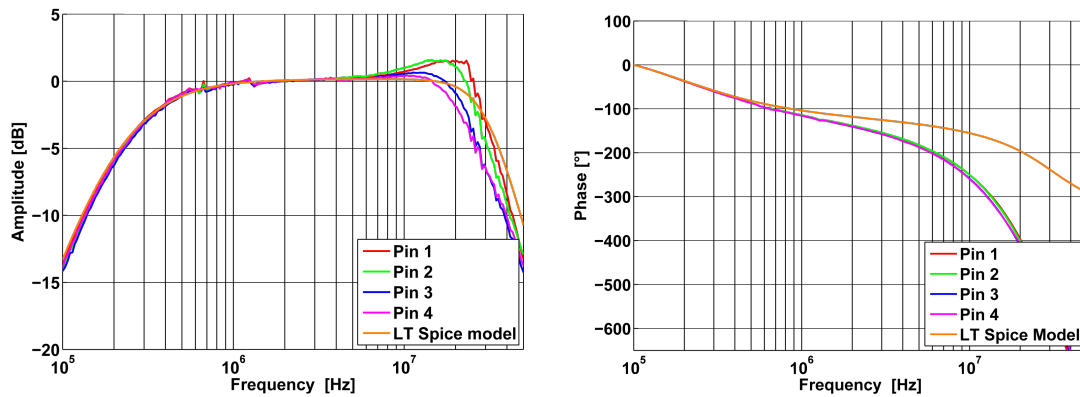
4.3.3.2 Transfer function

The spectrum analyser 4396B from Agilent was used to obtain transfer functions [85]. The light source was a so-called photodiode tester, which is available at the AEI. It consisted of a laser diode ($\lambda=1060$ nm) and modulation electronics, which can modulate the amplitude of the laser light from a few kHz up to 500 MHz.

The second prototype of the quadrant photodetector was designed upon the knowledge that has been gained during the investigations on the first prototype, see Subsection 4.3.2. The AC transfer functions of the second prototype are shown in Figure 4.17. The amplitude responses of the four channels were identical up to 10 MHz. Above 10 MHz the

Table 4.6: Power consumption of the four channel TIA based on the BFR181 and GAP1000Q photodiodes.

Supply [V]	LT SPICE IV		No light on PD		Light on PD	
	Current [mA]	Power [mW]	Current [mA]	Power [mW]	Current [mA]	Power [mW]
15	12.2	183.0	12.0	180.0	12.2	183.0
5	4.4	22.0	1.5	7.5	12.3	61.5
0	(0)	0	-10.6	0.0	-2.9	0.0
-5	-1.6	8.0	-1.5	7.5	-7.0	35.0
-15	-1.8	27.0	-1.5	22.5	-7.0	105.0
Sum		217.5		240.0		384.5



(a) Amplitude response.

(b) Phase response.

Figure 4.19: Transfer function of the GAP1000Q photodiode with 1 mm diameter and the BFR181 transistor as TIA. Version 2.

amplitude responses of channel 1 and 2, and channel 3 and 4 were almost identical. This was due to the fact that these channels were located on the same PCB. The comparison to the LT Spice model indicated that Channel 1 and 2 had a lower impedance than in the simulation. Channel 3 and 4 had a higher impedance than in the LT Spice model. Thus the difference in the amplitude response can be suppressed by modifying the transistor stages of two channels on the same PCB. Therefore the difference in the amplitude response was believed to be uncritical. The phase responses of the four channels were identical in the whole frequency range. The difference of the phase responses of the four channels to the LT Spice model was introduced by a missing calibration of the phase response of the photodiode tester.

Thus the second prototype is an excellent basis for a quadrant photodetector for testing of the LOB.

4.3.3.3 Input current noise

The input current noise n_{el} of a TIA was measured indirectly via the output voltage of the TIA. Here, this procedure is described briefly. More details can be found in [87, pp. 58] and [109]. A key point of this measurement procedure is the availability of

a shot-noise limited light source. Usually this a light bulb, whose spectrum is assumed to be shot noise limited in the frequency range between 1 MHz and 20 MHz. First, the output voltage noise v_{sn} of the AC output of the TIA is measured while the light bulb is shining on the photodiode. In this case the output voltage is given by the AC gain of the photodetector $g(f)$ times the uncorrelated sum of shot noise n_{shot} induced by the light bulb and the input current noise n_{el} of the TIA

$$v_{\text{sn}} = g(f) \cdot \sqrt{n_{\text{shot}}(f)^2 + n_{\text{el}}(f)^2} \quad (4.28)$$

The output voltage of the DC part during the measurement is written down and is required in a later step. The output voltage noise v_{el} is measured with no light shining on the photodiode to eliminate the dependency of $g(f)$

$$v_{\text{el}} = g(f) \cdot n_{\text{el}}(f) \quad (4.29)$$

The combination of the last two equations leads to the input current noise n_{el} of the TIA

$$n_{\text{el}}(f) = \frac{n_{\text{shot}}(f)}{\sqrt{\left[\left(\frac{v_{\text{sn}}(f)}{v_{\text{el}}(f)}\right)^2 - 1\right]}} \quad (4.30)$$

The shot noise n_{shot} can be calculated from the measured DC current induced by the light bulb

$$n_{\text{shot}}(f) = \sqrt{2e \frac{U_{\text{DC}}}{R}} \quad (4.31)$$

whereby R is the transimpedance gain of the DC part of the TIA.

Figure 4.20 presents the measurement of the output power noise levels and the calculated input current noise. The output noise is shown in Figure 4.20(a). The lower curve shows the noise level of the spectrum analyser. The four dashed curves above show the output power noise equivalent to v_{el} of the four AC-channels of the photodetector without light on the photodiode. The four curves at the top are the equivalent output power noise of v_{sn} with a light bulb shining on the photodiode. The input current noise n_{el} of the four AC-channels of the photodetector is shown in Figure 4.20(b). The PCBs of the TIAs were not shielded. Thus the spikes at 10 MHz and 16 MHz, which have been identified to be electro-magnetic pick-up from frequency generators in the laboratory, are expected to vanish when the PCBs are properly shielded. The input current noise n_{el} of the four channels were of the same shape and below the goal for the input current noise up to 25 MHz. The comparison to the LT Spice model showed no significant differences.

4.4 Conclusions

In this chapter the electro-optical chain of an interferometer on the LOB was introduced and explained in great detail with special focus on the development of a quadrant photodetector. The quadrant photodiode and the TIA were individually investigated.

The properties of p-i-n photodiodes and different semiconductor materials were explained briefly. Calculations on the bandwidth of silicon and InGaAs photodiodes indicated that the bandwidth of silicon photodiodes with a responsivity comparable to

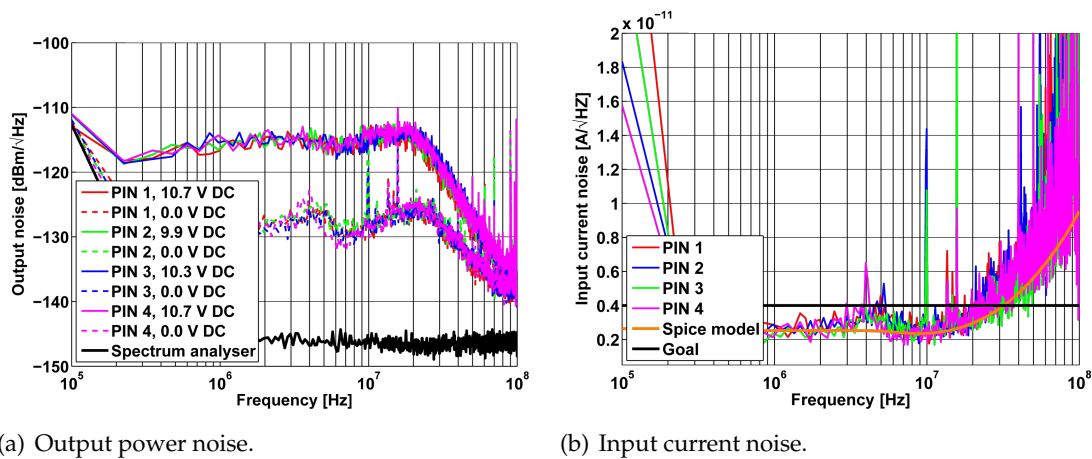


Figure 4.20: Noise of the GAP1000Q photodiode with 1 mm diameter and the BFR181 transistor as TIA.

InGaAs photodiodes are electron transit-time limited. The bandwidth of InGaAs photodiodes are RC -time constant limited with respect to the LISA beat note range. Silicon quadrant photodiodes which are comparable to InGaAs quadrant photodiodes in their low frequency responsivity have been presented. The measurement of the responsivity as a function of frequency revealed that the silicon photodiode QP22-Q from First Sensor has a responsivity of 0.45 A/W at 30 MHz with a bias voltage of 150 V. Thus the QP22-Q photodiode is incompatible with the requirements of the science interferometer in LISA. This outcome is also valid for the other mentioned silicon photodiodes, because they share the principle of operation which limits their responsivity for frequencies above 10 MHz.

It was theoretically shown that the optical pathlength read-out in the science interferometer using APDs is increased due to shot noise. This is because the amplification of noise within an APD is higher than the amplification of the signal. A comparison of the different p-i-n photodiode types showed that InGaAs p-i-n quadrant photodiodes are optimal for the science interferometer with LISA. Thus this type of photodiode is best for the other interferometers, because the quadrant photodetectors in the interferometers should be identical with respect to the used technologies. Among several InGaAs photodiodes the GAP1000Q photodiode was selected for testing the LOB, because it had the best properties of COTS photodiodes with respect to the photodiode requirements.

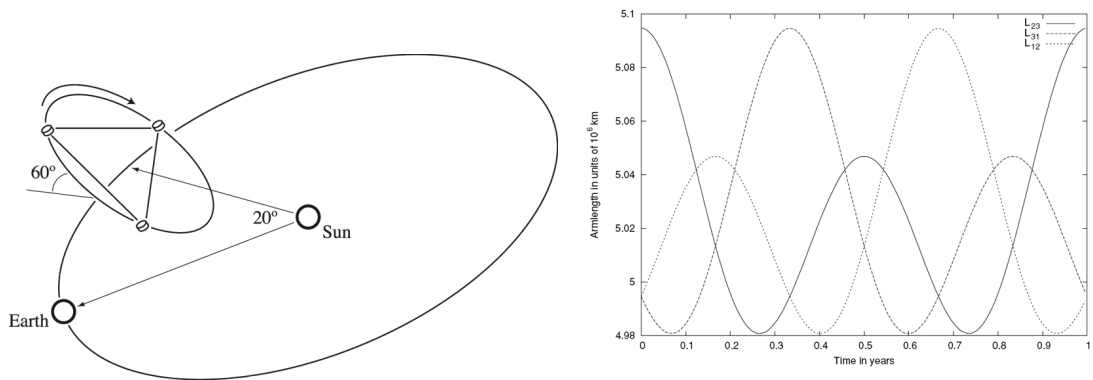
A simple model of a TIA has been introduced to motivate important parameters of a TIA for a LISA photodetector. It was shown that the input voltage noise of a TIA of a LISA photodetector is as important as its input current noise for the optical pathlength read-out limit due to its amplification by the noise gain, which in turn depends on the photodiode capacitance. Furthermore, it was described why the impedance of a LISA photodiode is important for the optical pathlength read-out limit due to electronic noise and for the bandwidth of a LISA photodetector. A quadrant photodetector, which is compatible with the stringent dimension requirements of the LOB was developed. Its measured power consumption was approximately 380 mW. The -3 dB bandwidth of all four channels was at least 20 MHz. The input current noise of all four channels was below the requirement of $4 \text{ pA}/\sqrt{\text{Hz}}$ up to 25 MHz.

The backlink connection of the two OBs within a single LISA satellite is one of the key technologies within the current LISA baseline design. Therefore the necessity of a backlink path within the current LISA baseline design is motivated in the introduction of this chapter and it is put into the context to other LISA baseline designs. This is followed by a summary of the investigations that have been performed at the AEI on optical fibres for the backlink path. Afterwards a closer look on their results is taken and their impact on current and new implementations of the backlink path is considered. In the end the proposed solutions for the backlink connection are compared and the most promising ones are recommended for further investigations. For these, possible technology demonstrator experiments are described.

5.1 Introduction

The triangular shape of the planned space-based gravitational-wave detector LISA is shown in Figure 5.1(a). This constellation is achieved by placing the three spacecraft in individual Earth-like Keplerian orbits in an orbital plane which is inclined by an angle of 60° to the ecliptic. In that plane the three satellites are placed as an equilateral triangle with an armlength of 5 (original LISA) or 1 (reduced eLISA) million km. The whole constellation is placed about 20° (about 50 million km) behind the Earth. The result is that the whole constellation follows the Earth with a counter-clockwise cartwheel motion. Figure 5.1(b) shows the time series of the armlengths for each of the LISA arms for the period of one year. The armlengths are not constant and are changing independently from each other. The reasons for the non-common mode armlength changes within the constellation are the “external perturbations of Jupiter and Venus and the secular effect due to the Earth’s gravitational field” [23]. The important impacts of the non-common mode armlength changes on the design of LISA will be explained now.

Length measurements performed with an unequal armlength interferometer are influenced by laser frequency noise [6, pp. 154]. The armlength mismatch within the LISA constellation is up to 10^5 km. A stabilised Nd:YAG laser with a frequency noise of $30 \text{ Hz}/\sqrt{\text{Hz}}$ in the LMB increases the measurable optical pathlength to a level of $10 \mu\text{m}\sqrt{\text{Hz}}$ [61, pp. 13]. This is six orders of magnitudes above the target single-link noise budget of



(a) Sketch of the LISA orbits. The orbits of the individual satellites are chosen in a way that the three LISA satellites form a triangle. Thereby the whole constellation follows the Earth with a counter-clockwise cartwheel motion [123].

(b) Time series of the three armlengths of the LISA constellation. The difference between the armlengths is up to 10^5 km [23].

Figure 5.1: Depiction of the orbits for the LISA satellites and their effect on the stability of the constellation.

around $12 \text{ pm}/\sqrt{\text{Hz}}$ [14, pp. 21]. To overcome this problem the Time Delay Interferometry (TDI) algorithm was implemented in the data post-processing chain of the LISA baseline design [124]. The key part of it synthesizes equal armlengths in data post-processing and thereby suppresses the influence of the laser frequency noise due to the armlength mismatch below the required level. A key part of this suppression method is the knowledge of the differential phase noise between the TX lasers within one satellite.

The calculation of the phase difference between the two TX lasers within a single satellite via individual measurements of the laser's phases is technically not possible due to the THz frequencies of the lasers. Therefore the TX lasers are compared via heterodyne interferometry to extract the differential phase information. The breathing of the armlengths of the LISA constellation results also in a change of the angles within the LISA constellation up to $\pm 1.5^\circ$ [1, pp. 88]. Therefore the beam directions of the RX beams would change significantly in the reference coordinate system of TX beams during operation. An angular mismatch between the RX and the TX beams within the science interferometer in the order of a degree results in a complete loss of heterodyne efficiency and therefore loss of the link.

One approach for solving this problem is the so-called in-field pointing [125, 126]. Figure 5.2 shows three different realisations of in-field pointing all sharing a non-movable optical subassembly. Therefore the telescopes have to be designed with a Field of View (FOV) which is compatible to the angular deviations of the constellation. The change of the RX beam angle is compensated by mounting a mirror on an ultra-stable actuator which is located on the OB as a part of the telescope optics. The displacement noise of the reflective mirror surface has to be at least one order of magnitude below the shot noise limited optical pathlength read-out requirement of the science interferometer, which is about $9 \text{ pm}/\sqrt{\text{Hz}}$. This will lead to a negligible error contribution to the optical pathlength read-out noise budget of the science interferometer. The pointing range and stability of the actuator are also critical because angular changes of the beam are magnified with the telescope magnification at the mirror surface. The result is a required alignment range of $\pm 2.5^\circ$ for the actuator when the constellation angle changes by $\pm 0.8^\circ$ [125]. The technical design of an actuator with an actuation range of $\pm 2.5^\circ$ and

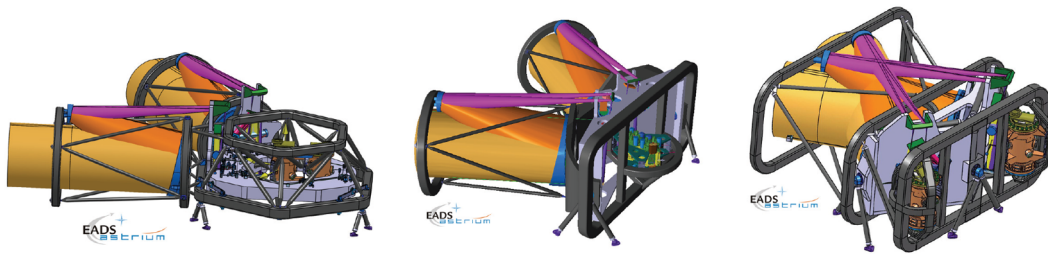


Figure 5.2: Three different implementations of the in-field pointing concept for LISA. The telescopes and optical bench(es) are not movable within this concept. Therefore it relies strongly on the pointing range and length stability of an actuator within the telescope optics. This compensates the beam pointing range on the OB introduced by angle fluctuations within the LISA constellation [125].

a displacement stability for the reflective surface in a range of a few $\text{pm}/\sqrt{\text{Hz}}$ in the LMB was demonstrated in [126]. Its design would be comparable to the PAAM, the performance of which was verified at the AEI [49]. The actuation range of the PAAM is $\pm 824 \mu\text{rad}$, orders of magnitudes smaller than the actuation range needed for in-field pointing. Furthermore, the PAAM has to change its alignment stepwise every few days, while the in-field pointing mechanism has to change its alignment continually. Therefore experimental demonstration of the in-field pointing actuator performance is crucial and is believed to be critical in the LISA community. The advantage of this concept is that both telescopes on one satellite can be connected via one large OB made of ZerodurTM and the TX beams can be directly compared on the stable OB.

The second approach to cope with the breathing of the LISA constellation is the “optical assembly pointing”, see Figure 5.3. This foresees two separated MOSA in one satellite, such that each MOSA rotates around its pivot axis to follow the angular deviation of the constellation. This results in a negligible beam tilt of the RX beams on the OBs. In contrast to the in-field pointing solution the MOSA solution cannot be realised with a single OB because the OB needs to be rigidly connected to the telescope to suppress beam pointing noise on the OB. Both MOSAs on one satellite need to be independent. Therefore the beam pointing problem has been moved from the telescope to the LO beam, which is exchanged between the two OBs. The advantage is that the required stability of this exchange path is in first order irrelevant because a common mode optical pathlength change of that path will cancel out in data post-processing [124]. Only the non-common mode optical pathlength changes in both directions between the OBs is of concern. This is often called non-reciprocity.

The implementation of an exchange path between the two OBs with a stable beam direction and a negligible non-reciprocity can be realised via a free beam link or a fibre link. The free beam solution needs movable mirrors to steer the beams between the OBs and to keep the LO beam direction stable on the opposite OB. In comparison to that, the fibre link does not need actuators. The light from the OB is coupled into the fibre via a fibre interface rigidly connected to the OB. The light propagation properties of the optical fibre preserve the light properties until the second fibre interface which is also rigidly connected to the second OB. The fibre link between the two OBs was thought to be much simpler than the actuator link. Therefore so far experimental investigations have concentrated on the fibre solution for the backlink path.

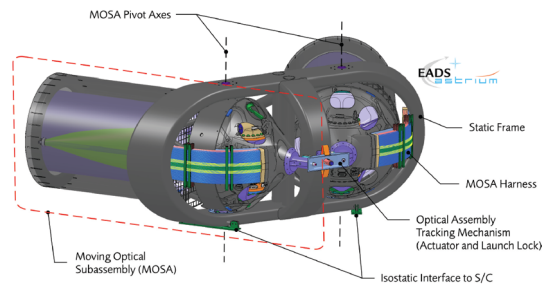


Figure 5.3: Implementation of the compensation of the constellation breathing via MOSA. Both MOSA rotate around their pivot axes to track the opposite satellites with the telescopes and keep the beam pointing on the OB below a negligible level [14, p. 11].

5.2 Previous work

The realisation of the backlink path via a fibre was studied in great detail at the AEI. The author worked with Roland Fleddermann on the so-called backlink fibre experiment. The author started to work on this experiment in April 2008 after the experimental setup was already build by Roland Fleddermann and Frank Steier until the end of 2009. Within the before mentioned time frame the most important discoveries have been made at the backlink fibre experiment which are documented in [19, pp. 5]. In 2010 the measurement scheme of the backlink fibre experiment was changed by Roland Fleddermann in collaboration with Danielle Wuchenich from the Australian National University (ANU) from the LTP modulation scheme to Digital Interferometry (DI), see [19, pp. 91].

The backlink fibre experiment focused on the effects of the fibre link solution on the LISA heterodyne measurement scheme and an estimation of the non-reciprocity of the fibre under test. It revealed that the heterodyne measurement scheme suffers by backreflection from the fibre under test. It effectively appears like harmful optical pathlength non-reciprocity in the data. On these grounds a dedicated spin-off experiment was carried out to measure and characterise the backreflection from different fibres. Its results are documented briefly in [19, pp. 83] and in more detail in [127]. The starting point of the investigations in this thesis is a recapitulation of the most important results of the experiments performed in the aforementioned references.

Figure 5.4 shows a schematic of the setup of the AEI backlink fibre experiment. Its assembly process is documented in [12, pp. 63]. The design aimed for the similarity to the interferometer onboard the LISA satellites but was slightly changed to serve its particular test purpose. In contrast to LISA the two backlink fibre interferometers are located on a single ZerodurTM baseplate. This was required to implement a (direct) reference interferometer DR which compares the lasers directly. The difference of the interferometer DR and the comparison of the two lasers via the backlink path yields the non-reciprocity of the fibre under test [19, pp. 14]. Additionally the direct reference interferometer was needed to be able to use the LPF modulation scheme and suppress sideband induced phase noise within the phasemeter [37]. The path called “setup noise” was normally blocked. It could be used to measure the noise of the measurement setup without the fibre by blocking the fibre backlink path and unblocking the setup noise path. If the beam splitter labelled “4” in Figure 5.4 is replaced by a High Reflectivity (HR) mirror the similarity to a free beam implementation of the backlink path is visible. Thus the backlink fibre experiment could also be used to make some statement about the

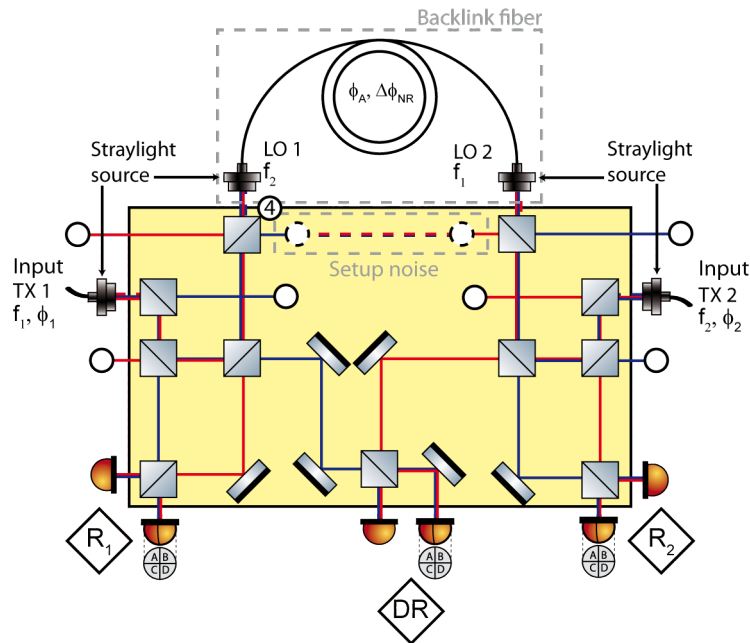
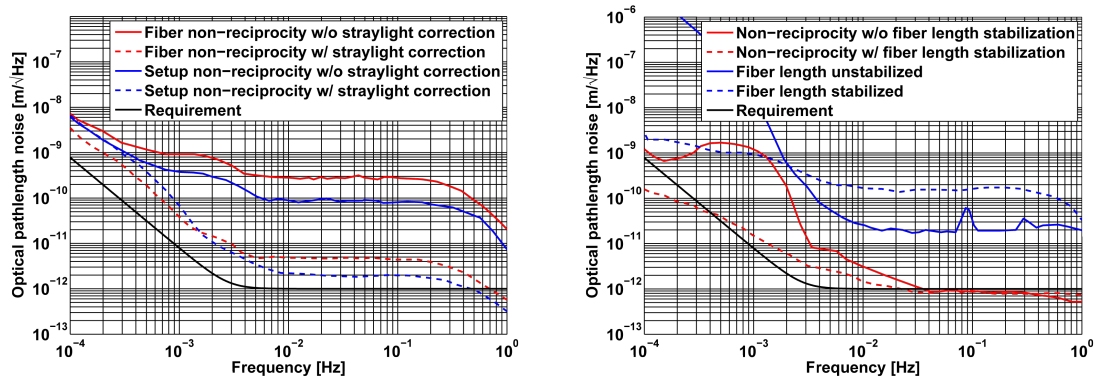


Figure 5.4: Layout of the backlink fibre setup. The TX laser 1 and 2 are guided from the MB to the setup. Their phase is compared directly in the direct reference interferometer DR. The light from the TX laser 1 and 2 is exchanged via the backlink path and is then called LO 1 and 2. The two reference interferometers are then used to derive the indirect comparison of the two TX laser.

backlink free beam.

Figure 5.5(a) compares the non-reciprocal optical pathlength noise of a polarisation-maintaining fibre to the equivalent “non-reciprocity” of only the measurement setup. Thereby the individual non-reciprocal optical pathlength noise are shown without and with straylight correction by balanced heterodyne detection [128] [12, pp. 52] [19, pp. 62]. The LSD of the straylight influence has a shoulder shaped envelope which is comparable to the one of the OPD induced noise [37]. For comparison see Figure 2.16(a) on page 20. The non-reciprocity of the fibre without straylight correction was at a level of $300 \text{ pm}/\sqrt{\text{Hz}}$ in the frequency range between 10 mHz and 200 mHz. In the same measurement the setup has shown a noise level of $88 \text{ pm}/\sqrt{\text{Hz}}$. With straylight correction via balanced detection the non-reciprocity of the fibre was measured at a level of $5 \text{ pm}/\sqrt{\text{Hz}}$ in the same frequency range as before and the noise of the measurement setup was at a level of $2 \text{ pm}/\sqrt{\text{Hz}}$. An important conclusion from this result is that even with straylight correction the non-reciprocity of the fibre and the setup could not be measured below the requirements.

Figure 5.5(b) presents the measurements of the optical pathlength noise of the fibre lengths without and with fibre length stabilisation. During the measurements the active stabilisations for the OPD, the laser intensity at low frequencies and for the laser frequency were used. In data post-processing straylight was subtracted and DWS was used to suppress the influence of beam pointing noise. Without the stabilisation of the fibre length the optical pathlength noise of the fibre was at a level of $20 \text{ pm}/\sqrt{\text{Hz}}$ at 1 Hz and increased with a $1/f^2$ at frequencies below 10 mHz. With the fibre stabilisation turned on the optical pathlength noise was below $200 \text{ pm}/\sqrt{\text{Hz}}$ at 200 mHz and increased with a $1/\sqrt{f}$ at frequencies below 10 mHz. The stability of the fibre is worse at high frequencies



(a) Comparison of the non-reciprocal optical pathlength noise of a polarisation maintaining fibre and of the according measurement setup without and with straylight correction [19, p. 78, p. 80].

(b) Comparison of the non-reciprocal optical pathlength noise of a polarisation maintaining fibre without and with fibre length stabilisation. The optical pathlength noise of the fibre is also plotted for both measurements [19, p. 61].

Figure 5.5: Measurements of the optical pathlength and the non-reciprocity of a single-mode polarisation maintaining fibre taken from [19].

with stabilisation. The noise source for this is thought to be the analog circuit that was used for the stabilisation. It is similar to the OPD stabilisation. The optical pathlength stability with a running OPD stabilisation can be seen in Figure 2.16(b) on page 20. At high frequencies it is at a level of $6 \text{ nm}/\sqrt{\text{Hz}}$. The difference between the picometer experiment and the backlink fibre experiment is the heterodyne frequency. For the first it was 1.624 kHz and for the second 17.859 kHz. Thus the OPD stabilisation at the backlink fibre experiment can achieve a higher bandwidth and therefore a better suppression of noise in the measurement band. Figure 5.5(b) also shows the simultaneously measured non-reciprocity with and without fibre length stabilisation. The non-reciprocal noise of the fibre for frequencies below 30 mHz can be significantly suppressed by stabilising the fibre length. Thus the sideband induced noise of the LTP modulation scheme is hence considered a likely source of the non-reciprocal noise of the fibre at low frequencies.

Figure 5.6 illustrates the composition of the backreflection of a fibre. Backreflection is not dominantly generated at a certain point of a fibre. Most of the backreflection is continuously and constantly generated over the length of a fibre. A smaller portion is generated at the front surface of a fibre.

Figure 5.4 depicts the locations of the straylight sources for this kind of implementation of the backlink path of the optical assembly pointing. The fibre interfaces and the fibre itself of the backlink fibre and the TX lasers generate straylight. If the backlink fibre is replaced by a free beam backlink, the fibre interfaces and the fibres of the TX lasers will still generate straylight.

A backlink fibre experiment of the second generation based on the research at the AEI was planned in 2011 at UGL [129, pp. 16]. The main differences are the usage of monolithic fibre couplers instead of metallic, adjustable ones to suppress the influence of beam pointing on the non-reciprocity and the usage of the OB at one end of the backlink fibre. Due to time constraints at UGL this experiment was not started so far.

Although the measurement of the non-reciprocity of the fibre under test yields in the end to a result that is close to the requirement, there are still open questions. These questions are:

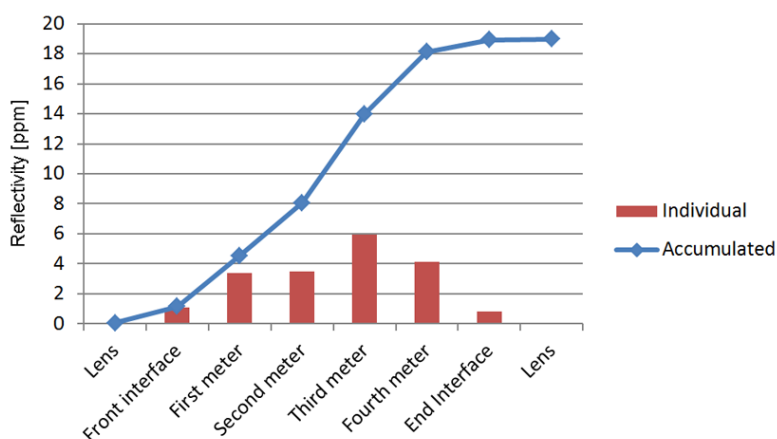


Figure 5.6: Composition of the backreflection of a polarisation-maintaining single-mode fibre [19, p. 88].

- what are the limitations of the balanced detection to suppress straylight?
- are there different ways to measure or suppress straylight?
- do straylight free solutions for the backlink path exist?
- does the beam pointing correction still need to be done using monolithic fibre couplers?
- is length stabilisation of the backlink fibre required when using the LISA measurement scheme?
- what happens to the non-reciprocity if the backlink fibre is moved during the measurement?

5.3 Straylight degraded backlink path

Straylight degraded length measurements are a fundamental problem within the current LISA measurement scheme. This is not really surprising since straylight has been identified as limiting noise source in many precision interferometers before fundamental noise limits are reached [130, 131]. This section explains the influence of straylight and presents techniques to suppress it.

5.3.1 Straylight influence

Figure 5.7 illustrates the influence of straylight within a heterodyne interferometer and its suppression by balanced detection. The upper left part (a) of this picture explicitly shows the according beams at a beam combiner. The combination of the straylight with one of the measurement beams has occurred before the beam combiner and the straylight beat signal is entering only via one port of the beam combiner. Thus it has the same phase at both output ports, in contrast to the main beat note which - due to energy conservation - exits at both ports of the beam combiner with opposite signs as shown in Figure 5.7 (d). Figure 5.7 (b) shows the according complex amplitude of the beat note in the complex plane at one output of the beam combiner. The complex amplitude is composed of the

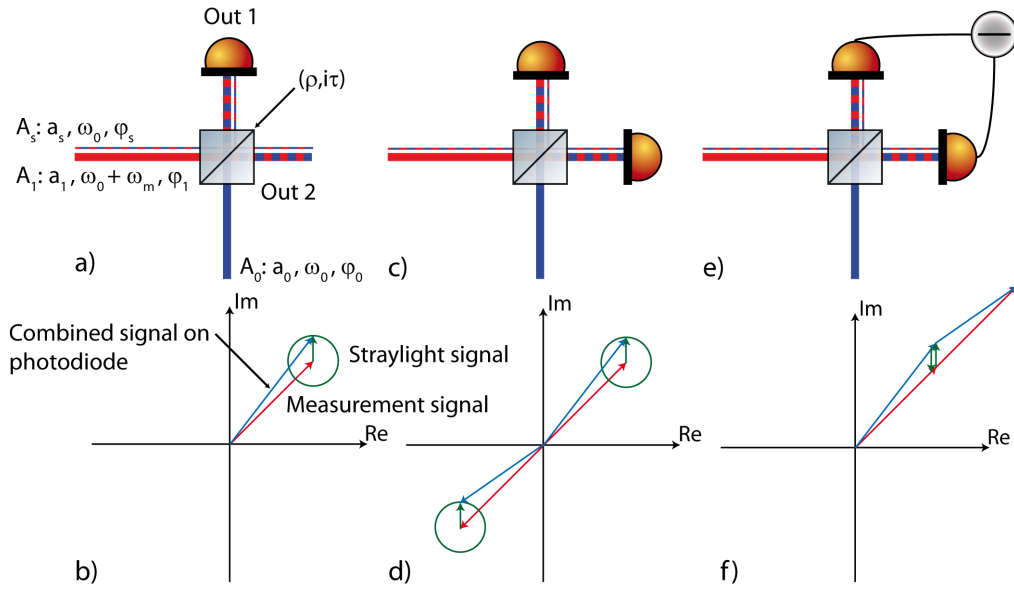


Figure 5.7: Influence of straylight on a MS within a heterodyne interferometer and its correction by balanced detection. The upper part illustrates the optical signals within the setup and the lower part the process within the phase measurement system to reduce the influence of straylight by balanced detection.

Measurement Signal (MS) and the StrayLight Signal (SLS). It is a good assumption that the complex amplitude of the MS is relatively stable in comparison to the one of the SLS. In this picture the complex amplitude of the SLS rotates around the end point of the complex amplitude of the MS.

The complex amplitudes of the SLS A_s and the MSs $A_{0,1}$ at the input of the beam combiner as shown in Figure 5.7 (a) can be written to calculate the influence of the straylight onto the MS,

$$A_s = a_s \cdot e^{i(\omega_0 t + \phi_s)} \quad (5.1)$$

$$A_0 = a_0 \cdot e^{i(\omega_0 t + \phi_0)} \quad (5.2)$$

$$A_1 = a_1 \cdot e^{i[(\omega_0 + \omega_m)t + \phi_1]} \quad (5.3)$$

a_s is the magnitude and ϕ_s is the phase of the SLS. $a_{1,2}$ are the magnitudes and $\phi_{0,1}$ are the phases of the MSs. ω_0 is the base frequency and ω_m the modulation frequency of the heterodyne interferometer. The base frequency ω_0 is neglected in the following because it is common to all signals. The beam combiner has a power reflectivity of R (amplitude reflectivity of ρ) and a power transmission of T (amplitude transmission of τ),

$$R + T = 1 \Leftrightarrow \rho^2 + \tau^2 = 1 \quad (5.4)$$

assuming that the loss in standard optics is almost zero. The complex amplitudes at both output ports $A_{O1,2}$ of the beam combiner can be inscribed as:

$$A_{O1} = \rho(A_s + A_1) + i\tau A_0|_{\omega_m t} \quad (5.5)$$

$$= \rho \left(a_s \cdot e^{i\phi_s} + a_1 \cdot e^{i(\omega_m t + \phi_1)} \right) + i\tau \cdot a_0 \cdot e^{i\phi_0} \quad (5.6)$$

$$A_{O2} = i\tau(A_s + A_1) + \rho A_0|_{\omega_m t} \quad (5.7)$$

$$= i\tau \left(a_s \cdot e^{i\phi_s} + a_1 \cdot e^{i(\omega_m t + \phi_1)} \right) + \rho \cdot a_0 \cdot e^{i\phi_0} \quad (5.8)$$

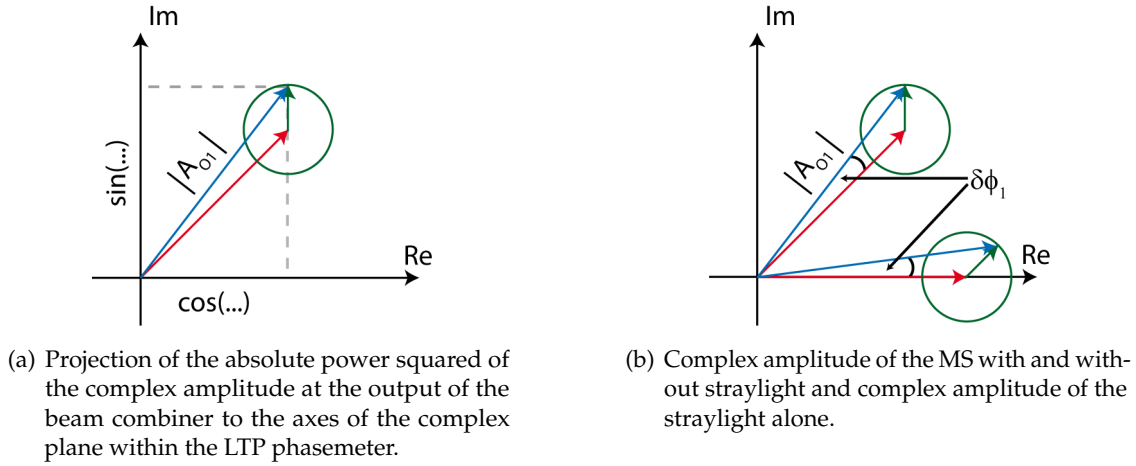


Figure 5.8: Schematics for the calculation of the influence of straylight onto the phase measurement with the LTP phasemeter.

The absolute values squared of the amplitudes or the powers at both output ports of the beam combiner at the angular frequency ω_m (neglecting the DC signal content) are

$$|A_{O1}| = A_{O1} \cdot A_{O1}^* \quad (5.9)$$

$$= 2\rho^2 a_s a_1 \cos(\omega_m t + \phi_1 - \phi_s) + 2\tau \rho a_0 a_1 \sin(\omega_m t + \phi_1 - \phi_0) \quad (5.10)$$

$$|A_{O2}| = A_{O2} \cdot A_{O2}^* \quad (5.11)$$

$$= 2\tau^2 a_s a_1 \cos(\omega_m t + \phi_1 - \phi_s) + 2\tau \rho a_0 a_1 \sin(\omega_m t + \phi_1 - \phi_0) \quad (5.12)$$

The influence of the straylight magnitude a_s onto the measurement phase ϕ at the output port number 1 of the beam combiner within in the LTP phasemeter is calculated now. The calculations for the output port number 2 are identical. A Mathematica script has been written in cooperation with Gerhard Heinzl to avoid several pages of algebraic conversion using trigonometric identities, see Appendix 2. First, from the complex amplitudes at the input of the beam combiner the script calculates the complex amplitudes at the output port number 1 of the beam combiner (Equations 5.6 to 5.8). Afterwards the absolute values squared of the complex amplitudes or the powers at the outputs of the beam combiner are calculated and the signal content at the angular frequency ω_m is extracted (Equations 5.10 to 5.12). So far, these calculations were presented in the last paragraphs. In a next step the sum and differences in the arguments of the cosine and sine in $|A_{O1}|$ are resolved via trigonometric expansion into cosine and sine functions with a single argument. This is done to be able to calculate the real and imaginary part of the complex amplitude of this expression according to the LTP phasemeter procedure. Thus the content of this expression is sorted by sine and cosine elements with arguments $\omega_m t$. The phase reference in LTP phasemeter has the same angular frequency ω_m . Therefore this signal content of the sorted arguments is set to zero in a next step and the expanded sine and cosine arguments are simplified again. The LTP phasemeter combines the sine and cosine elements to the magnitude and phase of a complex amplitude, see Figure 5.8(a).

The complex amplitude without straylight is obtained by setting the straylight magnitude a_s zero. The difference between the two complex amplitudes in the complex plane is the influence of straylight, see Figure 5.8(b). Afterwards the phase behaviour of the

straylight influence is calculated. Due to its complexity it is developed in a Taylor series around the straylight magnitude a_s around zero to first order. This is valid because the straylight magnitude is generated by backreflection of the fibre which is of the order of 20 ppm in power, corresponding to $4.5 \cdot 10^{-3}$ in amplitude, see Figure 5.6. Thus the straylight magnitude a_s is at least one order of magnitude lower than the measurement beam magnitude a_1 . This expression is simplified once more and the result is the influence of the straylight magnitude a_s on the measurement phase, called $\delta\phi_1$

$$\delta\phi_1 \approx -\frac{\rho a_s}{\tau a_0} \cdot \cos(\phi_0 - \phi_s) \quad (5.13)$$

Two conclusions arise from Equation 5.13. First and most importantly the influence of straylight on the measurement phase is proportional to the ratio between straylight beam magnitude a_s and measurement beam magnitude a_0 . The second conclusion is that the straylight influence is only arising if the straylight source (ϕ_s) is moving with respect to the reference system (ϕ_0).

Equation 5.13 will be used to derive the equation for the case, when straylight enters via both input ports of a beam combiner. This was the case at the backlink fibre experiment during the measurements of the fibre non-reciprocity. According to Figure 5.7 (a) the straylight is added via the lower input port of the beam combiner. Its complex amplitude at the lower input port is described as

$$A_t = a_t \cdot e^{i[(\omega_0 + \omega_m)t + \phi_t]} \quad (5.14)$$

Furthermore, it is assumed that the magnitude a_t equals the magnitude a_s . This is a good approximation for the backlink fibre experiment because the backlink fibre was of approximately the same length as the fibres from the MB. Thus their level of backreflection (straylight) was almost identical. At the output port of the beam combiner the complex amplitudes A_t and A_s generate a beat signal at the angular frequency ω_m . The magnitude of both amplitudes is $4.5 \cdot 10^{-3}$. Thus the magnitude of this SLS is small compared to the magnitudes of the first order SLSs which were generated by combining the straylight amplitudes and the MS amplitudes. Therefore it is neglected in the following. The aforementioned Mathematica script was used to derive the degradation of the measurement phase, called $\delta\phi_2$, when straylight enters via both input ports of a beam combiner. It is given by

$$\delta\phi_2 \approx \frac{\tau a_s}{\rho a_1} \cos(\phi_1 - \phi_t) - \frac{\rho a_s}{\tau a_0} \cos(\phi_0 - \phi_s) \quad (5.15)$$

Two additional conclusions can be drawn, when straylight enters with identical amplitudes via both inputs of a beam combiner, in addition to the conclusions from Equation 5.13. First, the influence of straylight onto the measurement phase is increased at worst by a factor of two. Second, the influence of straylight can vanish if the phases of the straylight amplitudes compensate the straylight amplitude of their sum.

In the following the influence of a changing straylight phase onto the measurement phase is discussed briefly. It will be analysed in more detail in Subsection 5.3.2.2. The investigations presented in [127] show that most of the straylight within the backlink fibre experiment was generated continuously inside the fibre core. A smaller amount of straylight was created at the fibre interface and is neglected in this consideration. Therefore the straylight magnitude is the sum of the backreflection within the fibre and the straylight phase is the mean length of the fibre. A time series of the relevant fibre length is needed to calculate the influence of straylight onto the measurement phase

from Equation 5.13. The absolute value of the noise shape is given by the ratio of the SLS magnitude to the MS magnitude. Assuming that the fibre length is changed by $20 \mu\text{m}$ at 0.1 mHz , the straylight vector is rotating 20 times around the measurement vector. Therefore the measured straylight frequency is increasing up to 2 mHz (upconversion). In Subsection 5.3.2.2 time series of the lengths of the backlink fibre and the MB bench fibres will be used to generate straylight noise spectra for the backlink fibre experiment and for a possible implementation of the LOB. These spectra are compared to the measured noise spectra at the backlink fibre experiment.

5.3.2 Suppression of straylight

This subsection introduces techniques for the suppression of straylight onboard the LISA satellites, which have been described in [19, pp. 109]. The focus is put on the mathematical description of these techniques and the development of new aspects of the straylight suppression.

5.3.2.1 Balanced detection

Balanced detection is one solution to overcome the problem of straylight. Figures 5.7 (a) - (b) show the influence of straylight on the measurement beam. The magnitude and phase of the MS (red arrow) are superimposed with the magnitude and phase of the SLS (green arrow) to produce a combined signal on the photodiode (blue arrow). Figures 5.7 (c)-(d) describe the situation for both beam combiner outputs. The second output of the beam combiner is identical to the first port except for a small but important difference since straylight has already interfered with one of the measurement beam before the beam combiner. Thus at the beam combiner the straylight is split in power. The phase difference of the straylight is 0 , whereas the phase difference of the non-straylight light is π due to energy conservation at the beam combiner. Thus straylight will cancel when the phases of the two output ports are subtracted, see Figures 5.7 (e)-(f).

As described in [12, pp. 55] the main limitation of the balanced detection scheme is the asymmetry of the detection of the straylight magnitude through a non-ideal 50/50 beam combiner. The other asymmetries like photodiode efficiency, transimpedance gain, *etc.* will cancel when the complex amplitudes $|A_{O1}|$ and $|A_{O2}|$ are normalised. The measured complex amplitudes of the MSs can be normalised in data-post processing by just neglecting their magnitude. The influence of the splitting ratio of a beam combiner can be compensated by changing the magnitude of one normalised MS from 1 in small steps towards lower and higher values. For each step the spectrum of the straylight corrected length measurement is calculated. The right beam splitting ratio has been found when the spectrum of the length measurement is minimal in the frequency range where straylight normally degrades the spectrum.

The same calculation that has been performed for the straylight influence onto the measurement phase in Subsection 5.3.1 can be performed for the balanced detection assuming an amplitude splitting ratio of the beam combiner of ρ and τ , whereby $\rho^2 + \tau^2$ equals 1. With balanced heterodyne detection the influence of straylight onto the measurement phase with straylight entering via one input port of a beam combiner is

$$\Delta\phi_1 \approx \frac{a_s}{a_0} \cdot \cos(\phi_0 - \phi_s) \cdot \frac{\tau^2 - \rho^2}{2\rho\tau} \quad (5.16)$$

whereas the influence of straylight onto the measurement phase with straylight enter-

Table 5.1: Calculation of the straylight suppression factor from the optical pathlength noise of the non-reciprocity measurements depicted in Figure 5.5(a). Followed by the calculation of the reflectivity and the transmission of the beam combiner from the straylight suppression factor.

	Backlink fibre	Backlink free beam	Unit
w/o Straylight correction	$3.0 \cdot 10^{-10}$	$8.8 \cdot 10^{-11}$	$[\text{m}/\sqrt{\text{Hz}}]$
w/ Straylight correction	$4.7 \cdot 10^{-12}$	$1.8 \cdot 10^{-12}$	$[\text{m}/\sqrt{\text{Hz}}]$
Suppression factor	63.8	48.9	[1]
Reflectivity R	49.22	48.98	[%]
Transmission T	50.78	51.02	[%]

ing via both input ports of a beam combiner is

$$\Delta\phi_2 \approx \left[\frac{a_s}{a_1} \cos(\phi_1 - \phi_t) - \frac{a_s}{a_0} \cos(\phi_0 - \phi_s) \right] \cdot \frac{\tau^2 - \rho^2}{2\rho\tau} \quad (5.17)$$

The last factors in Equation 5.16 and 5.17 are straylight influence factor. If ρ equals τ the influence of straylight is zero with balanced heterodyne detection. The straylight suppression factor is the inverse of the straylight influence factor and the first one was measured at the backlink fibre experiment. It can be derived from Figure 5.5(a). The mean values of the individual spectra between 10 and 100 mHz with and without straylight correction have been used to calculate the straylight suppression factor. Table 5.1 summarises the results. The straylight suppression factor of the backlink fibre and the backlink free beam setup were with 63.8 and 48.9 in the same order of magnitude. These value indicated that the straylight suppression by balanced detection did not remove straylight completely.

The straylight influence factors $SIF_{1,2}$ can be written as a function of power reflectivity R and power transmission T of the beam combiner.

$$SIF_{1,2} = \frac{R - T}{2\sqrt{R \cdot T}} \quad (5.18)$$

Table 5.1 shows the estimated beam combiner power splitting ratios calculated from the straylight suppression factor. The difference between reflection R and transmission T of the beam combiners for both setups is around 2%, whereby this small difference between the two splitting ratios is given by the fact that they were measured with two different setups. A typical value for the precision of R and T is $\pm 5\%$ [132]. Therefore the measured values are well within the specifications and its influence can be suppressed by the aforementioned fitting procedure.

5.3.2.2 Attenuation

The investigation of the influence of straylight onto the measurement phase in Subsection 5.3.1 revealed that the influence is proportional to the ratio of SLS magnitude to MS magnitude. Therefore a suppression of the influence of straylight can be achieved by an attenuation of the SLS magnitude while maintaining the MS magnitude. Equation 5.13 for the influence of straylight onto the measurement phase can also be written down

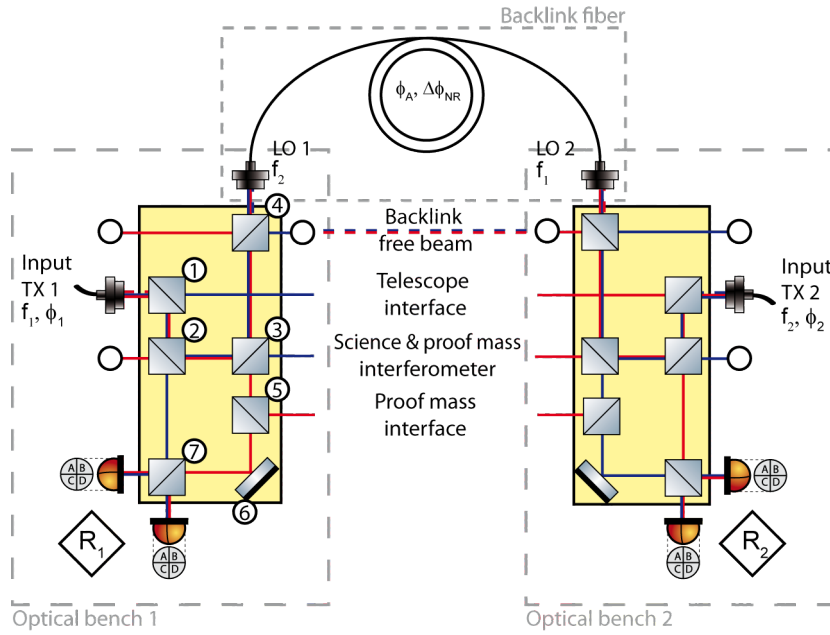


Figure 5.9: Layout of the interferometers on the two optical benches within one LISA satellite, which are connected via the backlink fibre. The layout shows the backlink interferometer and the beam routings to additional interfaces. The optics on one OB are numbered consecutively to be able to calculate the exact values for the measurement and SLS magnitudes.

using powers at the output of the beam combiner instead of magnitudes. The result is

$$\delta\phi \approx -\frac{\sqrt{R \cdot P_s}}{\sqrt{T \cdot P_0}} \cdot \cos(\phi_0 - \phi_s) \quad (5.19)$$

The same holds for Equation 5.15. Thus in this subsection powers instead of magnitudes will be used. Figure 5.9 depicts for both OBs on one satellite the layout of the backlink interferometers and the beam routing to the interfaces of the telescope and the PM. The key elements of straylight suppression by attenuation are attenuating elements in front of the fibre interfaces. Thus the splitting ratio of the beam splitters with number 1 and 4 have to be imbalanced to a large extent. The TX and LO measurement beams pass only once through these elements but the straylight does twice. The usage of neutral density filters were not in discussion. First, the attenuated beam power is lost completely for other measurements. Second, the heating of the neutral density filters cannot be neglected when several mW to W are absorbed in vacuum. Third, it is assumed that even grey filters with a good AR coating can produce straylight. So it cannot be avoided that a small portion is strayed back into the interferometer.

The influence of straylight onto the measurement phase is calculated in two steps. First, the ratios of the MS and the SLS powers are calculated according to Equation 5.13 and 5.15. Second, the behaviour of the cosine and sine parts of Equation 5.13 and 5.15 is calculated via time series of optical pathlengths of fibres measured in the laboratory. This procedure is performed for an imaginary LOB and the AEI backlink fibre experiment. For each a free beam backlink and a fibre backlink is taken into account. In the end the spectra are compared to the measured influence of straylight within the AEI backlink fibre experiment, which is presented in Figure 5.5(a) on page 100.

Table 5.2: Transmission and reflectivity of optics for different realisations of the backlink path sketched in Figure 5.9. Shown are possible realisations of the LOB which are compared to the optics used in the backlink fibre experiment at the AEI.

Optic No.	LISA Optical Bench		Backlink fibre exp.			
	Fibre Transm. [%]	Free beam Refl. [%]	Fibre Transm. [%]	Free beam Refl. [%]	Fibre / Free beam Transm. [%]	Fibre / Free beam Refl. [%]
1	99	1	99	1	50	50
2	25	75	25	75	50	50
3	66	33	66	33	50	50
4	1	99	100	0	50	50
5	50	50	50	50	100	0
6	0	100	0	100	0	100
7	50	50	50	50	50	50

The optical layout in Figure 5.9 can be used to derive the MS and the SLS powers. The power emitted by the TX 1 fibre coupler is called P_1 . The power emitted by the LO 1 fibre coupler is called P_{L1} to account for the loss from the TX 2 fibre coupler to the output of the backlink fibre coupler LO 1. Now the individual powers of the laser beams at the output of the beam combiner in interferometer R_1 can be written down, see Figure 5.9. SLS 1,2 is generated by the respective fibre coupler TX 1 and LO 1. The reflectivities of the fibre couplers TX 1 and LO 1 are called R_{BR} . They are set to the measured value of 20 ppm [19, pp. 83]

$$P_{TX1} = R_1 \cdot T_2 \cdot R_7 \cdot P_1 \quad (5.20)$$

$$P_{LO1} = T_4 \cdot T_3 \cdot T_5 \cdot R_6 \cdot T_7 \cdot P_{L1} \quad (5.21)$$

$$P_{SL1} = T_4 \cdot R_3 \cdot R_2 \cdot R_1 \cdot R_{BR} \cdot R_1 \cdot T_2 \cdot R_7 \cdot P_{L1} \quad (5.22)$$

$$P_{SL2} = R_1 \cdot R_2 \cdot R_3 \cdot T_4 \cdot R_{BR} \cdot T_4 \cdot T_3 \cdot T_5 \cdot R_6 \cdot T_7 \cdot P_1 \quad (5.23)$$

According to Equation 5.19 the influence of straylight onto the measurement phase is proportional to the ratio of SLS power and MS power at the output of the beam combiner. The ratios for both straylight sources SL 1 (Source: TX 1 fibre coupler) and 2 (Source: LO 1 fibre coupler) are

$$\sqrt{\frac{P_{SL1}}{P_{LO1}}} = \sqrt{\frac{R_3 R_2 R_1 R_{BR} R_1 T_2}{T_5 T_5 R_6}} \quad (5.24)$$

$$\sqrt{\frac{P_{SL2}}{P_{TX1}}} = \sqrt{\frac{R_2 R_3 T_4 R_{BR} T_4 T_3 T_5 R_6}{T_2}} \quad (5.25)$$

Table 5.2 presents the characteristics of the optics for an imaginary LOB with a fibre and a free beam implementation at the backlink path. The values for the optics, which were used within the backlink fibre experiment at the AEI according to Figure 5.9 can also be found in Table 5.2. Implementations of the LOB already integrate straylight attenuation via the optics number 1 and 4. The numbers presented in Table 5.2 can be used to calculate the influence of straylight onto the measurements signals for the AEI backlink experiment and the imaginary LOB using Equation 5.24 and 5.25.

Table 5.3: Comparison of the MS magnitude to SLS magnitude for the LOB with attenuation and the backlink fibre experiment at the AEI.

Source		LISA Optical Bench		Backlink fibre experiment	
fibre	Signal	Transmission	SL/MS	Transmission	SL/MS
coupler		[1]	[1]	[1]	[1]
TX 1, LO 1	MS	$2.725 \cdot 10^{-3}$		$2.371 \cdot 10^{-1}$	
TX 1	SL1	$6.062 \cdot 10^{-8}$	$2.225 \cdot 10^{-5}$	$2.652 \cdot 10^{-4}$	$1.118 \cdot 10^{-3}$
LO 1	SL2	$6.062 \cdot 10^{-8}$	$2.225 \cdot 10^{-5}$	$2.652 \cdot 10^{-4}$	$1.118 \cdot 10^{-3}$

Table 5.3 shows the relative powers of SLS and MS for the LOB and the performed backlink fibre experiment as well as their ratios (SL/MS). The values for the ratio of straylight to MS indicate that the attenuation solution decreases the influence of straylight by a factor of 50. In a next step the phase behaviour of the straylight is calculated.

The optical pathlength noise of the passively stabilised (thermally stable environment) and actively stabilised (piezo-actuation on the fibre length) backlink fibre is shown in Figure 5.5(b). The according time series were used to derive the phase behaviour of straylight that is generated in the backlink fibre. The optical pathlengths of the input fibres of the TX beams were not directly measured. Figure 2.16(b) on page 20 shows the differential optical pathlength noise of the two measurement beams ($\phi_0 - \phi_1$) in the reference interferometer of the picometer experiment with respect to a reference phase ϕ_{ref} from the modulation electronic. The OPD stabilisation was switched off during that measurement. Assuming that ϕ_{ref} is much more stable than $(\phi_0 - \phi_1)$ this curve is a measurement of the non-common mode noise of ϕ_0 and ϕ_1 with respect to ϕ_{ref} . The two measurement beams were guided via two spatially separated input fibres to the picometer experiment. Thus the common mode optical pathlength noise of the fibres can be neglected in this context. Therefore it is a good assumption that the measured phase in the reference interferometer is a rough estimate of the optical pathlength behaviour of a fibre, which connects a LPF MB to an experiment in a vacuum chamber. The time series of the optical pathlength noise in Figure 2.16(b) was used to derive the phase behaviour of the straylight that is generated in the input fibers (TX fibres). The time series and the numbers in Table 5.3 were used to estimate the optical pathlength noise induced by straylight via Equation 5.13 and 5.15. Figure 5.10(a) presents the calculated optical pathlength noise of the straylight influence for the measurement of the setup noise (comparable to free beam backlink) and the fibre measurement of the backlink experiment at the AEI. The calculated optical pathlength noise for the fibre setup is for frequencies above 4 mHz at the same level as the measured optical pathlength noise at the experiment. The influence of straylight onto the MS was derived for one beam combiner. The presented measurement of the non-reciprocity of the fiber was a combination of signals measured at three beam combiners. The good agreement indicates that a more complex straylight model is not necessary. The calculated optical pathlength noise of the setup is for frequencies above 6 mHz a factor of three above the measured value. This difference can be explained by the different alignment methods at the AEI backlink experiment. The investigations on the non-reciprocity of the backlink fibre required that coupling into the backlink fibre as well as contrast in the interferometers was optimised. For the measurement of the non-reciprocity of the setup the alignment was slightly changed. The contrast in the interferometers were optimised and thereby the coupling

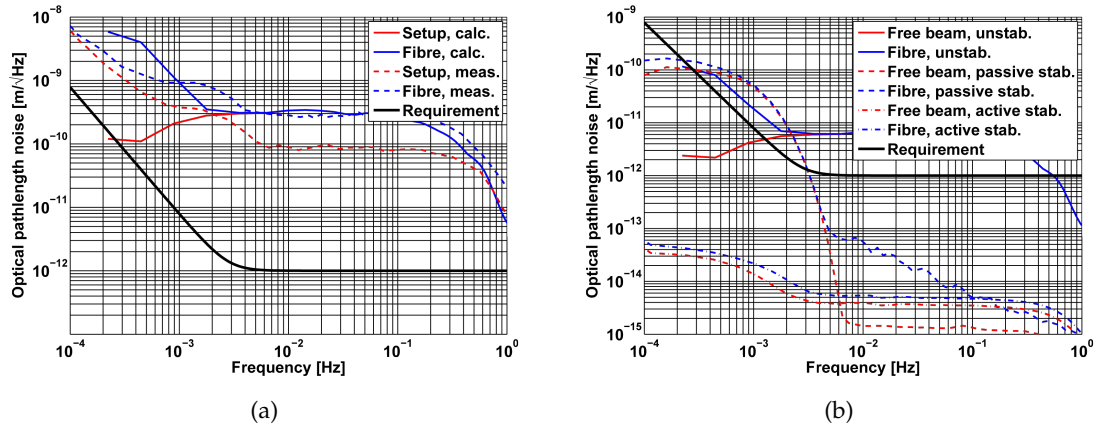


Figure 5.10: Optical pathlength noise calculated via the ratio of straylight and MS amplitude and via time series of measured optical pathlength of fibres.

efficiency between the input fibres was degraded. This in turn reduced straylight because no light was coupled into the input fibres.

Figure 5.10(b) presents the calculated optical pathlength noise of the straylight influence at an imaginary LOB for a free beam backlink and a fibre backlink. Thereby different optical pathlength stabilities of the TX input fibres and the backlink fibre were assumed. For the unstabilised case the fibre length stabilities were assumed to be identical to the AEI backlink fibre experiment. The optical pathlength of the TX input fibres was unstable and the backlink fibre was relatively stable due to the low temperature noise. In this case the straylight induced optical pathlength noise is even with attenuation above the requirement for frequencies above 1 mHz. In the next case the optical pathlength stability of the TX fibre was reduced to that of the backlink fibre in the last case. The straylight induced optical pathlength noise is above the requirement for frequencies below 3 mHz and above 0.3 mHz. In the last case the TX fibres and the backlink fibres were actively stabilised. Here the straylight induced optical pathlength noise is well below the requirement. A results of this is that the TX fibres and the backlink fibre need to be stabilised even with an attenuation of straylight.

A drawback of the attenuation solution is the reduction of optical power from the LO. Therefore the read-out limit for the optical pathlength noise of the backlink interferometer is derived. The laser power of the light emitted by fibre coupler TX 1 is 1.54 W for the LOB [14, pp. 46]. In a next step the laser power emitted by fibre coupler LO 1 is calculated. The transmission of power from fibre coupler TX 2 on LOB 2 to fibre coupler LO 1 on LOB 1 is calculated assuming a fibre coupling efficiency η of 90 %.

$$P_{\text{LO2}} = \eta \cdot (P_{\text{TX1}} \cdot R_1 \cdot R_2 \cdot R_3 \cdot T_4) \quad (5.26)$$

$$= 34.3 \mu\text{W} \quad (5.27)$$

The optical power emitted by fibre coupler LO 1 is approximately 34.3 μW , which leads to an optical power of around 14.2 nW on each segment of the two quadrant photodetectors within the reference interferometer R_1 . The optical power impinging on each segment from fibre coupler TX 1 is around 0.48 mW.

In Subsection 4.1.4 important contributions to the read-out limit for a heterodyne MZI as a function of optical power at the input of the interferometer were discussed. These are namely the shot noise, the electronic noise, and the relative intensity noise. The

Table 5.4: Read-out limits of the optical pathlength due to electronic noise in the reference interferometer of the LOB for the fibre and the free beam implementation of the backlink path with straylight suppression by attenuation.

	Fibre		Free beam	
	Per segment	Total	Per segment	Total
	$[\text{pm}/\sqrt{\text{Hz}}]$	$[\text{pm}/\sqrt{\text{Hz}}]$	$[\text{fm}/\sqrt{\text{Hz}}]$	$[\text{fm}/\sqrt{\text{Hz}}]$
Shot noise	1.02	0.51	11.1	5.6
Electronic noise	0.48	0.24	4.6	2.3
Laser intensity	0.23	0.23	2.9	2.9
Sum	1.15	0.61	12.3	6.7

individual contributions and their sum in the reference interferometer are summarised in Table 5.4. The attenuation solution in combination with a fibre backlink yields a lower limit for the optical pathlength read-out for each photodetector in the reference interferometer of $0.61 \text{ pm}/\sqrt{\text{Hz}}$. This is very close to the requirement for the optical pathlength read-out of the PM position of $2.84 \text{ pm}/\sqrt{\text{Hz}}$. To derive the lower limit for the optical pathlength read-out of the PM interferometer the same calculation has to be done for the PM interferometer. Thereby a perfect and also non-perfect angular alignment of the PM assuming a reflectivity of $80\% \pm 5\%$ for the PM surface has to be taken into account [14, R<130-080>]. The uncorrelated sum of the lower limits for the optical pathlength read-outs of the reference and the PM interferometer gives then the lower limit for the optical pathlength read-out of the PM position with respect to the OB.

The same calculation has to be performed for the PM interferometer to get a lower limit for the PM position read-out. This is not part of this work but typically the individual noise contributions within an interferometer have to be kept an order of magnitude below the requirement to get reasonable performance under any conditions. Therefore the attenuation solution in combination with the fibre backlink can only be recommended if an experimental demonstration verifies the feasibility with the requirements.

The same calculation for the free beam backlink with the attenuation solution yields $6.7 \text{ fm}/\sqrt{\text{Hz}}$. This is 2 orders of magnitude below the requirement of the PM optical pathlength read-out. More details on the realisation of the free beam backlink can be found in Subsection 5.4.3.

5.3.2.3 Direct measurement

The main noise sources of straylight within the OB for LISA were identified in [19] and are the input fibres of the OB. This includes the backlink fibre. The direct measurement technique of the straylight is based on the matter of fact that the straylight beat signal can be measured individually between its source, the input fibres of the OB and the beam combiners of the interferometers.

Figure 5.11 depicts a possible solution for the OB. The fibre for the TX beam and the LO beam (backlink fibre) pass different parts of the satellite and therefore the phase of the straylight of the two fibres cannot be assumed to be common-mode. Therefore the straylight beat signal has to be measured at two ports of the OB with photodiodes SL1 and SL2.

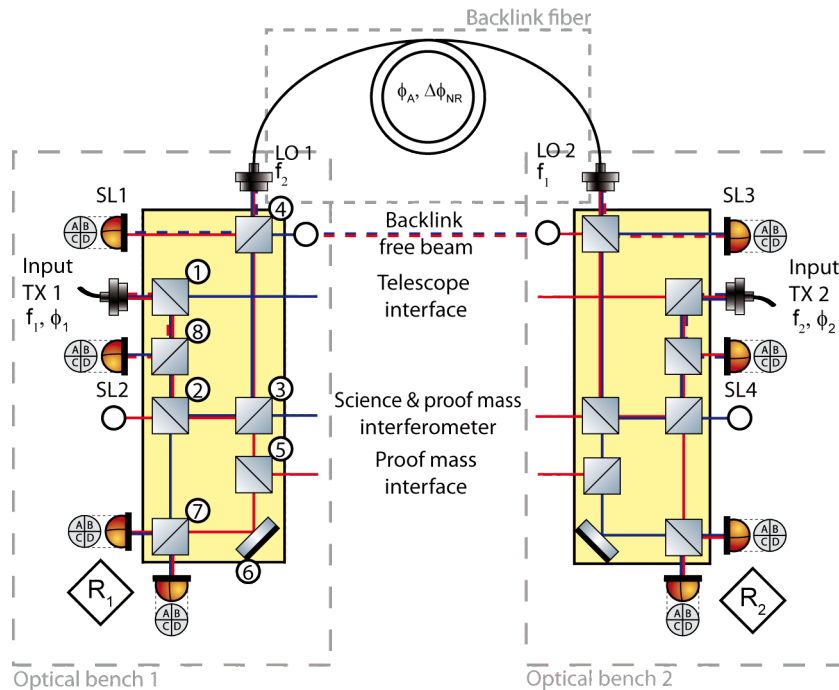


Figure 5.11: Layout of the interferometers on the two optical benches within one LISA satellite, which are connected via the backlink fibre. To measure the straylight directly at least two photodiode (SL1 and SL2) have to measure the straylight from the source fibre and the backlink fibre.

This procedure was already investigated in [19, pp. 64] using the LTP modulation scheme. Additional electronics were needed to separate the high DC signal from the small AC straylight beat signal and to amplify the latter to get a reasonable SNR within the phasemeter. The straylight beat signal was thereby measured only at one port of the backlink fibre experiment. Then the subtraction was performed using the signals to stabilise the laser intensities via the AOM drivers or by direct measurement and subtraction in data post-processing. The results obtained with these two techniques were not as good as the straylight subtraction by balanced detection. These might be because only one straylight port was measured.

The implementation of two straylight measurement ports within LISA measurement scheme is much easier than in the LPF modulation scheme. The interferometer photodetectors are already AC/DC decoupled and one interferometer port for the direct measurement of the straylight is already implemented: the port for power stabilisation of the TX beam has to be equipped with interferometer photodetectors. So only a second interferometer port for measurement of the straylight from the backlink fibre needs to be added. The amplitudes of straylight at both measurement ports have to be measured after building of the OB to optimise the SNR via the gain of the photodetectors, because the straylight strongly depends on the characteristics of the fibre, i.e. alignment, length, *etc.* The measured straylight phase and magnitude can be used in data post-processing to correct the optical pathlength noise of the interferometers.

The direct subtraction of straylight by stabilising the laser power such that it compensates the straylight as in [19, pp. 47] can be seen as critical for LISA. The AM at the heterodyne frequency to compensate straylight in the local interferometers will lead to AM at the heterodyne frequency in other interferometers. Thus this solution is out of question for LISA. Additionally a stable feedback loop requires that the phase at the unity

gain frequency is more than -180° . A goal is typical -145° or bigger. The straylight frequencies are in the range of the interferometer beat notes. These are up to 20 MHz. When the TX laser and the OB are spatially separated by about 1 m this means a phase loss of 24° at 20 MHz. The phase loss at 20 MHz introduced by the photodetector is thought to be around 60° . When this is implemented via a bandpass filter at the heterodyne frequency, which will be continuously shifted, the phase loss of the bandpass is critical for the remaining 61 degree of phase reserve.

A verification of the procedure to measure the properties of straylight and subtract them in data post-processing to yield a straylight-free MS signal is still outstanding.

5.4 Straylight free backlink path

The degradation of the optical pathlength read-out within the current LISA measurement scheme due to straylight is determined by the fact that the backlink fibre is symmetric in the following ways

1. The beat note frequencies of the local interferometers on both OBs are identical.
2. The polarisations of the counter-propagating beams within the backlink path are identical.
3. The beams are exchanged via the same optical beam path.

Breaking one of these symmetries will mitigate the straylight problem. The next section presents measurement schemes which break the first two symmetries. The last symmetry can only be broken via an in-field pointing solution with only one optical bench per satellite, which was mentioned in the introduction of this chapter. Due to the fact that it changes the overall structure within the satellite, it is not further studied in this work.

5.4.1 Frequency separation

The idea of the frequency separation topology is to separate the straylight beat signal from the measurement beat signal in frequency, although the straylight source and therefore the straylight remains unchanged. Figure 5.12 shows a proposed implementation of the frequency separation scheme for an imaginary LOB. The light emitted by the fibre couplers TX 1 and TX 2 is the TX light which is sent out via the telescopes. A fraction of this TX light is also used as the reference beam for the read-out of the local science interferometer and the local PM interferometer. For the backlink path two additional low power lasers (a few mW) are needed. Their light is emitted by fibre coupler ALO 1 and ALO 2. The additional lasers are exchanged via the backlink path and become LO 1 and LO 2. These are the measurement beams for the reference and the PM interferometers. The frequencies and phase of the lasers are denoted at the output end of the fibre couplers. ϕ_A is the fiber length and $\phi_U - \phi_D$ the non-reciprocity of the fibre.

According to Section 5.2 two straylight sources spoil the performance of the optical length read-out with the symmetric backlink path. First the TX laser light is back reflected from the backlink fibre. Second the LO light is back reflected from the TX fibre. The back reflections do also occur in this setup. The additional laser beams ALO 1 and ALO 2 are back reflected from the fibre interfaces LO 1 and LO 2 and vice versa. No back reflections occur at the TX fibre couplers TX 1 and TX 2. Table 5.5 lists the beat note frequencies and phases of the SLS and MS. The MSs and the SLSs are separated by frequency. The last

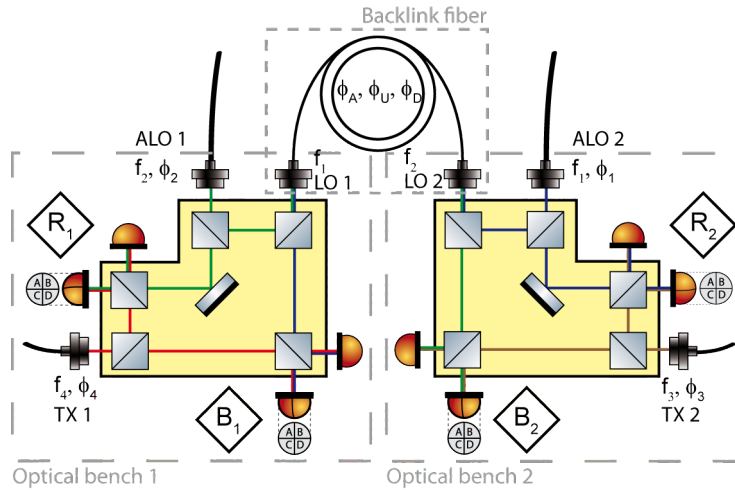


Figure 5.12: Layout of the interferometers on the two optical benches within one LISA satellite, which are connected via the backlink fibre. The comparison of the TX lasers is implemented via an additional local oscillator laser, which is exchanged via the backlink fibre.

Table 5.5: Characteristics of the signals within the OB interferometers, when the frequency separation topology is used for the comparison of the TX lasers.

IFO	Frequency	Phase	Signal	$f_3 = f_4$
R ₁	$\Delta(f_2, f_4)$	$\Delta(\phi_2, \phi_4)$	MS	$\Delta(f_2, f_3)$
	$\Delta(f_1, f_4)$	$\Delta(\phi_1 + \phi_A + \phi_D, \phi_4)$	SL	$\Delta(f_1, f_3)$
B ₁	$\Delta(f_1, f_4)$	$\Delta(\phi_1 + \phi_A + \phi_D, \phi_4)$	MS	$\Delta(f_1, f_3)$
	$\Delta(f_2, f_4)$	$\Delta(\phi_2, \phi_4)$	SL	$\Delta(f_2, f_3)$
R ₂	$\Delta(f_1, f_3)$	$\Delta(\phi_1, \phi_3)$	MS	$\Delta(f_1, f_3)$
	$\Delta(f_2, f_3)$	$\Delta(\phi_2 + \phi_A + \phi_U, \phi_3)$	SL	$\Delta(f_2, f_3)$
B ₂	$\Delta(f_2, f_3)$	$\Delta(\phi_2 + \phi_A + \phi_U, \phi_3)$	MS	$\Delta(f_2, f_3)$
	$\Delta(f_1, f_3)$	$\Delta(\phi_1, \phi_3)$	SL	$\Delta(f_1, f_3)$

column of the table points out that even if laser 3 and 4 are set to the same frequency (or are the same laser) the separation of the MS and the SLS remains.

The main purpose of the backlink path is to compare the phases of TX laser 1 and 2. Therefore the phases of the recombined beams in the interferometers are written down to check if this information can be derived. Assuming without loss of generality $f_4 < f_3 < f_2 < f_1$, and that the phasemeter output is defined as $\phi_{\text{higher}} - \phi_{\text{lower}}$,

$$\phi_{R1} = \phi_2 - \phi_4 \quad (5.28)$$

$$\phi_{R2} = \phi_1 - \phi_3 \quad (5.29)$$

$$\phi_{B1} = \phi_1 + \phi_A + \phi_D - \phi_4 \quad (5.30)$$

$$\phi_{B2} = \phi_2 + \phi_A + \phi_U - \phi_3 \quad (5.31)$$

The next step is to calculate the sum and the difference of the reference and the backlink

fibre interferometers.

$$\phi_{R1} + \phi_{R2} = \phi_1 + \phi_2 - \phi_3 - \phi_4 \quad (5.32)$$

$$\phi_{R1} - \phi_{R2} = \phi_1 - \phi_2 - \phi_3 + \phi_4 \quad (5.33)$$

$$\phi_{B1} + \phi_{B2} = \phi_1 + \phi_2 - \phi_3 - \phi_4 + 2 \cdot \phi_A + \phi_U + \phi_D \quad (5.34)$$

$$\phi_{B1} - \phi_{B2} = -\phi_1 + \phi_2 - \phi_3 + \phi_4 + \phi_U - \phi_D \quad (5.35)$$

With these combinations the equations for the comparison of the phases of TX laser 1 and 2 can be calculated.

$$\phi_{R1} - \phi_{R2} + \phi_{B1} - \phi_{B2} = 2 \cdot (\phi_4 - \phi_3) + \phi_U - \phi_D \quad (5.36)$$

Additionally laser ALO 1 and 2 can be compared and the length of the exchange path can be measured.

$$\phi_{R1} - \phi_{R2} - \phi_{B1} + \phi_{B2} = 2 \cdot (\phi_1 - \phi_2) + \phi_D - \phi_U \quad (5.37)$$

$$\phi_{R1} + \phi_{R2} - \phi_{B1} - \phi_{B2} = -2 \cdot \phi_A - \phi_D - \phi_U \quad (5.38)$$

5.4.2 Polarisation

The idea of the polarisation topology is to separate the measurement and straylight beams by their polarisation. Figure 5.13 shows a possible topology, which can be realised in both implementations of the backlink path: with a fibre and in a free beam configuration. The counter-propagating light fields along the backlink path are of orthogonal polarisation. The TX laser systems on the OBs on each satellite are also orthogonal in polarisation for this consideration. The main problem of this solution is that the optics with number 3 and 4 in Figure 5.13 have to deal with both polarisations. This has to be taken into account for the design of their coating. The wave plate between optic number 3 and 5 takes care that the polarisation of the light from the backlink path, which is of opposite polarisation relative to the local TX beam, is rotated to the correct polarisation in the interferometers. The suitability in principle of polarisation optics for LISA was demonstrated in [17, pp. 59]. The backreflection of TX beam 1 at the fibre interface of LO beam 1 interferes with the backreflection of LO beam 1 at the fibre interface of TX beam 1 at the beam combiner 7 in Figure 5.13. This type of straylight can not be suppressed with balanced detection. Its influence should be negligible however, because the magnitudes of the individual straylight beams have been attenuated by the small coefficient of power reflection of the fibres. This is in the order of $20 \cdot 10^{-6}$. Additionally the straylight from the fibre coupler TX 1 is reduced further by the splitting ratio of the light power between the telescope interface and the local interferometers, which will be implemented in any case.

The fibre backlink solution can be realised via a polarisation-maintaining fibre or a non-polarisation-maintaining fibre. The latter was not selected for the backlink fibre experiment at the AEI. The low-frequency polarisation noise of the TX beams after passing such a backlink fibre was believed to introduce optical pathlength noise via amplitude noise of the beat notes. Although the phase measurement technique is nominally insensitive to amplitude noise at low frequencies, the effect was nevertheless measured at different experiments including the picometer experiment, see Subsection 2.4.3.5. The reason for this is thought to be power-dependent phase fluctuations at the photodiodes.

The usage of a polarisation-maintaining fibre in the polarisation topology becomes questionable because of the remaining difference in the refractive index between the two

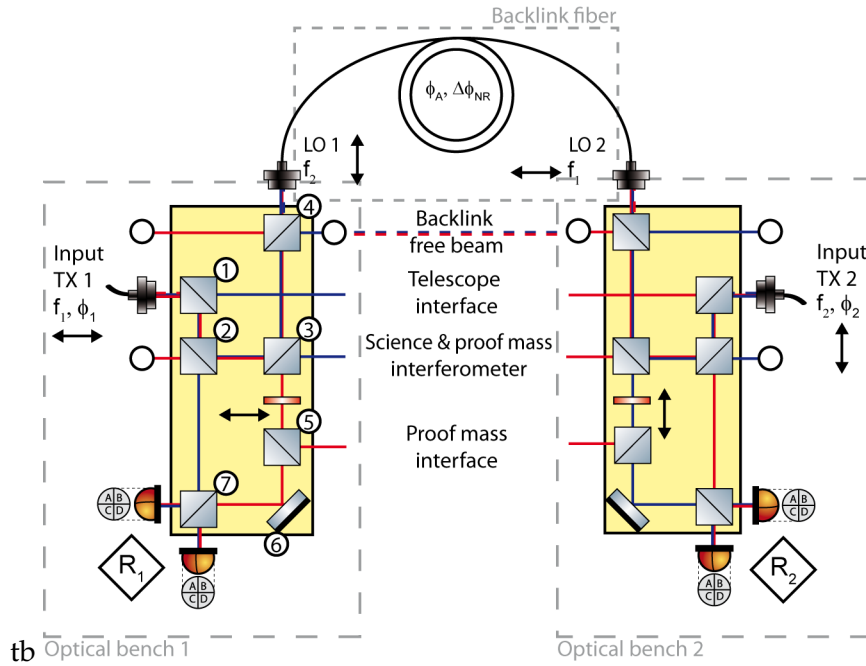


Figure 5.13: Layout of the interferometers on the two optical benches within one LISA satellite, which are connected via the backlink fibre. Straylight is suppressed by using perpendicular polarisation within the backlink path. An additional wave plate is needed to align the polarisation within the interferometers.

axis of the fibre. The difference of the refractive index of the two axes of a polarisation-maintaining fibre is called modal birefringence B and is typically expressed in form of a beat length l_p [133]. This is the length of a polarisation-maintaining fiber after which light in both axes of the polarisation-maintaining fibre has a relative phase offset of 2π . The equation for the beat length l_p is

$$l_p = \frac{\lambda}{B} \quad (5.39)$$

whereby λ is the wavelength [133]. The polarisation-maintaining fibre that was used at the backlink fibre experiment at the AEI had a beat length l_p of 1.5 to 2.7 mm [19, pp. 55] [134, p. 3]. This yield a difference of the refractive indices of the fibre axes between $4.3 \cdot 10^{-4}$ and $7.1 \cdot 10^{-4}$. The physical length change of the fibre needs to be known to calculate the optical pathlength difference between the two direction of propagation (non-reciprocity) inside the fibre. The physical length change of the fibre without length stabilisation is about $10 \text{ nm}/\sqrt{\text{Hz}}$ at 1 mHz, shown in Figure 5.5(b). This results in an optical pathlength difference between both fibre axes of $7 \text{ pm}/\sqrt{\text{Hz}}$ at 1 mHz. With the fibre length stabilisation turned on the optical pathlength difference between both fibre axes is reduced to $0.7 \text{ pm}/\sqrt{\text{Hz}}$ at 1 mHz. Thus the fibre length has to be stabilised to suppress the non-reciprocal noise due to a length change of the fibre below the requirements. This could, for example, be done by increasing the fibre length, winding the extra fibre length on a ring piezo and actuation with the piezo on the fibre [19, pp. 58]. This could, however, produce in turn other side-effects.

A small portion of straylight is created due to the polarisation contrast of only around 20 dB of a polarisation-maintaining fibre. The s-polarised TX beam 2 is coupled into the backlink fibre via the fibre coupler LO 2. Within the backlink fibre about 1 percent of the s-polarised light is converted into p-polarised light. This p-polarised light interferes

at the output fibre coupler LO 1 of backlink fiber with the back reflected light from the TX beam 1, which is also p-polarised. In the reference interferometer R1 the MS is p-polarized and the SLS is s-polarized due to the half-wave plate between optic number 3 and 5. In the end the polarisers in front of the photodetectors will remove the SLS from the MS. The same reasoning can be done for the backreflection of the LO 1 beam from the TX 1 fibre coupler.

The free beam backlink can be seen as uncritical for the polarisation solution because optics that can handle both polarisations are available. The results from the straylight suppression by attenuation suggest that the polarisation solution is not needed for the free beam backlink.

5.4.3 Free beam backlink

The free beam implementation of the backlink path is essentially free from straylight if the splitting ratio of the beam splitter, which separates the reference and the PM interferometer beams from the science interferometer beam, is unbalanced of the order of 1:99, see Subsection 5.3.2.2. If the splitting ratio of these interferometers and the telescope interface for the TX beam cannot be made unbalanced enough to suppress straylight to the required level, a completely straylight-free free beam backlink path can be realised with orthogonal polarisations in the counter-propagating beam directions, see Subsection 5.4.2.

A schematic of a free beam implementation is depicted in Figure 5.14. Both optical benches within one satellite are continuously moved with the MOSAs which track the change of angle between the LISA arms. According to orbit simulations this angle is around $60^\circ \pm 1.5^\circ$ [1, pp. 88]. The error signals for the control of the MOSAs are derived from the DWS signals of the science interferometers. As already mentioned in the introduction of this chapter the TX beam of one OB serves as LO for the other OB and vice versa. To compensate the angular change of the LO on the OBs two movable mirrors steer the light between both OBs through the satellite. These actuators are rigidly connected to the OBs to guarantee that the beams do not move on the actuators when the MOSAs are moving.

The alignment range of the actuators in the plane of Figure 5.14 have to be able to compensate a beam direction change even if one MOSA is damaged and stays in the worst position. This leads to a required alignment range of at least $\pm 2.25^\circ$. The alignment range of the actuators out of plane of Figure 5.14 can be much smaller because this dimension can be regarded as constant. The actuators should be able to stabilise the beam directions of the LOs on the OBs in order to measure the PM jitter correctly. The actuation bandwidth has to be at least one order of magnitude above the LISA measurement band, which leads to a minimum required bandwidth of 10 Hz. Also vibrations within the spacecraft have to be taken into account to suppress aliasing. Otherwise the DWS signals of the PM interferometer have to be corrected with the DWS signals from the reference interferometer. The actuators should be able to make continuous movements without steps to prevent glitches in the optical pathlength and DWS measurements. Therefore slip-stick actuators as for the PM simulator cannot be used. The actuators would, for example, be made with piezo-stacks or voice coils. The actuators will be used in a control loop and not out of loop as in the LTP campaign. Therefore the high noise of these actuators that has been observed within the LTP campaign can be neglected, if the open-loop gain is high enough [18]. It is worthwhile to note that their pathlength error cancels to first order as opposed to the PAAM or in-field-pointing actuators.

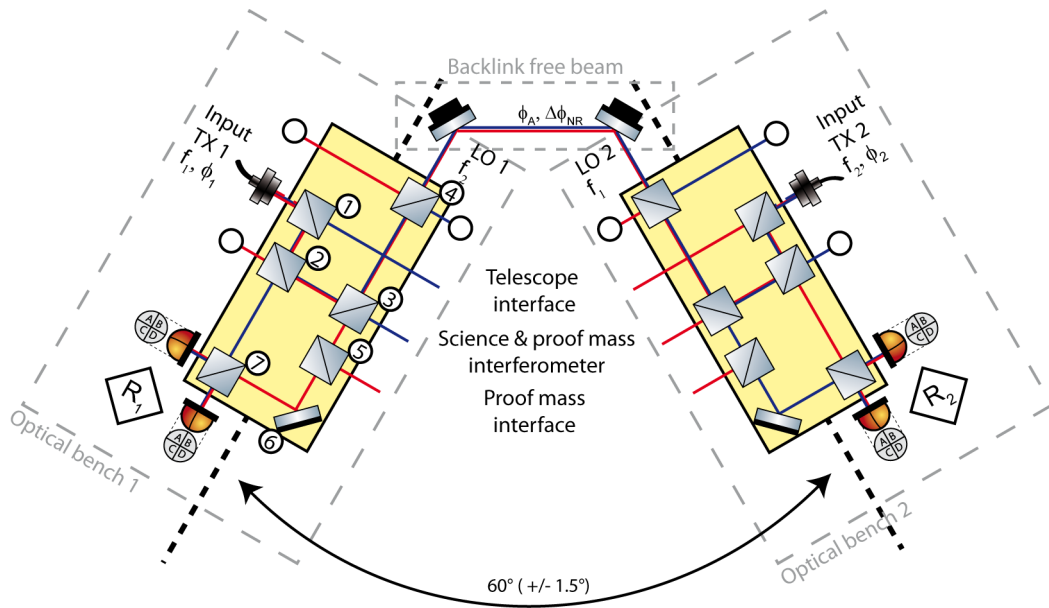


Figure 5.14: Layout of the interferometers on the two optical benches within one LISA satellite, which are connected via a free beam backlink. Movable mirrors are needed to stabilise the beam direction on the OBs.

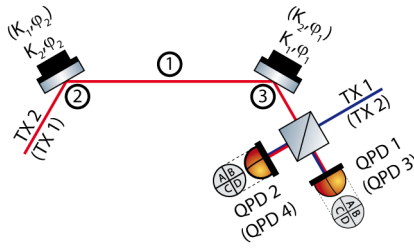


Figure 5.15: A simple schematic of the free beam backlink path to calculate the DWS signals and coupling factors.

The beam centroid and DWS signals from the quadrant photodetectors in the reference interferometers can be used to generate the error signals for the control loop of the actuators. The general properties of these error signals can be deduced from a simplified interferometer setup, as shown in Figure 5.15. It displays the situation for one OB. The situation for the second OB is symmetric. The according variables are put into brackets in Figure 5.15. The TX beam 2 of the second OB is guided via two movable mirrors to the beam combiner of the reference interferometer on the first OB. Here it is interfered with TX beam 1. The interferometer signals are detected with QPD 1 and 2, whose signal content should be identical. For this consideration the reflection points on the movable mirrors are identical with the pivot points of the mirrors.

A first question with respect to the control of the movable mirrors is if the rotation of the mirrors can be measured separately if the MOSAs are considered stationary and the mirrors move. For this the DWS signal of QPD 1 on the first OB and the DWS signal of QPD 3 on the second OB are used. The DWS signal content is described with

$$\begin{pmatrix} \text{DWS}_1 \\ \text{DWS}_3 \end{pmatrix} = \begin{pmatrix} K_1 & K_2 \\ K_2 & K_1 \end{pmatrix} \begin{pmatrix} \phi_1 \\ \phi_2 \end{pmatrix} \quad (5.40)$$

Table 5.6: DWS coupling factors for both actuators of the free beam backlink path for different waist positions.

Waist position	K_1 [rad/rad]	K_2 [rad/rad]
1	8413.5	9437.3
2	8401.4	9846.9
3	8758.3	9291.1

$K_{1,2}$ are the DWS coupling factors between a rotation of $\phi_{1,2}$ (movable mirror 1 and 2) and the measured DWS signal on QPD 1 and 3. This information can be used to calculate the rotation $\phi_{1,2}$ from the measured DWS signals $DWS_{1,3}$. It is

$$\phi_1 = \frac{1}{K_1} (DWS_1 - K_2 \phi_2) \quad (5.41)$$

$$\phi_2 = \frac{1}{K_1} (DWS_3 - K_2 \phi_1) \quad (5.42)$$

The last equations are inserted into each other to eliminate the dependency of ϕ_1 from ϕ_2 and vice versa. The solution for $\phi_{1,2}$ is

$$\phi_1 = \frac{1}{K_1} \left(1 - \frac{K_2^2}{K_1^2}\right)^{-1} \left(DWS_1 - \frac{K_2}{K_1} DWS_3\right) \quad (5.43)$$

$$\phi_2 = \frac{1}{K_1} \left(1 - \frac{K_2^2}{K_1^2}\right)^{-1} \left(DWS_3 - \frac{K_2}{K_1} DWS_1\right) \quad (5.44)$$

The equations indicate that the coupling factors $K_{1,2}$ need to be unequal to decouple the motion of the actuators. According to Subsection 2.4.3.4, the coupling factors $K_{1,2}$ depend on the distance between the according photodiodes and actuators. The coupling factors $K_{1,2}$ are calculated under the assumption that the distance between the actuators is approximately one meter and the distance between the actuator on one OB and the according photodiode is 0.5 m. The waist size of the LO beams are assumed to be 1 mm. Table 5.6 shows the DWS coupling factors for both actuators of the free beam backlink path for different waist positions according to Figure 5.15. The DWS coupling factors for all waist positions are sufficiently different. The symmetric waist position 1 should be preferred because it maximises the beam overlap between the LOs in the backlink path and the beam parameters of both LOs are symmetric.

A second question is what happens if the movable mirrors in the backlink path are fixed and the MOSAs rotate. Due to the fact that the movable mirrors are rigidly connected to the OBs the angular change of the LOs are almost identical to the situation when the MOSAs are fixed and the movable mirrors rotate. Only small differences to this arise in the optical pathlength change. First, the beam walk of the LO on the opposite mirror and second, the distance change between the actuators due to the MOSA movement.

In the last paragraphs it was shown that the control loops for the backlink path actuators can stabilise the DWS signals in the reference interferometers to zero during the movement of the MOSAs. The MOSAs will only change the absolute distance between the movable mirrors of the backlink path. This is in first order not of concern because optical pathlengths in vacuum are reciprocal under the assumption that the beams are

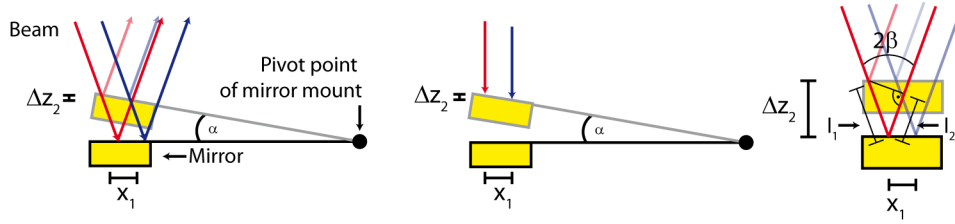


Figure 5.16: Optical pathlength change induced by an actuator tilt in the backlink path.

overlapped perfectly. A requirement for the overlap of the beams to keep the non-reciprocity below the requirement has to be calculated. First, the non-reciprocal noise is introduced by the pointing noise of the actuators. These induce optical pathlength changes which are different for both counter-propagating LO beams. Second, the optical pathlength change due to a distance change between the actuators is also different for the misaligned beam.

The influence of a pointing change of one actuator onto the optical pathlength of the non-reciprocity is comparable to the optical pathlength change induced by the actuator in the PM simulator, which was described in Subsection 3.5.4.2. A first difference is that the lateral misalignment x_1 of the beam from the rotation point of the mirror is equal to the lateral misalignment of the beams on the mirror surface. A second difference is that the angles of incidence of the beams onto the mirrors, which are attached to the actuators in the backlink path, are not perpendicular to the mirror surface. This is illustrated on the left-hand side of Figure 5.16. A movement of the mirror surface due to a jitter of the actuator can be split into two independent movements. These are displayed in the middle part and on the right-hand side of Figure 5.16. The movement, depicted in the middle part of Figure 5.16, was discussed in Subsection 3.5.4.2. A detailed discussion of the situation on the right-hand side can be found in [39, pp. 83]. The optical pathlength change due to a movement on the right-hand side of Figure 5.16 is

$$\Delta l_1 = 2 \cdot \Delta z_2 \cdot \cos(\beta) \quad (5.45)$$

whereby Δz_2 is the longitudinal motion of the mirror and β is the angle of incident of the beam.

The movement in the middle part of Figure 5.16 is described by Equation 3.22 on page 56. Thus the change of the optical pathlength of the non-reciprocity as a function of the lateral misalignment x_1 of the beams induced by a tilt α of one actuator is

$$\Delta l = 2 \cdot x_1 \cdot \alpha \cdot \cos(\beta) \quad (5.46)$$

It is further assumed that the control loop for the actuators keeps the DWS signals in the reference interferometers below the requirement for the absolute misalignment and the read-out of the beam pointing of the PM interferometer. This is $\pm 10 \mu\text{rad}$ and $10 \text{ nrad}/\sqrt{\text{Hz}} \cdot u_1(f)$ according to Section 2.1. A result of the beam pointing stabilisation is that the offset x_1 of the LO 1 beam from the LO 2 beam on one actuator of the backlink induces an almost identical offset at the other actuator and vice versa. The optical pathlength change of the non-reciprocity as a function of the beam misalignment x_1 induced by a tilt α of both actuators under the assumption that the remaining pointing noise of both actuators are correlated is

$$\Delta l = 4 \cdot x_1 \cdot \alpha \cdot \cos(\beta) \quad (5.47)$$

The requirement for the read-out of the non-reciprocity is set to the same value as for the read-out of the PM interferometer. According to Section 2.1 this is $2.84 \text{ pm} / \sqrt{\text{Hz}} \cdot u_1(f)$. The angle of incidence β is around 60° . With the already mentioned beam pointing stability α the maximum allowable offset x_1 from the pivot point of the actuator is 0.14 mm.

The initial alignment / acquisition and optimisation of the reference interferometer signals after launch and orbit transfer of the LISA satellites can be done by using the beam centroid measurement. Therefore the alignment of actuator 1 is slowly changed in one dimension from its upper boundary to its lower boundary. At the same time the alignment of actuator 2 is changed in the same dimension sinusoidally at a fixed amplitude A and frequency f . The offset C of actuator 2 is at the beginning 0 from its nominal position. If the sinusoidal signal is not observed within the beam centroid measurement in the reference interferometer on OB 2, the offset C of the sinusoidal signal is changed step by step until it is observed completely with a QPD. If TX beam 1 hits the mirror of actuator 2 not exactly in its pivot point the amplitude of the modulation which is measured in the length signal of the reference interferometer on OB 2, consists of the angular change of actuator 2 and the lateral shift of TX beam 1 due to the offset from the pivot point. Therefore the goal is to minimise the amplitude of the sinusoidal signal measured with the QPD in the reference interferometer by changing the offset of actuator 2 step-by-step and scanning actuator 1 slowly. When the amplitude is minimised TX beam 1 should be centred on the QPD in the reference interferometer. Due to the limited SNR of the beam centroid measurement the next step would be to optimise the interferometer signals with a similar method using the DWS signals. When the complete procedure is finished the signals in the reference interferometer on OB 1 should be optimised due to symmetry.

Compared to the fibre implementation the free beam option is much more complex. Therefore the possibility of failure is higher. A failure of one actuator means that the overlap of both beams in the backlink path, which is needed for the non-reciprocity, is not given for all MOSA movements anymore. Thus the non-reciprocity of the backlink path would increase significantly. Hence the free beam backlink path has to be redundant to guarantee operation. Redundancy can be implemented similarly to the fibre backlink path. This means an adjustable half-wave plate and a polarising beam splitter have to be implemented in order to switch between the backlink paths. The beam routing between the OBs is not as flexible as the backlink fibre. Space has to be reserved for the actuators on the OBs, which allow pointing of the TX beams towards the other OB.

5.5 Technology demonstrator experiments

In the last two sections several important modifications of the current LISA baseline design have been discussed that avoid degradation of the interferometer sensitivity by straylight. In this section these modifications will be compared by weighting their impact on different parts of the current LISA baseline design. A goal of this comparison is to select solutions which have the lowest impact on the design and can be tested individually within new technology demonstrator experiments. These technology demonstrator experiments will be described. In the end a LISA backlink simulator with moving OBs will be sketched.

Table 5.7: Trade-off table for the impact of different straylight suppression techniques on the current LISA baseline design. In every category the impact of each modification onto the reference design is compared to the other modifications. The impacts are weighted from 0 to -3.

	Balanced detection	Attenuation	Direct measurement
Laser system	0	0	0
Optics	-3	-1	-1
Mechanics	0	0	0
Opto-electronics	-3	0	-2
Phasemeter	-3	-1	-3

	Frequency separation	Polarisation	Free beam
Laser system	-2	0	0
Optics	-1	-2	0
Mechanics	0	-1	-2
Opto-electronics	-1	0	0
Phasemeter	-1	-2	-1

5.5.1 Comparison and selection

The afore mentioned modifications to the current LISA baseline design to avoid the influence of straylight on the interferometer signals need to be compared to select one or more of them for future experimental investigations. The reference for this trade-off table is an imaginary LISA where the backlink path is realised via a hypothetical fibre which is free of straylight. The introduced solutions for the straylight problem of a real optical bench backlink are then compared to this reference design in different categories that are set by the author. These categories are

1. **Laser system:** TX/LO laser, Electro-Optic Modulator (EOM), fibre amplifier, Fibre Injector Optical Subassembly (FIOS), frequency and intensity stabilisations
2. **Optics:** ultra-stable baseplate, beam splitter /combiner, imaging optics
3. **Mechanics:** actuators
4. **Opto-electronics:** quadrant photodiode, front-end electronic
5. **Phasemeter:** number of channels, quality of optical signals

The impacts of the modifications on the reference design are described in the following paragraphs. Thereby the impact of each modification onto the reference design is compared to the other modifications in every category. The impacts in each category are weighted from 0 to -3 to find out, which modification has the highest impact in each category. 0 means no changes with respect to the reference and -3 maximum changes. These numbers are collected in the trade-off Table 5.7.

So far, the straylight suppression via balanced detection was the only proven solution for the backlink fibre path. In this configuration in each interferometer both output ports of the beam combiner have to be equipped with an additional beam splitter, because

redundancy has to be guaranteed for balanced detection (Optics = -1). Each of the output ports of these beam splitters have to be equipped with imaging optics (Optics = -1) and quadrant photodetectors (Opto-electronics = -3). These consume including the imaging optics quite an amount of space on the OB. Therefore the size of the OB has to be increased (Optics = -1). At least the signals from all photodetectors in the science interferometer have to be analysed by a phasemeter to not waste power of the RX beam (Phasemeter = -2). Finally the optical signals are still degraded by straylight (Phasemeter = -1).

The attenuation of straylight by double passing of high transmissive optics at the input of the FIOS is a simple solution for the backlink fibre path. The splitting ratio in front of the TX FIOS is implemented by design and therefore an additional beam splitter with a ratio of 99:1 is needed at the backlink FIOS (Optics = -1). The lower limit for the phase read-out calculated via the available laser powers is close to the requirement for the local interferometers (Phasemeter = -1). The attenuation solution has a very small impact on the LISA baseline design with the drawback of the read-out limits due the electronic noise.

For a direct measurement of straylight with the fibre backlink path the DC single-element photodiodes for monitoring and stabilising the TX laser have to be replaced by LISA quadrant photodetectors. Additionally, a second monitor port with these interferometer photodetectors has to be installed in front of the backlink FIOS (Opto-electronics = -2). Therefore additional 16 phasemeter channels are needed (Phasemeter = -2). The optical signals are spoiled by straylight (Phasemeter = -1)

For frequency separation of the backlink fibre path an additional laser running on a separate frequency is used to decouple the reference interferometer from the remaining ones. At least one low power laser with a redundant partner is needed for this (Laser = -1). A redundant FIOS pair is needed, too. (Laser = -1). An additional interferometer with two quadrant photodetectors and eight phasemeter channels are needed (Optics = -1, Opto-electronics = -1, Phasemeter = -1). This solution can be used with the fibre and the free beam implementation of the backlink path. The free beam implementation is neglected here because it would increase the complexity due to the additional actuators.

The integration of the polarisation topology needs a fibre length stabilisation via an actuator to suppress the non-reciprocity due to the difference of the refractive index of the fibre axis (Mechanics = -1). A Digital to Analog Converter (DAC) in the phasemeter and gates within the FPGA are needed (Phasemeter = -1). Special optics on the OB are needed to handle two polarisations. Polarisation optics are needed, too (Optics = -2). The optical signal quality can be degraded by using both fibre axes (Phasemeter = -1).

The backlink free beam path uses the attenuation of the TX beam to suppress straylight. This is already implemented in the baseline design. Mirrors, mounted in actuators are needed to steer the beams between the OBs and to suppress beam pointing noise on the OBs via usage of the reference interferometer signal in a control loop (Mechanics = -2). Within the FPGA gates are needed for the controller and also an additional DAC for the control of the actuators (Phasemeter = -1).

The trade-off table 5.7 will slightly change if the weighting of the individual categories is changed but its key information will not change. The currently baselined balanced detection method has the highest impact in three categories with respect to the reference design. The attenuation and the free beam backlink solutions have the lowest impact with respect to the reference design and should be investigated in technology demonstrator experiments. The attenuation is critical due to the loss of SNR. Therefore the frequency separation topology is chosen as backup solution for the backlink fibre and it has to be tested also in a technology demonstrator experiment. The major drawback of the direct

measurement method is that the optical signals are still degraded by straylight. The polarisation solution for the backlink fibre is critical because both fibre axis are used.

The technology demonstrator experiments are now introduced in the logical order in which they could be performed in the lab. They have to be tested individually at the beginning to verify that each solution yields the required performance and to identify the important parameters to reach the performance. It starts with the attenuation solution for the fibre backlink, followed by the free beam backlink with actuators. Afterwards or in parallel the frequency separation can be investigated. Finally a technology demonstrator experiment, which implements moving OBs and implements three different ways to compare the TX lasers could be performed.

5.5.2 Attenuation demonstrator

According to the last subsection the suppression of straylight by attenuation was the solution which had the lowest impact on the current LISA baseline design. Testing of this method can be realised by an extension of the current backlink fibre experiment at the AEI. The experimental setup is presented in Figure 5.17. In a first step the current noise behavior of the setup should be checked with the LPF modulation scheme and LPF phasemeter. In a next step the current LPF silicon photodiodes have to be replaced by LISA InGaAs quadrant photodetectors which are compatible with the low light powers of the attenuation solution in a later stage of expansion. The contrast in both interferometers and the coupling efficiency into the backlink fibre have to be checked before the mount of fibre coupler TX 1 is exchanged by a new one, which has an integrated unbalanced beam splitter. After this the contrast in interferometer R_1 and the coupling into the fibre coupler LO 1 have to be optimised again. Next the mount of fibre coupler LO 1 has to be exchanged by a new one, which has also an integrated unbalanced beam splitter. Afterwards the contrast in this interferometer and the coupling into the fibre coupler need to be optimised. The same procedure has to be used for the second reference interferometer.

A first measurement will estimate the noise behavior of the setup. For that the fibre couplers of the backlink have to be blocked and the setup noise path needs to be unblocked. The lower limit for the phase read-out given by the beam powers is then well below the requirement and the attenuation of straylight by the beam splitter in front of fibre coupler TX 1 can be checked. If the splitting ratio is sufficient the sensitivity of the non-reciprocity measurement should yield without straylight correction a value which is below the requirement. The splitting ratio of the beam splitter is then changed step by step to check the boundaries. After the boundaries for the splitting ratio have been checked the splitting ratios of all beam splitters in front of the fibre couplers are set to these values.

The backlink fibre needs to be unblocked and the setup noise path needs to be blocked to measure the non-reciprocity of the backlink fibre. The photodetectors need to be replaced by others, which can handle the low power beams. Then the non-reciprocity of the backlink fibre is measured without straylight correction.

5.5.3 Backlink free-beam demonstrator

The general implementation of a backlink free beam within the current LISA baseline was described in Section 5.4.3. A technology demonstrator experiment can be performed with the available backlink fibre experiment at the AEI, too. Figure 5.18 shows the

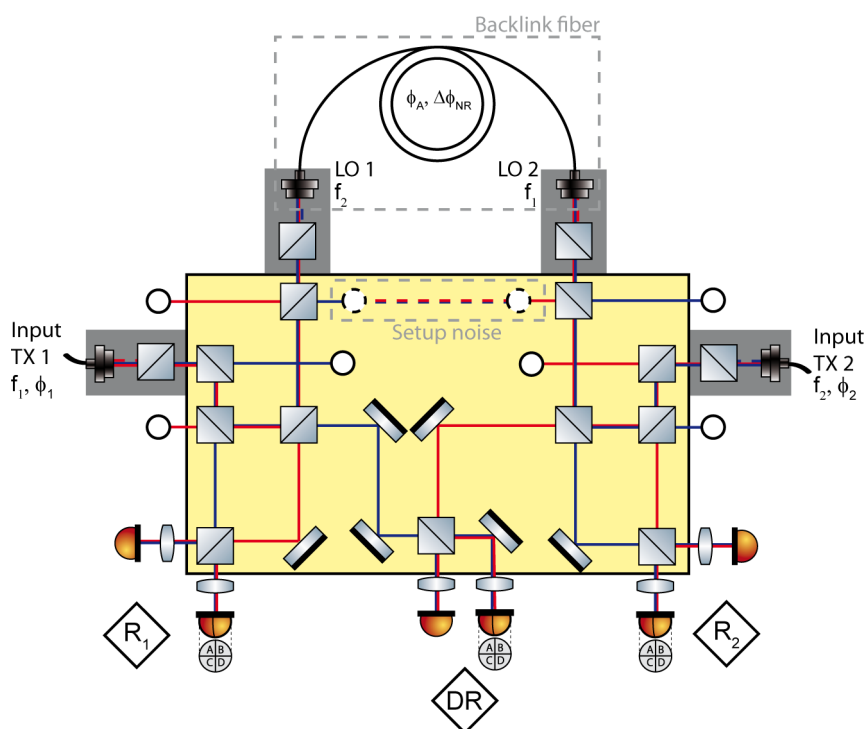


Figure 5.17: Technology demonstrator experiment for the TX laser comparison via a fibre backlink and suppression of straylight via attenuation. In front of each fibre coupler of the AEI backlink fibre experiment an additional optic with reflection to transmission ratio of 98 to 2 is installed to attenuate the SLS.

necessary modifications. The backlink fibre path has to be exchanged by a set of mirrors. The movement of the MOSAs have to be mimicked by mirrors on rotational mounts, see MOSA 1 and MOSA 2 in the inputs of the backlink paths of Figure 5.18. The two piezo-actuated mirrors Actuator 1 and Actuator 2 compensate beam pointing introduced by MOSA 1 and MOSA 2 in a feedback loop using the QPDs of the two reference interferometers as sensor.

The feasibility of performance measurements of the backlink free beam can be tested in three steps. First the rotational mounts are kept stable and the signals in the reference interferometers are optimised via the mirrors Actuator 1 and Actuator 2. Second the rotational mounts MOSA 1 and MOSA 2 simulate a small fraction of the real MOSA movement. The rotational mounts rotate the backlink beams to different points of operations. The backlink actuators Actuator 1 and Actuator 2 stabilise the beams in the reference interferometer and the non-reciprocity is measured over one day. Third the rotational mounts MOSA 1 and MOSA 2 mimic the one year cycle of the MOSA movement in one day. The backlink actuators Actuator 1 and Actuator 2 have to maintain the alignment within the reference interferometer without introducing non-reciprocity.

5.5.4 Frequency separation demonstrator

A technology demonstrator experiment for the frequency separation topology shall verify the separation of MSs from SLSs. Additionally, the results of the non-reciprocity, especially the length stabilisation requirement of the fibre, has to be checked.

Figure 5.19 presents a setup which has two additional interferometers for the estimation

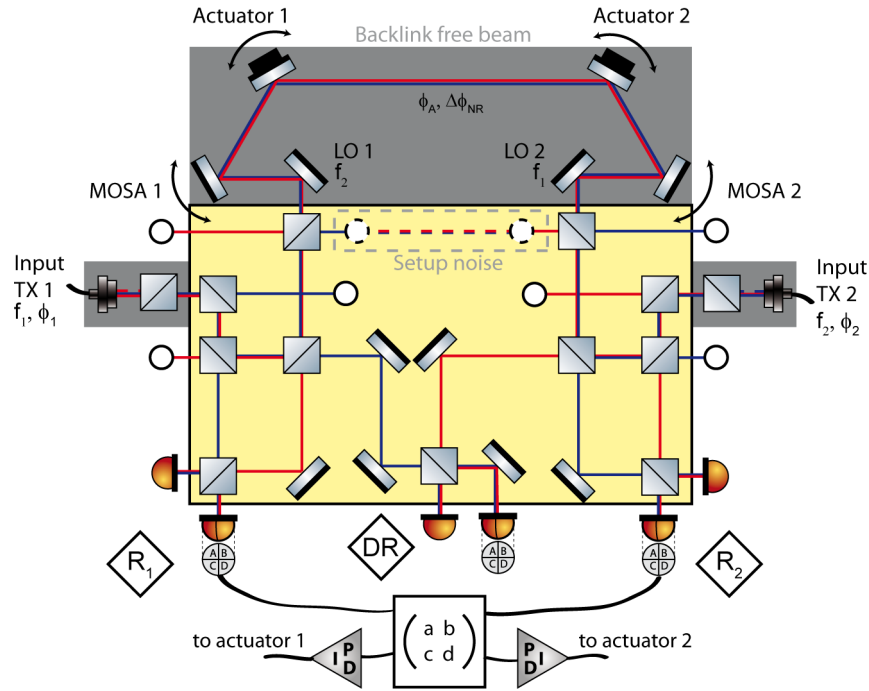


Figure 5.18: Technology demonstrator experiment for the comparison of the two TX lasers via a backlink free beam. A stable optical bench is needed to compare the TX lasers directly. Two movable mirrors are needed to simulate MOSA movements and the other two are needed to suppress beam pointing within the interferometers B1 and B2.

Table 5.8: Beat signals within the additional interferometers of the frequency separation topology.

IFO	Frequency	Phase	Signal	$f_3 = f_4$
DR ₁	$\Delta(f_1, f_4)$	$\Delta(\phi_1, \phi_4)$	MS	$\Delta(f_1, f_3)$
	$\Delta(f_2, f_4)$	$\Delta(\phi_2 + \phi_A + \phi_U, \phi_4)$	SL	$\Delta(f_2, f_3)$
DR ₂	$\Delta(f_2, f_3)$	$\Delta(\phi_2, \phi_3)$	MS	$\Delta(f_2, f_3)$
	$\Delta(f_1, f_3)$	$\Delta(\phi_2 + \phi_A + \phi_D, \phi_3)$	SL	$\Delta(f_1, f_3)$

of the non-reciprocity in comparison to the setup in Figure 5.12 on page 114.

The signals within the two interferometers DR₁ and DR₂ are written down in Table 5.8. The separation of measurement and the SLSs are also valid for these interferometers.

The phases measured within these interferometer are:

$$\phi_{DR1} = \phi_1 - \phi_4 \quad (5.48)$$

$$\phi_{DR2} = \phi_2 - \phi_3 \quad (5.49)$$

The following interferometer signals have to be combined in data post-processing to calculate the non-reciprocity of the fibre.

$$(\phi_{B1} - \phi_{DR2}) - (\phi_{B2} - \phi_{DR1}) = \phi_U - \phi_D \quad (5.50)$$

According to Subsection 3.5.3.1 the achievable length stability due to temperature noise depends on the armlength matching in the interferometers under the assumption that the

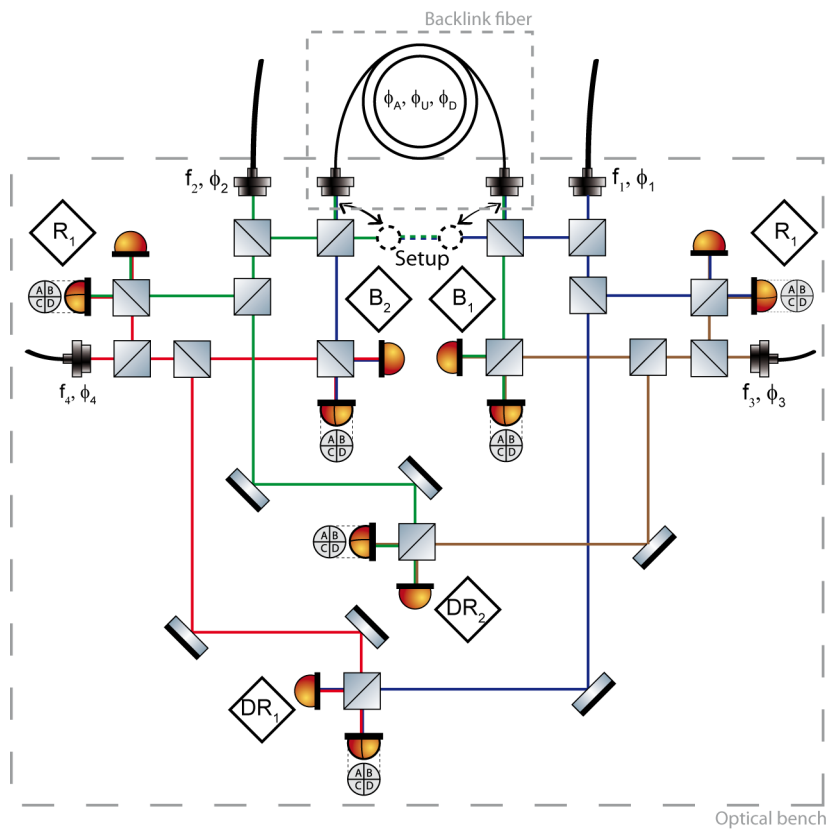


Figure 5.19: Technology demonstrator experiment for the comparison of the two TX lasers via a backlink fibre with an additional laser serving as LO. The upper part of the experiment is comparable to the layout for LISA. The lower part of the experiment with the two interferometer DR1 and DR2 is used to detect the non-reciprocity.

breadboard is isotropic in expansion at low frequencies. The pathlengths of the interferometer outside of the reciprocal paths can be matched easily to a value of about 0.1 m or better. A prototype of the frequency separation experiment can be built on a breadboard for example from the Carbon EC Series from PRO-Lite technology [135]. This has a CTE of $2.5 \cdot 10^{-6} \text{ 1/K}$. Taking a maximum temperature noise of $100 \mu\text{K}/\sqrt{\text{Hz}}$ at 1 mHz into account, the expansion of the breadboard should be at a level of $2.5 \cdot 10^{-10} \text{ 1}/\sqrt{\text{Hz}}$ at 1 mHz. This level is sufficient to clarify the questions of the requirement for the stabilisation of the backlink fibre and the straylight separation. Therefore baseplates made of a low expansion material like ULE, ZerodurTM or Super Invar (CTE $\approx 0.68 \cdot 10^{-6} \text{ 1/K}$) are not required.

The posts of optics are more sensitive to vibrations the higher they are. This might introduces tip and tilt noise of the posts which couples then into the optical pathlength noise. The coupling factor can be reduced by decreasing the beam height of the experiment from the standard 0.1 m down to 0.03 m or less. Additionally each interferometer can be built up by one single-element photodiode and one quadrant photodiode. The latter one can be used to perform DWS measurements and correct for this in data post-processing.

5.5.5 LISA like backlink path demonstrator

A LISA-like backlink path demonstrator needs two rotatable OBs which is incompatible with a direct comparison of the two TX lasers to obtain directly the non-reciprocity of the

backlink path. The information obtained from a single backlink path implementation is the comparison of the TX lasers plus the non-reciprocity of the backlink path implementation. Thus, the difference of two backlink paths is the difference of both non-reciprocities. Therefore comparing two identical implementations of two backlink paths would cancel common-mode noise of the non-reciprocity. Therefore different implementations of the backlink paths are needed to reduce the common-mode non-reciprocity. With two different backlink path implementations it would not be possible to identify, which backlink path is not working if the performance is not sufficient. Therefore the technology demonstrator experiment, which implements moving OBs needs at least three different techniques to compare the TX lasers.

Figure 1 in Appendix 3 sketches an experiment, which has moving OBs and three different implementations of the backlink path. These implementations are the backlink fibre with attenuation, the backlink fibre with additional LO and the backlink free beam. This results in five interferometers per OB. The optics for the interferometers need to be bonded with the technique hydroxide-catalysis bonding to an ultra-stable OB made of an ultra-low expansion material. To characterise the interferometers an additional direct reference interferometer is implemented, which can be used when the two OBs are rigidly connect via ultra-low CTE spacers. This interferometer does not prevent individual testing of the backlink paths. A quasi-monolithic setup cannot be modified after building. Therefore the risk to waste working hours have to be minimised by pre-experiments. A list of steps that needs to be taken to build this experiment and the required components are listed in the next paragraph briefly without making a claim to be complete.

From the knowledge obtained from the design of the picometer, the backlink fibre, the polarisation optic, the telescope simulator experiments each baseplate has to be at least 250 x 250 mm to bond five interferometers. For this approximately 25 optics with different coatings per baseplate are needed. Each interferometer needs to be equipped with one QPD and one SEPD. Therefore a phasemeter with 50 channel is required to measure all backlinks at the same time.

5.6 Conclusions

In conclusion, the possible implementations of the backlink path within the LOB were summarised, extended and reviewed. These information was used to propose new technology demonstrator experiment for the backlink path of the LOB.

A integral part of this discussion was the summary and the extension of the already performed non-reciprocity measurements of a single-mode polarisation-maintaining fibre at the AEI. This was complemented by the summary and extension of the theoretical knowledge regarding the backlink fibre and the straylight degradation of the optical signals. Finally a connection between the experimental data and the theoretical knowledge was drawn.

This was followed by the introduction of already known and completely new backlink path implementations for the LOB. These could be split into two groups: Techniques to suppress the influence of straylight and techniques to avoid the influence of straylight completely. The proposed backlink path implementations were compared to find techniques, which have the lowest impact on the LISA baseline design and do not suffer from straylight. For the selected techniques independent technology demonstrator experiment were described. In the end a LISA-like technology demonstrator experiment which uses three different ways to compare the TX lasers and does have movable OBs was sketched.

The main object of this thesis was the development of core elements to test the LOB focusing on electro-optical measurement systems and test devices.

In the second chapter of this thesis the emphasis was on possible solutions to measure optical pathlengths on the LOB. A LPF modulation scheme and a LPF phasemeter was used to verify the LISA requirements for the PM read-out with two quasi-monolithic, heterodyne MZIs on a ZerodurTM OB. The noise level of the phase measurement chain consisting of photodiodes, preamplifier, and LTP phasemeter was measured as $0.4 \text{ pm}/\sqrt{\text{Hz}}$ increasing with $1/f$ for frequencies below 4 mHz. A length measurement with an optical pathlength noise of $1.5 \text{ pm}/\sqrt{\text{Hz}}$ for frequencies above 20 mHz increasing with $1/f$ towards lower frequencies was demonstrated. A beam pointing read-out noise of $3 \text{ nrad}/\sqrt{\text{Hz}}$ for frequencies above 5 mHz increasing with $1/\sqrt{f}$ towards lower frequencies was experimentally verified, too. Two other solutions to measure optical pathlengths on the LOB have been discussed, too. First, a LISA modulation scheme and LISA phasemeter. Second, a LISA modulation scheme including LISA photodetectors and down-conversion to be able to measure with the LPF phasemeter. Both solutions were successfully tested against the requirement for the LISA PM read-out with electrical signals. Additionally, the results of the LPF modulation scheme and LPF phasemeter achieved with the quasi-monolithic MZIs can be transferred to the other two solutions. Thus, the picometer experiment is an important testbed for LISA photodetectors and LISA phasemeter in the future.

Chapter three dealt with options to close the optical interfaces of the LOB to the PM and to the telescope. An OB, comprising four interferometers, was used to measure the optical pathlength stability of actuators. These will be placed on the interface simulators to align the beams with respect to the LOB reference frame within the interfaces. The thermal expansion of the actuator assembly was theoretically assessed and experimentally verified by reducing the effective CTE of an actuator assembly by implementing a simple compensation stage. An optical pathlength noise of $1.5 \text{ pm}/\sqrt{\text{Hz}}$ at a frequency of 200 mHz increasing with $1/\sqrt{f}$ towards lower frequencies was demonstrated with the simple compensated actuator assembly installed. The effective CTE of the simple compensated actuator assembly was measured in a temperature stable environment. It was $50 \text{ nm}/\text{K}$. In a next step a more elegant compensation stage was integrated in the actuator assembly. An optical pathlength noise of $0.6 \text{ pm}/\sqrt{\text{Hz}}$ down to frequencies

of 20 mHz increasing with $1/f^2$ towards lower frequencies was demonstrated with the elegant compensated actuator assembly installed. The effective CTE of the elegant compensated actuator assembly was measured within a stable temperature environment and by modulating the temperature of the actuator assembly. The respective measured effective CTEs were 177 nm/K and 241.5 nm/K. The effective CTE has to be reduced further by improving the compensation stage in order to be compatible with the requirements of the LOB. It was recommended to build a smaller OB, with an interferometer setup similar to the polarisation experiment to be able to measure the required effective CTEs and to have comparable conditions to the tests of the LOB [17, pp. 59].

The fourth chapter of this thesis covers the read-out of the optical pathlengths on the LOB with focus on the development of a quadrant photodetector. It was experimentally verified that Silicon photodiodes with a high responsivity at low frequencies are incompatible with the LISA requirements due to their loss of responsivity towards higher frequencies. The silicon photodiode QP22-Q from First Sensor was tested with a responsivity of 0.45 A/W at 30 MHz with a bias voltage of 150 V. It was also shown by deduction from physical properties that APDs increase the shot noise limited read-out noise in the science interferometer of LISA. Therefore they are incompatible with the LISA requirements, too. Thus InGaAs p-i-n photodiodes are most suitable for the implementation in LISA photodetectors. The key aspects of the development of a quadrant photodetector to test the LOB were discussed. For the optical pathlength read-out limit due to electronic noise the input voltage noise of the implemented TIA is as important as its input current noise. Due to electronic noise the impedance of the photodiode is as important for the optical pathlength read-out limit as it is for the bandwidth of the photodetector. A quadrant photodetector using a GAP1000Q QPD from GPD was developed. Its power consumption was measured to approximately 380 mW. The -3 dB bandwidth of all four channels was measured to be 20 MHz. The measured input current noise was less than $4 \text{ pA}/\sqrt{\text{Hz}}$ up to 25 MHz.

The emphasis of the last chapter is on the backlink interface of a LOB to the other LOB on the same satellite. The experimental results of the AEI backlink fibre experimentally were reviewed and a connection between the experimental data and the theoretical knowledge was established. Several new implementations of the backlink path, which completely avoid the degradation of the measurement signal by straylight, were discussed. The most important are: attenuation, frequency separation, and a free beam backlink. According technology demonstrator experiments were proposed and described in detail

1 Matlab code for data post-processing

This Matlab code was used at the picometer experiment, see Chapter 2, and at the actuator experiment, see Chapter 3, for post-processing of the measured data. The presented snippet of code was used to improve the measured optical pathlength noise of the length measurement via linear fitting of measured beam pointing, obtained using DWS, to the length measurement. The general procedure presented in this snippet of code can be used for the improvement of the length measurement using laser intensity or temperature at the experiment, too.

```
%% Correct DWS noise

% Setup of filter
pl_hip = plist(...
    'type', 'bandpass', ...
    'fs', fs, ...
    'fc', [0.005 0.05], ...
    'order', 2 ...
);
hp = miir( pl_hip );
pl_hp = plist(param('filter', hp));

% Filter length measurement and noise source
DWS_eta_1_fil = filter(DWS_eta_2, pl_hp);
DWS_phi_1_fil = filter(DWS_phi_2, pl_hp);
length_n_fil = filter(length_n, pl_hp);

% Split unfiltered and filtered length measurement and noise
source
length_n_split = split(length_n, spl1);
length_n_fil_split = split(length_n_fil, spl1);
DWS_eta_1_fil_split = split(DWS_eta_1_fil, spl1);
DWS_phi_1_fil_split = split(DWS_phi_1_fil, spl1);
DWS_eta_1_split = split(DWS_eta_2, spl1);
DWS_phi_1_split = split(DWS_phi_2, spl1);

% Estimate linear coupling coefficient and calculate fitted
noise source
```

```
coeffs_dws = lscov(DWS_eta_1_fil_split, DWS_phi_1_fil_split,
    length_n_fil_split);
fit_dws     = lincom(DWS_eta_1_split, DWS_phi_1_split,
    coeffs_dws);

% Correct length measurement with fitted noise source
length_n_DWS_split      = length_n_split - fit_dws;
length_n_DWS_split_plus = length_n_split + fit_dws;

% Plot comparison of uncorrected and correct noise spectra
iplot(length_n_split_lpsd, lpsd(length_n_DWS_split_plus, p1),
    length_n_DWS_split_lpsd);
```


2 Mathematica code for straylight calculations

This Mathematica Code was used in Chapter 5 to calculate the influence of straylight onto the measurement phase in a heterodyne MZI and to calculate the reduction of the influence of straylight onto the measurement phase via heterodyne balanced detection.

```
(* :: Package :: *)

<<clear.m
<<demod.m

(*Combined complex amplitude of the straylight beam "as" and the
  measurement beam "a1" at the input of the beam combiner*)
a1s = a1 Exp[I wm t + I phi1] + as Exp[I phis]

(*Complex amplitudes at the outputs "out1" and "out2" of the
  beam combiner*)
o1 = rho a1s + I tau a0 Exp[I phi0]
o2 = rho a0 Exp[I phi0] + I tau a1s

(*Absolute value squared of the complex amplitude or power at
  the outputs "out1" and "out2" of the beam combiner *)
p1 = power[o1]
p2 = power[o2]

(*Extraction of the signal content at the angular frequency "
  omega_m"*)
sig1 = s[p1,1]
sig2 = s[p2,1]

(**)
(*Calculation of the influence of the straylight onto the
  measurement phase for output 1 of the beam combiner*)
(**)

(*Expansion of the equation for the power at output 1 of the
  beam combiner in expressions*)
x1 = TrigExpand[sig1]

(*Sorting of the expanded equation x1 after sine "sx" and cosine
  "cx" content. Verification of procedure with "cx". "cx"
  should be equal to zero*)
sx = x1 /. {Cos[t wm]->0}
cx = x1 /. {Sin[t wm]->0}
ex = Simplify[x1-sx-cx]

(*Reference in LTP phasemeter has identical angular frequency "
  omega_m". Thus this part of "sx" and "cx" can be removed*)
```

```

sx2 = Simplify[sx/Sin[wm t]]
cx2 = Simplify[cx/Cos[wm t]]

(*Amplitude and phase of the complex amplitude of the
  measurement signal with straylight within the LTP phasemeter
  *)
pm = cx2 + I sx2

(*Amplitude and phase of the complex amplitude of the
  measurement signal without straylight within the LTP
  phasemeter*)
pmr = pm /. as ->0

(*Difference between the complex amplitude with and without
  straylight / meaning straylight influence*)
pmdiffVector = FullSimplify[pm/pmr]

(*Influence of the straylight onto the phase measurement with
  the LTP phasemeter*)
pmPhase=ComplexExpand[Arg[pmdiffVector], TargetFunctions -> {Re,
Im}]

(*Series expansion of the influence of the straylight onto the
  phase measurement around "as" around zero to first order*)
pmPhaseTaylor=Normal[Series[pmPhase,{as,0,1}]]

(*Result: Simple equation for the influence of the straylight
  onto the phase measurement*)
pmPhaseTaylor=FullSimplify[ComplexExpand[pmPhaseTaylor]]

(**)
(*Calculation of the straylight influence onto the phase
  measurement with the LTP phasemeter using balanced heterodyne
  detection*)
(**)

(*Balanced heterodyne detection by subtraction of the signals
  measured at both output port of the beam combiner*)
baldet = sig1-sig2

(*Expansion of the equation for balanced heterodyne detection*)
x1 = TrigExpand[baldet]

(*Sorting of the expanded equation x1 after sinus "sx" and
  cosine "cx" content. Verification of procedure "cx". "cx"
  should be equal to zero*)
sx = x1 /. {Cos[t wm]->0}

```

```

cx = x1 /. {Sin[t wm] -> 0}
ex = Simplify[x1 - sx - cx]

(*Reference in LTP phasemeter has identical angular frequency "
  omega_m". Thus this part of "sx" and "cx" can be removed*)
sx2 = Simplify[sx/Sin[wm t]]
cx2 = Simplify[cx/Cos[wm t]]

(*Amplitude and phase of the complex amplitude of the
  measurement signal with straylight within the LTP phasemeter
  *)
pm = cx2 + I sx2

(*Amplitude and phase of the complex amplitude of the
  measurement signal without straylight within the LTP
  phasemeter*)
pmr = pm /. as -> 0

(*Difference between the complex amplitude with and without
  straylight / meaning straylight influence*)
pmdiffVector = FullSimplify[pm/pmr]

(*Influence of the straylight onto the phase measurement with
  the LTP phasemeter*)
pmPhase = ComplexExpand[Arg[pmdiffVector], TargetFunctions -> {Re,
  Im}]

(*Series expansion of the influence of the straylight onto the
  phase measurement around "as" around zero to first order*)
pmPhaseTaylor = Normal[Series[pmPhase, {as, 0, 1}]]

(*Result: Simple equation for the influence of the straylight
  onto the phase measurement with balanced detection*)
pmPhaseTaylor = FullSimplify[ComplexExpand[pmPhaseTaylor]]

```

3 Backlink fibre experiment

The experiment, which is sketched in Figure 1, was proposed at the end of Chapter 5. It is a backlink fibre experiment, which consists of two moving OBs and integrates three different implementations of the backlink path. These implementations are the backlink fibre with attenuation, the backlink fibre with additional LO and the backlink free beam. An additional direct reference interferometer is implemented to characterise the interferometers, when both OBs are rigidly connect via ultra-low CTE spacers.

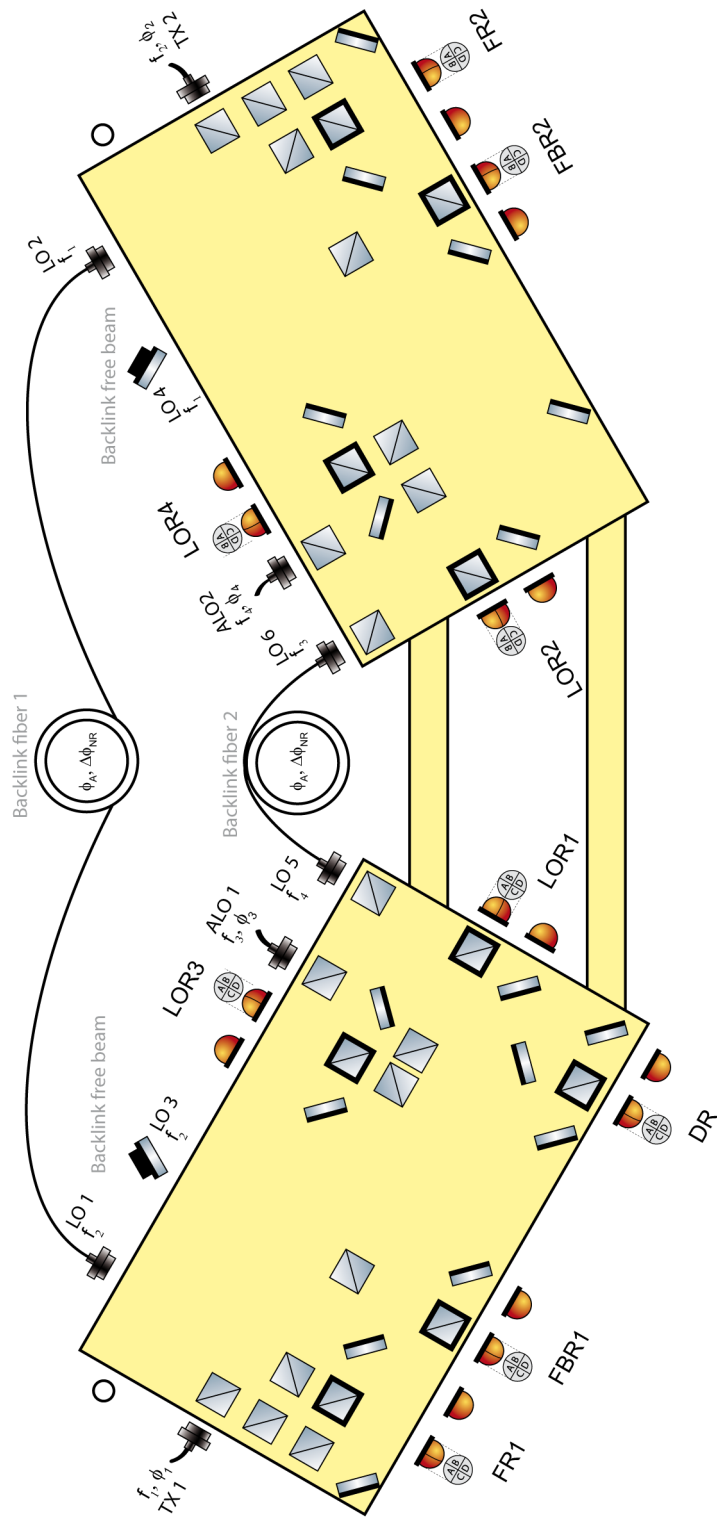


Figure 1: Schematic of a backlink fibre experiment to measure the non-reciprocity of one backlink via the comparison two other backlink implementation. During the measurement the optical benches are rotated by actuators below the optical benches.

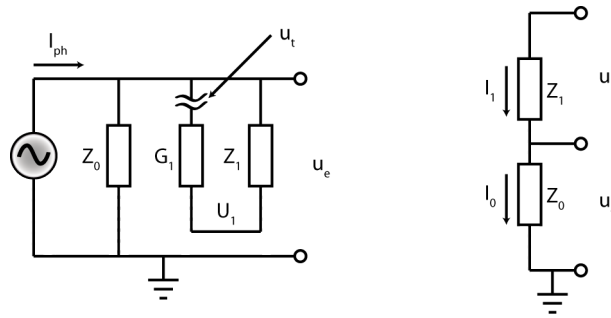


Figure 2: Equivalent circuit of DC coupled TIA for the estimation of the OLG and the according voltage divider.

4 Stability analysis

During the development of the AC/DC decoupled photodetectors for LISA, it was observed that the outputs of the TIAs oscillate at a certain frequency. This behaviour could not be explained in the beginning. The simulated transfer functions of the individual TIAs as well as the DC/AC combinations did not indicate any oscillation. The same holds for the input current noise simulations done with LT Spice IV. A stability analysis of the feedback control within dynamic systems can be performed using a closed-loop transfer function. When the closed loop transfer function is not known the open-loop transfer function can be used to estimate the stability of a feedback control [136].

Figure 4.15 on page 87 depicts a typical TIA under investigation. The theoretical derivation of the OLG of such a TIA is complex due to the fact that it is not only composed of OpAmps but also of transistors. Therefore the calculation of the OLG of an AC/DC decoupled TIA was done numerically by using LT Spice IV. This simulation tool cannot directly measure the OLG. Thus a simple model of an AC/DC decoupled TIA for the measurement of the OLG was developed. This model contains properties, which can be simulated with LT Spice IV. This subsection starts with the derivation of the OLG equation of a DC coupled TIA for LT Spice IV. Afterwards the OLG equations are derived for an AC/DC decoupled TIA. This work has been done in cooperation with Gerhard Heinzl.

4.1 DC coupled transimpedance amplifier

On the left-hand side of Figure 2 an equivalent circuit diagram of a DC coupled TIA is shown. The photocurrent I_{ph} is generated by the current source I_1 . Together with impedance Z_0 the current source represents the photodiode. The DC path is formed by controller G_1 and feedback impedance Z_1 . The input impedance of the gain stage G_1 is integrated into impedance Z_0 . Due to this, they are perfect voltage sensors and no current will flow into G_1 . The control loop has to be split at the input of controller G_1 to disconnect the current source I_{ph} in order to calculate the OLG. At the break point a test voltage u_t is applied. The OLG is the voltage at the output of the control loop u_e divided by the test voltage u_t .

The voltage u_1 at the point between the controller G_1 and the feedback impedance Z_1 is

$$u_1 = G_1 \cdot u_t \quad (1)$$

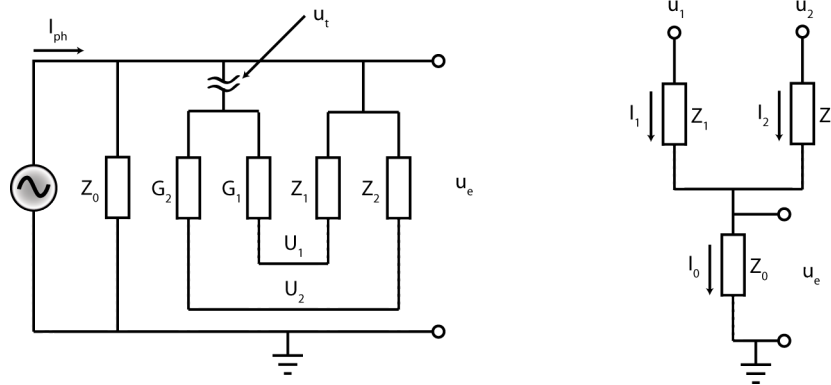


Figure 3: Equivalent circuit of an AC/DC decoupled TIA for the estimation of the OLG.

The voltage divider on the right-hand side of Figure 2 has to be determined to calculate the output voltage of the control loop u_e . The current flowing through the impedances $Z_{1,2}$ are identical. Currents $I_{0,1}$ as function of voltages $u_{e,t}$ are

$$I_0 = I_1 \quad (2)$$

$$I_0 = \frac{u_t \cdot G_1 - u_e}{Z_1} \quad (3)$$

$$I_1 = \frac{u_e}{Z_0} \quad (4)$$

The equations for currents $I_{0,1}$ are used to calculate the OLG.

$$\frac{u_e}{Z_0} = \frac{u_t \cdot G_1 - u_e}{Z_1} \quad (5)$$

$$\Leftrightarrow u_e \left(\frac{1}{Z_0} + \frac{1}{Z_1} \right) = \frac{u_t \cdot G_1}{Z_1} \quad (6)$$

$$\Leftrightarrow \frac{u_e}{u_t} = \frac{G_1}{Z_1} \cdot \frac{Z_0 \cdot Z_1}{Z_0 + Z_1} \quad (7)$$

$$= G_1 \cdot \frac{Z_0}{Z_0 + Z_1} \quad (8)$$

4.2 AC/DC decoupled transimpedance amplifier

On the left-hand side of Figure 3 an equivalent circuit diagram of an AC/DC decoupled TIA is depicted. The photocurrent I_{ph} is generated by the current source I_1 . The current source together with impedance Z_0 represents the photodiode. The DC path is formed by controller G_1 and feedback impedance Z_1 . The AC path is formed by controller G_2 and feedback impedance Z_2 . The input impedances of two gain stages $G_{1,2}$ are integrated into impedance Z_0 . This makes them to perfect voltage sensors and no current will flow into $G_{1,2}$. The OLG of the control loop can be calculated by splitting the feedback loop at the inputs of gain stages $G_{1,2}$. At this point a test voltage u_t is applied. The OLG is the voltage at the output of the control loop u_e divided by the test voltage u_t .

Voltages $u_{1,2}$ at the points between controllers $G_{1,2}$ and feedback impedances $Z_{1,2}$ are

$$u_1 = G_1 \cdot u_t \quad (9)$$

$$u_2 = G_2 \cdot u_t \quad (10)$$

The output voltage of control loop u_e can be calculated by determining the voltage divider shown on the right-hand side of Figure 3. The current flowing through impedance Z_0 is the sum of the current flowing through impedances $Z_{1,2}$. Currents $I_{0,1,2}$ as function of voltages $u_{e,t}$ are

$$I_0 = I_1 + I_2 \quad (11)$$

$$I_0 = \frac{u_e}{Z_0} \quad (12)$$

$$I_1 = \frac{G_1 \cdot u_t - u_e}{Z_1} \quad (13)$$

$$I_2 = \frac{G_2 \cdot u_t - u_e}{Z_2} \quad (14)$$

The equations for currents $I_{0,1,2}$ are used to calculate the OLG.

$$\frac{u_e}{Z_0} = \frac{G_1 \cdot u_t - u_e}{Z_1} + \frac{G_2 \cdot u_t - u_e}{Z_2} \quad (15)$$

$$= u_t \left(\frac{G_2}{Z_2} - \frac{u_e}{u_t Z_2} + \frac{G_1}{Z_1} - \frac{u_e}{Z_1 u_t} \right) \quad (16)$$

$$\Leftrightarrow \frac{u_e}{u_t Z_0} = \frac{G_1}{Z_1} + \frac{G_2}{Z_2} - \frac{u_e}{u_t} \left(\frac{1}{Z_1} + \frac{1}{Z_2} \right) \quad (17)$$

$$\Leftrightarrow \frac{u_e}{u_t} \left(\frac{1}{Z_0} + \frac{1}{Z_1} + \frac{1}{Z_2} \right) = \frac{G_1}{Z_1} + \frac{G_2}{Z_2} \quad (18)$$

$$\Rightarrow \frac{u_e}{u_t} = \left(\frac{G_1}{Z_1} + \frac{G_2}{Z_2} \right) \cdot \frac{Z_0 Z_1 Z_2}{Z_0 + Z_1 + Z_2} \quad (19)$$

The next step is to exchange the non-measurable values within the calculated OLG, i.e. $G_{1,2}$, by measurable values, i.e. $u_{1,2}$ within LT Spice IV. Thus some more dependencies have to be written down.

$$u_1 = G_1 \cdot u_e \quad (20)$$

$$i_1 \cdot Z_1 = u_e - u_1 \quad (21)$$

$$u_2 = G_2 \cdot u_e \quad (22)$$

$$i_2 \cdot Z_2 = u_e - u_2 \quad (23)$$

$$i_0 \cdot z_0 = u_e \quad (24)$$

$$i_{ph} = i_0 + i_1 + i_2 \quad (25)$$

The dependencies are used to exchange non-measurable values in Equation 19 by measurable ones. The final equation for the measurement of the OLG with LT Spice IV is

$$\Rightarrow \frac{u_e}{u_t} = \frac{i_1 + i_2 u_1 u_2 - (i_1 u_1 - i_2 u_2) u_e}{i_1 u_1 (u_2 - u_e) + (u_1 - u_e) [i_2 u_2 - i_{ph} (+u_2 - u_e)]} \quad (26)$$

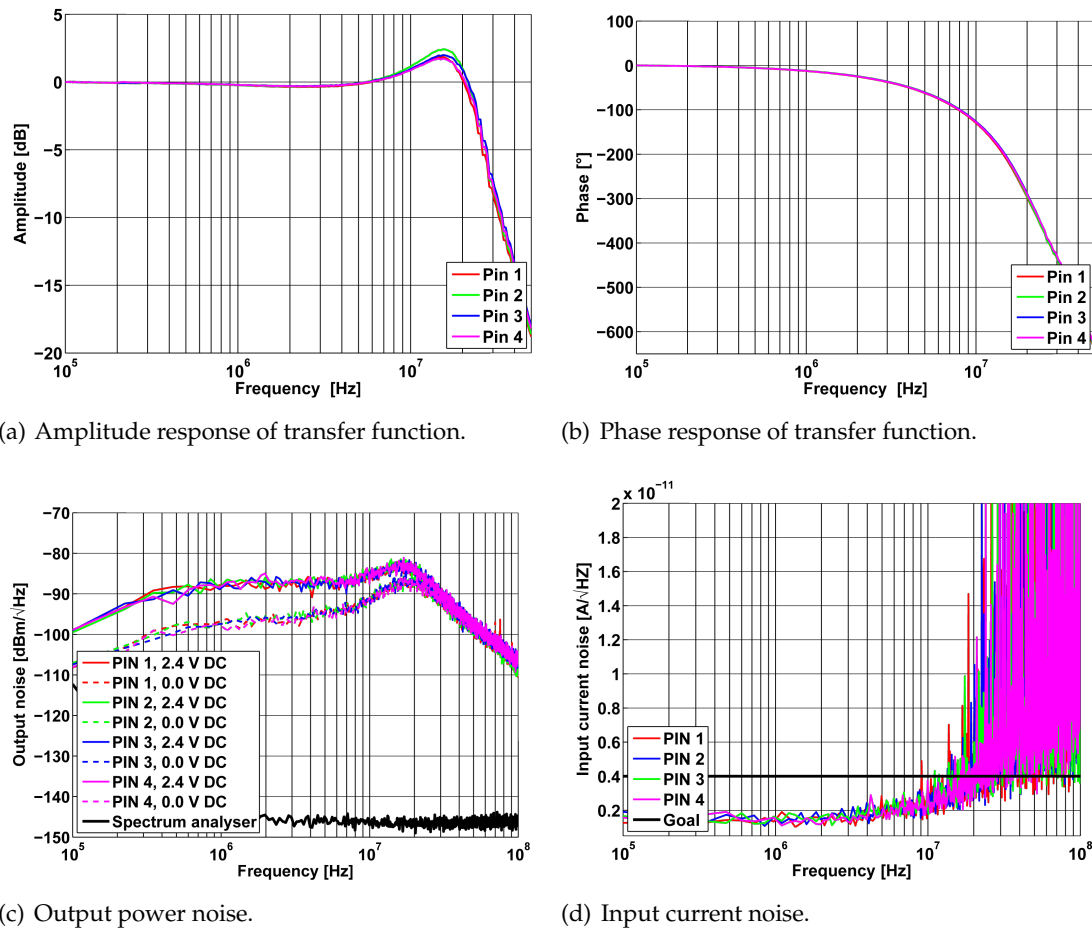


Figure 4: Transfer function and input current noise of a prototype QPD from DSC with 2 mm diameter and a EL5135 OpAmp as TIA.

5 DC coupled photodetector

The DC coupled photodetector is based on the EL5135 OpAmp and the prototype InGaAs photodiode from DSC with 2 mm diameter. This photodiode has a capacitance of approximately 10 pF at 5 V bias voltage. Thus it is electrically comparable to the GAP1000Q photodiode. The schematic is shown in the Appendix 6 in Figure 10. The transfer function is presented in Figure 4. The -3 dB bandwidth of the photodetector is approximately 25 MHz.

Figure 4(c) presents the measurement of the output voltage noise and Figure 4(d) the calculated input current noise of the alternative photodetector design. The lower curve shows the noise of the spectrum analyser. The four dashed curves above show the output voltage voltage of the four channels of the photodetector. The four curves at the top are the output voltage v_{sn} with the light bulb shining on the photodiode. The input current noise n_{el} of the four DC-channels of the photodetector is shown in Figure 4(d). The PCB of this TIAs were shielded. Thus the spikes at 10 MHz and 16 MHz are suppressed. The input current noise n_{el} of the four channels have the same shape and are below the goal for the input current noise up to 20 MHz.

6 Schematics

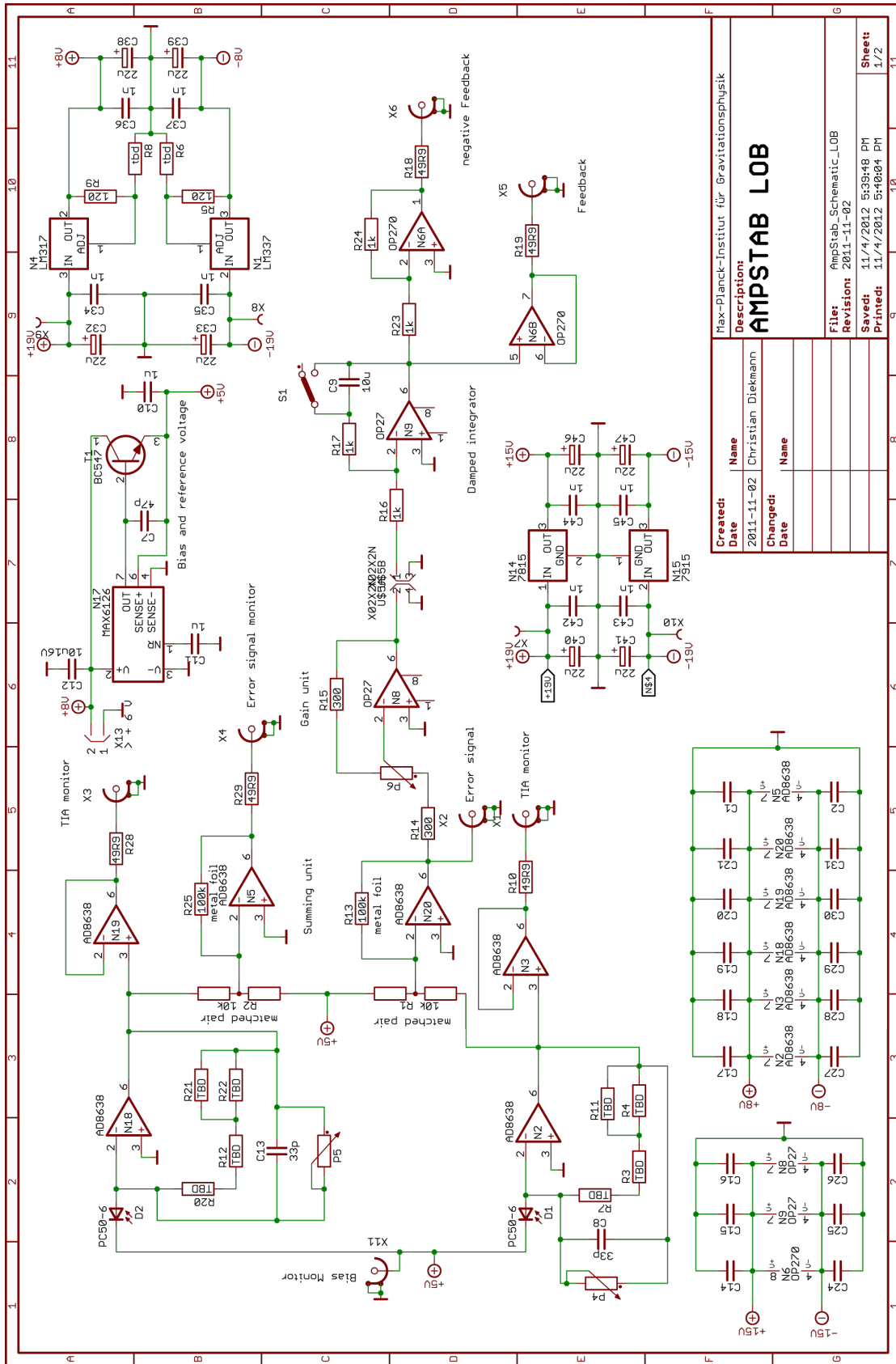


Figure 5: Schematic of a laser intensity stabilisation at low frequencies for the LOB.

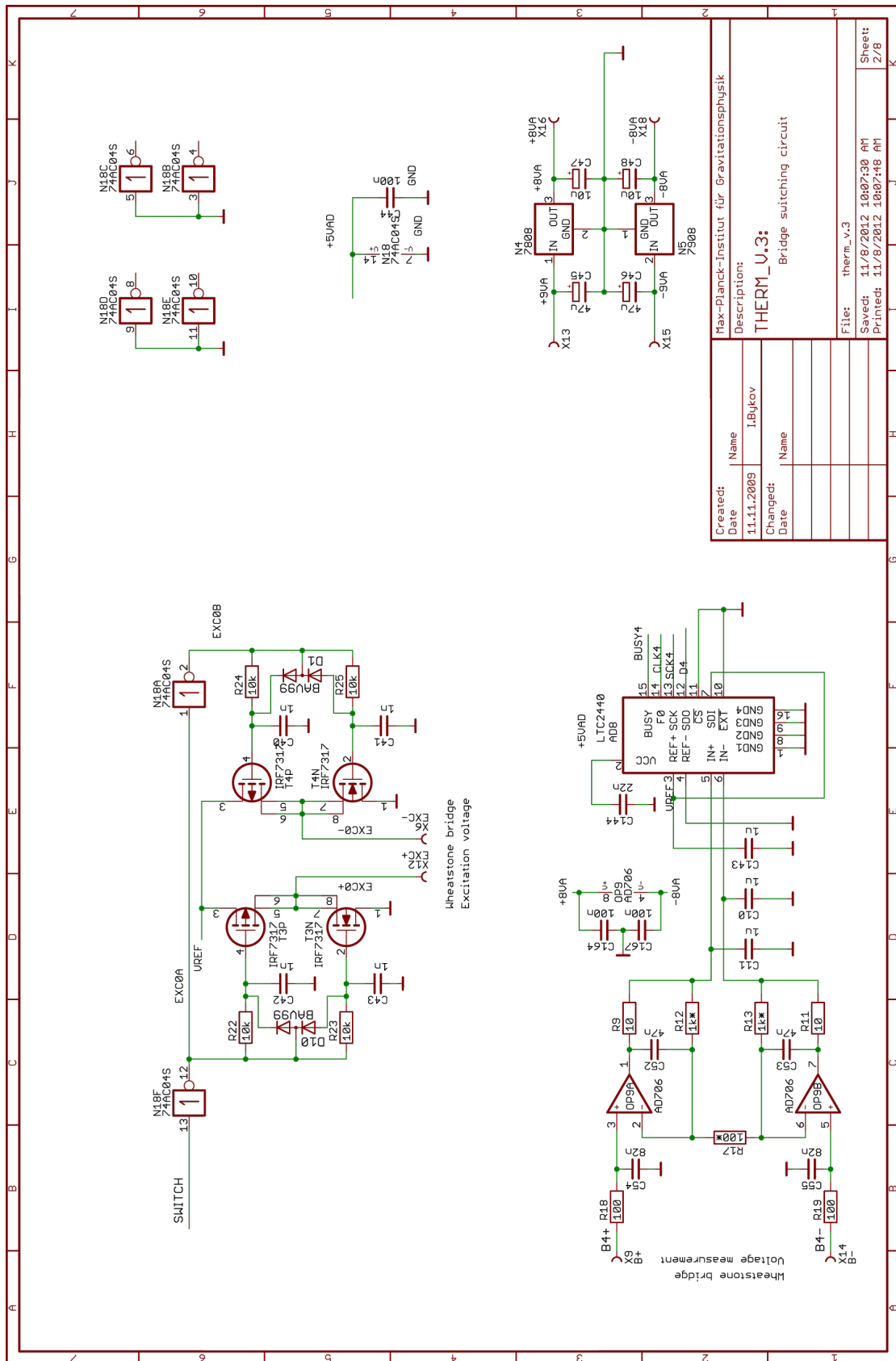


Figure 6: Schematic of the voltage measurement and excitation voltage part of the FPGA-thermometer.

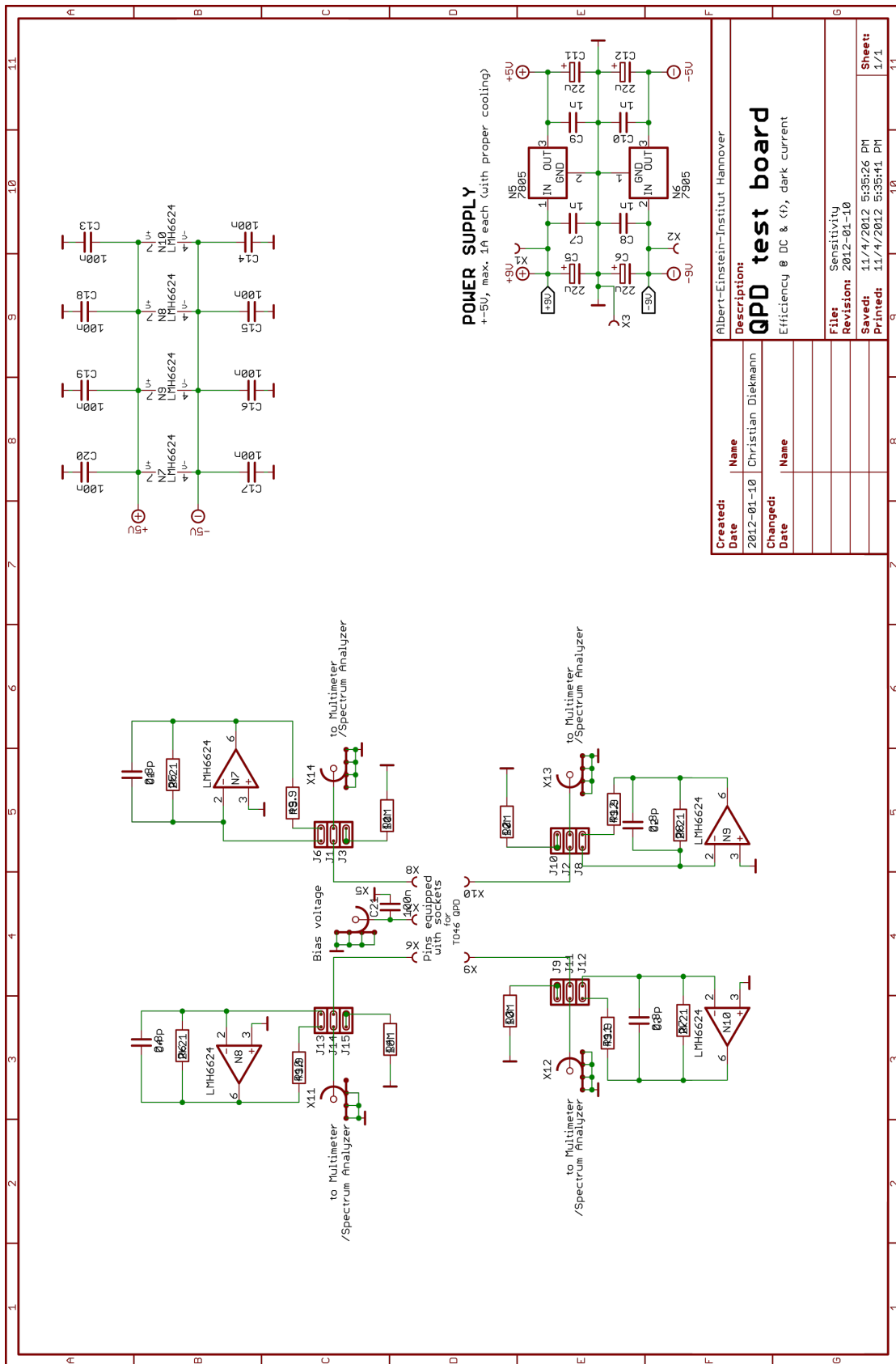


Figure 7: Schematic of a circuit to measure the efficiency of a photodiode as a function of frequency and to measure its dark current.

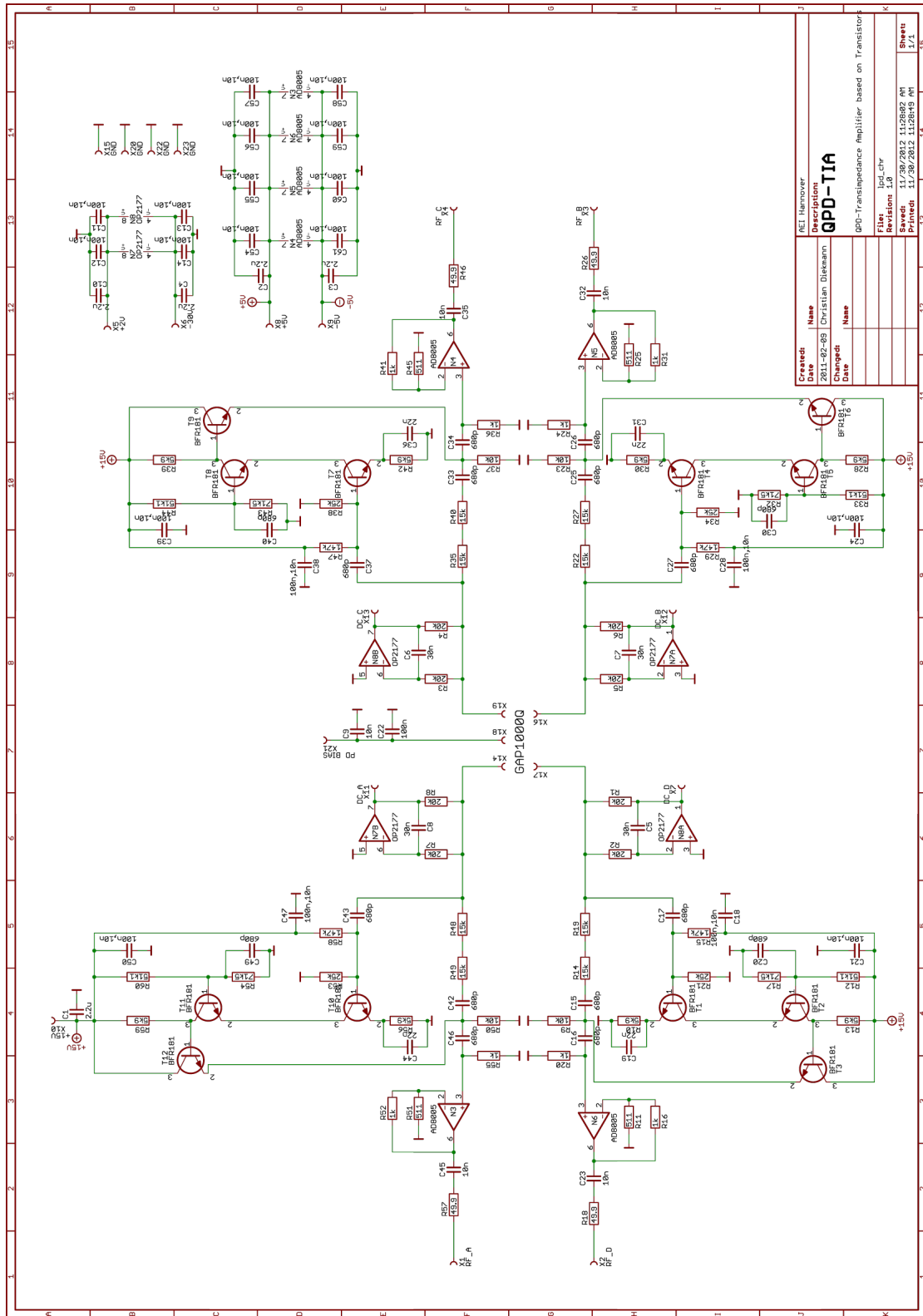


Figure 8: Schematic of an AC/DC-decoupled LOB quadrant photodetector based on the BFR181 transistor and a GAP100Q 1 mm InGaAs QPD. 4 channels per PCB.

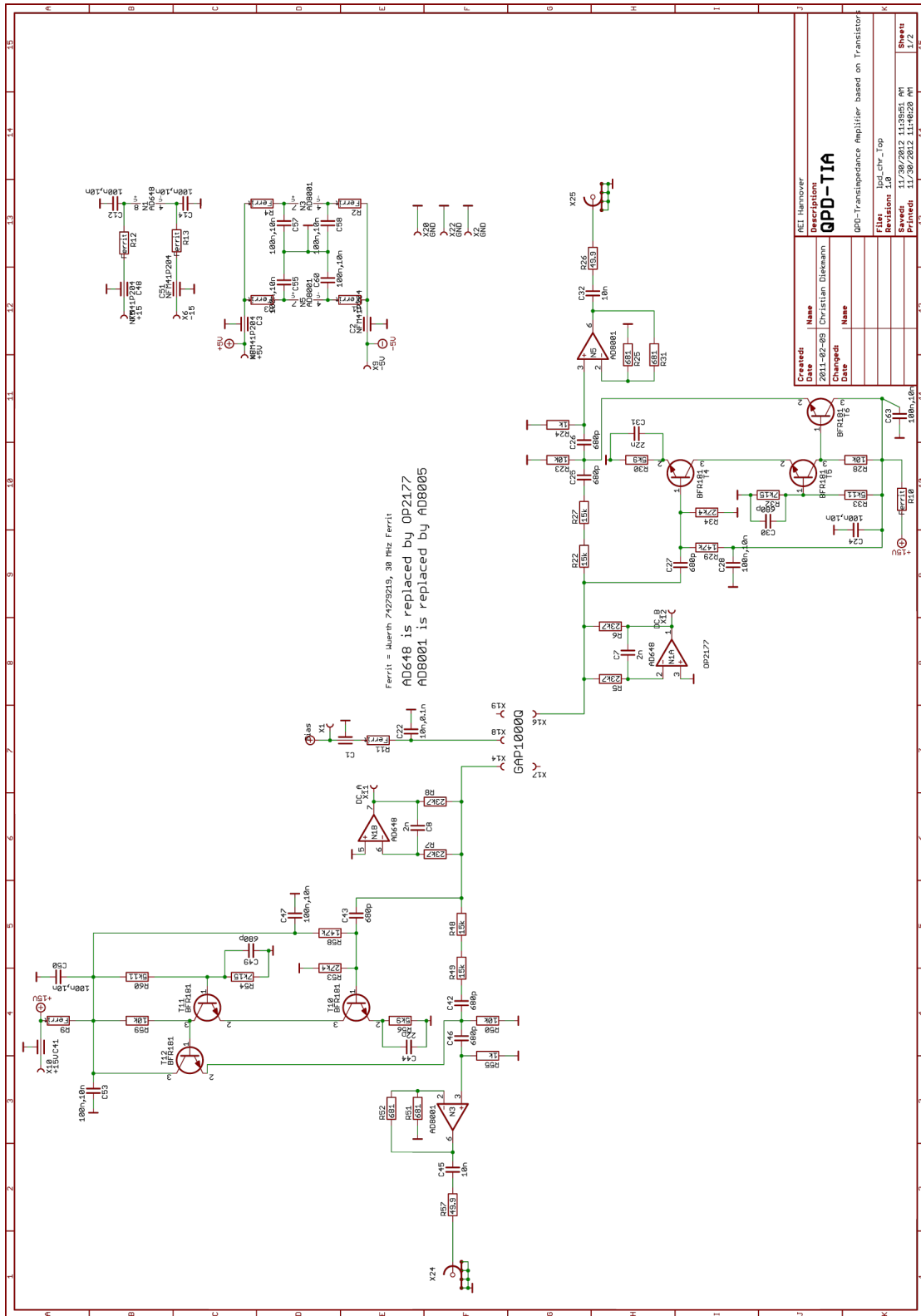


Figure 9: Schematic of an AC/DC-decoupled LOB quadrant photodetector based on the BFR181 transistor and a GAP1000 1 mm InGaAs QPD. 2 channels per PCB.

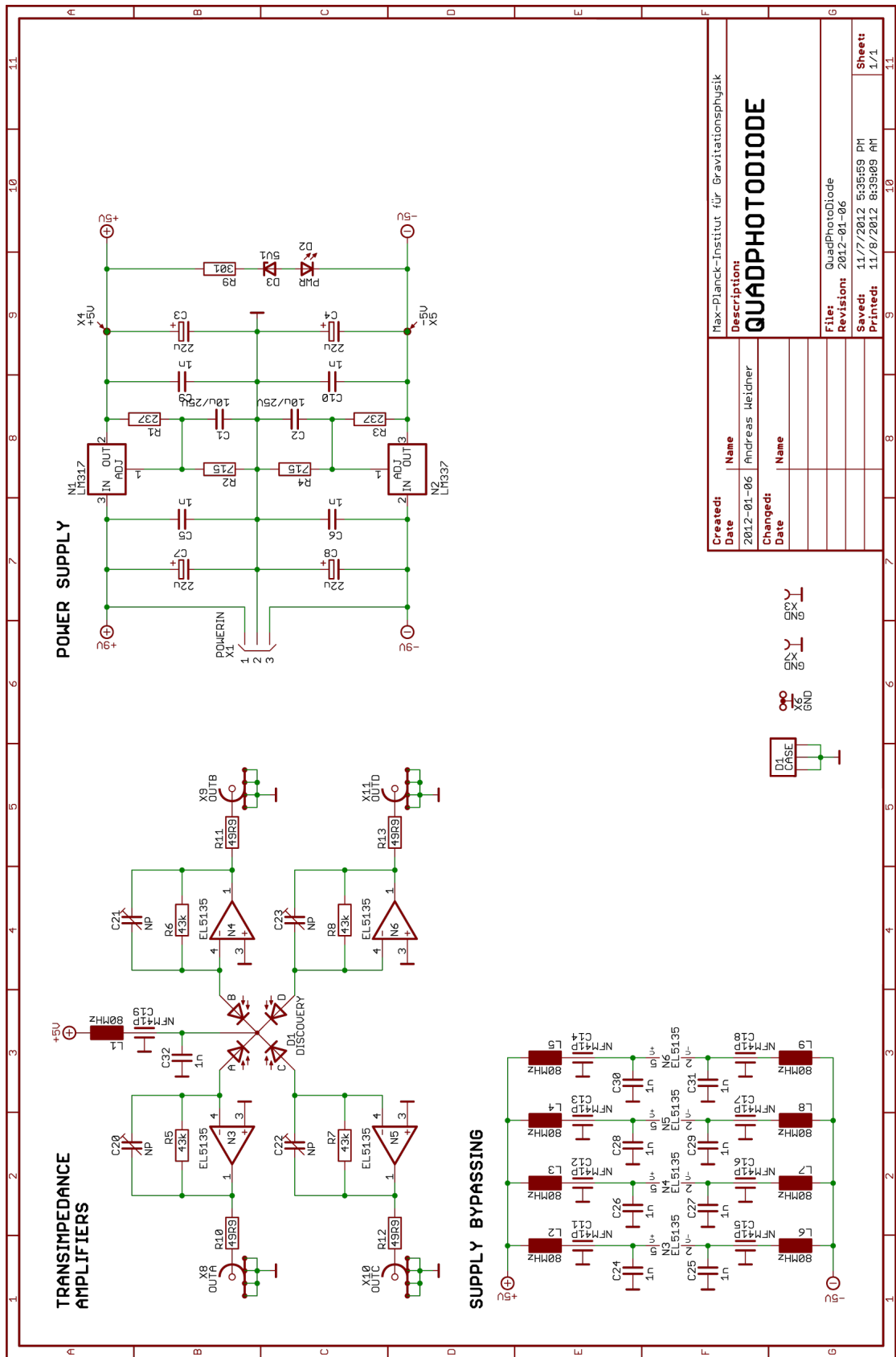



Figure 10: Schematic of a DC-coupled quadrant photodetector based on the EL5135 OpAmp and a DSC 2 mm InGaAs QPD prototype.

7 Data sheets

OEC
Opto-Electronic
Components



YOUR PARTNER

InGaAs Quadrant**GAP1000Q**

Wavelength Range

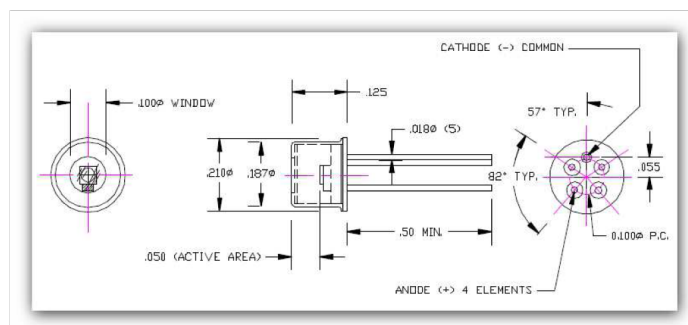
800 nm – 1700nm

Technical Data

Symbol	Conditions @ 25°C	Min.	Max.	Units
Active Area	Dia	1		mm
R _D	850 nm	0.15		A/W
R _D	1300 nm	0.85		A/W
R _D	1550 nm	0.90		A/W
I _D	@ 5V		3.0	nA
C _T	@ 5V, 1MHz		15.0	pF
V _f	@ 10mA		1.2	V
Crosstalk	@ 5V		3.0	%
Tr / Tf	@ 5V		2.5	ns

Maximum Ratings

Symbol	Conditions @ 25°C	Max.	Units
V _R		20	V
T _{OP}	-40 to +85°C		
T _{ST}	-40 to +125°C		
Saturation	Power, per quadrant	600	μW

Package Dimensions**TO46mod Header 5-Pin**

OEC GmbH
Vogelbergstraße 20
D-86441 Zusmarshausen

Tel. +49-(0)8291-18 86-0
Fax. +49-(0)8291-18 86-79
info@oec-gmbh.de
www.oec-gmbh.de

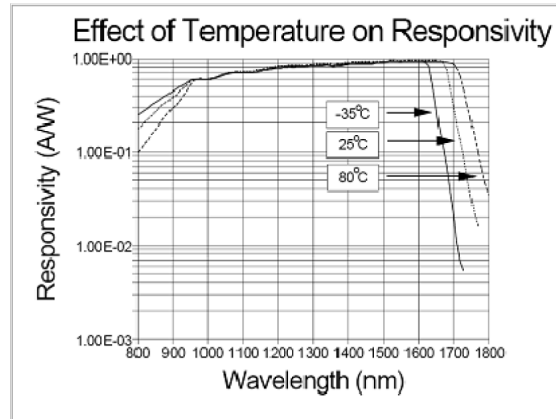
OEC GmbH, Büro Pilsting
Im Langen Moos 7
D-94431 Pilsting
Tel. und Fax. +49-(0)99 53-31 36

Figure 11: Data sheet of the GAP1000Q photodiode from GPD, Page 1 of 2.

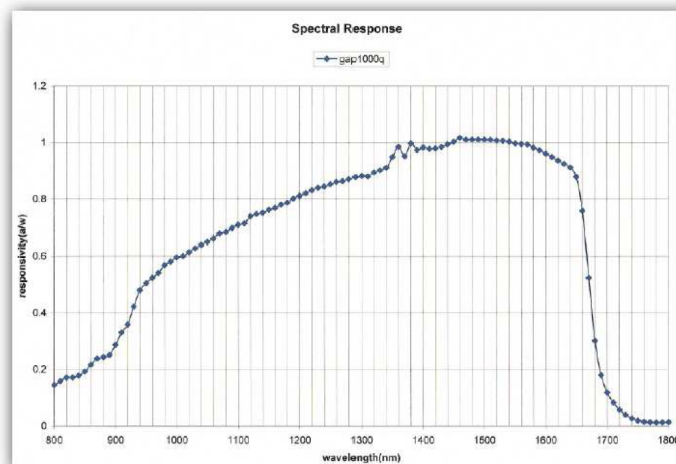
OEC
Opto-Electronic
Components



OEC
YOUR PARTNER



Spectral Response, typically



Other

Centring of chip relative to cap $\pm 25\mu\text{m}$
Separation between quadrants $20\mu\text{m}$

OEC GmbH
Vogelbergstraße 20
D-86441 Zusmarshausen

Tel. +49-(0)8291-18 86-0
Fax. +49-(0)8291-18 86-79
info@oec-gmbh.de
www.oec-gmbh.de

OEC GmbH, Büro Pilsting
Im Langen Moos 7
D-94431 Pilsting
Tel. und Fax. +49-(0)99 53-31 36

Figure 12: Data sheet of the GAP1000Q photodiode from GPD, Page 2 of 2.

PROPERTIES OF TEFLON* TFE FLUOROCARBON RESIN

The combination of chemical and physical properties of Teflon TFE is a consequence of its true fluorocarbon structure. This unusual structure leads to a material which has an almost universal chemical inertness; complete insolubility in all known solvents below 300°C; excellent thermal stability; and unsurpassed electrical properties, including low dielectric loss, low dielectric constant and high dielectric strength. Furthermore, Teflon does not embrittle at very high or at very low temperatures.

PHYSICAL AND THERMAL	
PROPERTIES	TYPICAL VALUES
Specific Gravity	2.15
Tensile Strength, (p.s.i.)	4000
Elongation, (%)	300
Modulus of Elasticity in Tension, (p.s.i.)	0.58×10^5
Thermal Conductivity (cal sec ⁻¹ cm ⁻¹ °C ⁻¹)	6×10^{-4}
Specific Heat (cal gm ⁻¹ °C ⁻¹)	0.25
Thermal Expansion, (°C ⁻¹)	10×10^{-5}
Continuous Use Temperature (°C)	260
10 Minute Endurance Temperature (°C)	325
Melt Temperature (°C)	327
Low Temperature Limit (°C)	Near -273
Flammability	Non-Flammable

ELECTRICAL	
PROPERTIES	TYPICAL VALUES
Dielectric Constant	2.1
Dissipation Factor	.0002
Volume Resistivity (ohm-cm)	$>10^{18}$
Corona Resistance	Fair

ENVIRONMENTAL	
RESISTANCE TO:	RATING
Cold Flow or Cut Through	Fair
Ultraviolet Radiation	Excellent
Nuclear Radiation	Poor †
Electrical-Mechanical Stress Cracking	Excellent
Chemical-Mechanical Stress Cracking	Excellent

*Du Pont Trademark

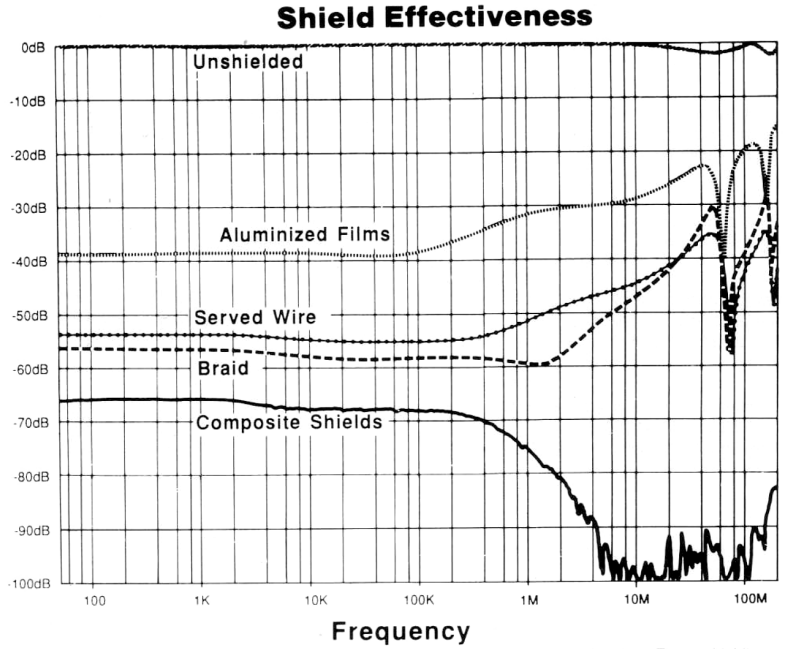
†In the absence of oxygen, radiation resistance is improved by a factor of more than 100.



W. L. GORE & ASSOCIATES, INC.

Figure 13: Data sheet of the GORE PTFE Cable, Page 1 of 3.

SHIELDING METHODS



The graph above indicates only how those particular shields are capable of performing. These shielding values can be changed depending on the method of termination and how the cable is used in a system. The test method used is per MIL-C-85485.

Type	Flexibility	% Coverage	Termination	Mechanical Protection or Resistance to Mech. Abuse	Common Shielding Materials	O.D. Increase	Relative Weight
Braided Shield	Good	85% to 97%	Pigtail, Crimp, Drain Wire & Solder Sleeve, Welded Drain Wire & Shrink Tube	Excellent	Stainless Steel Tungsten Nichrome Iron Nickel Silver-Plated Copper Tinned Copper	.012" - .020"	Heaviest
Served Wire Shield	Excellent	97%	Pigtail, Drain Wire & Solder Sleeve	Very Good	Stainless Steel Tungsten Iron Nickel Silver-Plated Copper Tinned Copper	.008" - .010"	Heavy
Aluminized Film Shields	Excellent	Up to 100%	Drain Wire	Fair	Aluminized Polyester, Polyimide and GORE-TEX [®] Laminates	.002" - .005"	Lightest

[®] GORE-TEX is a registered trademark of W.L. Gore & Associates, Inc.

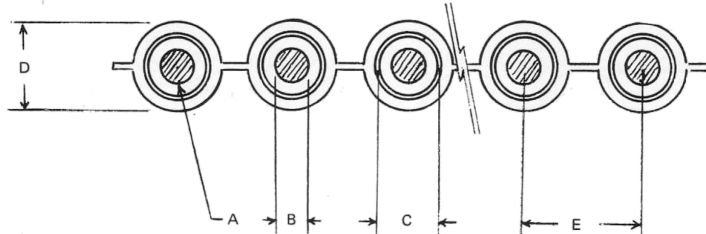
W. L. GORE & ASSOCIATES, INC.

Figure 14: Data sheet of the GORE PTFE Cable, Page 2 of 3.

ROUND CONDUCTOR RIBBON CABLE

TYPE E TEFLON* BRAIDED SHIELD

600 VOLTS



CONSTRUCTION: Primaries are insulated with Teflon PTFE resin in accordance with MIL-W-16878E shielded, and formed into a ribbon cable with homogeneous Teflon jackets and webs.

TEMPERATURE RATING: Insulation -65°C to 200°C SPC Conductors - per MIL-W-16878E.
 -65°C to 260°C NPC Conductors - per MIL-W-16878E.

CONDUCTORS: Silver-plated copper conductors are standard. Special conductors such as nickel-clad copper, stainless steel strands, high-strength copper alloys, silver, pure nickel, copperweld, beryllium copper, etc., may be supplied. Strandings other than those listed are also available.

SHIELDING: Standard braiding material is silver-plated copper. Other materials can be supplied.

COLOR CODING: Standard cables are supplied in a solid color or with different jacket color top and bottom. However, individual color coding of primaries and/or jackets is available.

CONDUCTOR SPACING: The center-to-center spacing of conductors in standard cables is shown under "E" in the table. However, other center-to-center spacings, can be specified including variations with the same cable.

CABLE WIDTH: Any number of conductors up to the maximum shown in the table can be specified. To determine maximum cable width for any given number of conductors, use the following formula:

$$\text{Maximum Width} = (\text{number of conductors} \times \text{center-to-center spacing}) + .010'' \text{ -- or -- } (\text{number of conductors} \times \text{center-to-center spacing}) \times 1.025 \text{ -- which ever is greater.}$$

BONDABILITY: Surface treatment to make the insulation bondable can be specified.

*Du Pont Trademark

**GORE CATALOG NUMBER	AWG (Stranding) A	CONDUCTOR DIAMETER B	NOMINAL OD OF PRIMARIES C	NOMINAL CABLE THICKNESS D	MAXIMUM CENTER-TO-CENTER SPACING E	MAX. NO. OF CONDS.	NOMINAL WEIGHT OF RIBBONS, Lbs/M CONDUCTOR Ft.
A03B010/	18 (19/30)	.049"	.069"	.115"	.146"	14	19.3
A03B020/	20 (19/32)	.040"	.060"	.106"	.138"	15	15.6
A03B030/	22 (19/34)	.032"	.052"	.098"	.130"	16	13.4
A03B040/	24 (7/32)	.024"	.044"	.090"	.122"	17	11.2
A03B050/	24 (19/36)	.025"	.045"	.091"	.122"	17	11.2
A03B060/	26 (7/34)	.019"	.039"	.085"	.114"	18	8.0
A03B070/	26 (19/38)	.020"	.040"	.086"	.114"	18	8.0
A03B080/	28 (7/36)	.015"	.035"	.081"	.106"	19	7.1
A03B090/	30 (7/38)	.012"	.032"	.078"	.103"	19	6.5

**Number of conductors is designated after slash.

W. L. GORE & ASSOCIATES, INC.

Figure 15: Data sheet of the GORE PTFE Cable, Page 3 of 3.

Bibliography

- [1] LISA science team. LISA - Unveiling a hidden universe - Assessment Study Report. Technical report, European Space Agency, February 2011.
- [2] F. Acernese, P. Amico, N. Arnaud, D. Babusci, R. Barille, F. Barone, L. Barsotti, M. Barsuglia, F. Beauville, M. A. Bizouard, C. Boccara, F. Bondu, L. Bosi, C. Bradaschia, L. Bracci, S. Braccini, A. Brillet, V. Brisson, L. Brocco, D. Buskulic, G. Calamai, E. Calloni, E. Campagna, F. Cavalier, G. Cella, E. Chassande-Mottin, F. Cleva, T. Cokelaer, G. Conforto, C. Corda, P. J.-Coulon, E. Cuoco, V. Dattilo, M. Davier, R. De Rosa, L. Di Fiore, A. DiVirgilio, B. Dujardin, A. Eleuteri, D. Enard, I. Ferrante, F. Fidecaro, I. Fiori, R. Flaminio, J.-D. Fournier, S. Frasca, F. Frasconi, L. Gammaitoni, A. Gennai, A. Giazotto, G. Giordano, G. Guidi, H. Heitmann, P. Hello, P. Heusse, L. Holloway, S. Kreckelberg, P. LaPenna, V. Loriette, M. Loupias, G. Losurdo, M. J.-Mackowski, E. Majorana, C. N. Man, F. Marion, F. Martelli, A. Masserot, L. Massonnet, M. Mazzoni, L. Milano, J. Moreau, F. Moreau, N. Morgado, F. Mornet, B. Mours, J. Pacheco, A. Pai, C. Palomba, F. Paoletti, R. Passaquieti, D. Passuello, B. Perniola, L. Pinard, R. Poggiani, M. Punturo, P. Puppo, K. Qipiani, J. Ramonet, P. Rapagnani, V. Reita, A. Remillieux, F. Ricci, I. Ricciardi, G. Russo, S. Solimeno, R. Stanga, A. Toncelli, M. Tonelli, E. Tournefier, F. Travasso, H. Trinquet, M. Varvella, D. Verkindt, F. Vetrano, O. Veziant, A. Vicere, J.-Y. Vinet, H. Vocca, and M. Yvert. Status of virgo. *Class. Quantum Grav.*, 21(5):385–394, 2004.
- [3] B.C. Barish and R. Weiss. Ligo and the detection of gravitational waves. *Physics Today*, 52:44–50, 1999.
- [4] A. Abramovici, W. E. Althouse, R. W. P. Drever, Y. Gursel, S. Kawamura, F. J. Raab, D. Shoemaker, L. Sievers, R. E. Spero, K. S. Thorne, R. E. Vogt, R. Weiss, S. E. Whitcomb, and M. E. Zucker. Ligo: the laser interferometer gravitational-wave observatory. *Science*, 256(5055):325–333, 1992.
- [5] B. Willke, P. Aufmuth, C. Aulbert, S. Babak, R. Balasubramanian, B. W. Barr, S. Berukoff, G. Cagnoli, A. C. Cantley, M. M. Casey, S. Chelkowski, D. Churches, C. N. Colacino, D. R. M. Crooks, C. Cutler, K. Danzmann, R. Davies, R. J. Dupuis, E. Elliffe, C. Fallnich, A. Freise, S. Goßler, A. Grant, H. Grote, S. Grunewald, J. Harms, G. Heinzl, I. S. Heng, A. Hepstonstall, M. Heurs, M. Hewitson, S. Hild, J. Hough, R. Ingley, Y. Itoh, O. Jennrich, R. Jones, S. H. Hutter, K. Kawabe, C. Killow, K. Kötter, B. Krishnan, V. Leonhardt, H. Lück, B. Machenschalk, M. Malec, R. A.

- Mercer, C. Messenger, S. Mohanty, K. Mossavi, S. Mukherjee, S. Nagano, G. P. Newton, M. A. Papa, M. Perreur-Lloyd, M. Pitkin, M. V. Plissi, V. Quetschke, V. Re. S. Reid, L. Ribichini, D. I. Robertson, N. A. Robertson, S. Rowan, A. Rüdiger, B. S. Sathyaprakash, R. Schilling, R. Schnabel, B. F. Schutz, F. Seifert, A. M. Sintes, J. R. Smith, P. H. Sneddon, K. A. Strain, I. Taylor, C. I. Torrie, C. Ungarelli, A. Vecchio, H. Ward, U. Weiland, H. Welling, P. Williams, W. Winkler, G. Woan, and I. Zawischa. Status of geo600. *Class. Quantum Grav.*, 21(5):417–423, 2004.
- [6] P. R. Saulson. *Fundamentals of interferometric gravitational wave detectors*. World Scientific Publishing Co. Pte. Ltd., 1994.
- [7] G. Goßler. *The suspension system of the interferometric gravitational-wave detector GEO 600*. PhD thesis, Gottfried Wilhelm Leibniz Universität Hannover, May 2004.
- [8] F. Antonucci, M. Armano, H. Audley, G. Auger, M. Benedetti, P. Binetruy, J. Bogenstahl, D. Bortoluzzi, P. Bosetti, N. Brandt, M. Caleno, P. Caaizares, A. Cavalleri, M. Cesa, M. Chmeissani, A. Conchillo, G. Congedo, I. Cristofolini, M. Cruise, K. Danzmann, F. De Marchi, M. Diaz-Aguilo, I. Diepholz, G. Dixon, R. Dolesi, N. Dunbar, J. Fauste, L. Ferraioli, V. Ferrone, W. Fichter, E. Fitzsimons, M. Freschi, A. Garcia Marin, C. Garcia Marirrodriga, R. Gerndt, L. Gesa, F. Gilbert, D. Giardini, C. Grimani, A. Grynagier, B. Guillaume, F. Guzman, I. Harrison, G. Heinzel, V. Hernandez, M. Hewitson, D. Hollington, J. Hough, D. Hoyland, M. Hueller, J. Huesler, O. Jennrich, P. Jetzer, B. Johlander, N. Karnesis, C. Killow, X. Llamas, I. Lloro, A. Lobo, R. Maarschalkerweerd, S. Madden, D. Mance, I. Mateos, P. W. McNamara, J. Mendes, E. Mitchell, A. Monsky, D. Nicolini, D. Nicolodi, M. Nofrarias, F. Pedersen, M. Perreur-Lloyd, E. Plagnol, P. Prat, G. D. Racca, J. Ramos-Castro, J. Reiche, J. A. Romera Perez, D. Robertson, H. Rozemeijer, J. Sanjuan, A. Schleicher, M. Schulte, D. Shaul, L. Stagnaro, S. Strandmoe, F. Steier, T. J. Sumner, A. Taylor, D. Texier, C. Trenkel, H.-B. Tu, S. Vitale, G. Wanner, H. Ward, S. Waschke, P. Wass, W. J. Weber, T. Ziegler, and P. Zweifel. The lisa pathfinder mission. *Classical and Quantum Gravity*, 29(12):124014, 2012.
- [9] P. McNamara. LISA Pathfinder: Mission Status. In *9th LISA Symposium, Paris, 2012*.
- [10] A. Monsky. *Understanding interferometric drag-free sensors in space using intelligent data analysis tools*. PhD thesis, Gottfried Wilhelm Leibniz Universität Hannover, June 2010.
- [11] LISA Technology Package artwork [Online; accessed 10-November-2012]. <http://sci.esa.int/science-e/www/object/index.cfm?fobjectid=42235>.
- [12] F. Steier. *Interferometry techniques for spaceborne gravitational wave detectors*. PhD thesis, Gottfried Wilhelm Leibniz Universität Hannover, November 2008.
- [13] LISA science team. NGO - Unveiling a hidden universe: opening a new chapter of discovery - Assessment Study Report. Technical report, European Space Agency, December 2011.
- [14] D. Weise. OB Requirements Specification and Justification. *Astrium GmbH*, (Doc.No.: LOB-ASD-TN-006-02), 2010.
- [15] L. d’Arcio, J. Bogenstahl, M. Dehne, C. Diekmann, E. D. Fitzsimons, R. Fleddermann, E. Granova, G. Heinzel, H. Hogenhuis, C. J. Killow, M. Perreur-Lloyd,

- J. Pijnenburg, D. I. Robertson, A. Shoda, A. Sohmer, A. Taylor, M. Tröbs, G. Wanner, H. Ward, and D. Weise. Optical bench development for LISA. In *ICSO - International Conference on Space Optics*, 2010.
- [16] G. Hechenblaikner. Measurement of the absolute wavefront curvature radius in a heterodyne interferometer. *Journal of the Optical Society of America*, 27, 2010.
- [17] M. Dehne. *Construction and noise behaviour of ultra-stable optical systems for space interferometers*. PhD thesis, Gottfried Wilhelm Leibniz Universität Hannover, November 2012.
- [18] F. Guzmán Cervantes, F. Steier, G. Wanner, G. Heinzel, and K. Danzmann. Subtraction of test mass angular noise in the LISA technology package interferometer. *Applied Physics B*, 90, 2008.
- [19] R. Fleddermann. *Interferometry for a space-based gravitational wave observatory: reciprocity of an optical fiber*. PhD thesis, Gottfried Wilhelm Leibniz Universität Hannover, January 2012.
- [20] V. Wand. *Interferometry at low frequencies: optical phase measurement for LISA and LISA Pathfinder*. PhD thesis, Gottfried Wilhelm Leibniz Universität Hannover, April 2007.
- [21] C. Braxmaier, A. García, F. Guzmán, G. Heinzel, C. Killow, D. Robertson, F. Steier, V. Wand, and H. Ward. Investigation of noise sources in the LTP interferometer. Technical report, Albert Einstein Institute Hannover, October 2005.
- [22] A. Schreiber. Subpikometer-stabiles Frequenzkonvertierungssystem für die optische Bank von LISA. Bachelor's thesis, Leibniz Universität Hannover, 2011.
- [23] S. V. Dhurandhar. Fundamentals of the LISA stable flight formation. *Classical Quantum Gravity*, 22:481–487, 2005.
- [24] J. Kullmann. *Development of a digital phase measuring system with microradian precision for LISA*. PhD thesis, Gottfried Wilhelm Leibniz Universität Hannover, July 2012.
- [25] Xilinx Virtex-6 FPGA ML605 Evaluation Kit data sheet [Online; accessed 11-November-2012]. <http://www.xilinx.com/products/boards-and-kits/EK-V6-ML605-G.htm>.
- [26] 4dsp FMC 116 data sheet [Online; accessed 11-November-2012]. <http://www.4dsp.com/FMC116.php>.
- [27] Mini Circuits PHP 50 data sheet [Online; accessed 11-November-2012]. <http://217.34.103.131/pdfs/PHP-50+.pdf>.
- [28] Mini Circuits PSC-2-1 data sheet [Online; accessed 11-November-2012]. <http://217.34.103.131/pdfs/PSC-2-1+.pdf>.
- [29] Innolight Mephisto data sheet [Online; accessed 06-August-2010]. http://www.innolight.de/pdf/laser_accessories.pdf.
- [30] Isomet AOM data sheet [Online; accessed 06-August-2010]. <http://www.isomet.com/FinalWebSite/PDFDocs/AO%20Sheets/1205-1206-1250C%20NIR.pdf>.

- [31] H. J. Eichler. *Laser: Bauformen, Strahlführung, Anwendungen*. Springer-Verlag Berlin Heidelberg, 2010.
- [32] Schäfter und Kirchhoff Polarimeter data sheet [Online; accessed 20-July-2012]. http://www.sukhamburg.com/onTEAM/pdf/polarizationAnalyzer_e.pdf.
- [33] E. Morrison, B. J. Meers, D. I. Robertson, and H. Ward. Automatic alignment of optical interferometers. *Applied optics*, 33:5041–5049, 1994.
- [34] E. Morrison, B. J. Meers, D. I. Robertson, and H. Ward. Experimental demonstration of an automatic alignment system for optical interferometers. *Applied optics*, 33:5037–5040, 1994.
- [35] F. Guzman Cervantes. *Gravitational wave observation from space: optical measurement techniques for LISA and LISA Pathfinder*. PhD thesis, Gottfried Wilhelm Leibniz Universität Hannover, June 2009.
- [36] G. Heinzel, V. Wand, A. García Marin, O. Jennrich, C. Braxmaier, D. Robertson, K. Middleton, D. Hoyland, A. Rüdiger, R. Schilling, U. Johann, and K. Danzmann. The LTP interferometer and phasemeter. *Classical quantum gravity*, 21, 2003.
- [37] V. Wand, J. Bogenstahl, C. Braxmaier, K. Danzmann, A. Garcia, F. Guzman, G. Heinzel, J. Hough, O. Jennrich, C. Killow, D. Robertson, Z. Sodnik, F. Steier, and H. Ward. Noise sources in the LTP heterodyne interferometer. *Class. Quantum Grav*, 23:159–167, 2006.
- [38] A. F. Garcia Marin. *Minimisation of optical pathlength noise for the detection of gravitational waves with the spaceborne laser interferometer LISA and LISA Pathfinder*. PhD thesis, University of Hannover, July 2007.
- [39] G. Wanner. *Complex optical systems in space: numerical modelling of the heterodyne interferometry of LISA Pathfinder and LISA*. PhD thesis, Gottfried Wilhelm Leibniz Universität Hannover, December 2010.
- [40] G. Hechenblaikner, R. Gerndt, U. Johann, P. Luetzow-Wentzky, V. Wand, H. Audley, K. Danzmann, A. Garcia-Marin, G. Heinzel, M. Nofrarias, and F. Steier. Coupling characterization and noise studies of the optical metrology system onboard the LISA pathfinder mission. *Applied optics*, 49, 2010.
- [41] M. Perreur-Lloyd, C. Killow, E. Fitzsimons, D. Robertson, H. Ward, and A. Taylor. Optical Bench EBB Design Definition File. *University of Glasgow*, (Doc.No.: LOB-UGL-TN-008.2-11), 2011.
- [42] J. Sanjuán Mu noz. *Development and validation of the thermal diagnostics instrumentation in LISA Pathfinder*. PhD thesis, Universitat Politècnica de Catalunya, May 2009.
- [43] PT10k sensor data sheet [Online; accessed 11-October-2012]. http://www.sab-kabel.de/fileadmin/user_upload/pdf/catalog_dt/Thermotechnik_dt/MTE_und_MWT/Grundwerte_der_Messwiderstaende.pdf.
- [44] W. Demtröder. *Experimentalphysik 2 - Elektrizität und Optik*. Springer, 1999.

- [45] B. Kaune. Kontrolle und Charakterisierung von piezobetriebenen Kipp- und Linearaktuatoren für die optische von Bank von LISA. Bachelor's thesis, Leibniz Universität Hannover, 2011.
- [46] J. Bogenstahl. Interferometer zur Charakterisierung von optischen Komponenten. Master's thesis, Universität Hannover, 2005.
- [47] J. Bogenstahl, M. Tröbs, and J.-S. Hennig. Telescope simulator design. *Albert Einstein Institute Hannover*, (Doc.No.: LOB-AEI-TN-0102), 2012.
- [48] R. Fleddermann, M. Tröbs, F. Steier, G. Heinzl, and K. Danzmann. Intrinsic noise and temperature coefficients of selected voltage references. *IEEE Transactions on instrumentation and measurement*, 58:2002–2007, 2009.
- [49] J. A. C. M. Pijnenburg and N. Rijnveld. Picometer stable scan mechanism for gravitational wave detection in space: LISA PAAM. In *ICSO - International Conference on Space Optics*, 2010.
- [50] Newport AG-LS25V6 data sheet [Online; accessed 17-October-2012]. http://search.newport.com/?q=*x2=sku&q2=AG-LS25V6.
- [51] Newport AG-M100LV6 data sheet [Online; accessed 17-October-2012]. http://search.newport.com/?q=*x2=sku&q2=AG-M100LV6.
- [52] O. Kranz. Suspension Platform Interferometer. Diploma thesis, Leibniz Universität Hannover, 2009.
- [53] Corning ULE datasheet [Online; accessed 29-October-2012]. <http://www.corning.com/docs/specialtymaterials/pisheets/UleBro91106.pdf>.
- [54] I. Libman. Design and characterisation of a thermal shield for LISA optical bench testing. Bachelor's thesis, Leibniz Universität Hannover, 2011.
- [55] Innolight iodine-stabilised Nd:YAG laser data sheet [Online; accessed 20-July-2012]. http://www.innolight.de/fileadmin/user_upload/produktblatt_pdf/Produktblatt_Laser_Accessoires.pdf.
- [56] T. Schuldt. Frequenzstabilisierter Nd:YAG-Laser für Weltraumanwendungen. Diploma thesis, Universität Hamburg, 2003.
- [57] Schäfter und Kirchhoff polarisation-maintaining fibre data sheet [Online; accessed 20-July-2012]. http://www.sukhamburg.com/onTEAM/pdf/smfkb_e.pdf.
- [58] First Sensor PC50-6 data sheet [Online; accessed 19-July-2012]. http://www.first-sensor.com/sites/www.first-sensor.com/files/downloads/datasheets/optical_sensors/components/detectors/pin_photodiodes/series_6/pc50-6-500103.pdf.
- [59] S. Alexander. *Optical communication receiver design*. SPIE Optical Engineering Press, 1997.
- [60] M. Tröbs. *Laser development and stabilization for the spaceborne interferometric gravitational wave detector LISA*. PhD thesis, Gottfried Wilhelm Leibniz Universität Hannover, February 2005.

- [61] S. Skorupka. *Rauschuntersuchungen an hochstabilen Lasersystemen für die wissenschaftliche Weltraummission LISA*. PhD thesis, Gottfried Wilhelm Leibniz Universität Hannover, June 2007.
- [62] Innolight Prometheus data sheet [Online; accessed 06-August-2010]. http://www.innolight.de/fileadmin/user_upload/produktblatt_pdf/Produktblatt_Prometheus_Diabolo.pdf.
- [63] Stanford Research SR 620 data sheet [Online; accessed 18-June-2012]. http://www.rohde-schwarz.de/file_13094/SR620c_rev_RS_12-2009.pdf.
- [64] J. C. Owen. Optical refractive index of air: dependence on pressure, temperature and composition. *Applied Optics*, 6:51–59, 1967.
- [65] Schott ZerodurTM data sheet no. 1 [Online; accessed 20-August-2012]. http://www.schott.com/advanced_optics/german/download/schott_zerodur-cte_may_2012_eng.pdf.
- [66] Schott ZerodurTM data sheet no. 2 [Online; accessed 20-August-2012]. http://www.schott.com/advanced_optics/german/download/schott_zerodur_katalog_july_2011_en.pdf.
- [67] Fused silica physical properties [Online; accessed 25-October-2012]. <http://accuratus.com/pdf/SiO2props.pdf>.
- [68] J. J. Wray. Refractive index of several glasses as a function of wavelength and temperature. *Journal of the optical society of america*, 59, 1969.
- [69] Hygrosens SEMI833ET data sheet [Online; accessed 25-October-2012]. http://www.produktinfo.conrad.com/datenblaetter/175000-199999/188506-da-01-de-NTC_833_TEMPERATURSENSOR.pdf.
- [70] Schott optical transmission of ZerodurTM [Online; accessed 20-August-2012]. http://www.schott.com/advanced_optics/german/download/tie-43_properties_of_zerodur.pdf.
- [71] W. Demtröder. *Experimentalphysik 3 - Atome, Moleküle und Festkörper*. Springer, 2000.
- [72] Corning optical transmission of ULE [Online; accessed 29-October-2012]. <http://www.pgo-online.com/intl/katalog/ule.html>.
- [73] J. Bogenstahl. *Interferometry for the space mission LISA Pathfinder*. PhD thesis, Department of Physics and Astronomy, University of Glasgow, February 2010.
- [74] Aluminum reflectivity [Online; accessed 30-Oktober-2012]. <http://en.wikipedia.org/wiki/Reflectivity>.
- [75] RUAG MLI foil Coolcat 2 data sheet [Online; accessed 30-October-2012]. http://www.ruag.com/space/Products/Satellite_Structures2C_Mechanisms_Mechanical_Equipment/Thermal_Systems/Cryogenic_Insulation_Coolcat/Coolcat_Products.
- [76] Invar physical properties [Online; accessed 23-Oktober-2012]. <http://en.wikipedia.org/wiki/Invar>.

- [77] F. G. Hey. Mount design for telescope and pm simulator actuators. *Astrium GmbH*, (Doc.No.: LOB-MO-008-01-ASD), 2012.
- [78] T. Peikert. Systematische Entwurfsmethoden rauscharmer Photodetektor-Verstärkerschaltungen für satellitengestützte Präzisionsinterferometer. Diploma thesis, Leibniz Universität Hannover, 2011.
- [79] S. Weber. Kreuzkopplung von Verkippungen in das longitudinale Signal in der Präzisionsinterferometrie. Diploma thesis, Leibniz Universität Hannover, 2012.
- [80] Thorlabs XY flexure mount data sheet [Online; accessed 22-August-2012]. <http://www.thorlabs.com/thorProduct.cfm?partNumber=CP1XY>.
- [81] T. Williams. *The circuit designer's companion*. Newnes, 2008.
- [82] H. W. Ott. *Noise reduction techniques in electronic systems, second edition*. John Wiley & Sons, 1988.
- [83] S. Barke. Inter-spacecraft clock transfer phase stability for the Laser Interferometer Space Antenna. Diploma thesis, Leibniz Universität Hannover, 2008.
- [84] A. Pal-Singh. Computation of phase-stability over temperature - Thermal testing of microwave cables for the Laser Interferometer Space Antenna. Bachelor's thesis, Leibniz Universität Hannover, 2010.
- [85] Agilent 4396B datasheet [Online; accessed 25-July-2012]. <http://cp.literature.agilent.com/litweb/pdf/5965-6311E.pdf>.
- [86] C. Diekmann, F. Steier, B. Sheard, G. Heinzl, and K. Danzmann. Analog phase lock between two lasers at LISA power levels. *Journal of Physics: Conference Series* 154, 154, 2009.
- [87] C. Diekmann. Phasenstabilisierung und -auslesung für LISA. Diploma thesis, Leibniz Universität Hannover, 2008.
- [88] J. J. Esteban Delgado. *Laser ranging and data communication for the Laser Interferometer Space Antenna*. PhD thesis, Gottfried Wilhelm Leibniz Universität Hannover, January 2012.
- [89] M. Tröbs, L. d'Arcio, S. Barke, J. Bogenstahl, M. Dehne, C. Diekmann, E. D. Fitzsimons, R. Fleddermann, O. Gerberding, J.-S. Hennig, F. G. Hey, H. Hogenhuis, C. J. Killow, E. Kochkina, M. Lieser, S. Lucarelli, M. Perreur-Lloyd, J. Pijnenburg, D. I. Robertson, A. Shoda, A. Sohmer, A. Tayler, G. Wanner, H. Ward, D. Weise, and K. Danzmann. Testing the LISA optical bench. In *ICSO - International Conference on Space Optics*, 2012.
- [90] T. N. Swe and K. S. Yeo. An accurate photodiode model for DC and high frequency SPICE circuit simulation. *Nanotech*, 1:362–365, 2001.
- [91] Linear Technology LT Spice IV Homepage [Online; accessed 15-November-2012]. <http://www.linear.com/designtools/software/#LTspice>.
- [92] D. Kundu, D. Sarker, Md. G. Hasan, P. Podder, and Md. M. Rahman. Performance analysis of an InGaAs based p-i-n photodetector. *International journal of soft computing and engineering*, 2:316–321, 2012.

- [93] G. Wang, T. Tokumitsu, I. Hanawa, Y. Yoneda, K. Sato, and M. Kobayashi. A time-delay equivalent-circuit model of ultrafast p-i-n photodiodes. *IEEE transactions on microwave theory and techniques*, 51:1227–1233, 2003.
- [94] G. Wang, T. Tokumitsu, I. Hanawa, K. Sato, and M. Kobayashi. Analysis of high speed p-i-n photodiodes s-parameters by a novel small-signal equivalent circuit model. *IEEE microwave and wireless component letters*, 12:378–380, 2002.
- [95] First Sensor QP22-Q data sheet [Online; accessed 19-July-2012]. http://www.first-sensor.com/sites/www.first-sensor.com/files/downloads/datasheets/optical_sensors/components/detectors/quadrant_photodiodes_qp_-_qp_series/series_q/qp22-q-501049-chip-500595.pdf.
- [96] OSI Optoelectronic SPOT-9-YAG data sheet [Online; accessed 19-July-2012]. <http://www.oec-gmbh.de/files/pdfs/detectors/yag.pdf>.
- [97] Excelitas YAG-444-4AH data sheet [Online; accessed 19-July-2012]. http://www.excelitas.com/downloads/ingaas_si_pin_diodes.pdf.
- [98] R. Flatscher. Performance measurements on qp22e photodiodes from lewicki and degradation by irradiation. *Astrium GmbH*, (QP22E Post-radiation Performance Test Results), 2010.
- [99] M. Mehmet, S. Ast, T. Eberle, S. Steinlechner, H. Vahlbruch, and R. Schnabel. Squeezed light at 1550 nm with a quantum noise reduction of 12.3 dB. *Opt. Express*, 19(25):25763–25772, Dec 2011.
- [100] A. Joshi, J. Rue, and S. Datta. Low-noise large-area quad photoreceivers based on low-capacitance quad InGaAs photodiodes. *IEEE Photonics Technology Letters*, 12(21), 2009.
- [101] S. Datta, A. Joshi, and J. Rue. Large-area InGaAs quad photoreceiver for laser interferometer space antenna. *Proceedings of SPIE*, 7817, 2010.
- [102] Excelitas ADP receiver modules data sheet [Online; accessed 27-November-2012]. http://www.excelitas.com/downloads/DTS_LLAM.pdf.
- [103] G. Heinzl. *Advanced optical techniques for laser-interferometric gravitational-wave detectors*. PhD thesis, Gottfried Wilhelm Leibniz Universität Hannover, February 1999.
- [104] Ophir NOVA II power meter data sheet [Online; accessed 24-November-2012]. http://www.ophiropt.com/laser/pdf/nova_ii_catalog.pdf.
- [105] Ophir PD300 power sensor data sheet [Online; accessed 24-November-2012]. http://www.ophiropt.com/laser/pdf/PD300_PD300-1W_PD300-3W_PD300-TP.pdf.
- [106] Excelitas 30619GH data sheet [Online; accessed 27-November-2012]. <http://www.excelitas.com/Lists/Photodiodes%20and%20Phototransistors/DispForm.aspx?ID=130>.
- [107] J. Burkhardt, T. de la Villegeorges, and D. Weise. Analyses and specifications for ob detailed design. *Astrium GmbH*, (Doc.No.: LOB-TN-007-02-ASD), 2011.

- [108] G. Lucovsky, R. F. Schwarz, and R. B. Emmons. Transit-time considerations in p-i-n diodes. *Journal of applied physics*, 35:622–628, 1964.
- [109] F. Guzman Cervantes, J. Livas, R. Silverberg, E. Buchanan, and R. Stebbins. Characterization of photoreceivers for LISA. *Classical quantum gravity*, 28, 2011.
- [110] Texas Instruments LMH6624 data sheet [Online; accessed 18-November-2012]. <http://www.ti.com/lit/ds/symlink/lmh6624.pdf>.
- [111] T. Vanisri and C. Toumazou. On the design of low-noise current-mode optical preamplifiers. *Analog Integrated Circuits and Signal Processing*, 2, 1992.
- [112] T. Vanisri and C. Toumazou. Integrated high frequency low-noise current-mode optical transimpedance preamplifiers: theory and practice. *IEEE Journal of solid-state circuits*, 30, 1995.
- [113] Infineon BFR 181 data sheet [Online; accessed 14-November-2012]. <http://www.infineon.com/dgdl/bfr181.pdf?folderId=db3a30431400ef68011425b1354605c1&fileId=db3a30431400ef680114268848380638>.
- [114] D. A. Neamen. *Microelectronics: Circuit analysis and design, third edition*. McGraw-Hill, 2007.
- [115] J. Ardizzoni. A practical guide to high-speed printed-circuit-board layout. *Analog Dialogue*, 39(09), 2005.
- [116] D. Grant and S. Wurcer. Avoiding passive-component pitfalls. *Analog Dialogue*, 17(02), 1983.
- [117] Murata NFM41PC204 data sheet [Online; accessed 27-November-2012]. <http://search.murata.co.jp/Ceramy/image/img/PDF/ENG/L0111S0111NFM41P.pdf>.
- [118] Comparison of two- and three-terminal capacitors [Online; accessed 27-November-2012]. <http://www.murata.com/products/emc/knowhow/pdf/20to22.pdf>.
- [119] Wuerth 30 MHz ferrite data sheet [Online; accessed 27-November-2012]. <http://katalog.we-online.de/pbs/datasheet/74279219.pdf>.
- [120] P. Brokaw and J. Barrow. Grounding for low- and high-frequency circuits. *Analog Dialogue*, 23(03), 1989.
- [121] Analog Devices OP 2177 data sheet [Online; accessed 24-November-2012]. http://www.analog.com/static/imported-files/data_sheets/OP1177_2177_4177.pdf.
- [122] Analog Devices AD8005 data sheet [Online; accessed 24-November-2012]. http://www.analog.com/static/imported-files/data_sheets/AD8005.pdf.
- [123] Shane Larson. LISA: A modern astrophysical observatory. 33rd SLAC Summer Institute on Particle Physics (SSI 2005), 2005.

- [124] M. Tinto and J. W. Armstrong. Cancellation of laser noise in an unequal-arm interferometer detector of gravitational radiation. *Phys. Rev. D*, 59, 1999.
- [125] P. Gath, D. Weise, H. R. Schulte, P. Gath, and U. Johann. LISA mission and system architectures and performances. *Journal of Physics: Conference Series*, 154, 2009.
- [126] D. R. Weise, P. Marenaci, P. Weimer, H. R. Schulte, P. Gath, and U. Johann. Alternative opto-mechanical architectures for the LISA instrument. *Journal of Physics: Conference Series*, 154, 2009.
- [127] J. Rybizki. LISA back-link fibre: back reflection of a polarization maintaining single-mode optical fiber, Master thesis. Diploma thesis, Leibniz Universität Hannover, 2011.
- [128] Y. Painchaud, M. Poulin, M. Morin, and M. Tetu. Performance of balanced detection in a coherent receiver. *Optical Society of America*, 17:3659–3672, 2009.
- [129] D. Robertson and E. Fitzsimons. Functional Test Plan. *University of Glasgow*, (Doc.No.: LOB-UGL-TN-009.1), 2011.
- [130] D. Shoemaker, R. Schilling, L. Schnupp, W. Winkler, K. Maischberger, and A. Rüdiger. Noise behavior of the Garching 30-meter prototype gravitational-wave detector. *Physical Review D - Particles and Fields*, 38(2), 1988.
- [131] S. Hild, H. Grote, J. R. Smith, and M. Hewitson. Towards gravitational wave astronomy: Commissioning and characterization of GEO 600. *Classical quantum gravity*, 21, 2003.
- [132] Laser 2000 beam splitter/combiner data sheet [Online; accessed 02-October-2012]. <http://www.laser2000.de/fileadmin/Produktdaten/SIG/Datenblaetter/SIG-039-02xx.pdf>.
- [133] J. Noda, K. Okamoto, and Y. Sasaki. Polarization-maintaining fibers and their applications. *Journal of lightwave technology*, LT-4:1071 – 1089, 1986.
- [134] Fujikura polarisation-maintaining fibre overview [Online; accessed 19-November-2012]. http://www.fujikura.co.jp/eng/products/tele/o_device/data/16pnb04.pdf.
- [135] Pro-lite carbon fiber breadboard data sheet [Online; accessed 09-July-2012]. http://www.pro-lite.co.uk/File/EC-Series_Breadboard.php.
- [136] G. F. Franklin, J. D. Powell, and A. Emami-Naeini. *Feedback control of dynamic systems*. Pearson Education, Inc., 5 edition, 2006.

Acknowledgements

The LISA project is a fascinating field of science to work in. I enjoyed my time in the LISA group at the AEI and it was a privilege for me to contribute to the development of an optical bench for LISA.

I would like to thank Prof. Dr. Karsten Danzmann for giving me the opportunity to work in the LISA optical bench project and for making the AEI such a valuable institute in the LISA community.

The knowledge of PD Dr. Gerhard Heinzl about electronics and interferometry widened my horizon. His approaches and hints to solve problems in an experiment are inestimable and his recommendations for items to investigate motivated me a lot during my time at the AEI. Thank you, Gerhard.

I would like to thank Dr. Michael Tröbs for supervising and supporting me in the LISA optical bench project in the last years.

I appreciated the work with Roland Fleddermann on the backlink fibre experiment in the first year of my PhD time. The discussions with him about the experiment helped me to deepen my understanding of interferometry.

I thank Katrin, Michael, and Gerhard for proof-reading my thesis. Your comments and suggestions for improvement raised the quality of my thesis a lot.

Last but not least I thank Katrin for supporting me in every part of my life during the time of writing my PhD thesis.

Curriculum vitae

Personal details

Name	Christian Diekmann
Nationality	German
Date of birth	28.10.1980
Place of birth	Cloppenburg, Germany

School education

1987 - 1991	Grundschule Galgenmoor, Cloppenburg
1991 - 1993	Orientierungsstufe Cappelner Damm, Cloppenburg
1993 - 2001	Clemens August Gymnasium, Cloppenburg

University education

2002 - 2008	Diploma studies in physics at the Leibniz Universität Hannover
03 / 2008	Physik-Diplom, Leibniz Universität Hannover
2008 - 2012	Doctoral Studies in physics at the Leibniz Universität Hannover Member of the International Max-Planck-Research School Scientific assistant at the Max-Planck Institute for gravitational physics (Albert-Einstein-Institute) Hannover

2012

M. Tröbs, L. d'Arcio, S. Barke, J. Bogenstahl, M. Dehne, **C. Diekmann**, E. D. Fitzsimons, R. Fleddermann, O. Gerberding, J.-S. Hennig, F.G. Hey, H. Hogenhuis, C.J. Killow, E. Kochkina, M. Lieser, S. Lucarelli, M. Perreur-Lloyd, J. Pijenburg, D. I. Robertson, A. Shoda, A. Sohmer, A. Tayler, G. Wanner, H. Ward, D. Weise and K. Danzmann. Testing the LISA optical bench. International Conference on Space Optics, 2012.

L. d'Arcio, J. Bogenstahl, **C. Diekmann**, E. D. Fitzsimons, G. Heinzl, H. Hogenhuis, C. J. Killow, M. Lieser, M. Perreur-Lloyd, J. Pijenburg, D. I. Robertson, A. Taylor, M. Tröbs, H. Ward and D. Weise. An Elegant Breadboard of the Optical Bench for eLISA/NGO. International Conference on Space Optics, 2012.

2010

L. d'Arcio, J. Bogenstahl, M. Dehne, **C. Diekmann**, E. D. Fitzsimons, R. Fleddermann, E. Granova, G. Heinzl, H. Hogenhuis, C. J. Killow, M. Perreur-Lloyd, J. Pijenburg, D. I. Robertson, A. Shoda, A. Sohmer, A. Taylor, M. Tröbs, G. Wanner, H. Ward and D. Weise. Optical Bench Development for LISA. International Conference on Space Optics, 2010.

2009

F. Steier, R. Fleddermann, J. Bogenstahl, **C. Diekmann**, G. Heinzl and K. Danzmann, Construction of the LISA back-side fibre link interferometer prototype. Classical and Quantum Gravity, 26, 175016, 2009.

C. Diekmann, F. Steier, B. Sheard, G. Heinzl and K. Danzmann. Analog phase lock between two lasers at LISA power levels. Journal of Physics: Conference Series 154, 012020, 2009.

In preparation

R. Fleddermann, **C. Diekmann**, F. Steier, M. Tröbs, G. and K. Danzmann. Successful demonstration of stray light subtraction in data post-processing for the LISA backlink fiber non-reciprocity experiment.

C. Diekmann, R. Fleddermann, F. Steier, M. Tröbs, G. Heinzl and K. Danzmann. Demonstration of pm/ $\sqrt{\text{Hz}}$ precision for displacement measurements.